THE HONG KONG POLYTECHNIC UNIVERSITY

DEPARTMENT OF CIVIL AND ENVIRONMENTAL ENGINEERING

CROSSWIND EFFECTS ON ROAD VEHICLES MOVING ON GROUND AND LONG-SPAN BRIDGES

Bin Wang

A thesis submitted in partial fulfillment of the requirements for the

Degree of **Doctor of Philosophy**

February 2014

CERTIFICATE OF ORIGINALITY

I hereby declare that this dissertation entitled "***Crosswind Effects on Road Vehicles Moving on Ground and Long-Span Bridges***" is my own work and that, to the best of my knowledge and belief, it reproduces no material previously published or written, nor material that has been accepted for the award of any other degree or diploma, except where due acknowledgement has been made in the text.

___________________________ (Signed)

Bin Wang (Name of student)

To my family

for their love and support

ABSTRACT

This thesis mainly focuses on the ride comfort and safety of road vehicles moving on either the ground or long-span bridges under crosswinds using advanced vehicle models and considering aerodynamic interferences among moving vehicles, bridge deck, bridge tower and the ground.

The aerodynamic interferences between a moving vehicle and the ground are first explored using the Computational Fluid Dynamics (CFD) technique. A delicate numerical model simulating the flows around a stationary road vehicle on the ground is set up. The aerodynamic forces on the vehicle are computed in terms of the aerodynamic coefficients of the vehicle under different yaw angles. The computed aerodynamic coefficients are compared with wind tunnel test results, and the comparison is very good. The validated numerical model is then extended to simulate the flows around the moving vehicle by considering a moving ground simulation. The aerodynamic coefficients of the moving vehicle on the ground are accordingly determined and compared with those of the stationary vehicle on the ground. The comparative results show that the motion of the ground affects the flows around the vehicle only in the boundary layer of the ground and the flows around and the pressure distributions over the surfaces of the vehicle are slightly affected. The effects become even weak with the increase of yaw angle. The aerodynamic coefficients of the chosen moving vehicle show no obvious differences with these on the stationary vehicle if the relative motion between the vehicle and the ground is taken into account as currently adopted.

An advanced vehicle model is then presented in order to demonstrate the progressive instability of the moving vehicle on the ground with emphasis in the lateral motions under the action of both crosswinds and drivers. The dynamic equations of the vehicle model are established in a local coordinate system fixed on the vehicle body. The small displacement assumption commonly used in the previous studies is no

longer required. Some of the tires can be allowed to lose contact with the road. The traditional singe-variable random method to simulate the road surface roughness in a line is extended to model the surface roughness in a plane to consider the asynchronous road excitation to the wheels of the two sides of the vehicle. The wind loads on the vehicle are the function of not only wind speeds but also the attitude of the vehicle. Based on the advanced model and using the aerodynamic coefficients determined by CFD, the progressive instability of the moving vehicle is demonstrated. The safety and ride comfort of the moving vehicle on the ground are assessed against several criteria. The critical vehicle speeds are given as the function of the critical wind speed for practical use.

The aerodynamic interferences between a moving vehicle and the deck of a real long span bridge are explored using the CFD. A new numerical model simulating the flows around the stationary vehicle on the first lane of the bridge deck is generated. The aerodynamic coefficients of the stationary vehicle on the bridge deck are computed and compared with the results from wind tunnel tests, and the comparison is found satisfactory. The simulation of the relative motion between the vehicle and the deck is achieved by considering a moving deck simulation. The computer simulation shows that the movement of the vehicle on the first lane of the bridge deck does affect the aerodynamic coefficients of the bridge deck but has only slight effects on the aerodynamic coefficients of the vehicle if the relative motion between the vehicle and the deck is taken into account.

A new framework of the coupled Road Vehicle-Bridge-Wind (RVBW) system is then formed by incorporating the advanced road vehicle model, the road roughness in plane, and the driver's model. The ride comfort of the moving vehicle on the bridge deck is investigated. The wind loads on both the vehicle and the bridge deck are updated with the computed aerodynamic coefficients considering the interference between the moving vehicle and the bridge deck. The computed results show that the slight differences exist if adopting the aerodynamic coefficients of a road vehicle on the ground and the aerodynamic coefficients of the pure bridge deck compared with the actual aerodynamic coefficients in the situation of the moving vehicle on the deck. The ride comfort of the moving vehicle over a long span cable-stayed bridge is evaluated in terms of ISO criteria and compared with that of the vehicle on the ground situation. Slight differences exist in the ride comfort of the single vehicle moving on the ground and the bridge deck.

The variation of aerodynamic forces on the vehicle during its passage by the bridge tower and the shielding effects of the tower are also investigated using CFD. A lower-level numerical model is set up to simulate the flows around a stationary vehicle on the deck at different locations relative to the bridge tower. The computed aerodynamic forces on the vehicle are compared with the results from wind tunnel tests. It is found that the simulated aerodynamic coefficients are in general larger than those measured from the wind tunnel. Since the vehicle-deck-tower system is very complicated and there are uncertainties in both numerical simulation and wind tunnel test, it is difficult to judge the accuracy of the numerical simulation at this moment. The CFD simulation is then extended to simulate the motion of the vehicle using the dynamic mesh method. The computed results show that the shielding effects of the tower on the aerodynamic forces of the moving vehicle are very significant. The aerodynamic coefficients exhibit sharp changes.

The framework of the RVBW system incorporated with the advanced road vehicle model is then employed to assess the safety of a road vehicle passing by a bridge tower. The computed varying aerodynamic coefficients of the moving vehicle passing by a bridge tower are formulized and incorporated into the RVBW system. The computation results show that neglecting the variation of aerodynamic coefficients induced by the tower would underestimate the overturning and course deviation risk of the vehicle passing by the bridge tower. It is also found that the dynamic responses of the bridge deck have slightly effects on the safety of the vehicle passing by the tower, and using the ground condition with the existence of the tower is feasible to assess the safety of a single vehicle passing by a bridge tower. Compared with the moving vehicle on the ground, the critical vehicle speed/critical wind speed of the vehicle passing by the tower is much lower.

LIST OF PUBLICATIONS

Refereed Journal Papers:

Wang, B., Xu, Y. L., Zhu, L. D., Cao, S. Y. and Li, Y. L. (2013). Determination of Aerodynamic Forces on Stationary/Moving Vehicle-Bridge Deck System under Crosswinds Using Computational Fluid Dynamics. *Engineering Applications of Computational Fluid Mechanics*, *7*(3), 355-368.

Li, Y. L., Xiang, H. Y., **Wang, B.**, Xu, Y. L. and Qiang, S. Z. (2013). Dynamic Analysis of Wind-Vehicle-Bridge Coupling System during the Meeting of Two Trains. *Advances in Structural Engineering*, *16*(10), 1663-1670.

Wang B., Xu, Y. L., Zhu, L. D. and Li, Y. L. (2013). Crosswind Effects on High-sided Road Vehicles with and without Movement. *Wind & Structures*, *18*(2), 155-180.

Wang B., Xu, Y. L., Zhu, L. D. and Li, Y. L. (2013). Crosswind Effect Studies on a Road Vehicle Passing by a Bridge Tower Using Computational Fluid Dynamics. *Engineering Applications of Computational Fluid Mechanics* (in press).

Refereed Conference Papers:

Wang B., Xu Y. L., Zhu L. D. and Li, Y. L. (2010). Determination of Aerodynamic Characteristics of Vehicle-Bridge Systems Using Les Method. Proceedings of the Eleventh International Symposium on Structural Engineering, Vol I and II, 1654-1660, Decenber 18-20, Guangzhou.

Wang B., Xu Y. L. and Li, Y. L. (2011). Numerical simulation of aerodynamic characteristics of vehicle-bridge systems. Proceedings of 13th International Conference on Wind Engineering, July 10-15, Amsterdam.

Wang B., Xu Y. L., Zhu L. D. and Li, Y. L. (2012). Determination of aerodynamic characteristics of a vehicle immerged in the wake of bridge tower using computational fluid dynamics. Proceedings of the Seventh International Colloquium on Bluff Body Aerodynamics and Applications, September 2-6, Shanghai.

ACKNOWLEDGEMENTS

I would like to express my sincere gratitude to chief supervisor Prof. You-lin Xu for his excellent guidance, invaluable advise, high responsibility, and deep insight in the scientific research. I sincerely appreciate his efforts for providing me the unique opportunity to pursue my PhD study, which will definitely influence my personal lift in the future. I would also like to thank my co-supervisor Prof. Yong-le Li from Southwest Jiaotong University for this constant encouragement in the course of my PhD project.

I am very grateful to the scholarship from The Hong Kong Polytechnic University through my PhD project and the financial support from the Hong Kong Polytechnic University through its Niche Area Project (1-BB68). Special thanks should go to the staff in the Department of Civil and Environmental Engineering, Library, Research Office, and Finance Office in the university for their kind help.

I particularly thank Prof. Shu-yang Cao from Tongji University for his helpful guidance of computational fluid dynamics. I especially feel gratitude to Prof. Le-dong Zhu and Mr. Lei Li from Tongji University for their excellent results of wind tunnel experiments. I also thank Prof. Jun Teng, Dr. Cao Li, and Dr. Zuo-hua Li from Harbin Institute of Technology Shenzhen Graduate School for their supports in computations. Thanks also given to National Supercomputing Center in Shenzhen and Wuxi Supercomputing Center for the computing time.

Special thanks are also given to my friends and colleagues, Dr. Song-ye, Zhu, Mr. Zhao K. Dr. Juan Zhang, Dr. Zhi-wei Chen, Dr. Xiao-hua Zhang, Dr. Bo Chen, Dr. Hong-wen Xia, Dr. Xian-ting Du, Dr. Liang Hu, Mr. Shen Zhan, Dr. Wen-feng Huang, Dr. Qin Huang, Ms. Ying-jie Jin, Mr. Feng-yang Wang, Mr. Yue Zheng, Mr. Wen-ai Shen, Mr. Qing Zhu, Dr. Lin Huang, Mr. Wen-yu He, Mr. Jin-hua Lin, Mr. Chao-dong Zhang, Ms. Yi-xin Peng, Mr. Xiao-liang Meng, Dr. Xiang Xiao, Dr. Jia, He, Mr. Jian-fu Lin, Mr. Rong-pan Hu, for their constructive discussion.

Finally, I am deeply grateful to my parents, girl friend and her parents, for their constant love and support during my study.

CONTENTS

LIST OF TABLES

LIST OF FIGURES

CHAPTER 1
INTRODUCTION

1.1 MOTIVATION

Road vehicle accidents caused by crosswinds happen throughout the world. Baker and Reynolds (1992) carried out a post-disaster survey of wind induced vehicle accidents that occurred in the United Kingdom during a major storm. In that storm, there were over 400 vehicle accidents. It was also reported that over 5.78 million vehicle accidents occur on highways each year in the USA, and 23% of them are caused by slick pavement or adverse weather conditions including crosswinds (Federal Highway Administration, 2014). In China, the public data show that about 2.65, 2.38, and 3.90 million vehicle accidents occurred in 2008, 2009, and 2010, respectively (Transport Administration of Public Security Ministry of China, 2014), in which crosswind was a significant factor causing the vehicle accidents.

To meet the requirements of modern society for safe, efficient and convenient transportation systems, many long span bridges have been built around the world. The examples of long span suspension bridges are the Akashi Kaikyo Bridge in Japan with a main span of 1,991m, the Xihoumen Bridge in China with a main span of 1,650m, and the Great Belt Bridge in the Denmark with a main span of 1,624m. The examples of long span cable-stayed bridges are the Russky Bridge in Russia with a main span of 1104m, the Sutong Bridge in China with a main span of 1088m, and the Stonecutters Bridge in Hong Kong with a main span of 1018m. The probability becomes higher and higher that road vehicles running on bridges are subject to crosswinds. As road vehicles are running on a long span bridge under crosswinds, the complicated dynamic interaction among road vehicles, bridge and wind occurs. Since long span bridges tend to be flexible and lightly damped, considerable wind-induced forces and vibrations happen within a wide range of wind speeds. The wind-induced responses of the bridge are superimposed with the dynamic responses of the bridge caused by the running vehicles. The large vibration of the bridge will, in turn, affect considerably the safety and ride comfort of the road vehicles. Furthermore, vehicles running on a long span bridge may significantly change the aerodynamic forces of the bridge due to the alteration of wind flow around the bridge deck caused by the presence of the vehicles. On the other hand, a complex wind environment is generated around the moving vehicle because of the geometric shape of bridge deck and the layout of rails equipped on the deck. Vehicles have to confront a new situation from crosswinds as they move on the bridge compared with on the ground. Particularly, the vehicles will be shielded from crosswinds and then enter into a sharp crosswind gust when they pass by the bridge tower. In China, it was reported that seven high-sided road vehicles overturned as they moved on the Humen suspension bridge in strong winds in 2004. It was also reported that wind-induced vehicle accidents occurred on the Mingjiang cable-stayed bridge in 2005.

Research works have been therefore carried out on the safety and ride comfort of road vehicle caused by crosswinds. For example, Baker (1986, 1987, 1988), Xu and Guo (2003b), and Chen and Chen (2010) conducted safety analyses of road vehicles on the ground under crosswinds; Guo (2003) studied the ride comfort of a road vehicle on the ground subjected to crosswinds; Xu and Guo (2003a) and Cai and Chen (2004) investigated the dynamic responses of a coupled road vehicle and long span bridge systems under high winds; Xu and Guo (2003a), Cai and Chen (2004), and Cheung and Chan (2010) also analyzed the safety of road vehicles on the bridge under crosswinds. However, the safety related progressive instability of the road vehicle under crosswinds and the ride comfort of the vehicle under the combined action of crosswinds and driver have not been assessed properly. Moreover, the aerodynamic forces on the moving vehicles were approximated using those on the stationary vehicles on the ground. The aerodynamic forces on the bridge deck were also approximated using those on the pure bridge deck. The effects of the aerodynamic interferences among the moving vehicles, bridge deck, bridge tower and the ground were not considered at all.

1.2 OBJECTIVES

This thesis therefore mainly investigates the ride comfort and safety of road vehicles moving on either the ground or long-span bridges under crosswinds with the following specific objectives:

(1) To explore the aerodynamic interferences between a moving vehicle and the ground using Computational Fluid Dynamics (CFD). Find out the feasibility of the currently-used aerodynamic coefficients of the stationary vehicle, without consideration of the relative motion between the vehicle and the wind.

(2) To present an advanced road vehicle dynamic model simulating the progressive instability under the combined action of crosswinds and drive. Assess the safety and ride comfort of a moving vehicle on the ground, based on the advanced model and the computed aerodynamic forces on a moving vehicle.

(3) To reveal the aerodynamic interferences between a moving vehicle and a real long span bridge using CFD. To determine the aerodynamic coefficients of the moving vehicle affected by the bridge deck and those of the bridge with the existence of the moving vehicle.

(4) To present a framework for dynamic analysis of a coupled road vehicle and long span bridge system under crosswinds by integrating the advanced vehicle model and the aerodynamic forces on the moving vehicle and the bridge deck, considering the interferences between them. Compare the ride comfort of the moving vehicle on the bridge with that of the vehicle on the ground.

(5) To investigate the abrupt change of the aerodynamic forces on the vehicle as it passes by the bridge tower using the CFD. To determine the varying aerodynamic coefficients of the vehicle passing by a bridge tower for safety analysis.

(6) To evaluate the safety of a moving vehicle passing by a bridge tower using the proposed framework of road vehicle-bridge-crosswinds and the varying aerodynamic forces acting on the vehicle passing by the bridge tower. Find out the feasibility of neglecting the dynamic responses of the bridge to assess the safety of the moving vehicle passing by the bridge tower. Compare the critical vehicle speed of the vehicle passing by the tower with that of the vehicle on the ground.

1.3 ASSUMPTIONS AND LIMITATIONS

The computation of aerodynamic forces and the assessment of ride comfort and safety of the road vehicle moving on either the ground or a long span bridge in this thesis are subjected to the following assumptions and limitations:

(1) Wind loads on a moving vehicle are determined based on the quasi-steady assumption, in which the averaged aerodynamic coefficients related to the mean wind are used. The effects of turbulence on the averaged aerodynamic coefficients are neglected.

(2) The Reynolds-averaged Navier-Stokes equations method is employed to compute averaged aerodynamic coefficients rather than other advanced methods, such as Large Eddy Simulation or Detached Eddy Simulation, which require tremendous computation efforts for the problems concerned and could hardly be offered by the current used computer.

(3) The mean wind approaching to the road vehicle and the bridge deck is assumed to be perpendicular to the longitudinal axis of the vehicle and the deck. The speeds

of the vehicle wheels are assumed to be equal to the speed of the vehicle along its moving direction and the vehicle speed is assumed to be a constant.

(4) Since the flows around and the aerodynamic forces on a group of vehicles are much more complex than those on a single vehicle, and the relevant studies are beyond this thesis, the ride comfort of the road vehicle moving on the deck and the safety of the vehicle passing by the bridge tower are evaluated based on a single vehicle instead of a group of vehicles.

(5) The equations of motion of both the road vehicle and the bridge are formed and solved in the time domain. In this regard, the fluctuating wind and road roughness are also simulated in the time domain, which are assumed as homogeneous and ergodic random field satisfying a Gaussian distribution with a zero mean.

1.4 LAYOUT OF THE THESIS

This thesis is divided into nine chapters to achieve the aforementioned objectives. Its layout is listed as follows:

Chapter 1 introduces the motivation, objectives, assumptions and limitations for the study and clearly states the layout of the thesis.

Chapter 2 reviews the extensive literature on relevant topics, including aerodynamic forces on road vehicles, response analyses of road vehicles on the ground, response analyses of road vehicles on a bridge deck, response analyses of road vehicles passing by a bridge tower, safety and ride comfort evaluation of road vehicles, and basic elements of Computational Fluid Dynamics.

Chapter 3 explores the aerodynamic interferences between a moving vehicle and the ground using CFD. A numerical model is set up to simulate the flows around the stationary vehicle on the ground. The computed aerodynamic forces (in terms of aerodynamic coefficients) and surface pressure distributions are validated with the results from wind tunnel experiments at different yaw angles. The numerical model is then extended to simulate the flows around the moving vehicle by considering a moving ground simulation. The computed aerodynamic coefficients are compared with those on the stationary vehicle.

Chapter 4 presents an advanced vehicle model to demonstrate the progressive instability of the moving vehicle on the ground under the action of both crosswinds and drivers. The dynamic equations of motion of the vehicle are established in the local coordinate system fixed on the vehicle body integrated with a simple driver model. Some tires can be allowed to lose contact with the ground. The traditional single-variable random method to model road surface roughness in a line is extended to model the surface roughness in a plane to consider the asynchronous road excitation to the wheels of the two sides of the vehicle. The wind loads on the vehicle depends on not only the wind velocity, but also the attitude of the vehicle. The safety and ride comfort of the vehicle are evaluated against several criteria.

Chapter 5 explores the aerodynamic interferences between a moving vehicle and the deck of a real long span bridge using the CFD. A new numerical model to simulate the flows around the stationary vehicle on the first lane of the bridge deck is formed. The computed aerodynamic coefficients of the stationary vehicle are compared with the results from wind tunnel tests. The simulation of the relative motion between the vehicle and the deck is achieved by considering a moving deck simulation. The computed aerodynamic coefficients are compared with those of the stationary vehicle on the bridge deck.

Chapter 6 forms a new dynamic analysis framework of the coupled Road Vehicle-Bridge-Wind (RVBW) system by incorporating the advanced vehicle model, the road roughness in plane, and the driver model. The wind loads on both the vehicle and the bridge deck are updated with the computed aerodynamic coefficients considering the aerodynamic interference between the moving vehicle and the bridge deck. The effects of the aerodynamic coefficients on the ride comfort of the vehicle are investigated. The ride comfort of the moving road vehicle on the bridge deck is evaluated and compared with that of the moving road vehicle on the ground.

Chapter 7 investigates the variation of the aerodynamic forces on the vehicle passing by a bridge tower employing CFD. A lower-lever numeral model is first established to simulate the flows around a stationary vehicle on the deck at different locations relative to the bridge tower. The computed aerodynamic coefficients of the vehicle are compared with the results from wind tunnel tests. The CFD simulation is then extended to simulate the motion of the vehicle using the dynamic mesh method to study the variation of the aerodynamic coefficients of the moving vehicle during passage by a bridge tower.

Chapter 8 investigates the safety of vehicle passing by the bridge tower based on the proposed dynamic analysis framework of RVBW. The commutated varying aerodynamic coefficients of the moving vehicle passing by the bridge tower are formulized and incorporated into the RVBW framework. The effects of the varying aerodynamic coefficients and the dynamic responses of the bridge on the safety of the vehicle are studied. The accident vehicle speed passing by the bridge tower is assessed and compared with that of the vehicle on the ground.

Chapter 9 summarizes the main conclusions attained from the investigations conducted in this study. Some recommendations for future study are also provided.

CHAPTER 2

LITERATURE REVIEW

As mentioned in Chapter 1, this thesis mainly focuses on the ride comfort and safety of road vehicles moving on either the ground or long-span bridges under crosswinds using advanced vehicle models and considering aerodynamic interferences among moving vehicles, bridge deck, bridge tower and the ground. The current research status of aerodynamic forces on road vehicles, response analyses of road vehicles on the ground, response analyses of road vehicles on a bridge deck, response analyses of road vehicles passing by a bridge tower, and safety and ride comfort evaluation of road vehicles will be reviewed in this chapter. Since this thesis will use the Computational Fluid Dynamics (CFD) technique to explore aerodynamic forces on both the vehicles and the bridge, its basic elements are also presented in this chapter.

2.1 AERODYNAMIC FORCES ON ROAD VEHICLES

Aerodynamic forces acting on road vehicles are determined mainly based on the quasi-steady assumption (Baker, 1986; Sigbjörnsson and Snæbjörnsson, 1998; Xu and Guo, 2003a, b; Cai and Chen, 2004; Cheli *et al*., 2006; Chen and Chen, 2010; Cheung and Chan, 2010). They are the multiplication functions of aerodynamic coefficients and wind velocities referring to the vehicles. Wind velocities are assumed as gust winds or modeled as random processes. The aerodynamic coefficients of road vehicles are obtained normally through field measurements, wind tunnel tests, or numerical simulation using CFD.

2.1.1 Field Measurement

Quinn *et al*. (2007) completed a field measurement work on a fully scaled commercial vehicle to get the aerodynamic coefficients. For the stationary vehicle on the ground, four weigh-pad-load cells were installed beneath the vehicle to get the lift and rotating moment. Forty-eight static pressure probes were distributed on the sides and roof surfaces of the vehicle. The rotating moment was then calculated from the static pressure measured with probes in spite of the lack of information on the pressure contribution over the bottom surface of the vehicle. The measured rotating moment coefficients from both the load cells and the pressure probes were compared. About 9 months were spent for the sake of waiting for the appropriate wind conditions on the stationary vehicle. Then, the vehicle moved on the road and the corresponding rotating moment was measured based on the pressure probes on the sides and roof of the vehicle. In the field measurement mentioned, huge time was required to await adequate wind conditions. Moreover, very limited information could be obtained due to the limitation of equipment, e.g. only the rotating moment from scarce pressure taps on limited surfaces for the moving vehicle in Quinn *et al.* (2007).

2.1.2 Wind Tunnel Test

In a wind tunnel, wind conditions can be adjusted conveniently to test the aerodynamic coefficients compared with the field measurement. Testing the aerodynamic forces on a road vehicle in a wind tunnel thus becomes a most common choice. Early wind tunnel tests focused on the aerodynamic drag and lift forces with winds blowing from the head to the tail without considering crosswinds. Lower drag forces are beneficial to reduce the consumption of fuel, and negative lift forces ensure the vehicles are to be adhered to the road for safety. In the wind tunnel, vehicles were fixed on the ground and winds blew from the head to the tail to model the relative motion between the vehicle and the winds. An important factor in wind tunnel tests without considering crosswinds is to realize the relative motion between a vehicle and the ground to correct the boundary layer of the ground. A couple of techniques were adopted, in which the moving belt provided the ideal simulation of real conditions (Beauvais *et al.*, 1968). In the moving belt method, the vehicle was fixed on the ground and a moving belt was installed under the vehicle. The relative motion between the vehicle and the ground can therefore be realized through setting the velocity of the moving belt. Bonis *et al.* (1987) implied that the moving belt is necessary, depending on the type of the vehicle and the ground clearance. Through the moving belt wind tunnel tests, Fago *et al.* (1991) concluded that the effect of a moving ground was significant for low ground clearance vehicles.

In order to consider the stability of vehicles in crosswinds, the aerodynamic forces including not only the drag force and the lift force but also the side force, yawing moment, rotating moment and pitching moment of stationary vehicles on the ground in crosswinds were measured in wind tunnels. Baker (1988) conducted wind tunnel experiments on a 1/25 scale articulated lorry model in low turbulence winds. The vehicle model was sharp edged and fixed on the ground. As the yaw angle decreases, the measured side force and rotating moment coefficients increased; the lift coefficient increased first and then decreased; the drag coefficient increased first in magnitude and then decreased to zero; and the aerodynamic centre was located behind and above the gravity centre. A similar geometrical vehicle model was then tested with a scale of 1/50 by Coleman and Baker (1990). It was believed that the Reynolds number of the vehicle model of 1/25 to 1/50 length ratio tested in a wind tunnel was large enough and the Reynolds number effects on the aerodynamic forces are small. Wind conditions with both low turbulence and atmospheric turbulence were generated. The results showed that the turbulence had a slight effect on the side coefficient. The lift coefficient was strongly sensitive to a small change of the road camber. The vortex occurring on the roof for yaw angles larger than 30° in turbulence flow no longer happened in low turbulence flow, which led the lift coefficient in turbulence flow higher than that in the low turbulence beyond 30°yaw angle. The side force spectra had the same form as the wind spectra. The lift force spectra showed vortex shedding. The vortexes were visualized in Coleman and Baker (1994). Baker and Humphreys (1996) collected the aerodynamic force results of the lorry model in a wind tunnel. They concluded that the mean side coefficients were insensitive to the nature of wind tunnel simulation; the lift force coefficients were very dependent upon the nature of the wind tunnel test; and the use of a moving model may be necessary to obtain accurate results for mean lift coefficient. Passmore *et al*. (2001) tested the transient side force and yaw moment of a simplified car-type bluff body in upcoming winds with a different dominant frequency. An oscillating aerofoil gust generator was installed to simulate sinusoidal crosswinds with different frequency. The results showed that the yaw moment was undereducated about 5% to 30% by the quasi-steady method, while the side force was overestimated except at the lowest frequency. Petzäll *et al*. (2008) studied the aerodynamic properties of high-sided coaches with different body shapes. It was shown that the aerodynamic characteristics of high-sided coaches in crosswinds were sensitive to the geometrical body shape. Through the wind tunnel experiments, they found the ideal shape of the coach was rounded front face, rounded top sides and sharp rear corners one. Gohlke *et al*. (2010) studied the influence of shape changes on aerodynamic forces and moments, as well as on flow structures. The 1/5 scaled model of a min-van type vehicle was tested. It was shown that small variations of the A-pillar radius had significant effect on the side-force and yawing moment. For the works mentioned above, aerodynamic forces on the stationary road vehicle on the ground were explored. Compared with the cases of stationary vehicles, it is a challenging task to model a moving vehicle in wind tunnels. Humphreys and Baker (1992) carried out a series of wind tunnel experiments to study the significance of atmospheric boundary layer and vehicle motion to the aerodynamic forces on the 1/50 lorry model. The experimental data appeared to be very noisy with mechanical high frequency. Only side force and lift fore measurement results were presented. It was concluded that the effect of model motion was very substantial, particularly for the lower yaw angle range. The six aerodynamic forces on the road vehicle moving on the ground in crosswinds are required and the importance of modeling a moving vehicle should be further clarified.

As road vehicles run on a long span bridge, a complex external wind circumvent for the vehicle is generated due to the geometric shape of the bridge deck and the layout of rails equipped on the deck. Vehicles have to confront a new situation from crosswinds as they are moving on the bridge, compared with on the ground. Accordingly, aerodynamic effects on the vehicles may enhance remarkably due to their locations being immersed in the flow field of the bridge. Zhou and Ge (2008) fixed the vehicles on the bridge deck and measured the vortex-excited characteristics of the vehicle-bridge system. The results showed that the vehicles have much influence on vortex-induced vibration of the vehicle-bridge system. Zhu *et al*. (2012) conducted wind tunnel tests to obtain the aerodynamic forces and moments on different types of vehicles staying on the bridge deck. Compared with vehicles staying on the ground, the bridge deck reduced the side forces remarkably and increased the rolling moments to some level. Dorigatti *et al*. (2012) completed the similar wind tunnel measurement, in which the vehicles were fixed on the bridge deck. The results showed that the lorry was the critical vehicle for overturning compared with van and bus. Approximate linear decrease of the side force and rolling moment was found as the vehicle progressively moved a large distance from the windward vehicles. Kozmar *et al*. (2012) investigated the transient aerodynamic loads on vehicles staying on bridge deck in a wind tunnel. Vortex shedding and wind gust on the transient aerodynamic loads of a vehicle were studied. In the previous wind tunnel tests about vehicles on the bridge deck, the vehicles stay on the bridge deck without any motion. The influences of the moving effect on the aerodynamic forces of vehicles moving on the bridge deck require investigation.

As road vehicles enter into a bridge tower under crosswinds, the vehicles will be briefly shielded from the crosswinds within a very short period. Moreover, they enter a sharp-edged crosswind gust as they move out of the bridge tower. The aerodynamic forces on a vehicle passing by the bridge towers should be studied in order to have a reliable assessment of the running safety of the vehicle. Argentini *et al.* (2011) performed wind tunnel tests to measure the aerodynamic forces and surface pressures on a stationary vehicle at different locations of the wake of a bridge tower. Smoke visualization was used to observe the flow patterns around the vehicle. The side coefficient, rotating moment coefficient and yawing moment coefficient were presented. The length scale they used was 1:40 and the ratio of the vehicle length to the tower width was 1.66. Their results showed that the aerodynamic forces on the stationary vehicle actually increased when the vehicle was behind the bridge tower, due to the fact that the vehicle is longer than the tower width and that the extremities of the vehicles were blown over by the flow that was accelerated by the interaction with the tower. The smoke visualization also showed that suction appeared between the vehicle and the bridge tower with an axial flow moving upwards along the tower axis. The pressures were negative on all the surfaces of the vehicle. The moving of the vehicle, partially passing by the bridge tower, is not easy to realize in wind tunnel tests. To model the moving vehicles passing by bridge towers, Charuvisit *et al*. (2004) carried out wind tunnel tests to measure the side force and yawing moment of both stationary and moving vehicles in the wake of bridge tower models. The length scale they used was 1:30, and the ratio of the vehicle length to the tower width was 1.39. The test results showed that, compared with the stationary cases, the peak side-force on the moving vehicle when it exited the wake region was higher than that when the vehicle entered the wake region. Only side force and yawing moment were presented in Charuvisit *et al*. (2004), as effective methods to determine all the six aerodynamic forces on moving vehicles passing by bridge towers need to be found.

2.1.3 Computational Fluid Dynamics Simulation

With the increased availability of high-end computing capability and user-friendly commercial codes, CFD is gradually being adopted as an attractive tool to solve wind engineering problems (Cochran and Derickson, 2011; Murakami, 1997). CFD is commonly used in the prediction of drag force of moving vehicles. Han (1989) simulated the flow around Ahmed's vehicle-like body. The Reynolds-averaged Navier-Stokes equations (RANS) with the κ-ε turbulence model were solved. Most of the essential features including the formation of trailing vortices and the reverse flow region from separation were predicted in sense. It was pointed out that the

RANS method with the κ-ε turbulence model underestimated the base pressure of the vehicle model. Krajnović and Davidson (2003) employed the large eddy simulation (LES) method to simulate the flow around a simplified bus on the ground. A uniform profile of upcoming wind velocity was defined on the inlet boundary of flow. A moving velocity equal to the upcoming wind was assigned on the ground to model the relative motion between the vehicle and the ground. No-slip boundary conditions with wall function "instantaneous logarithmic law" were used on the walls. Both convective and viscous terms were approximated by central differences of second-order accuracy. The time integration was done using the Crank-Nicolson second-order scheme. The pressure and velocity was coupled in SIMPLEC method. The simulated aerodynamic forces on and flow features around the bus model agreed well with the experimental data. Khondge *et al*. (2004) simulated the drag force of a tractor-trailer truck and flow around it. Three turbulence models including Realizable κ-ε, RNG κ-ε and DES were employed. Both steady and transient flows were conducted. Second order upwind schemes were adopted for pressure and momentum discretization, respectively. Time is advanced with the implicit form in second order. SIMPLE and SIMPLEC were used to consider the pressure-velocity coupling. High accurate drag coefficients were achieved using RNG κ-ε and DES. Tsubokura *et al*. (2007) simulated the unsteady turbulence simulations of flow around vehicle models including an Aerodynamishches Studien Modell, a racing motorcycle and a formula car using the LES method. The Smagorinsky's eddy viscosity subgrid model was used. The central finite difference scheme with the second order accurate was adopted for spatial discretization, while the second order Adams-Bashforth scheme was adopted for time marching. The simulated pressure distribution on the surface of the ASMO model was in excellent agreement with the wind tunnel data. Tsubokura *et al*. (2010) employed the LES method to investigate the unsteady aerodynamic response of a road vehicle subjected to transient crosswinds. The simulated aerodynamic forces and moment as well as the surface pressure distributions agreed well with wind-tunnel data.

Recently, the aerodynamic characteristics of vehicles on the ground under crosswinds were also simulated using CFD methods. Hargreaves and Morvan (2008) described the simulation set-up of vehicles subject to strong crosswinds. Unsteady RANS simulations method with the κ-ε turbulence model was utilized. The aerodynamic forces of the stationary vehicle under different wind yaw angles were compared with the results from the full-scale measurements and wind tunnel tests. The rotating moment coefficients and the windward pressure coefficients agreed well with the wind tunnel experiments, while the flow separation on the roof and the lift coefficient agreed poorly. Krajnović (2009) reviewed the application of LES simulation to simulate the flow around bluff-bodies including ground vehicles. It was concluded that accurate near-wall modeling is required for an increase of the Reynolds number. Tsubokura *et al*. (2009) simulated the flow around a full-scaled sedan model using the LES method. The unsteady flow structures were validated with the experimental visualization in the wind tunnel test. Guilmineau and Chometon (2009) studied the steady flow characteristics of a willy square back vehicle model through with the RANS method. The results confirmed the capability of the RANS method to capture the three-dimensional separated flows around the vehicle model. Sterling *et al*. (2010) examined the wind-induced forces and moments experienced by a high-sided lorry with full-scale measurements, wind tunnel tests and CFD simulations. The CFD simulation was conducted using the RANS method with the κ-ε turbulence model. Excellent agreement between the CFD results and the filed measurement was obtained. Side coefficients had similar trends between the CFD data and the wind tunnel tests. There were large differences in the trend of lift force coefficient between CFD and other two methods. Tsubokua *et al*. (2010) instigated the unsteady aerodynamic response of a stationary car subjected to transient crosswinds using Large Eddy Simulation (LES). The simulated aerodynamic forces and moments agreed well with the results from wind tunnel experiments. The aerodynamic characteristics of vehicles on the ground under crosswinds had also been simulated using CFD methods (Krajnović *et* a*l*., 2012). All the previous studies focused on the stationary vehicle. Using CFD to simulate the aerodynamic forces on a moving vehicle is required.

Bettle *et al*. (2003) simulated the North American transport truck traveling across a bridge under the conditions of cross-winds using CFD. The truck and trailer were modeled as a series of solid blocks with sharp edges. The steady RANS equations supplemented with the κ-ε turbulence model were solved. The aerodynamic lift, drag and moment coefficients were calculated at different relative wind directions. Although the results show qualitative agreement with the scale model wind tunnel tests, the simulation results were a crude approximation due to the limitation of the numerical method and the number of cells. Chu *et al*. (2013) used the LES model to investigate the protective effect of windbreak on road vehicles against crosswinds. The predicted side force and lift coefficients agreed well with the experiments. Similar to the works in the wind tunnel, the relative velocity between the truck and bridge deck was not considered. No previous study has been conducted about a vehicle passing by a bridge tower using CFD.

2.2 RESPONSE ANALYSIS OF ROAD VEHICLE ON GROUND UNDER CROSSWINDS

Once aerodynamic forces on a road vehicle are determined, the response analysis of the road vehicle can be performed. Baker (1986) firstly presented an analysis method in the time domain for determining responses of a vehicle on the ground to crosswinds. The method was employed to provide critical vehicle speed during windy environments (Baker, 1987). Baker (1988) supplemented the method by taking into account the driver-vehicle interaction, road curvature and camber effects. Baker (1993) also solved the responses of a vehicle in crosswinds in the frequency domain. The risk of wind-induced accident was further introduced by Baker (1994). Macadam (1992) conducted dynamic responses analysis of a road vehicle exposed to sudden crosswind gusts. Sigbjörnsson and Snæbjörnsson (1998) presented a general probabilistic model for assessment of road vehicle accidents in windy environments. Xu and Guo (2003) investigated the dynamic behaviors and possible accidents of high-sided road vehicles entering a sharp-edged crosswind gust with road surface roughness and vehicle suspension included. Through wind tunnel experiments, Cheli *et al.* (2006) obtained the aerodynamic admittance function and aerodynamic forces of a road vehicle with three scenarios: flat terrain, viaduct and embankment. The turbulent wind condition thus was enforced on the vehicle model using corrected quasi-steady theory. Maruyama and Yamazaki (2006) modeled the driver action under crosswind gust. Proppe and Wetzel (2010), Wetzel and Proppe (2010) combined a random variable gust model with constrained simulation techniques and variation reducing Monte Carlo methods for an efficient computation of failure probabilities of vehicle under gust wind. Chen and Chen (2010) developed a single-vehicle accident assessment model considering the coupling effects between vehicles and hazardous driving conditions. In addition, a reliability-based assessment model of vehicle safety was presented by Chen and Chen (2011). Fuller *et al*. (2013) modeled a road vehicle with the lateral and yawing motion and the driver. Mansor and Passmore (2013) studied the effect of rear slant angle of a surface vehicle on crosswind sensitivity for stability analysis with a simple order lateral dynamic model. For the simulations of vehicles on the ground in crosswinds, the vehicle model, road roughness, wind loads, and driver behavior are fundamentals, and they have to be modeled appropriately.

2.2.1 Modeling of Road Vehicles

In the previous behavior analysis of a vehicle subject to crosswinds mentioned above, several vehicle dynamic models with different levels of complexity were presented; for instance, the ridge body model with 6 Degrees of Freedom (DoFs) of Bake (1986, 1987 and 1993), the mass-spring-damp model with 17 DoFs of Xu and Guo (2003), the mass-spring-damp model with 14 DoFs of Cheli *et al*. (2006), the three-mass five DoFs model of Chen and Chen (2010), and the two-mass six DoFs model of Proppe and Wetzel (2010), and only the lateral and yawing motion in Mansor and Passmore (2013) and Fuller (2013). Most of them focus on searching the accident vehicle velocity directly, without exploring the progressive instability of a vehicle under crosswinds. The models of Baker (1986, 1987, and 1993), Xu and Guo (2003), and Cheli *et al*. (2006) were established in a fixed coordinate system coincident to the road. In these models, small angular displacements of the vehicle were assumed when the dynamic equations were derived. Moreover, the mass moments were kept constant as their initial values. In fact, when a vehicle approaches instability, angle displacements of the vehicle are quite large, and the small angular assumption and the constant mass moments are not valid any more. Moreover, the tires always kept contact with the ground in their study, which may not be an actual situation. The jumping of tires from the ground should also be simulated to evaluate the ride comfort in a more accurate and natural sense. Although the model used in Chen and Chen (2010) was set up on the local coordinate system of the vehicle body, small displacement assumption remains in the dynamic equation. Understanding the progressive instability of a moving vehicle is very important for avoiding possible dangerous situations and finding the true accident vehicle velocity. A more rational vehicle model capable of demonstrating the progressive instability is thus required.

2.2.2 Modeling of Road Surface Roughness

Surface roughness is a significant excitation source of the vibrations of vehicles besides crosswinds. Guo (2003) evaluated the ride comfort of a road vehicle with both random inputs of crosswinds and road roughness. The ride comfort was assessed based on the acceleration in both vertical and lateral directions. However, the vehicle moved forward without any lateral displacement and road roughness in a line was simulated to excite the vehicle model. Actually, vehicles can move in the lateral direction under crosswinds. The coherence of the road roughness in the lateral direction is important to the responses of the vehicle in addition to crosswinds (Oliva *et al*., 2013), particularly for the rotating motion. Therefore, the limitation of the vehicle movement in the lateral direction should be released after considering the effects of road roughness on a plane.

2.2.3 Modeling of Wind loads

In all the vehicle models mentioned above, the effect of the attitude of the vehicle to wind loads was not included. It will affect the responses of the vehicle, particularly in the analysis of the progressive instability. Wind conditions should be determined firstly to acquire the aerodynamic loads on road vehicles. Sharp-edged winds, representing the sudden change of wind velocity due to the wind gust or shielding of environment such as bridge tower, buildings, other vehicles, are adopted for the safety analysis (Baker, 1986; Xu and Guo, 2003b). For normal wind conditions, wind velocity time histories, representing the nature winds containing fluctuating winds, are simulated for investigating the dynamic behavior of vehicles (Cheli *et al.*, 2006; Chen and Chen, 2010). Typically, wind velocity time history can be decomposed as a mean component and fluctuating components in three orthogonal spatial directions. Fluctuating winds can be regarded as zero-averaged random processes with statistic features in space and time domain. The statistic features including the cross- and auto- correlations should be satisfied in numerical simulations. The spectral representation method proposed by Shinozuka (Shinozuko, 1971) is a typical technique to simulate the fluctuating winds. The method was modified by Yang *et al*. (1997, 1998) and Cao *et al*. (2000) to enhance the computational speed.

2.2.4 Modeling of Driver Behaviors

Besides the external excitations including winds and surface roughness, driver behavior is another controlling factor to the motion of the vehicle. Baker (1988) adopted a simple drive model, of which the steering angle was taken to be proportional to the lateral displacement and velocity of the vehicle. It was concluded that the accident wind speed might be overestimated without introduction of driver model. Cheli *et al*. (2006) introduced a proportional integral-derivative controller, of which the steering angle was evaluated on the error between the vehicle position on the optical lever and the position on the desired path. Proppe and Wetzel (2010), Wetzel and Proppe (2010) employed a first-order predictive driver model with driver preview time, driver delay time, and gain factor. Maruyama and Yamazaki (2006) employed a second-order predictable correction driver model proposed by Yoshimoto (1968), of which the uncertain model parameters were tested by experiments. With a more advanced model, more driver parameters are required to be determined.

2.3 RESPONSE ANALYSIS OF ROAD VEHICLE ON BRIDGE DECK UNDER CROSSWINDS

Compared with moving on the ground, vehicles moving on the deck of long span bridges experience different situations. Long span bridges tend to be flexible and lightly damped. They may suffer considerable wind-induced vibration and deformation under high winds. As road vehicles run on, the responses of long span bridges become more serious under the combined actions of both wind and vehicles. As a return, the ride comfort and safety of road vehicles may worsen due to the dynamic vibration and deformation of the bridges. Therefore, it is necessary to carry out response analysis of road vehicles moving on the long span bridges. In addition to the vehicle model, road surface roughness, driver behaviors, and crosswinds as already described in Section 2.2, the interaction between the vehicle and the bridge should be clarified, and a coupled analysis frame wind-road vehicle-bridge system should be formed to solve the responses.

2.3.1 Wind Loads on Bridge

After experiencing the wind-induced collapse of Tacoma Narrows Bridge in 1940, a great deal of research has been conducted to study the wind-bridge interaction. Wind loads on a bridge deck are commonly modeled as a combination of three components: static wind loads related to mean wind, buffeting loads due to turbulent flow and self-excited loads dependent on structural motion. In addition, the possible interactions between components are neglected.

2.3.1.1 Static wind loads

Static wind loads are the effects of time-averaged mean wind components of the upcoming winds. Exceeding static wind loads may lead to over-deformations or even stability loss of bridges. Static wind loads on a pure bridge deck per unit of length are decomposed as drag force F_D along the wind direction, lift force F_L vertical to the wind direction and moment M. They are the functions of non-dimensional aerodynamic coefficients as follows (Simiu and Scanlan, 1996).

$$F_D = \frac{1}{2}\rho U^2 C_D(\alpha) H \tag{2.1a}$$

$$F_L = \frac{1}{2}\rho U^2 C_L(\alpha) B \tag{2.1b}$$

$$F_M = \frac{1}{2}\rho U^2 C_M(\alpha) B^2 \tag{2.1c}$$

where ρ is the air density; U is the averaging wind velocity; B and H are the width and height of the deck; C_D, C_L and C_M are the drag, the lift and the moment coefficients, respectively; α is the angle of attack.

The aerodynamic coefficients (C_D, C_L and C_M) are dependent on the section shape of bridge decks. A segmental model test in a wind tunnel is the common way to obtain the aerodynamic coefficients. With the advancement of computer hardware, the numerical method using CFD techniques is widely employed to simulate the aerodynamic coefficients from 1990s. Various solution methods have been adopted, including: the finite element method (Fujiwara *et al.*, 1993; Watanabe *et al.*, 2004; Braun and Awruch, 2008), the finite different method (Kuroda, 1997; Onyemelukwe *et al.*, 1997), and the finite volume method (Bruno *et al.*, 2001; Bruno and Khris, 2003; Sarwar *et al.*, 2008; Fransos and Bruno, 2010; Nieto *et al.*, 2010), and the discrete vortex method (Larsen and Walther, 1997, 1998; Taylor and Vezza, 2001, 2002, 2009; Taylor *et al.*, 2008; Zhou and Ma, 2010).

2.3.1.2 Buffeting loads

Buffeting loads are caused by the fluctuating part of the winds. The buffeting forces per unit span of bridge deck to wind fluctuations can be written as (Davenport, 1962; Scanlan, 1978):

$$D_b(x,t)=\frac{1}{2}\rho U^2 B\left[2C_D\chi_{Du}\frac{u(x,t)}{U}+C_D^{'}\chi_{Dw}\frac{w(x,t)}{U}\right] \quad (2.2a)$$

$$L_b(x,t)=\frac{1}{2}\rho U^2 B\left[2C_L\chi_{Lu}\frac{u(x,t)}{U}+\left(C_L^{'}+C_D\right)\chi_{Lw}\frac{w(x,t)}{U}\right] \quad (2.2b)$$

$$M_b(x,t)=\frac{1}{2}\rho U^2 B^2\left[2C_M\chi_{Mu}\frac{u(x,t)}{U}+C_M^{'}\chi_{Mw}\frac{w(x,t)}{U}\right] \quad (2.2c)$$

where $C_D^{'}$, $C_L^{'}$ and $C_M^{'}$ are the slopes of C_D, C_L and C_M, respectively; $u(t)$, $w(t)$ are the fluctuating wind velocity along the mean wind or vertical to the mean wind. χ_{Lu}, χ_{Lw}, χ_{Pu}, χ_{Mu}, χ_{Mw} are the aerodynamic admittance functions.

The theoretical aerodynamic admittance function for a thin airfoil, originally derived by Sears (Sears, 1941), is commonly used for the aerodynamic admittances. It is successful in streamlined box sections such as Great Belt East Bridge (Larose *et al.*, 1998). For some bridge deck section, the measured aerodynamic admittance functions were different from Sears' function (Jancauskas and Melbourme, 1986). Some experimental formulas were thus proposed (e.g. Jancauskas and Melbourme, 1986). However, the experimental formulas are applicable only to limited types of deck sections. The aerodynamic admittance function can also be derived from flutter derivatives tested in experiments as in Scanlan (2001), Hatanaka and Tanaka (2002). Diana *et al*. (2002) defined the admittance functions in complex functions by amplitude and phase shift.

2.3.1.3 Self-excited loads

Self-excited loads are the results of the motions of the bridge deck. Motion of the bridge decks may change the flow status of the upcoming winds and active self-excited aerodynamic forces, which may result in divergent vibration called flutter. In the case of thin airfoil, Theodorsen (1935) derived its self-excited lift force and moment for small amplitude harmonic oscillation in the principles of potential flow theory. The self-excited loads were expressed as the linear functions of the displacements, velocities, and accelerations of the motions in the vertical and rotational direction as follows.

$$L_{se} = \pi\rho b^2 (U\dot{\alpha} + \ddot{h} - ba\ddot{\alpha}) + 2\pi\rho bUC(k)[U\alpha + \dot{h} + b(\frac{1}{2} - a)\dot{\alpha}] \quad (2.3a)$$

$$M_{se} = -\pi\rho b^2 [(\frac{1}{2} - a)Ub\dot{\alpha} + b^2(\frac{1}{8} + a^2)\ddot{\alpha} - ab\ddot{h}] + 2\pi\rho Ub^2(\frac{1}{2} + a)C(k)[U\alpha + \dot{h} + b(\frac{1}{2} - a)\dot{\alpha}] \quad (2.3b)$$

Where L_{se} and M_{se} are the self-excited lift and moment; α, $\dot{\alpha}$, and $\ddot{\alpha}$ are the rotational displacement, velocity, and acceleration, respectively; h, $\dot{h}$, and $\ddot{h}$ are the vertical displacement, velocity and acceleration, respectively; a is the distance from the chord centre to the rotational center; b is the semi-chord; k is a non-dimensional frequency and equal to $(b\omega)/U$; $C(k)$ is the so-called Theodorsen's circulatory function and has the following expressions:

$$C(k) = F(k) + iG(k) \quad (2.4)$$

Approximate expressions for $F(k)$ and $G(k)$ have been presented in Fung (1955):

$$F(k) = 1 + \frac{c_1 k^2}{c_2^2 + k^2} + \frac{c_3 k^2}{c_4^2 + k^2} \quad (2.5a)$$

$$G(k) = -k(\frac{c_1 c_2}{c_2^2 + k^2} + \frac{c_3 c_4}{c_4^2 + k^2}) \quad (2.5b)$$

with c_1=-0.165, c_2=-0.0455, c_3=-0.335, c_4=-0.300

Scanlan and Tomko (1971) extended the expressions of self-excited force/moment to the bridge deck by relating the self-excited force/moment to the displacements and velocities of the deck as:

$$F_L = \frac{1}{2}\rho U^2 B(KH_1^* \frac{\dot{h}}{U} + KH_2^* \frac{B\dot{\alpha}}{U} + K^2 H_3^* \alpha + K^2 H_4^* \frac{h}{B}) \quad (2.6a)$$

$$M = \frac{1}{2}\rho U^2 B(KA_1^* \frac{\dot{h}}{U} + KA_2^* \frac{B\dot{\alpha}}{U} + K^2 A_3^* \alpha + K^2 A_4^* \frac{h}{B}) \quad (2.6b)$$

where F_L and M represent the self-excited force and moment on the deck, respectively; h and α are the vertical and torsional displacements of the deck;

$K(=(B\omega)/U)$ is a non-dimensional frequency; H_i^* and A_i^* (i=1, 2, 3, 4) are flutter derivatives. They are the functions of the non-dimensional frequency and vary with the shape of the cross-section of the bridge deck.

For a bridge deck with a geometric shape of thin plate, the flutter derivatives can be extracted from Equation 2.3. However, there are no theoretical values of flutter derivatives for decks with other geometric shapes. Wind tunnel tests or simulations through CFD are carried out to determine them. In the wind tunnel test, the free vibration method (Scanlan and Tomko, 1971; Poulsen *et al.*, 1992; Sarkar *et al.*, 1994) and forced vibration method (Falco *et al.*, 1992; Hatanaka and Tanaka, 2002; Chen and Yu, 2002; Sarkar *et al.*, 2009) are two common ways. And various methods have been presented to determine the flutter derivatives from the tested aerodynamic forces, including the Scanlan's method in Scanlan and Tomko (1971), the Poulsen's method in Poulsen *et al.* (1992), the Extended Kalman Filter Algorithm in Yamada *et al.* (1992), the Modified Ibrahim Time-Domain (MITD) method in Sarkar *et al.* (1994), the Unifying Least-Squares (ULS) method in Gu *et al.* (2000), the Iterative Least Squares (ILS) method in Chowdhury and Sarkar (2003 and 2004), the SSI-COV method in Gu and Qin (2004) and Mishra *et al.* (2006), the SSI-DATA in Boonyapinyo and Janesupassaeree (2010). In the simulations using CFD, the forced vibration method was applied to solve the flutter derivatives (Larsen and Walther, 1997 and 1998; Taylor and Vezza, 2001 and 2002; Selvam *et al.*, 2002; Jeong and Kwon, 2003; Amandolèse and Crémona, 2005; Zhu *et al.*, 2007; Huang *et al.*, 2009; Starossek *et al.*, 2009; Bai *et al.*, 2010).

The self-excited force/moment expressed in Equation 2.6 can be applied on the bridge directly to solve the responses of the bridge in the frequency domain (Scanlan, 1978; Agar, 1989; Miyata and Yamada, 1990; Dung *et al.*, 1998; Ge and Tanaka, 2000). In order to fully consider the nonlinear behavior of the bridge, the expressions of the self-excited force/moment in the time domain are required.

Scanlan *et al*. (1974) first introduced the indicial functions to express the self-excited force/moment into pure time domain. A similar manner has also been presented in Bucher and Lin (1988), Boonyapinyo *et al*. (1999) and Chen *et al*. (2000). In Bucher and Lin (1988), the self-excited force/moment is expressed in terms of convolution integrals as:

$$L(t) = L_{\alpha}(t) + L_{h}(t) = \int_{-\infty}^{t} f_{L\alpha}(t-\tau)\alpha(\tau)d\tau + \int_{-\infty}^{t} f_{Lh}(t-\tau)h(\tau)d\tau \tag{2.7a}$$

$$M(t) = M_{\alpha}(t) + M_{h}(t) = \int_{-\infty}^{t} f_{M\alpha}(t-\tau)\alpha(\tau)d\tau + \int_{-\infty}^{t} f_{Mh}(t-\tau)h(\tau)d\tau \tag{2.7b}$$

where $h(\tau)$, and $\alpha(\tau)$ are the vertical and rotational displacements of the bridge deck at time τ; f_{ij} (i=L, M; j=h, α) are the response functions caused by the unit impulse displacement of j.

Applying the Fourier transform to Equation 2.7, the following equations can be achieved:

$$\tilde{L}(t) = F_{L\alpha}(\omega)\tilde{\alpha}(\omega) + F_{Lh}(\omega)\tilde{h}(\omega) \tag{2.8a}$$

$$\tilde{M}(t) = F_{M\alpha}(\omega)\tilde{\alpha}(\omega) + F_{Mh}(\omega)\tilde{h}(\omega) \tag{2.8b}$$

where overbar represents the Fourier transforms; F_{ij} (i=L, M; j=h, α) are the response functions in frequency and can be expressed approximately by the rational functions of the first order linear filters (Bucher and Lin, 1988). Taking $F_{M\alpha}$ for example:

$$F_{M\alpha}(\omega) = \rho B^2 U^2 (C_1 + \frac{B}{U} i\omega C_2 + \sum_{k=3}^{n} C_k \frac{i\omega}{d_k \frac{U}{B} + i\omega}) \tag{2.9}$$

where $v = 2\pi U/(B\omega)$; the unknown coefficients C_k and d_k can be calculated by the least square fitting on the following expressions.

$$\frac{C_1 v^2}{4\pi^2} + \sum_{k=3}^{n} C_k \frac{C_k v^2}{d_k^2 v^2 + 4\pi^2} = A_3^*(v) \tag{2.10a}$$

$$\frac{C_2 v}{2\pi^2} + \sum_{k=3}^{n} C_k \frac{C_k d_k v^3}{2\pi d_k^2 v^2 + 4\pi^2} = A_2^*(v) \tag{2.10b}$$

where $A_2^*(v)$ and $A_3^*(v)$ are the flutter derivatives. The impulse response function

$f_{M\alpha}(t)$ in Equation 2.7 can then be derived through the inverse Fourier transformation of Equation 2.9 as:

$$f_{M\alpha}(t) = \rho U^2 B^2 \left[C_1 \delta(t) + C_2 \frac{B}{U} \dot{\delta}(t) + \delta(t) \sum_{k=3}^{n} C_k - \sum_{k=3}^{n} C_k d_k \frac{U}{B} \exp(-\frac{d_k U}{B} t) \right] \quad (2.11)$$

Similar to $f_{M\alpha}$, all other impulse response functions in Equations 2.7 can be derived.

2.3.2 Vehicle-Bridge Interaction

As vehicles move on the bridge, a coupled dynamic system of vehicle-bridge is formed automatically. The contact forces, both in the vertical and in the lateral directions from the tires, are imposed on the bridge deck and excite the dynamic responses of the bridge. The displacements of the bridge deck change the moving traces of the tires, in turn. The investigation of dynamic vehicle-bridge interaction has been a topic of interest since early in the last century (Lowan, 1935; Ayre and Jacobsen, 1950; Ayre *et al.*, 1950). The action of the vehicles on bridges were first approximated as moving load (Timoshenko *et al.*, 1974; Smith, 1988; Felszeghy 1996a, b; Henchi and Farard, 1997). Since the moving load method cannot take into acount the influcent of vehicle inertia, the vehicle was further treated as moving mass (Akin and Mofid, 1989; Esmailzadeh and Ghorashi, 1997; Stanišić and Hardin, 1969; Ting *et al.*, 1974; Sadiku and Leipholz, 1987). However, both moving load and moving mass methods neglect the effects of vehicle dynamics and therefore cannot be used to determine the vehicle responses. Accordingly, more sophisticated models considering the dynamic behaviour of vehicles should be devised. The vehicles are regarded as lumped mass supported by a spring-dashpot units. Three methods have been employed to handle the dynamic interaction between the bridges and the lumped mass models. The first one is treating the vehicle and the bridge as two subsystems (Henchi *et al.*, 1998; Fafard *et al.*, 1997; Akoussah *et al.*, 1997; Hwang and Nowak, 1997; Green and Cebon, 1997). An iterative process considering the contact conditions is performed between them. In the iteration, the geometric contact relations between the vehicle and the bridge are assumed, and the interaction forces between them are then calculated by solving the dynamic equations of vehicles. The assumed geometric contact relations are improved by solving the dynamic equations of the bridge. Through interactions, the status of the two subsystems will be convergent at each time step. During the interaction, the dynamic property matrices for the two subsystems remain constant. The second way is to solve the fully coupled dynamic equations of the vehicle-bridge interaction dynamic equations without any iteration (for example, Guo and Xu, 2001). In this method, the mass and stiffness matrixes change with the locations of vehicles and thus required to be updated at each time step. The third method is the so-called condensation method (Yang and Lin, 1995; Yang and Yau, 1997; Yang *et al*., 1999). Using the Guyan reduction or dynamic condensation method, the degrees of freedom of vehicles are condensed to the degrees of freedom of the bridge. The characteristic matrices of the system also have to be updated in a timely manner. And it is difficult to derive the essential condensation expressions for complex vehicle models.

2.3.3 Wind-Vehicle-Bridge Interaction

As road vehicles are running on the long span bridge in crosswinds, a complicated dynamic interaction among road vehicles, bridge and wind occurs. The action of winds leads to dynamic responses of both vehicles and bridge. The wind-induced vehicle dynamic responses will further be transferred to the bridge through the vehicle-bridge contact force, and the responses of the bridge changes the moving traces of the vehicles, in return. Crosswinds, vehicles and bridges should be regarded as a coupled, time-dependent system. Several analysis frames of road vehicle-bridge deck under crosswinds were generated in previous studies, such as Xu and Guo (2003), Cai and Chen (2004), Chen and Cai (2004), Guo and Xu (2006), Han (2006), Chen and Cai (2007), Chen (2007), Cheung and Chan (2010), and Chen *et al*. (2011). Based on these dynamic analysis frames of the wind-vehicle-bridge systems, many other issuers such as fatigue performance of bridges (Chen and Cai, 2007) and dynamic stress analysis (Chen *et al*., 2011), more complicated situations such as tuned-liquid-damper system installed on the bridge (Chen *et al*., 2008), stochastic traffic (Chen and Wu, 2010), traffic congestion (Wu and Chen, 2011) were studied. In their analysis frames, the aerodynamic coefficients of the bridge deck without considering the influence of the vehicles were adopted. Actually, the moving effect of the vehicle on the deck may also influence the aerodynamic forces, and the aerodynamic forces of the bridge deck are dependent on the locations of the vehicles. The aerodynamic forces on bridge decks, reflecting the moving effect and the interference effects between the vehicle and the deck, should be introduced into the coupled vehicle-bridge system in crosswinds.

2.4 RESPONSE ANALYSIS OF ROAD VEHICLE PASSING BY BRIDGE TOWER UNDER CROSSWINDS

As vehicles pass by the bridge tower, wind loads experience sudden decrease and increase. It is thus a critical situation for the safety of vehicles passing by the bridge tower. In the coupled analysis of vehicle-bridge system under crosswinds (Chen and Cai, 2004), the wind loads were suddenly decreased to zero to model the existence of a bridge tower. The transient aerodynamic forces on the vehicle passing by the bridge tower were not applied in real situations. Rocchi *et al*. (2012) solved the lateral and yawing displacements. The side force and yawing moment tested on the vehicle at different locations behind a bridge tower were employed. However, the dynamic response of the bridge and the moving effect of the vehicles were neglected. What is required is a whole frame of vehicle-bridge system under crosswinds analyses, considering the acting moving aerodynamic forces on vehicles as they pass by a bridge tower.

2.5 SAFETY AND COMFORT EVALUATION OF ROAD VEHICLES UNDER CROSSWINDS

Road vehicles are related to almost everyone’s daily life. Vehicle accidents may take away people’s lives or incur huge property loss. Discomfort in vehicles may harm people’s health of the spirit and the body. Safety and comfort in road vehicles are thus in high public demand. Safety and ride comfort of moving road vehicles in crosswinds should be ensured and assessed. The corresponding assessment critics and index will be reviewed in this section.

2.5.1 Safety

Baker (1986) presented three types of accidents that may occur: overturning, sideslip and rotation accidents. A 0.5s sudden step crosswind with velocity from zero is enforced on the vehicle, overturning occurred if the vertical reaction force of any tire reduced to zero; sideslip happened if the lateral displacement of the vehicle exceeded 0.5m; and rotation accident emerged if the yawing angle was larger than 0.2. This safety standard was further adopted in the later studies of road vehicles moving on the ground and on bridges (Xu and Guo, 2003b; Chen and Cai, 2004; Guo and Xu, 2006). Cheli *et al.*, (2006) took the so-called load transfer ratio of the axle (LTR) as the overturning index. LTR was defined as the ratio of the difference to the sum of the vertical reaction forces of the two tires on the same axel. If LTR was greater than 90%, the vehicle was deemed as overturning. Cheung and Chan (2010) proposed the potential vehicle instability situations to be that the normal tire reaction force turned to zero (overturning), the total tire lateral frictional force was smaller than lateral wind loads acting on the vehicle (sliding), and the overturning moment about the contact point was larger than the resisting overturning moment (side-slip overturning). Proppe and Wetzel (2010), Wetzel and Proppe (2010) took the ratio of current lateral displacement to the maximum tolerable displacement as the sideslip critic and LTR as the overturning index. In Chen and Chen (2010), a vehicle ultimately rolled over only when the lateral position of the center of gravity exceeded the wheel. The travel distance after sideslip was the critical variable for lateral displacement. In addition, critical sustained time was adopted. If the critical sustained time was smaller than the reaction time of the driver, the driver may not have sufficient time to take appropriate actions to prevent an accident. Generally, two types of wind-induced accident may occur: one is overturning; the other is course deviation, which may cause a collision with the vehicle in the adjacent lane or the equipment at the side of the road.

2.5.2 Ride Comfort

ISO 2631-1(1997) proposes the evaluation standard for evaluating the human exposure to whole-body vibration. Ride comfort is regarded as the environmental vibrations transmitted to the human body as a whole through the supporting surfaces. The ride comfort is then valued with an index named “frequency weighted root mean square acceleration” (FWRMSA for short).

For the seated driver, her/his buttocks are taken as the supporting surface from which the vibrations of the vehicle are transmitted to the driver. An orthogonal coordinate for the seated person is defined in ISO2631-1 as in Figure 2.1. The x-axis is the heading direction, the y-axis is the lateral direction and the z-axis is the vertical direction. The acceleration time history in each axis, except the x-axis at the seat, is firstly decomposed into time histories in octave third bands. The corresponding root mean square of acceleration for each band can be calculated in sequence. After being multiplied by frequency weighing factors, they are summed into FWRMSA in each axis (a_{wx} in x-axis, a_{wy} in y-axis, and a_{wz} in z-axis). The frequency weighting factors: W_k in the z-axis and W_d in the x-axis and y-axis are plotted in Figure 2.2.

FWRMSA in each axis is combined as a final FWRMSA as:

$$a_v = (k_x^2 a_{wx}^2 + k_y^2 a_{wy}^2 + k_z^2 a_{wz}^2)^{\frac{1}{2}} \tag{2.12}$$

where k_x, k_y, k_z are the multiplying factors. For evaluation the comfort of a seated person, k_x =1, k_y =1, k_z =1. The level of ride comfort can, therefore, be valued using the standard listed in Table 2.1.

2.6 COMPUTATIONAL FLUID DYNAMICS

Apart from wind tunnel tests, the computational fluid dynamics (CFD) simulation is now applied widely to solve flow-structure interaction problems in engineering (Murakami, 1997; Cochran and Derickson, 2011). The history of applying CFD to bridge wind engineering started in the 1990s. Many studies have been devoted to simulating the aerodynamics of bridge decks using different numerical methods (Fujiwara *et al.*, 1993; Larsen and Walther, 1997; Ge *et al.*, 2002; Jeong and Kwon, 2003; Li and Wang, 2004; Zhu *et al.*, 2007; Taylor and Vezza, 2009; Zhou and Ma, 2010; Huang and Liao, 2011). The aerodynamic forces of both stationary and moving bridge decks have been analyzed numerically. The aerodynamic characteristics of vehicles on the ground under crosswinds have also been simulated using CFD methods (Hargreaves and Morvan, 2008; Krajnović, 2009; Tsubokura *et al.*, 2009; Guilmineau and Chometon, 2009; Sterling *et al.*, 2010; Tsubokua *et al.*, 2010; Krajnović *et al.*, 2012). The governing equations and numerical schemes are reviewed in this section.

2.6.1 Navier-Stokes Equations

Computational fluid dynamics is a method to solve the governing equations of flow. The governing equations are formulated according to the mass conservation, momentum conservation, and energy conservation of flows (Versteeg and Malalasekera, 2007; Tannehill and Anderson, 1997). In wind engineering, the governing equations of air flow (also can be called Navier-Stokes equations) are accepted as incompressible flow neglecting the body forces and have the following forms in a Cartesian coordinate system:

$$\frac{\partial u}{\partial x}+\frac{\partial v}{\partial y}+\frac{\partial w}{\partial z}=0 \tag{2.13a}$$

$$\rho\frac{D(u)}{Dt}=-\frac{\partial p}{\partial x}+\mu(\frac{\partial^2 u}{\partial x^2}+\frac{\partial^2 u}{\partial y^2}+\frac{\partial^2 u}{\partial z^2}) \tag{2.13b}$$

$$\rho\frac{D(v)}{Dt}=-\frac{\partial p}{\partial y}+\mu(\frac{\partial^2 v}{\partial x^2}+\frac{\partial^2 v}{\partial y^2}+\frac{\partial^2 v}{\partial z^2}) \tag{2.13c}$$

$$\rho\frac{D(w)}{Dt}=-\frac{\partial p}{\partial z}+\mu(\frac{\partial^2 w}{\partial x^2}+\frac{\partial^2 w}{\partial y^2}+\frac{\partial^2 w}{\partial z^2}) \tag{2.13d}$$

where ρ is the air density; μ is the dynamic viscosity coefficient of air; t is the time; u, v, w are the velocity components in the x, y, z direction, respectively; and $\frac{D(\,)}{Dt}$ represents the total derivative; p is the pressure.

2.6.2 Modeling of Turbulence

The governing Equation 2.13 contains all the spatial and time scales. Actually, the flow around body has a large range of scales respect to the length and the time. Direct numerical simulation (DNS) on the governing equation with initial and boundary conditions requires spatial grids with the fine sizes to resolve the length scales and sufficiently small time step to resolve the fastest fluctuations with small time scales. It is therefore difficult to practice DNS to solve the flow around vehicles and a bridge deck with such a high Reynolds level. Approximation methods based on considering different scales have been proposed. The most prevalent methods are solving the Reynolds-averaged Navier-Stokes equations (RANS), large eddy simulation (LES), and detached eddy simulation (DES). RANS solves the time average variables and models the flectional variables with additional equations. Different from the time averaging in RANS, spatial filtering is operated on the governing equations in LES. LES computes the larger eddies directly and captures the smaller eddies of universal behavior with some models. DES is a hybrid method between the RANS and LES. It regards the boundary layers and nearby thin shear layers in RANS and the other regions in LES. To simulate the complicated flow around the vehicle, the vehicle-bridge deck system, and the vehicle-tower-deck system, LES is the good method to handle in consideration of accuracy. However, there is so great a range of spatial size in them, and a high level of mesh resolution with huge number of grids should be realized. The final computational efforts will be unaccepted for the current used computers. The main focus at this stage is only the turbulence-averaged aerodynamic forces/coefficients of a vehicle for engineering considerations. As the RANS method has less grid resolution and is cheaper, it is more practical than LES and DES.

Replacing the random flow variables *u*, *v*, *w* and *p* in the governing Equation 2.13 with their time averages values pulsing the corresponding fluctuations, the RANS equations can be derived as follows:

$$\frac{\partial \bar{u}}{\partial x}+\frac{\partial \bar{v}}{\partial y}+\frac{\partial \bar{w}}{\partial z}=0 \tag{2.14a}$$

$$\rho\frac{\partial \bar{u}}{\partial t}+\rho\bar{u}\frac{\partial \bar{u}}{\partial x}+\rho\bar{v}\frac{\partial \bar{u}}{\partial y}+\rho\bar{w}\frac{\partial \bar{u}}{\partial z}=-\frac{\partial \bar{p}}{\partial x}+\mu(\frac{\partial^2 \bar{u}}{\partial x^2}+\frac{\partial^2 \bar{u}}{\partial y^2}+\frac{\partial^2 \bar{u}}{\partial z^2})-\rho\frac{\partial \overline{u'u'}}{\partial x}-\rho\frac{\partial \overline{u'v'}}{\partial y}-\rho\frac{\partial \overline{u'w'}}{\partial z} \tag{2.14b}$$

$$\rho\frac{\partial \bar{v}}{\partial t}+\rho\bar{u}\frac{\partial \bar{v}}{\partial x}+\rho\bar{v}\frac{\partial \bar{v}}{\partial y}+\rho\bar{w}\frac{\partial \bar{v}}{\partial z}=-\frac{\partial \bar{p}}{\partial y}+\mu(\frac{\partial^2 \bar{v}}{\partial x^2}+\frac{\partial^2 \bar{v}}{\partial y^2}+\frac{\partial^2 \bar{v}}{\partial z^2})-\rho\frac{\partial \overline{v'u'}}{\partial x}-\rho\frac{\partial \overline{v'v'}}{\partial y}-\rho\frac{\partial \overline{v'w'}}{\partial z} \tag{2.14c}$$

$$\rho\frac{\partial \bar{w}}{\partial t}+\rho\bar{u}\frac{\partial \bar{w}}{\partial x}+\rho\bar{v}\frac{\partial \bar{w}}{\partial y}+\rho\bar{w}\frac{\partial \bar{w}}{\partial z}=-\frac{\partial \bar{p}}{\partial z}+\mu(\frac{\partial^2 \bar{w}}{\partial x^2}+\frac{\partial^2 \bar{w}}{\partial y^2}+\frac{\partial^2 \bar{w}}{\partial z^2})-\rho\frac{\partial \overline{w'u'}}{\partial x}-\rho\frac{\partial \overline{w'v'}}{\partial y}-\rho\frac{\partial \overline{w'w'}}{\partial z} \tag{2.14d}$$

where $\bar{p}$, $\bar{u}$, $\bar{v}$, $\bar{w}$ are the time averages of p, u, v, w, respectively; p', u', v', w' are the time averages of p, u, v, w, respectively; $-\rho\overline{u'u'}$, $-\rho\overline{v'v'}$, $-\rho\overline{w'w'}$, $-\rho\overline{u'v'}$, $-\rho\overline{u'w'}$, $-\rho\overline{v'w'}$ are the so-called Reynolds stresses and reflect the actions of fluctuation flow to the mean flow.

To solve the RANS Equation 2.14, the Reynolds stresses should be modeled through turbulence models. Most turbulence models are viscosity models generated on the Boussinesq's assumption. It is assumed that the Reynolds stresses are related to the rate of mean strain through an apparent scalar turbulent or eddy viscosity as:

$$-\rho\overline{u'u'}=2\mu_t\overline{S_{xx}}-\frac{2}{3}\rho k;\ -\rho\overline{v'v'}=2\mu_t\overline{S_{yy}}-\frac{2}{3}\rho k;\ -\rho\overline{w'w'}=2\mu_t\overline{S_{zz}}-\frac{2}{3}\rho k \tag{2.15a}$$

$$-\rho\overline{u'v'}=2\mu_t\overline{S_{xy}};\ -\rho\overline{u'w'}=2\mu_t\overline{S_{xz}};\ -\rho\overline{v'w'}=2\mu_t\overline{S_{yz}} \tag{2.15b}$$

where μ_t is the eddy viscosity; $\overline{S_{xx}}$, $\overline{S_{yy}}$, $\overline{S_{zz}}$, $\overline{S_{xy}}$, $\overline{S_{xy}}$, $\overline{S_{yz}}$ are the rates of mean strain have the following expressions:

$$\overline{S_{xx}} = \frac{\partial \overline{u}}{\partial x}; \overline{S_{yy}} = \frac{\partial \overline{v}}{\partial y}; \overline{S_{zz}} = \frac{\partial \overline{w}}{\partial z} \tag{2.16a}$$

$$\overline{S_{xy}} = \frac{1}{2}(\frac{\partial \overline{u}}{\partial y} + \frac{\partial \overline{v}}{\partial x}); \overline{S_{xz}} = \frac{1}{2}(\frac{\partial \overline{u}}{\partial z} + \frac{\partial \overline{w}}{\partial x}); \overline{S_{yz}} = \frac{1}{2}(\frac{\partial \overline{v}}{\partial z} + \frac{\partial \overline{w}}{\partial y}) \tag{2.16b}$$

and k, ε are the kinetic energy of turbulence and dissipation per unit mass respectively with:

$$k = \frac{1}{2}(\overline{u'u'} + \overline{v'v'} + \overline{w'w'}) \tag{2.17a}$$

$$\varepsilon = \frac{\mu}{\rho}(\overline{\frac{\partial u'}{\partial y}\frac{\partial u'}{\partial y}} + \overline{\frac{\partial v'}{\partial y}\frac{\partial v'}{\partial y}} + \overline{\frac{\partial w'}{\partial z}\frac{\partial w'}{\partial z}}) \tag{2.17b}$$

The commonly used viscosity models are the k-ε model series, k-ω model series, and SST k-ω model. In terms of the boundary layers with adverse pressure gradients, the k-ω model performs between than the standard k-ε model. But it is much less sensitive for the standard k-ε model dependent on the assumed free stream than the k-ω model. Menter (1994) thus proposed the shear-stress transport (SST) k-ω model to effectively blend the robust and accurate formulation of the κ-ω model in the near-wall region with the k-ε model in the far field. The eddy viscosity in Equation 2.15 is expressed as the product of the turbulent kinetic energy k and the turbulence frequency ω as follows:

$$\mu_t = \frac{a_1 \rho k}{\max(a_1 \omega, S^* F_2)} \tag{2.18a}$$

$$S^* = \sqrt{2(\overline{S_{xx}} + \overline{S_{yy}} + \overline{S_{zz}} + \overline{S_{xy}} + \overline{S_{xz}} + \overline{S_{yz}} + \overline{S_{yx}} + \overline{S_{zx}} + \overline{S_{zy}})} \tag{2.18b}$$

$$F_2 = \tanh(\Phi_2^2) \tag{2. 18c}$$

$$\Phi_2 = \max(\frac{\sqrt{k}}{0.045\omega y}, \frac{500\mu}{\rho y^2 \omega}) \tag{2. 18d}$$

$$\alpha_1 = 0.31 \tag{2. 18e}$$

where y is the distance of the flow to the near surface of target body.

The equations for k and ω are:

$$\rho\frac{\partial k}{\partial t}+\rho\overline{u}\frac{\partial k}{\partial x}+\rho\overline{v}\frac{\partial k}{\partial y}+\rho\overline{w}\frac{\partial k}{\partial z}=\frac{\partial}{\partial x}[(\mu+\frac{\mu_t}{\sigma_k})\frac{\partial k}{\partial x}]+\frac{\partial}{\partial y}[(\mu+\frac{\mu_t}{\sigma_k})\frac{\partial k}{\partial y}]$$
$$+\frac{\partial}{\partial z}[(\mu+\frac{\mu_t}{\sigma_k})\frac{\partial k}{\partial z}]+\min[(2\mu_t\overline{S_{xx}}-\frac{2}{3}\rho k)\frac{\partial\overline{u}}{\partial x}+\overline{S_{xy}}\frac{\partial\overline{u}}{\partial y}+\overline{S_{xz}}\frac{\partial\overline{u}}{\partial z}+(2\mu_t\overline{S_{yy}}-\frac{2}{3}\rho k)\frac{\partial\overline{v}}{\partial y}$$
$$+\overline{S_{yx}}\frac{\partial\overline{v}}{\partial x}+\overline{S_{yz}}\frac{\partial\overline{v}}{\partial z}+(2\mu_t\overline{S_{zz}}-\frac{2}{3}\rho k)\frac{\partial\overline{w}}{\partial z}+\overline{S_{zx}}\frac{\partial\overline{w}}{\partial x}+\overline{S_{zy}}\frac{\partial\overline{w}}{\partial y},10\rho\beta^* k\omega]-\beta^*\rho k\omega$$

(2.19a)

$$\rho\frac{\partial\omega}{\partial t}+\rho\overline{u}\frac{\partial\omega}{\partial x}+\rho\overline{v}\frac{\partial\omega}{\partial y}+\rho\overline{w}\frac{\partial\omega}{\partial z}=\frac{\partial}{\partial x}[(\mu+\frac{\mu_t}{\sigma_\varepsilon})\frac{\partial\omega}{\partial x}]+\frac{\partial}{\partial y}[(\mu+\frac{\mu_t}{\sigma_\varepsilon})\frac{\partial\omega}{\partial y}]$$
$$+\frac{\partial}{\partial z}[(\mu+\frac{\mu_t}{\sigma_\varepsilon})\frac{\partial\omega}{\partial z}]+\frac{\rho\alpha'}{\mu_t}[(2\mu_t\overline{S_{xx}}-\frac{2}{3}\rho k)\frac{\partial\overline{u}}{\partial x}+\overline{S_{xy}}\frac{\partial\overline{u}}{\partial y}+\overline{S_{xz}}\frac{\partial\overline{u}}{\partial z}+(2\mu_t\overline{S_{yy}}-\frac{2}{3}\rho k)\frac{\partial\overline{v}}{\partial y}$$
$$+\overline{S_{yx}}\frac{\partial\overline{v}}{\partial x}+\overline{S_{yz}}\frac{\partial\overline{v}}{\partial z}+(2\mu_t\overline{S_{zz}}-\frac{2}{3}\rho k)\frac{\partial\overline{w}}{\partial z}+\overline{S_{zx}}\frac{\partial\overline{w}}{\partial x}+\overline{S_{zy}}\frac{\partial\overline{w}}{\partial y}]-\rho\beta'\omega^2$$
$$+2(1-F_1)\rho\sigma_{\omega,2}\frac{1}{\omega}(\frac{\partial k}{\partial x}\frac{\partial\omega}{\partial x}+\frac{\partial k}{\partial y}\frac{\partial\omega}{\partial y}+\frac{\partial k}{\partial z}\frac{\partial\omega}{\partial z})$$

(2.19b)

where:

$$\sigma_k=\frac{1}{F_1/\sigma_{k,1}+(1-F_1)/\sigma_{k,2}} \tag{2.20a}$$

$$\sigma_\omega=\frac{1}{F_1/\sigma_{\omega,1}+(1-F_1)/\sigma_{\omega,2}} \tag{2.20b}$$

$$F_1=\tanh(\Phi_1^4) \tag{2.20c}$$

$$\Phi_1=\min[\max(\frac{\sqrt{k}}{0.09\omega y},\frac{500\mu}{\rho y^2\omega}),\frac{4\rho k}{\sigma_{\omega,2}D_\omega^+ y^2}] \tag{2.20d}$$

$$D_\omega^+=\max[2\rho\frac{1}{\sigma_{\omega,2}}\frac{1}{\omega}\frac{\partial k}{\partial x_j}\frac{\partial\omega}{\partial x_j},10^{-10}] \tag{2.20e}$$

$$\sigma_{k,1}=1.176,\ \ \sigma_{\omega,1}=2.0 \tag{2.20f}$$

$$\sigma_{k,2}=1.0,\sigma_{\omega,2}=1.168 \tag{2.20g}$$

$$\beta^*=\beta_\infty^*\left(\frac{4/15+(\mathrm{Re}_t/R_\beta)^4}{1+(\mathrm{Re}_t/R_\beta)^4}\right) \tag{2.20h}$$

$$\mathrm{Re}_t = \frac{\rho k}{\mu \omega} \tag{2.20i}$$

$$\beta_\infty^* = 0.09\,,\quad R_k = 6 \tag{2.20j}$$

$$\beta' = F_1 \beta_{i,1} + (1 - F_1)\beta_{i,2} \tag{2.20k}$$

$$\alpha' = \frac{\alpha_\infty^{'}}{\alpha^*}\left(\frac{\alpha_0 + \mathrm{Re}_t / R_\omega}{1 + \mathrm{Re}_t / R_\omega}\right) \tag{2.20l}$$

$$\alpha_\infty^{'} = F_1 \alpha_{\infty,1} + (1 - F_1)\alpha_{\infty,2} \tag{2.20m}$$

$$\alpha_{\infty,1} = \frac{\beta_{i,1}}{\beta_\infty^*} - \frac{\kappa^2}{\sigma_{\omega,1}\sqrt{\beta_\infty^*}} \tag{2.20n}$$

$$\alpha_{\infty,2} = \frac{\beta_{i,2}}{\beta_\infty^*} - \frac{\kappa^2}{\sigma_{\omega,2}\sqrt{\beta_\infty^*}} \tag{2.20o}$$

$$\beta_{i,1} = 0.075\,,\quad \beta_{i,2} = 0.0828\,,\quad \kappa = 0.41 \tag{2.20p}$$

2.6.3 Numerical Considerations

2.6.3.1 Discretization method

The flow governing equations are continuous Partial Differential Equations (PDE) in both space and time. In order to be solved numerically, they should be discrete into a system of algebraic equations involving the flow variables at discrete poisons and time instances. The Finite Difference Method (FDM), the Finite Element Method (FEM), and the Finite Volume Method (FVM) are the commonly-used discretization methods. Of them, the finite volume method is the most popular way to discretize the continuous PDE of the flow governing equations. In FVM, a series of continuous control volumes are required to be divided in the computational domain. On each control volume, the governing equations are rewritten in the integral form based on the flow variables at its center and surfaces. The flow variables at the surfaces f the each volume can be interpolated from them at the centers of the neighbor control volume. Eventually, a set of algebraic equations are generated on all the control volumes.

2.6.3.2 Pressure-velocity Coupling

For the governing equations, the variables velocity and pressure are coupled and can be solved directly using calculation of the equations. Alternatively, some iterative methods can be adopted to treat the issues related to the pressure-velocity coupling. The SIMPLE method is a basic treatment method and some developmental approaches are achieved. Of them, the SIMPLER and SIMPLEC are used broadly.

2.6.3.3 Boundary Condition

The flow problems are confined in a domain around the target objects and numerical conditions on boundaries should be defined. The boundaries: inlet, outlet, symmetry, periodicity and wall boundaries are employed commonly in wind engineering. Inlet boundaries are the sources where winds come from. And they are assigned with the magnitudes and directions of the upcoming winds. Particularly, the quantities related to turbulence such as k, ε, ω in RANS method are also required to be assigned on the inlet boundaries. Opposite to the inlet boundaries, outlet boundaries are the places where the winds blow out. They are usually far from the flow regions near the target objects and flows at them develop fully. Accordingly, zero gradients of the gradients of flow variables except the pressure are assumed. The symmetry boundaries mean the flow at the two sides of them are symmetric, therefore, the flow variables normal to them are zero. The periodic boundaries are used to couple the flows have same features. Wall boundaries are the faces where the flows can not penetrate. And the flows on them moves with the same velocities of them.

2.6.3.4 Computing Techniques

After the discretization of the governing equations of flows, a system of linear algebraic equations is achieved. They are commonly solved using interactive methods. Jacobi Gauss-Seidel and relaxation interactions are the traditional ones. In order to improve the converging rapid, multi-grid methods are complemented. It has been found that, as the meshes are refined, the convergence rate of iterative methods reduces rapidly. Based on this special characteristic, multi-grid method is developed with iterations completed on grids with various spatial resolutions. The errors having long wave components reduce on the finer grids while these having short wave components decrease on the coarser grids. Through the interaction between grids with different sizes, the rapidity of convergence has been advanced.

Table 2.1 Comfort evaluation standard in the ISO2631-1

L1	a_v <0.315m/s^2	Not uncomfortable
L2	0.315m/s^2≤a_v≤0.63m/s^2	A little uncomfortable
L3	0.5m/s^2≤a_v≤1m/s^2	Fairly uncomfortable
L4	0.8m/s^2≤a_v≤1.6m/s^2	Uncomfortable
L5	1.25m/s^2≤a_v≤2.5m/s^2	Very uncomfortable
L6	a_v >2m/s^2	Extremely uncomfortable

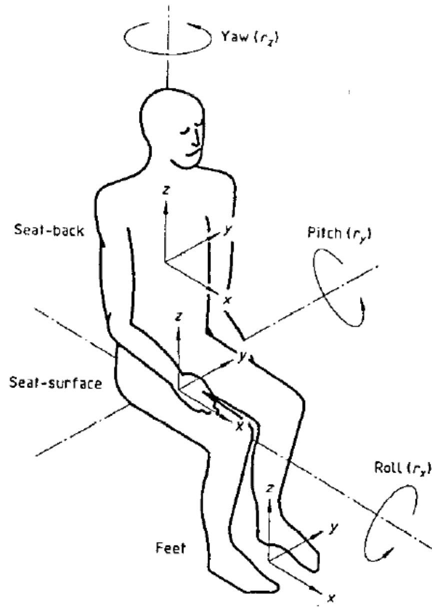

Figure 2.1 Coordinate system defined in the ISO 2631-1(1997)

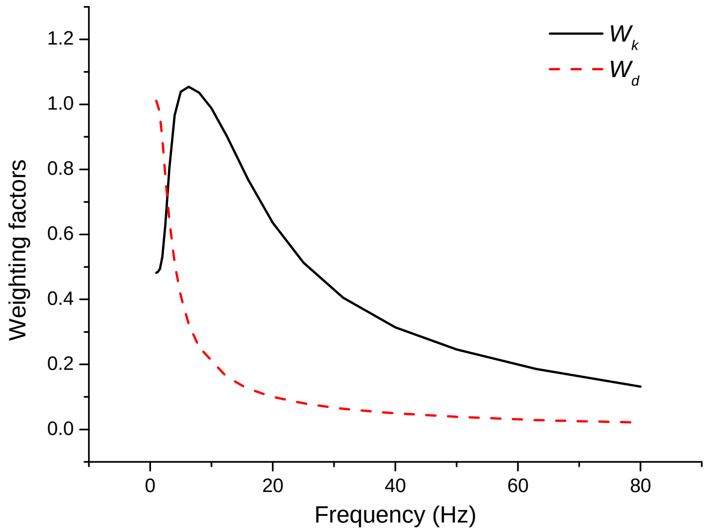

Figure 2.2 Frequency weighting factors

CHAPTER 3

AERODYNAMIC INTERFERENCES BETWEEN A MOVING VEHICLE AND THE GROUND UNDER CROSSWINDS

3.1 INTRODUCTION

To understand the behavior of a moving road vehicle on the ground under crosswinds, the aerodynamic forces on the vehicle considering the aerodynamic interferences between the moving vehicle and the ground under crosswinds shall be first studied. This chapter thus aims to explain how to simulate the flows around the vehicle and obtain the aerodynamic forces in terms of aerodynamic coefficients of the vehicle on the ground for the sake of exploring the aerodynamic interferences between the moving vehicle and the ground. The aerodynamic coefficients will be used to study the progressive instability, safety, and ride comfort of the moving vehicle on the ground in Chapter 4.

Figure 3.1(a) illustrates a vehicle moving on the ground with a velocity vector of $\mathbf{u}_v$ when the wind blows perpendicular to the vehicle with a velocity vector of $\mathbf{u}_w$. If the reference coordinate system is fixed on the vehicle rather than on the ground as shown in Figure 3.1(b), the moving velocity vector of the ground $\mathbf{u}_{gv}$, the velocity vector of the upcoming wind $\mathbf{u}_{wv}$ and its yaw angle a_{WV} can be found:

$$\mathbf{u}_{gv} = -\mathbf{u}_v;\ \mathbf{u}_{wv} = \mathbf{u}_w - \mathbf{u}_v;\quad a_{WV} = \arctan\left(\frac{|\mathbf{u}_w|}{|\mathbf{u}_v|}\right) \tag{3.1}$$

Therefore, the ways to obtain the aerodynamic forces on a moving vehicle are either to measure them on the moving vehicle ($\mathbf{u}_v$) under a perpendicular crosswind ($\mathbf{u}_w$) or to determine them on the stationary vehicle under a yawed crosswind ($\mathbf{u}_{wv}$) with the movement of the ground ($\mathbf{u}_{gv}$).

As reviewed in Chapter 2, a wind tunnel test is the common way to measure the aerodynamic forces on a vehicle under crosswinds. However, it is not easy to realize the movement of a vehicle ($\mathbf{u}_v$) or the movement of the ground ($\mathbf{u}_{gv}$) in a wind tunnel. An approximate way currently used is to neglect the relative motion between the vehicle and the ground and just measure the aerodynamic forces on the stationary vehicle under the yawed crosswind, such as in Baker (1988), Coleman and Baker (1990), Passmore *et al.* (2001), Petzäll *et al.* (2008), Gohlke *et al.* (2010), and Zhu *et al*. (2012) for different types of road vehicles. Humphreys and Baker (1992) did conduct tests of a moving vehicle in a wind tunnel, and the experimental data appeared to be noisy and only side and lift forces were provided. It was found that at low yaw angles, the effects of vehicle movement were obvious.

Due to the complexity of wind tunnel test equipment and procedures, the features of flow field around the vehicle under crosswinds are seldom explored in a wind tunnel. As a complementary tool to wind tunnel tests, the numerical method using computational fluid dynamics (CFD) can be employed effectively to explore the aerodynamic forces of, as well as flow features around, the vehicle. Hargreaves and Morvan (2008) simulated the aerodynamic forces of a stationary high-sided vehicle under crosswinds with different yaw angles using the unsteady RANS method. But few studies have been carried out to determine the aerodynamic forces on a moving vehicle under crosswind.

In this Chapter, a numerical model is set up to compute the aerodynamic forces on, and flow around, a moving high-sided road vehicle using CFD. The unsteady RANS method is employed with the SST k-ω turbulence model to simulate the flow around the stationary vehicle at different yaw angles, firstly. Appropriate meshing and time step are obtained through the comparison of different computational schemes. The simulated aerodynamic forces in terms of aerodynamic coefficients and the surface pressure distributions are validated against wind tunnel test results. Furthermore, the numerical method is extended to compute flows around and the aerodynamic forces on the moving vehicle by considering a moving ground simulation.

3.2 VEHICLE MODEL AND AERODYNAMIC FORCES

An articulated high-sided vehicle with sharp edges is considered in this study. It is scaled with a geometric ratio of 1:25. The geometric sizes of the vehicle model are shown in Figure 3.2. The total height, width and length of the vehicle model are 0.156m, 0.114m and 0.54m, respectively. The aerodynamic force measurements were carried out in the TJ-1 wind tunnel of the State Key Laboratory for Disaster Reduction in Civil Engineering at Tongji University in China. During the tests, both the vehicle model and the ground are fixed without any movement with reference to the wind tunnel. Different yaw angles of wind were realized by rotating the turntable. The Reynolds number is about 1.13×10^5 in terms of the height of vehicle. The details of the testing process can be found in Zhu *et al*. (2012).

The aerodynamic forces on the vehicle are illustrated in Figure 3.3. X, Y, Z are the three axes of a Cartesian coordinate system. The coordinate system is fixed on the vehicle with its origin located at the gravity center of the vehicle. The positive Y-axis is vertical to the ground with upward direction. The positive Z-axis points from the tail to the head of the vehicle in its central symmetric vertical plane. The positive X-axis is perpendicular to the YZ plane with a right hand rule. In this figure, three aerodynamic forces and three aerodynamic moments are defined. Side force F_S, lift force F_L and drag force F_D are along the X, Y, and Z axes, respectively. Side force drives the vehicle to sideslip. Lift force impels the vehicle to depart from the ground. Drag force impedes the movement of the vehicle. Pitching moment M_P, yawing moment M_Y and rolling moment M_R are defined as the moments around the X, Y, and Z axes, respectively. Corresponding to the aerodynamic forces and moments, six non-dimensional aerodynamic coefficients are presented, as follows:

$$C_L = \frac{F_L}{qA}; C_D = \frac{F_D}{qA}; C_S = \frac{F_S}{qA} \tag{3.2}$$

$$C_P = \frac{M_P}{qAL}; C_Y = \frac{M_Y}{qAL}; C_R = \frac{M_R}{qAL} \tag{3.3}$$

$$q = 0.5\rho U^2 \tag{3.4}$$

where C_L, C_D and C_S are the lift coefficient, drag coefficient and side coefficient, respectively; C_P, C_Y, C_R are the pitching moment coefficient, yawing moment coefficient and rotating moment coefficient, respectively; q is the dynamic pressure of air; ρ is the air density; U is the upcoming wind velocity; L is the length of the vehicle; and A is the frontal project area of the vehicle without wheels, and it refers to the project area in the X-Y plane in Figure 3.3.

3.3 TESTED AERODYNAMIC COEFFICIENTS ON STATIONARY VEHICLE

The aerodynamic coefficients of the stationary vehicle without the relative motion with the ground under the winds with four yaw angles (0°, 30°, 60° and 90°) are plotted in Figure 3.4. It can be seen that the side coefficient increases with the increasing yaw angle. The lift coefficient and pitching moment coefficient increase first and decrease later with a maximum value around 30°. The drag coefficient decreases first and increases later with a minimum value around 30°. The yawing moment coefficient decreases with the yaw angle. The rotating moment decreases first and becomes flat beyond 60°. Baker and his colleagues measured the aerodynamic coefficients of a similar vehicle in low turbulence (Baker, 1988; Coleman and Baker, 1990). The Reynolds numbers of the two wind tunnel tests they carried out are about 2.4×10^5 and 8.5×10^4 in terms of the height of vehicle. The absolute maximum differences of aerodynamic coefficients obtained from the three tests are listed in Table 3.1 for different yaw angles. The absolute maximum differences for the side coefficient, lift coefficient, drag coefficient, yawing moment coefficient, pitching moment coefficient, and rotating moment coefficient are 0.82, 1.56, 0.24, 0.48, 0.27 and 0.36, respectively.

3.4 NUMERICAL SIMULATION OF STATIONARY VEHICLE

3.4.1 Simulation Scheme

Owing to the less computation effort of RANS in solving the averaged flow feature, the unsteady RANS method is employed to numerically calculate the flow field around the vehicle. The basic ideal behind unsteady RANS is to average the instantaneous flow governing equations in the time domain. After being averaged, the impressible flow governing equations become

$$\frac{\partial \overline{u}_i}{\partial x_i} = 0 \tag{3.5}$$

$$\rho \frac{\partial \overline{u}_i}{\partial t} + \rho \overline{u}_j \frac{\partial \overline{u}_i}{\partial x_j} = -\frac{\partial \overline{p}}{\partial x_i} + \mu \nabla^2 \overline{u}_i - \frac{\partial \overline{\rho u_i' u_j'}}{\partial x_j} \tag{3.6}$$

where t is the time; x_i is the coordinate in the ith axis in the Cartesian coordinate system; ρ and μ are the density and dynamic viscosity coefficient of air, respectively; u_i is the velocity component along the x_i-axis; u'_i is the fluctuation part of u_i; p is the pressure; the over bar represents the mean value; $-\rho u'_i u'_j$ is the so-called Reynolds stress represented by the SST k-ω turbulence model in this study. The governing equations are discretized using QUICK scheme based on the finite volume method. SIMPLEC algorithm is employed for the coupling of velocity and pressure. The time integration is performed using the second-order implicit method. The CFD code Fluent is employed to solve the parameters of the flow field.

3.4.2 Computational Domain and Boundary Condition

As shown in Figure 3.5, the entire computation domain is a cube enclosed with six outer boundaries: *b_left*, *b_right*, *b_head*, *b_tail*, *b_up* and *ground*. Outer boundary *b_left* is the inflow face where wind blows into the domain. *b_right* is parallel to *b_left* with a offset of *Dx*. The *ground* represents the place where the vehicle stays on. *b_up* is parallel to *ground* with a distance of *Dy*. *b_head* and *b_tail* are the outer boundaries of the cube with *b_head* near the head of vehicle and *b_tail* near the tail of vehicle. The distance between *b_head* and *b_tail* is *Dz*. *z1* and *z2* are the distances of the head and tail surfaces of the vehicle to the boundaries *b_head* and *b_tail*, respectively. The total size of the domain is: Dx=10L, Dy=6.7H, and Dz=15L (H, L are the height and length of the vehicle, respectively). At 0° yaw angle, z_1 and z_2 are 3.5L and 10.5L, respectively. When the vehicle stays with its longitudinal axis perpendicular to the upcoming wind direction (90° yaw angle), the blockage ratio reaches the maximum value compared with other yaw angle cases. The maximum blockage ratio is about 1.5%.

All boundaries including the six outer boundaries and the surfaces of the vehicle are enforced with mathematic boundary conditions to approximate the real situation. *b_left* is the source of upcoming wind, and a uniform wind velocity of 10m/s, turbulence kinetic energy k of 0.05, and special dissipation ratio ω of 2 are assigned over the boundary. After the flow passes the vehicle, wind blows out of the domain through the outer boundary *b_right*. Thus, *b_right* is specified as flow outlet with zero pressure. The outer boundaries *b_up*, *b_head* and *b_tail* are parallel to the direction of the upcoming wind. The flows at these boundaries are assumed uniform and the gradients of flow variables (including wind velocity and pressure) normal to the boundaries are zero. The flow cannot penetrate the ground and the surfaces of vehicle, and no-slip wall is assigned to the ground and the vehicle surfaces.

3.4.3 Domain Decomposition and Meshing

For the sake of taking into account the variation of yaw angle, the computational domain is decomposed into three sub-domains: Circle Zone A, Circle Zone B and Outer Zone as shown in Figure 3.6. Circle Zone A has a geometric shape of cylinder with a radius of L. It enwraps the vehicle model directly and can be rotated together with the vehicle model as a whole to any yaw angle. Circle Zone B is set outside of Circle Zone A with an outer radius of 2L. It is a transition region between the Circle Zone A and the Outer Zone.

To check the independence of grids, three meshing schemes with different grid sizes are generated. In the three meshing schemes, the grid distributions on vehicle surfaces and the height of the first layer grid near the walls keep consistent, and the grid density in the left flow regions becomes the focus. The height of the first layer grid near the surfaces of vehicle and the ground is 1×10^{-5} m, which ensures that the y^+ of the first layer grid near the walls is below 1 in the simulation. The grid distributions on the surfaces of the vehicle are shown in Figure 3.7. Totally about 56 thousand grids are used for the vehicle surfaces. Meshing scheme 1 is the coarsest case with 3.0 million grids. Its grid distribution is shown in Figure 3.8. Meshing scheme 2 has a grid number of 3.8 million, which can be seen in Figure 3.9. Meshing scheme 3 is the finest case with 5.4 million grids. It has the densest grid around the vehicle, as shown in Figure 3.10.

3.4.4 Time Step and Length

A dimensional characteristic time t^* is defined as the ratio of a characteristic length to a characteristic velocity of the flow system. In the cases of a vehicle staying on the ground, wind blows around vehicle, and the characteristic length and characteristic velocity are selected as the width of the vehicle and the upcoming wind velocity. As a result, the characteristic time is expressed as

$$t^* = \frac{B}{U} \tag{3.7}$$

where B and U are the width of vehicle and the upcoming wind velocity. The time step and length for the calculation are set based on t^*. For the case of 90° yaw angle, two time step $0.1t^*$ and $0.05t^*$ are simulated to check the influence of time step on the results. For all the cases, the first $60t^*$ is treated as a converging process and the corresponding results will not be taken into account. The next $60t^*$ is accepted as the time length for the normal computational results. The following results including the aerodynamic coefficients, averaging velocity, velocity profile, and pressure coefficient are averaged values on the last $60t^*$. The streamlines and vorticity magnitudes are taken from the time at $120t^*$.

3.4.5 Numerical Simulation Results and Analyses

3.4.5.1 Influence of meshing and time step

The three grid systems, meshing scheme 1, meshing scheme 2, and meshing scheme 3, are used to calculate the aerodynamic forces with a time step of $0.1t^*$. The mean aerodynamic coefficients are presented in Table 3.2. It can be seen that the side coefficient, yawing moment coefficient, rotating moment coefficient keep nearly constant among the three meshing schemes. The lift coefficient, drag coefficient and pitching moment coefficient exhibit a tendency of convergence with a denser grid. The drag and pitching moment coefficient are nearly constant between meshing scheme 2 and meshing scheme 3. Although the relative differences of lift coefficient and pitching moment coefficient between meshing scheme 2 and meshing scheme 3 are about 11.1% and 16.7% respectively, the corresponding absolute differences are only 0.009 and 0.003. In view of accuracy, meshing scheme 3 is accepted as the proper meshing scheme. For the finest meshing scheme 3, a time step of $0.05t^*$ is tried to consider the influence of time step on the aerodynamic coefficients. The simulated aerodynamic coefficients of different time steps can be seen in Table 3.3. It can be seen that a time step of $0.1t^*$ is accurate enough compared with a shorter time step. $0.1t^*$ is selected as the time step used in the computation of aerodynamic forces on stationary vehicles on the ground.

3.4.5.2 Aerodynamic coefficients with different yaw angles

The flows around the vehicle staying on the ground are numerically calculated for four yaw angles, 0°, 30°, 60°, and 90°, to consider the influence of upcoming wind direction on the aerodynamic forces of the vehicle. The variations of aerodynamic coefficients with yaw angles are plotted in Figure 3.11. The results of wind tunnel tests are also presented for comparison. It can be seen that the variations of simulated aerodynamic coefficients with yaw angle are similar to the wind tunnel test results. The simulated side coefficients are slightly lower than the measured values, and the largest difference between the simulation and test values is about

0.62. The largest difference of lift coefficient between the simulation and test values is about 0.44. For drag coefficient, a largest difference of 0.17 is found. The greatest difference in moment coefficients is about 0.1 at 90° for yawing moment coefficients. As discussed in Section 3.3, the aerodynamic coefficients from the three tests are different to some extent. Nevertheless, the difference between the simulation and wind tunnel test results presented in this section is much smaller.

3.4.5.3 Flow field characteristics

The streamlines around the vehicle at different yaw angles are shown in Figure 3.12. The flows impact the upwind surfaces of the vehicle and form the separated regions around the vehicle. At the yaw angle of 30°, the flows reattach to the top surface of the vehicle. Clearly, the streamlines around the vehicle are different for different yaw angles.

(a) Flow features of main sections

The features of flows around the vehicle are now presented plane by plane. Two cross sections s1 and s2 in Figure 3.2 are selected. s1 is located at the half height of the vehicle while s2 is the middle cross section of the trailer. The vorticity magnitudes in s1 at different yaw angles are shown in Figure 3.13. It can be seen that vortices are generated from the upwind corners of the surfaces. The vorticity distribution for 0° is symmetry about the longitudinal axis of the vehicle. The averaging velocity magnitude contour and streamline of s1 are shown in Figure 3.14. With different yaw angles, the flows separate at different locations. At 0° yaw angle, wind blows to the head of the vehicle and separate at the both corners of the head surface of the tractor, and a pair of vortices are formed behind the tail surface of the trailer. At 30° yaw angle, the flows separate from the corners between the windward side surface and the tail surface of the trailer, the windward side surface and the tail surface of the tractor, the head surface of the tractor and the leeward side surface, and the leeward side surface and the head surface of the trailer. Different from 30° yaw angle, the separated flows in the gap between the trailer and tractor do not reattached to the tail surface of the tractor at 60° yaw angle. At 90° yaw angle, the flows separate from the corners between the windward side surface and the tail surface of the trailer, the windward side surface and the head surface of the trailer, and the head surface of the tractor and the windward side surface of the trailer.

The vorticity magnitudes in s2 at different yaw angles are shown in Figure 3.15. Vortices are generated from the corners of the vehicle at the yaw angles of 30°, 60° and 90°. The averaging velocity magnitude contour and streamline of s2 are shown in Figure 3.16. For the yaw angles of 60° and 90°, flows separate at the corners between the upwind side surface and the top surface, and the upwind side surface and the bottom surface. For 30°, the flows separate from the corner between the upwind side surface and the top surface first and then reattach to the top surface and finally separate again at the corner between the top surface and the leeward side surface. Several tail vortices are formed behind the leeward side surface.

(b) Flow features at 30° yaw angle

According to the flow fields shown above, flows around the vehicle at 30° yaw angle exhibit different characteristics from those at other yaw angels. The averaging Z-velocity magnitude contour and streamline in section s2 are shown in Figure 3.17. The flows separate at the corner between upwind side surface and top surface and then reattach on the top surface. Three vortices are generated in the separation region. These vortices have the velocity in the Z direction (the direction perpendicular to the plane). Thus, they move along z-direction. After separating at the corner between top surface and leeward side surface and the corner between leeward side surface and bottom surface, two vortexes are formed behind the leeward side surface. However, these two vortices have low velocity in the Z-direction. Figure 3.18 shows the surface averaging shear stress distributions, which are used to illustrate the surface flow feature. On the windward side surface of the tractor, the reattachment line along the Y-direction illustrates a separating phenomenon emerging there. In the wind direction of the top surface of the trailer, a reattached line, a separating line and a reattached line emerge sequentially which correspond to the flow separating region on the top surface in Figure 3.17. The three characteristic flow lines were also reported in the experiments of Coleman and Baker (1990). On the leeward side surface, a separating line is formed, which corresponds to the intersection line between the two vortices behind the leeward surface in Figure 3.17.

3.4.5.4 Pressure Distributions on Surfaces

The pressure coefficients (defined as the ratio of pressure to the dynamic pressure) over the surfaces of the vehicle are viewed from different directions in Figure 3.19. The position with a pressure coefficient of 1.0 means a stagnation point. From 0° to 90°, the stagnation points move from the head surface of the tractor to the upwind side surface. The pressures on the upwind surfaces are positive while negative on other surfaces. At 0° yaw angle, the pressure distributions on the two side surfaces are well symmetry. The pressure coefficient is about -0.5 on the tractor surfaces and about -0.1 on the trailer surfaces. At 30° yaw angle, the maximum pressure coefficient on the windward surface is about 0.5. The pressure coefficients on the leeward side surface are negative with an average value about -0.5. At 60° yaw angle, the maximum pressure coefficient on the wind ward surface is about 1.0. The pressure coefficients on the leeward side surface are negative with an average value about -0.5. At 90° yaw angle, the maximum pressure coefficient on the windward side surface is about 1.0. The pressure coefficients on the leeward side surface are negative with an average value about -0.4. From 0° to 30°, the positive pressures on the windward side increase, and the negative pressures on the leeward side surface become lower. From 30° to 60°, the positive pressures on the windward surface continue increasing and the distribution area become larger, and the negative pressures on the leeward surface remain similar. From 60° to 90°, the maximum positive pressure on the windward keeps constant and the distribution area of the large pressure increases while the negative pressure on the leeward surface keeps stable. Due to the interference of vehicle wheels, the pressure distributions on the bottom surfaces of the vehicle are much more complex than other surfaces. From 0° to 90°, the pressure on the bottom surface tends to be lower. A very low negative pressure about -1.5 is distributed on the top surface of the vehicle, which leads to a relative large lift coefficient at 30° yaw angle.

Coleman and Baker (1990) measured the pressure coefficients over the surfaces of a similar vehicle. The measured results are taken to compare with the simulation results obtained from this study. Figure 3.20 shows the differences of surface pressure coefficients between the simulation and wind tunnel test. The locations of the compared pressure coefficients are on the top surface, upwind and downwind side surfaces of the trailer as shown. At 0° yaw angle, all the three surfaces (top, upwind and downwind surfaces) are included in the flow separation regions. Very low negative pressure coefficients are detected in both the simulation and test. The differences between the simulation and test range from -0.08 to 0.05. At 30° yaw angle, very low negative pressure coefficients are measured at the tail points which are not found in the simulated results. The maximum differences between the simulation and test values are 0.19 and -0.17 on the top surface. The corresponding relative differences are about -22.6% and 27.9%. At 60° yaw angle, the pressure coefficients on the upwind surface are positive and those on other two surfaces are negative, which exhibit in both the simulation and test. The maximum differences between the simulation and test values are 0.28 and -0.11 on the upwind surface. At 90° yaw angle, the pressure coefficients on the upwind surface are positive and those on other two surfaces are negative, which again exhibit in both the simulation and test. The maximum differences between the simulation and test values are 0.36 on the upwind surface and -0.13 on the top surface.

3.5 NUMERICAL SIMULATION OF MOVING VEHICLE

3.5.1 Simulation Scheme

As discussed in Section 3.1, the difference between the stationary vehicle and the moving vehicle is whether the movement of the ground is considered or not. For the stationary vehicle, the ground is fixed but the ground moves with a velocity of $\mathbf{u}_{gv}$ in the moving vehicle case. The other numerical settings of the moving vehicle case are the same as the stationary case. For comparison, the moving cases of the vehicle with yaw angles of 0°, 30° and 60° are simulated.

3.5.2 Flow Field Characteristics

Figure 3.21 shows the velocity profiles at the position 2.5*B* away from the longitudinal line of the vehicle in the s1 cross section. The flow is not disturbed by the vehicle. The difference between the stationary modeling and the moving modeling is found mainly on the velocity v_z (the velocity component in the longitudinal direction of the vehicle) and the total velocity v. In the z direction (the longitudinal direction of the vehicle), a boundary layer with a height about 0.0385m emerges in the stationary modeling, which does not appear in the moving ground case. From 0° to 60°, the z-velocity components become lower, and the contribution of the z-velocity to the total velocity become lower as well. Thus, the difference in the profiles of total velocity between the stationary and moving vehicle cases becomes smaller and smaller from 0° to 60°. In other words, the heights of boundary layers tend to be coincident between the stationary and moving modeling from 0° to 60°. The velocity profiles in the s1 cross section are shown in Figure 3.22. From 0° to 60°, the differences in the profiles of velocity between the static modeling and moving modeling become smaller from 0° to 60°. Although the upcoming flows have some kind of difference in the low part of velocity profiles between the stationary and moving modeling, the velocity profiles for the vehicle are almost the same.

The s1 cross section is far from the ground compared with the boundary layer of the ground and therefore the flow characteristics in this plane have been influenced slightly by changing ground boundary condition. Take the flow characteristics at the yaw angle of 30° as an example as shown in Figure 3.23. There is little difference when comparing the moving modeling with the static modeling. The vorticity magnitude and averaged velocity in section s2 are shown in Figures 3.24 and 3.25 respectively. Compared with the corresponding cases in the stationary modeling, it can be seen that influences of the moving ground conditions on the flow are only limited in the low boundary layer near the ground. Such influence becomes weaker and weaker from 0° to 60°.

3.5.3 Surface Flow and Pressure Distributions

As presented in Section 3.5.2, the influences of moving ground conditions on the flows near the vehicle surface are very small. Therefore, the shear stresses and pressure distribution on the vehicle surfaces remain almost unchanged no matter whether the ground is fixed or moving. Figure 3.26 shows the surface characteristics of the vehicle at 30° yaw angle for the moving ground. It can be seen that there is no significant change compared with the fixed ground case.

3.5.4 Aerodynamic Coefficients of Moving Vehicle

Figure 3.27 shows the aerodynamic coefficients of the vehicle in both the moving and fixed ground cases. It can be seen that the differences in the aerodynamic coefficients between the two conditions are small. The absolute aerodynamic coefficient values of the moving vehicle seem little larger than those of the stationary vehicle.

3.6 SUMMARY

In this Chapter, a numerical model is set up to computer the aerodynamic forces in terms of aerodynamic coefficients of, and the flows around, a stationary high-sided vehicle using CFD with unsteady RANS method and validated with the results from wind tunnel tests. Then the model is extended to solve the aerodynamic coefficients of, and the flows around, the moving vehicle. The major procedures and conclusions are summarized as follows:

- A cube computation domain enclosed with six outer boundaries is generated.

The entire computational domain is decomposed into three sub-domains for the sake of changing yaw angle. The independent studies of the grids are then conducted using three meshing schemes of different grid sizes. The grid numbers of the three meshing schemes are 3.0, 3.8, and 5.4 million respectively. The finest one is selected in terms of the accuracy of the aerodynamic coefficients. A time step of $0.1t^*$ is accurate enough compared with a shorter time step.

- The flows around the stationary vehicle on the ground are simulated for different yaw angles. The flows separate at different locations and form different vortices in the wake under the crosswind of different yaw angles. At 0°, the flows separate at the corners of the head surface of the tractor, and a pair of vortices is formed behind the tail surface of the trailer. At 30°, the flows separate from the corners between the windward side surface and the tail surface of the trailer, the windward side surface and the tail surface of the tractor, the head surface of the tractor and the leeward side surface, and the leeward side surface and the head surface of the trailer. Different from 30° yaw angle, the separated flows in the gap between the trailer and tractor do not reattached to the tail surface of the tractor at 60° yaw angle. At 90° yaw angle, the flows separate from the corners between the windward side surface and the tail surface of the trailer, the windward side surface and the head surface of the trailer, and the head surface of the tractor and the windward side surface of the trailer.

- Obviously different flows exist at 30° compared with other yaw angles. The flows separate from the corner between the upwind side surface and the top surface first, and then reattach to the top surface, and finally, separate again at the corner between the top surface and the leeward side surface. A reattached line, a separating line and a reattached line emerge sequentially on the top surface of the trailer viewed from the surface, which is consistent with the results from the experiments of Coleman and Baker (1990).

- Negative pressure coefficients exist on the surfaces of the vehicle in the flow separation regions. The differences of the pressure coefficients between the simulation and the tests of Coleman and Baker (1990) range from -0.08 to 0.05 at 0° yaw angle, from -0.17 to 0.19 at 30° yaw angle, from -0.11 to 0.28 at 60° yaw angle, and from -0.13 to 0.36 at 90° yaw angle.

- The aerodynamic coefficients of the stationary vehicle on the ground are calculated for different yaw angles. The variations of the computed aerodynamic coefficients with yaw angle are similar to the wind tunnel test results. The computed side coefficients are slightly lower than the measured values with a largest relative difference about 12%. The largest difference of the lift coefficient between the simulations and tests is about 0.44. For the drag coefficient, a maximum difference of 0.17 is found. The greatest difference in moment coefficients is about 0.1 at 90° for yawing moment coefficients and the corresponding relative difference is about 20%. The differences of the aerodynamic coefficients between the simulations and the wind tunnel tests are smaller than the variation from the different wind tunnel tests.

- The moving ground is set to model the relative motion between the vehicle and the ground. A boundary layer with a height about 0.0385m of the ground in the case of a stationary vehicle no longer exists at 0° yaw angle. With the increase of the yaw angle, the differences of the wind velocity profiles between the cases of a stationary and a moving vehicle reduce. Consequently, the influences of the relative motion between the vehicle and the ground are only limited in the low boundary layer near the ground, and such influences become weaker and weaker from 0° to 60°.

- The differences in the aerodynamic coefficients of the vehicle between the moving vehicle and the stationary vehicle with the same yaw angle are small.

The absolute values of the moving vehicle seem a little larger than those of the stationary vehicle.

Table 3.1 Absolute maximum differences of the aerodynamic coefficients from three tests

Yaw angle(°)	$D_{max}(C_S)$	$D_{max}(C_L)$	$D_{max}(C_D)$	$D_{max}(C_P)$	$D_{max}(C_Y)$	$D_{max}(C_R)$
0	0.29	0.23	0.23	0.03	0.07	0.02
30	0.82	0.40	0.24	0.08	0.14	0.15
60	0.51	1.30	0.04	0.33	0.27	0.31
90	0.81	1.56	0.16	0.48	0.27	0.36

Table 3.2 Simulated aerodynamic coefficients of the vehicle with different meshing schemes

Meshing	C_S	C_L	C_D	C_P	C_Y	C_R
1	5.022	0.094	0.400	-0.003	-0.595	-0.203
2	5.017	0.072	0.380	-0.021	-0.597	-0.204
3	4.997	0.081	0.383	-0.018	-0.593	-0.203

Table 3.3 Simulated aerodynamic coefficients of the vehicle with different time steps

Time step	C_S	C_L	C_D	C_P	C_Y	C_R
$0.1t^*$	4.997	0.081	0.383	-0.018	-0.593	-0.203
$0.05\ t^*$	4.999	0.084	0.386	-0.017	-0.593	-0.203

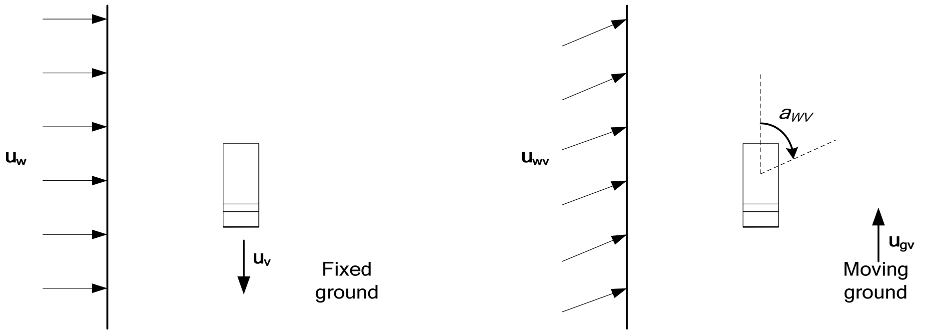

(a)Fixed ground system (b) Fixed vehicle system

Figure 3.1 Vehicle moving on the ground

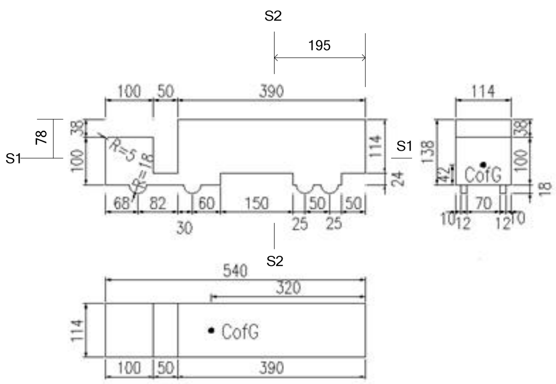

Figure 3.2 Vehicle Model (unit: mm)

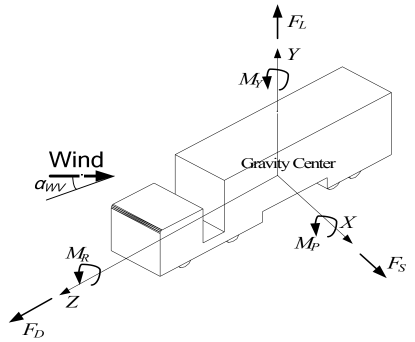

Figure 3.3 Aerodynamic forces and moments on the vehicle

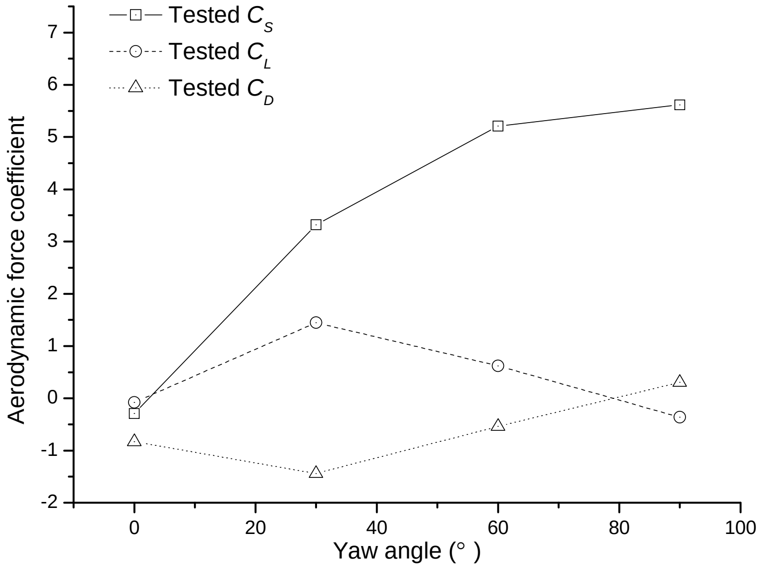

(a) Aerodynamic force coefficients

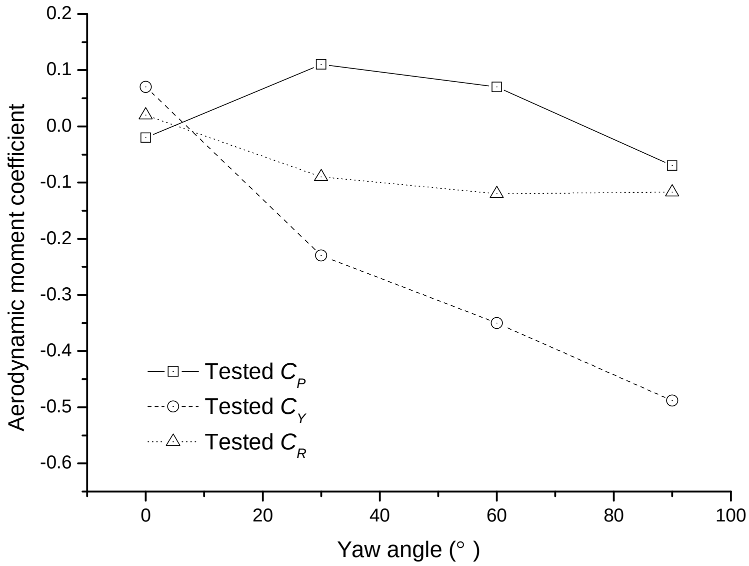

(b) Aerodynamic moment coefficients

Figure 3.4 Aerodynamic coefficients of the vehicle

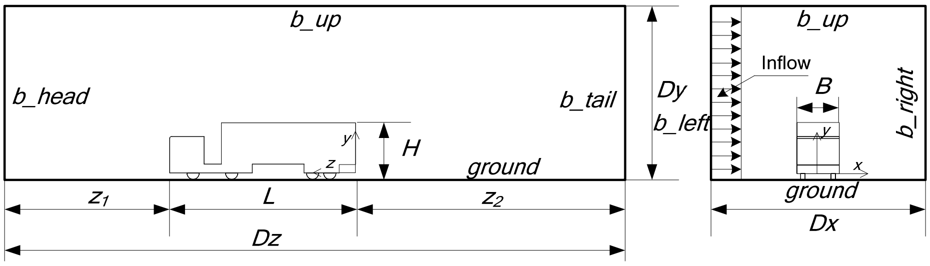

Figure 3.5 Computational domain sketch

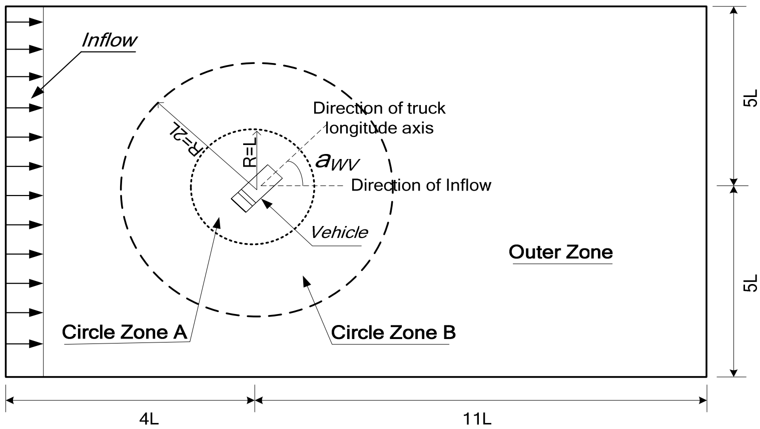

Figure 3.6 Schematic diagram of the domain decomposition

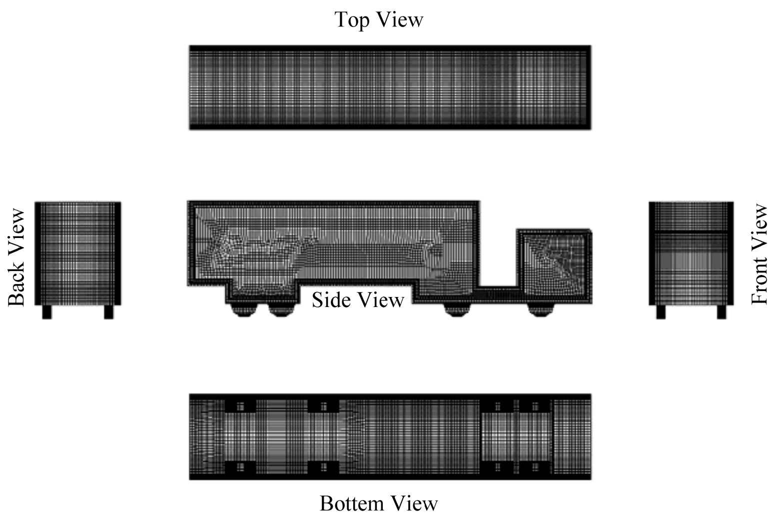

Figure 3.7 Grid distributions on the vehicle surfaces

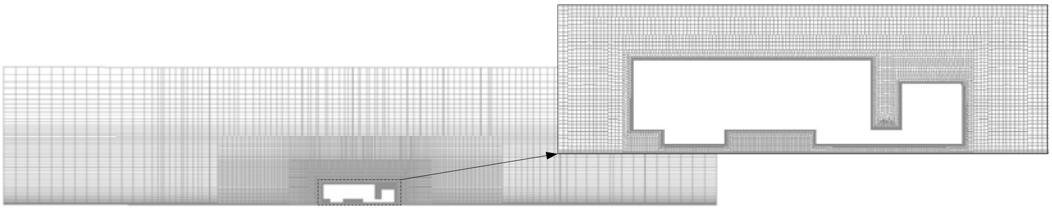

Figure 3.8 Grid distributions in meshing scheme 1 (side view)

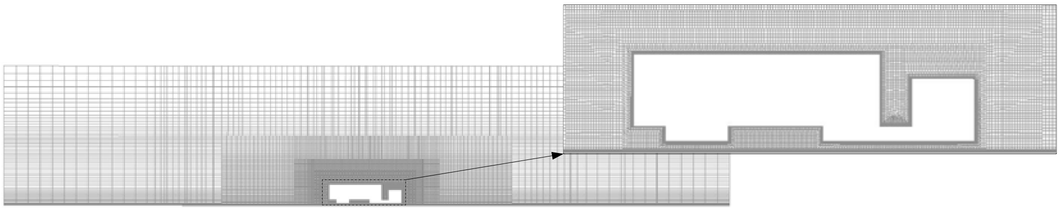

Figure 3.9 Grid distributions in meshing scheme 2 (side view)

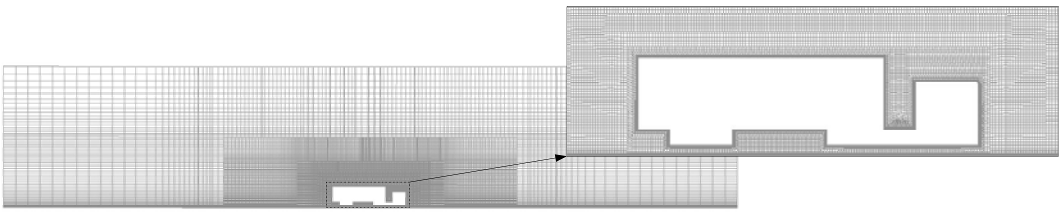

Figure 3.10 Grid distributions in meshing scheme 3 (side view)

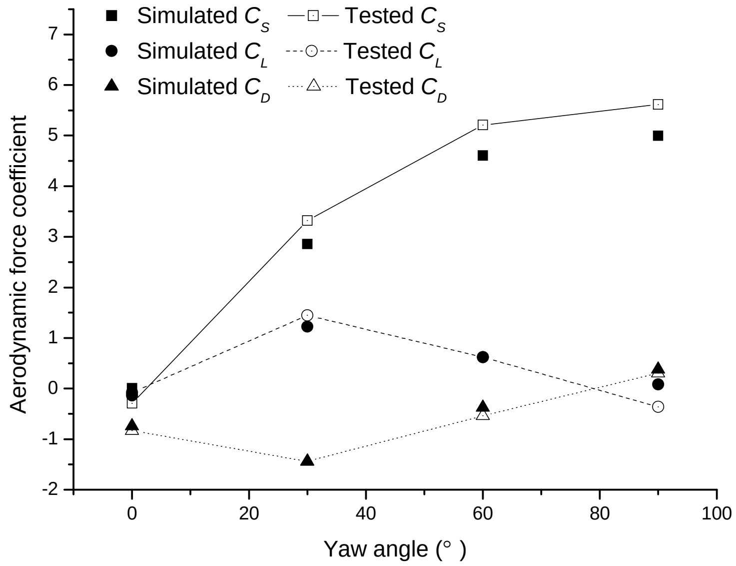

(a) Aerodynamic force coefficients

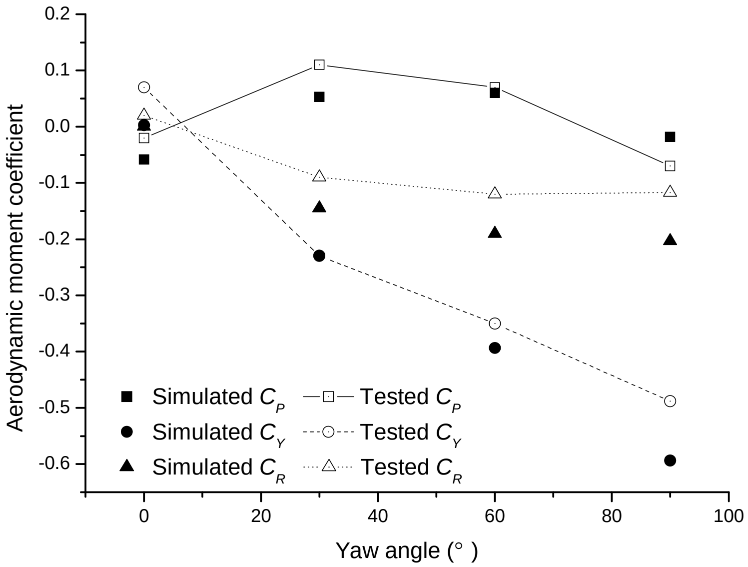

(b) Aerodynamic moment coefficients

Figure 3.11 Aerodynamic coefficient comparison between simulation and test

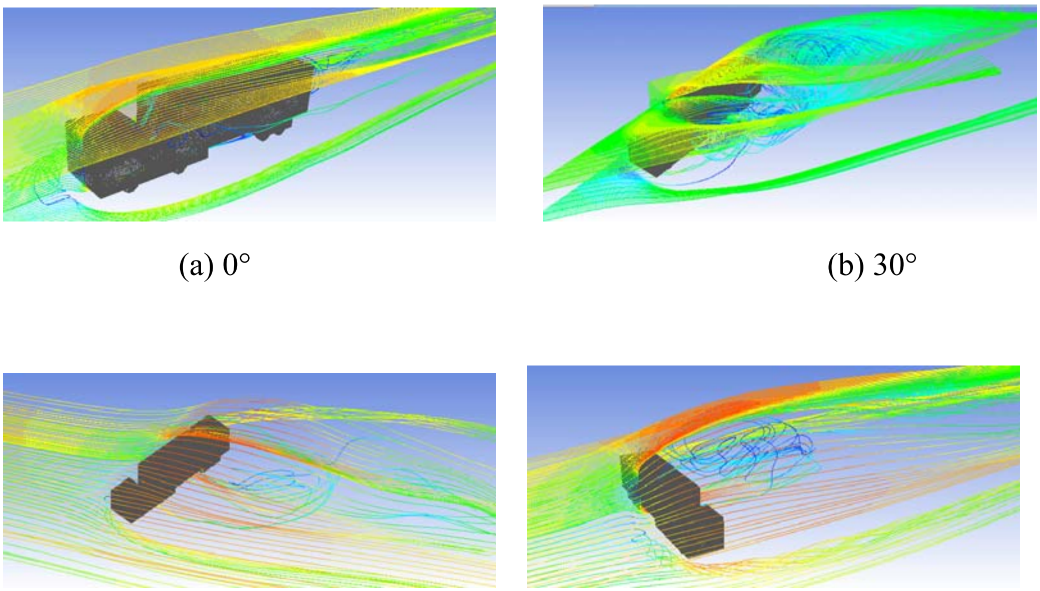

(a) 0° (b) 30°

(c) 60° (d) 90°

Figure 3.12 Streamlines around the vehicle at different yaw angles

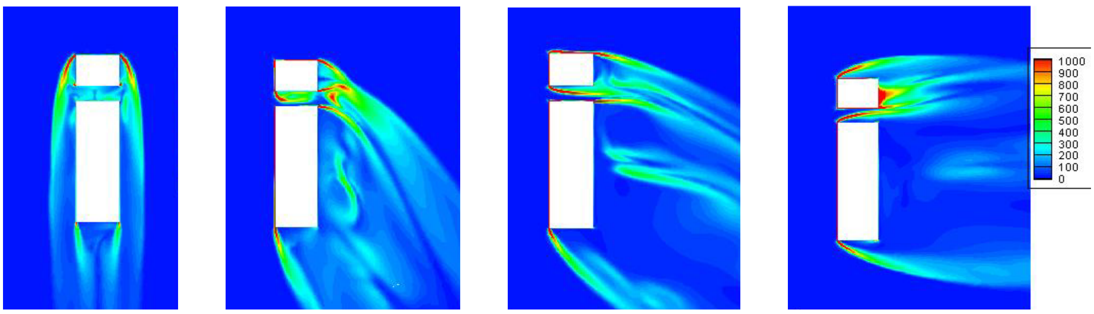

(a) 0° (b) 30° (c) 60° (d) 90°

Figure 3.13 Vorticity magnitudes in section s1

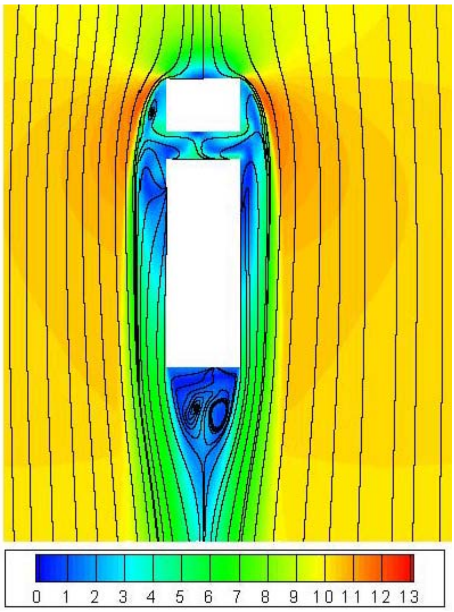

(a) 0°

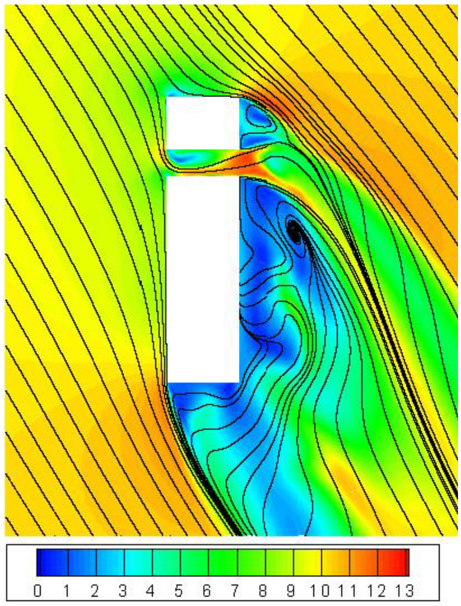

(b) 30°

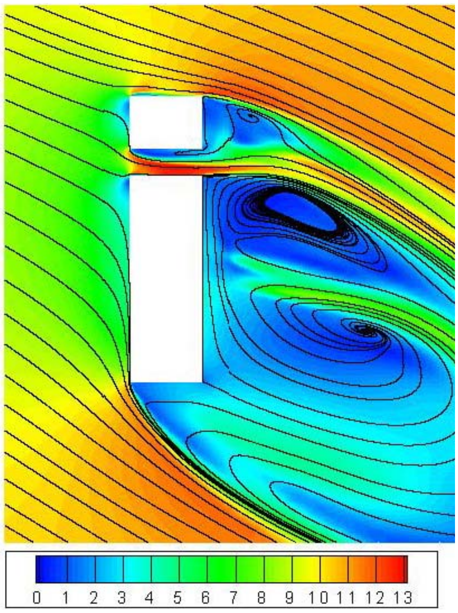

(c) 60°

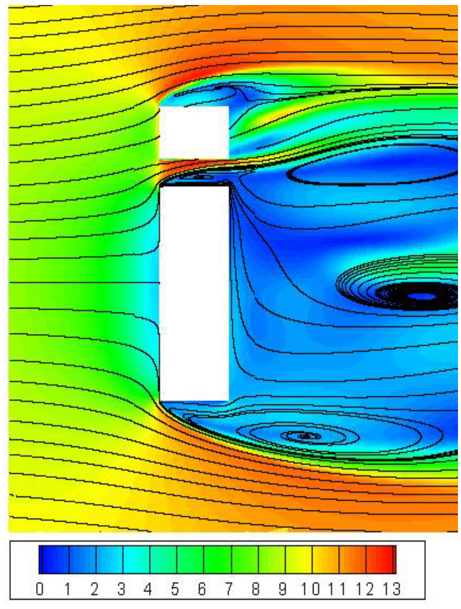

(d) 90°

Figure 3.14 Averaging velocity magnitude contour and streamline in section s1

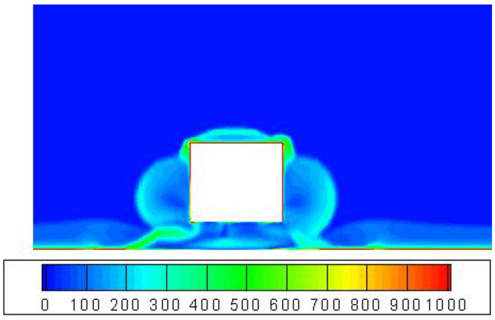

(a) 0°

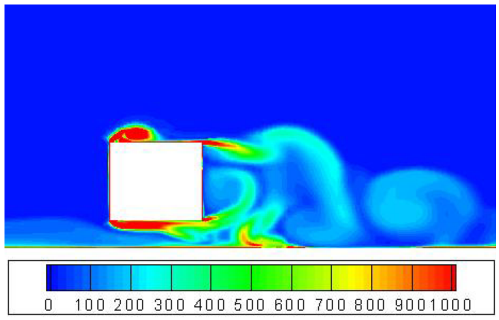

(b) 30°

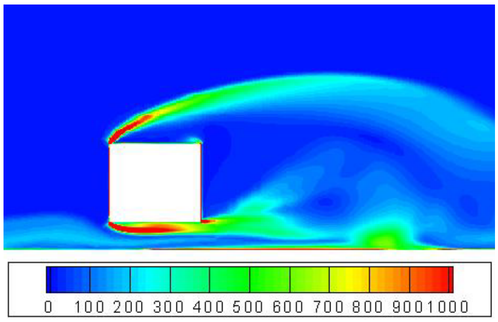

(c) 60°

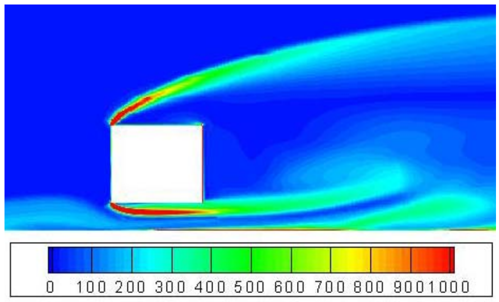

(d) 90°

Figure 3.15 Vorticity magnitudes in section s2

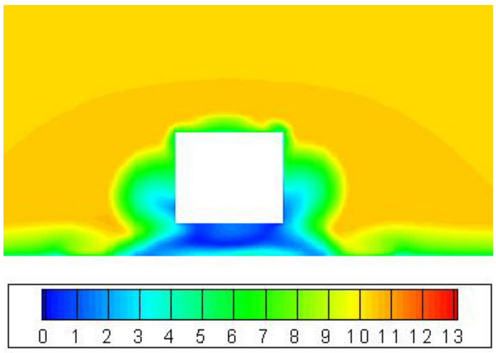

(a) 0°

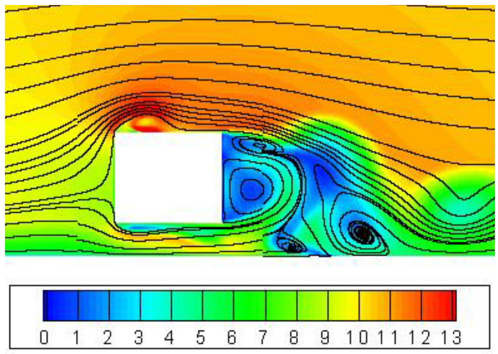

(b) 30°

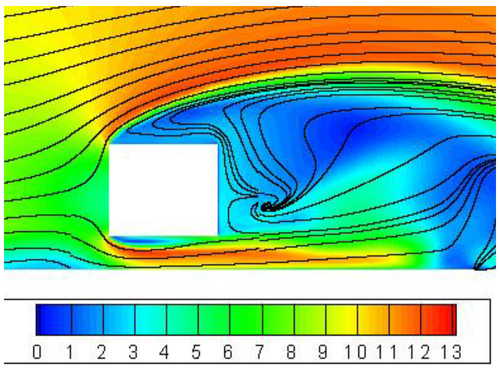

(c) 60°

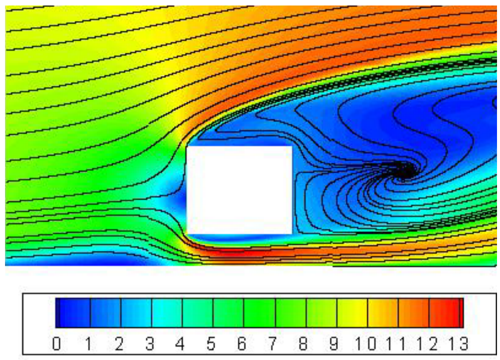

(d) 90°

Figure 3.16 Averaging velocity magnitude contour and streamline in section s2

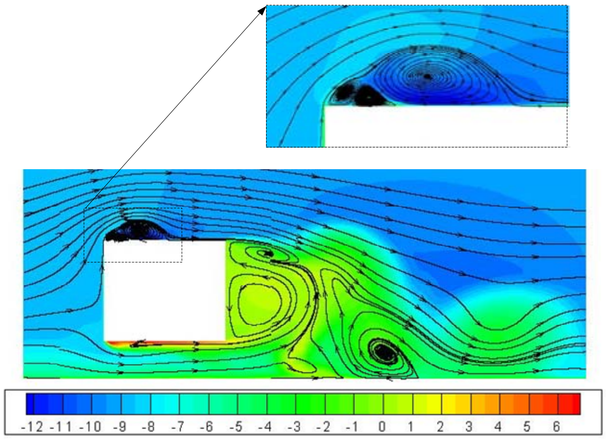

Figure 3.17 Averaging *Z*-velocity magnitude contour and streamline in section s2

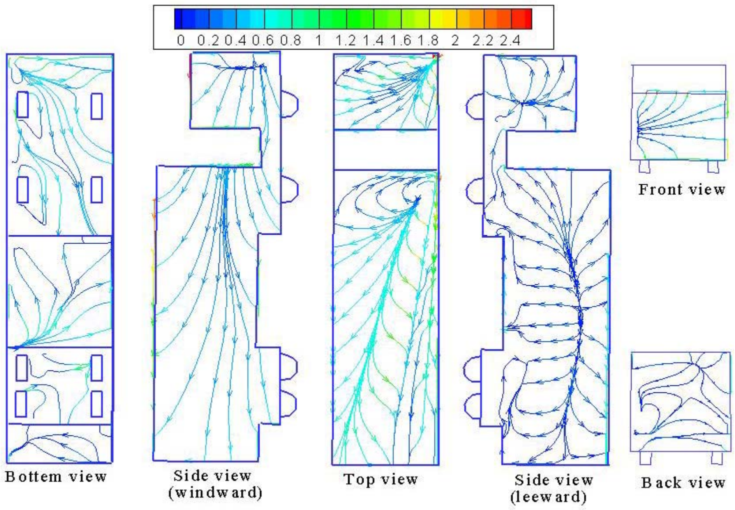

Figure 3.18 Averaging shear-stresses on the surfaces of the vehicle

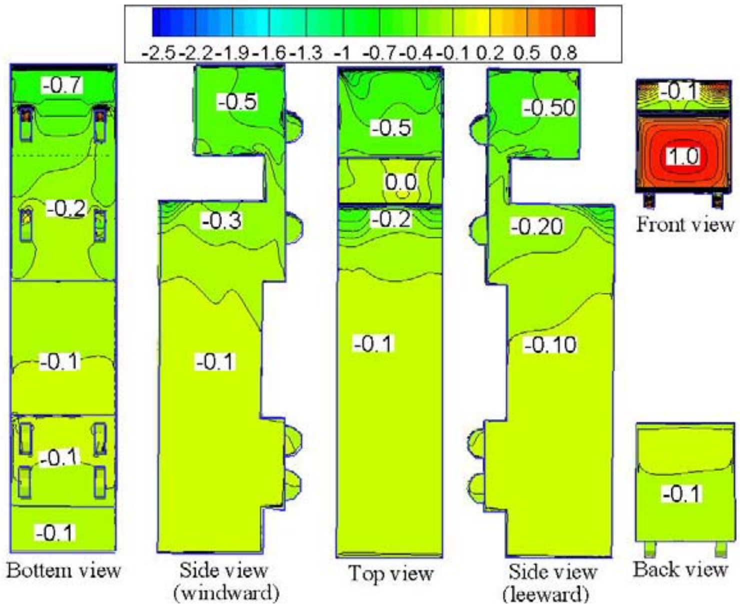

(a) 0°

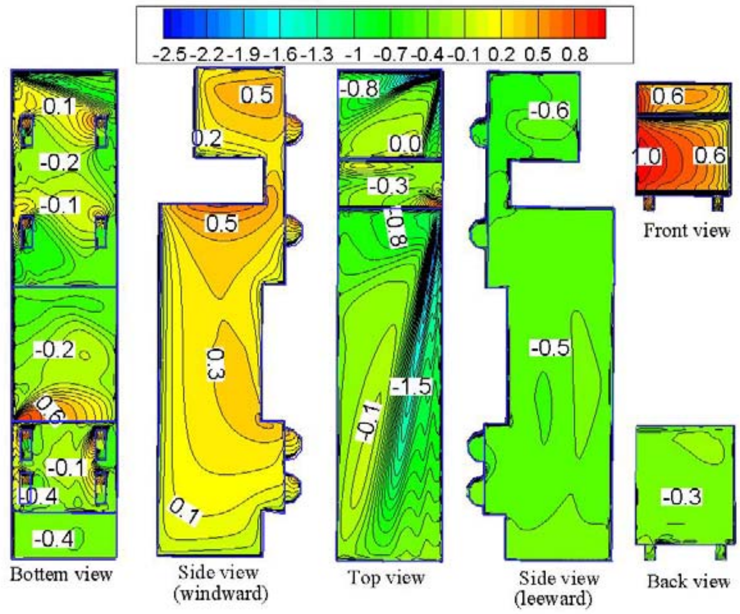

(b) 30°

Figure 3.19 Pressure distributions on the surfaces of the vehicle (to be continued)

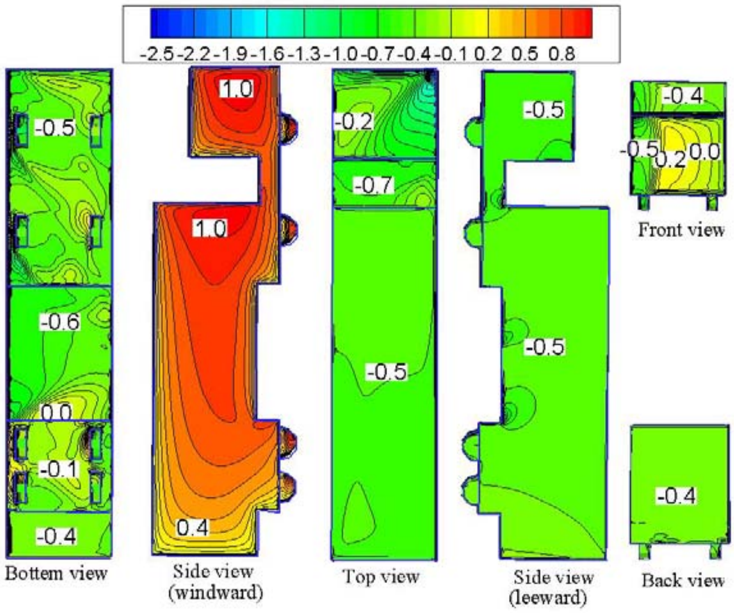

(c) 60°

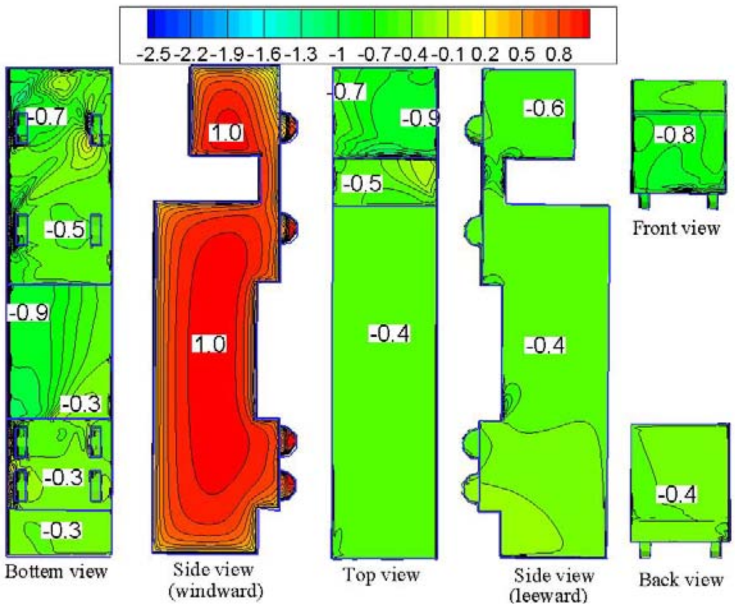

(d) 90°

Figure 3.19 Pressure distributions on the surfaces of the vehicle

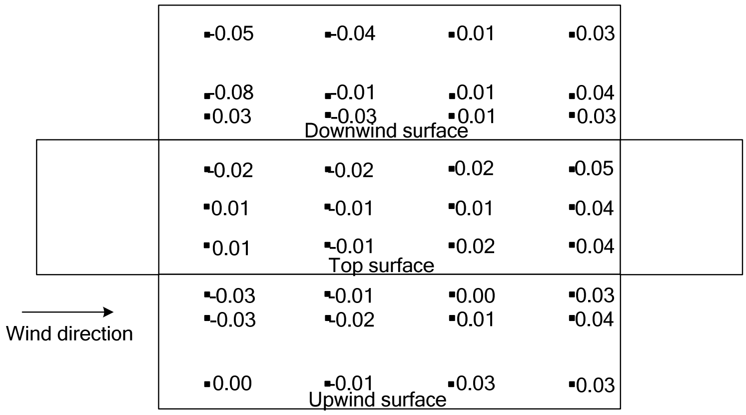

(a) 0°

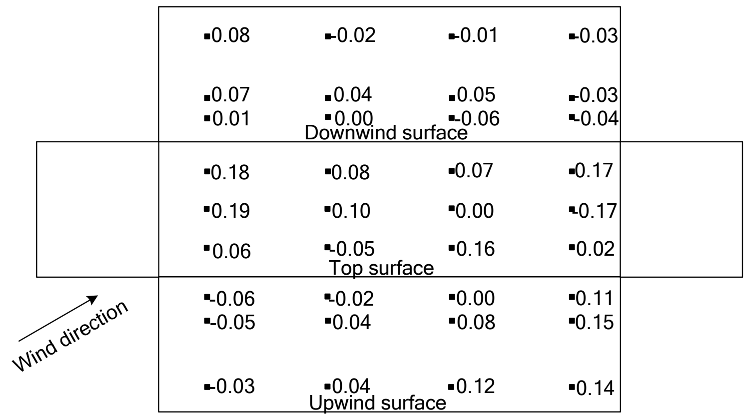

(b) 30°

Figure 3.20 Differences of the simulated and tested pressure coefficients on the surfaces (to be continued)

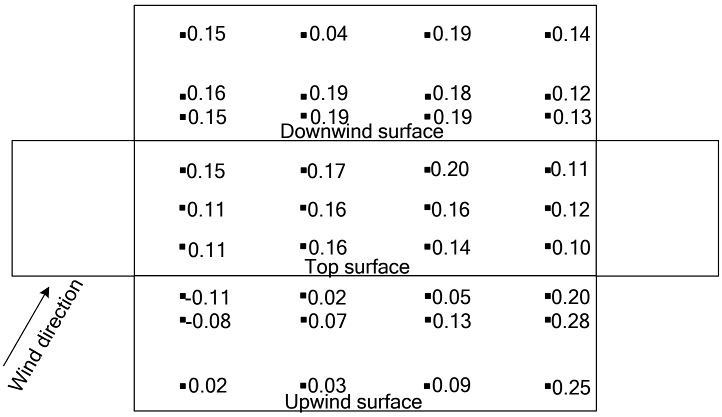

(c) 60°

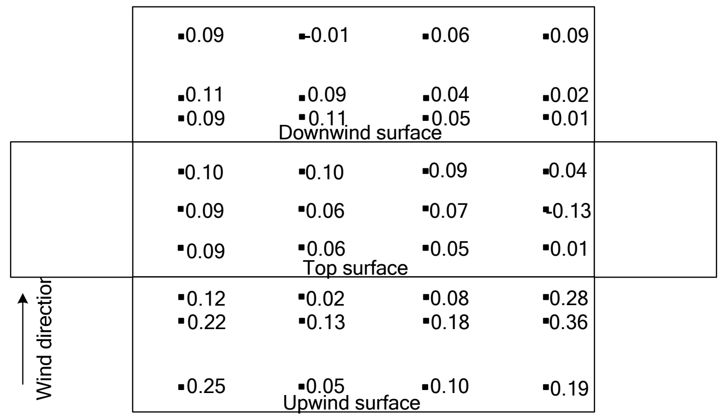

(d) 90°

Figure 3.20 Differences of the simulated and tested pressure coefficients on the surfaces

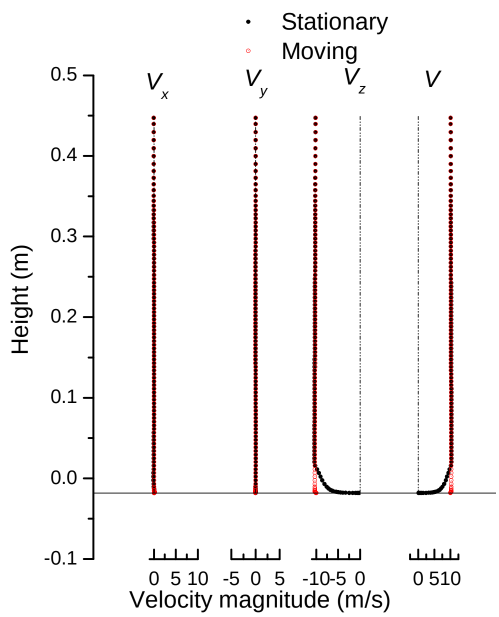

(a) 0°

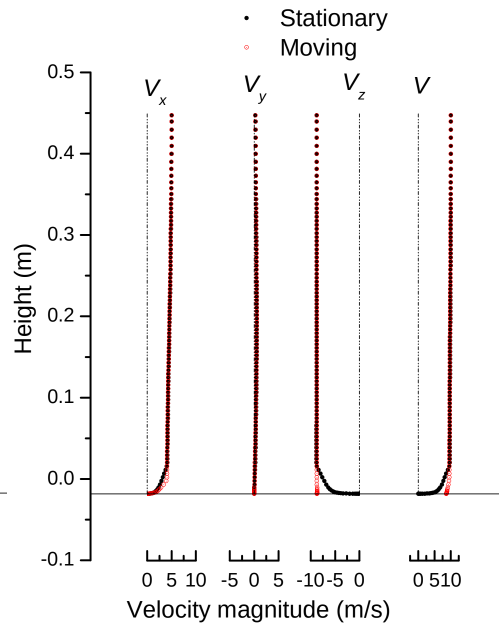

(b) 30°

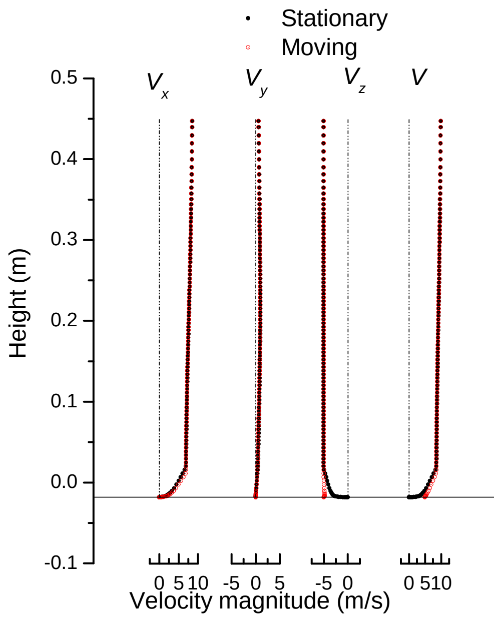

(c) 60°

Figure 3.21 Velocity profiles at the upcoming locations

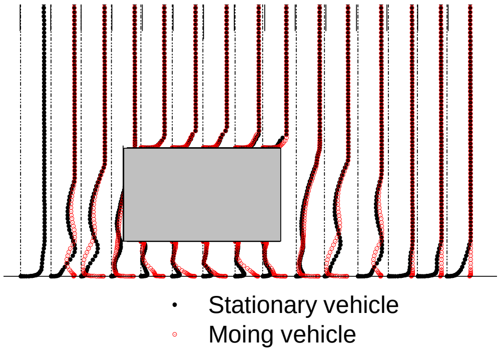

(a) 0°

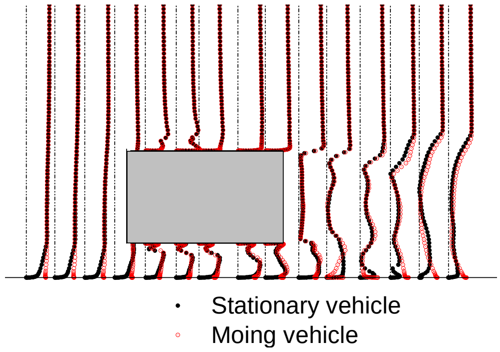

(b) 30°

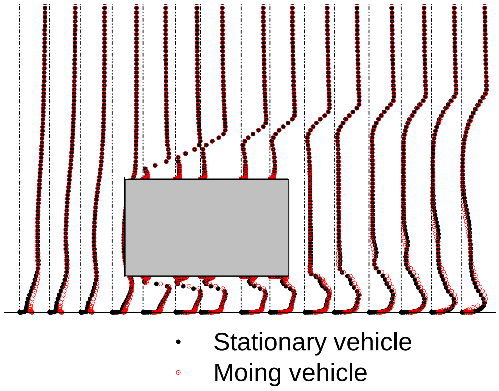

(c) 60°

Figure 3.22 Velocity profile at the cross sections of the vehicle

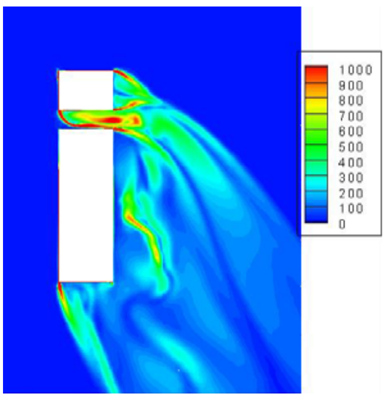

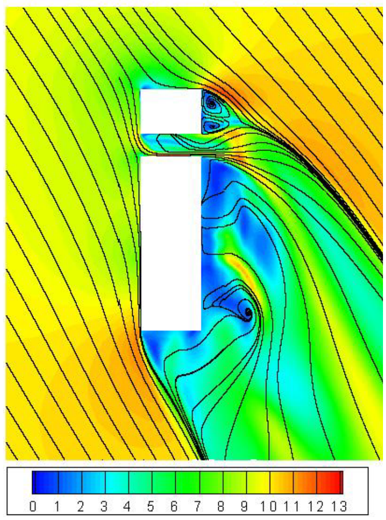

(a) Instantaneous vorticity magnitude (b) Averaging velocity magnitude contour and streamline

Figure 3.23 Flow characteristics in section s1 at 30° yaw angle

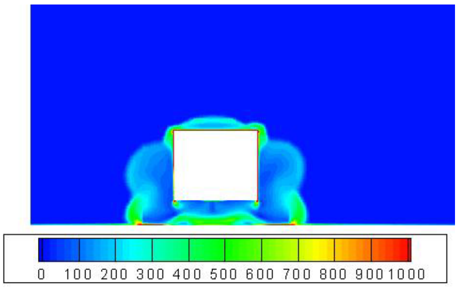

(a) 0°

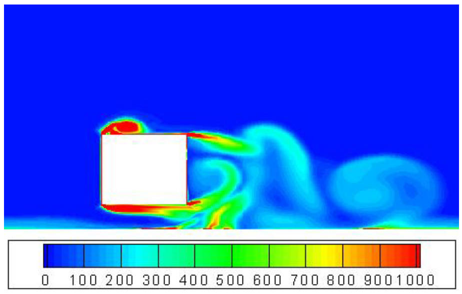

(b) 30°

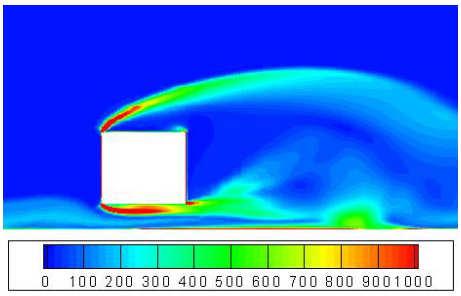

(c) 60°

Figure 3.24 Vorticity magnitudes in section s1

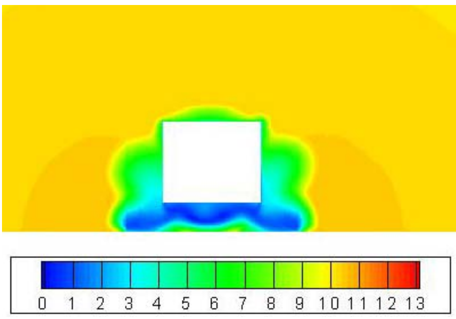

(a) 0°

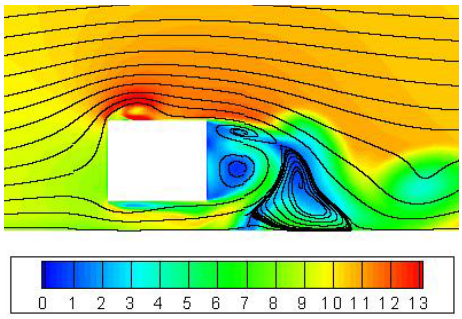

(b) 30°

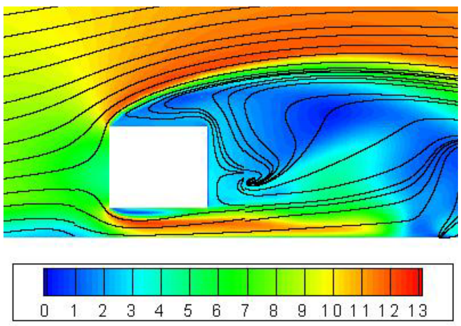

(c) 60°

Figure 3.25 Averaging velocity magnitude contour and streamline in section s1

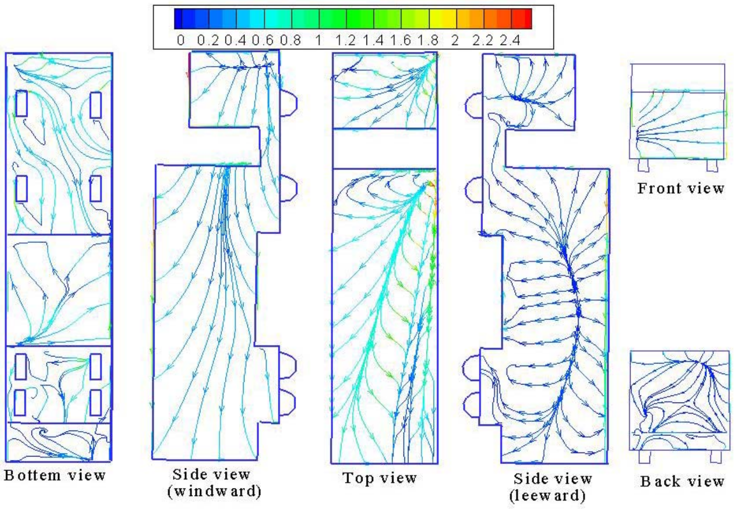

(a) Averaging shear-stresses

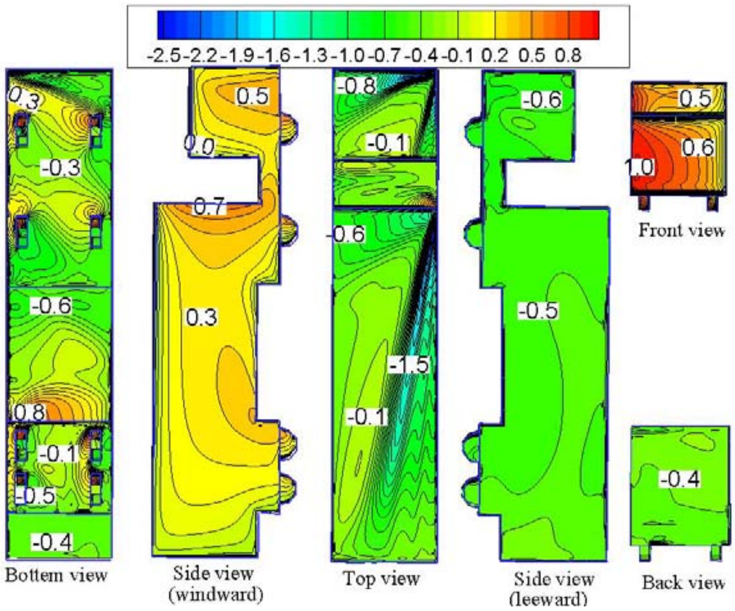

(b) Pressure distributions

Figure 3.26 Surface characteristics of the vehicle at 30° yaw angle

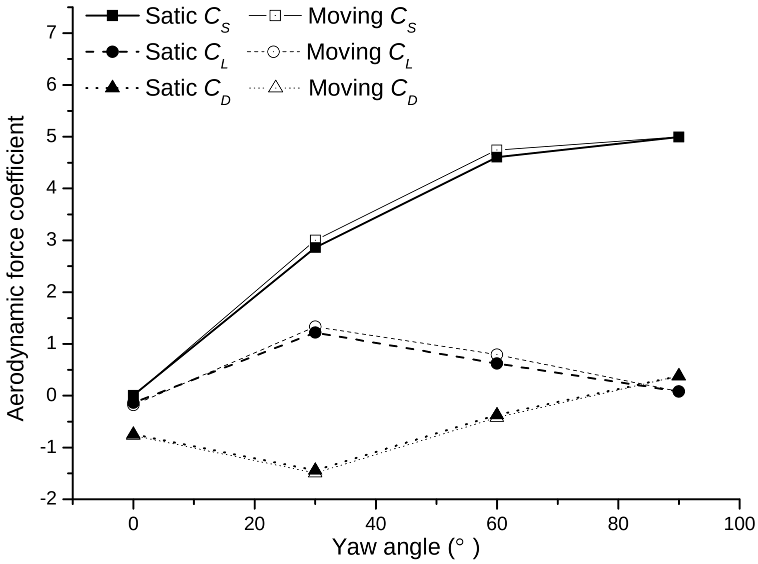

(a) Aerodynamic force coefficients

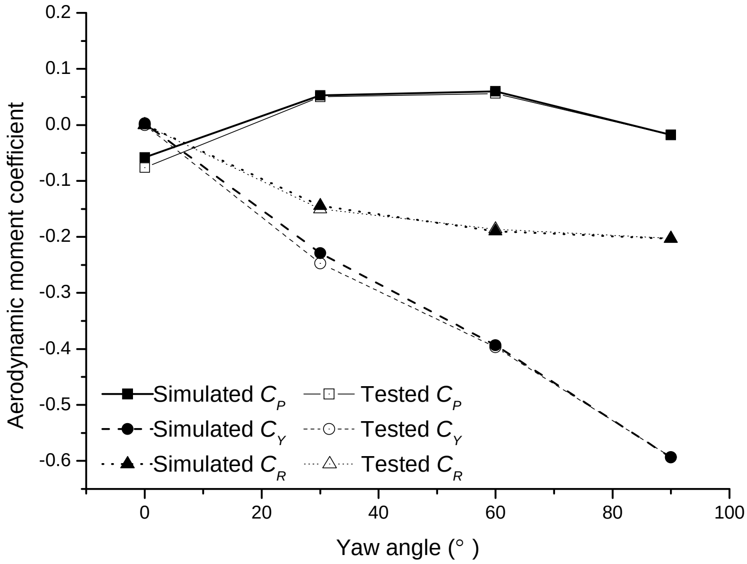

(b) Aerodynamic moment coefficients

Figure 3.27 Comparison of aerodynamic coefficients of the vehicle in stationary and moving ground cases

CHAPTER 4

SAFETY AND RIDE COMFORT OF A VEHICLE MOVING ON THE GROUND

4.1 INTRODUCTION

The aerodynamic coefficients of a high-sided road vehicle moving on the ground have been computed in Chapter 3 using CFD. The obtained aerodynamic coefficients of the moving vehicle on the ground in Chapter 3 will be enforced in this chapter to analyze the dynamic performance of the moving vehicle on the ground in crosswinds. The safety and ride comfort evaluation results gained from this chapter will then be compared with the results presented in Chapter 6, in which the vehicle moving on a bridge deck will be investigated, and the results presented in Chapter 8, in which the vehicle passing by a bridge tower will be studied.

Many works have been devoted to studying the safety of a vehicle in crosswinds. Accordingly, many road vehicle models were developed at different levels of complexity (Baker, 1986; Baker, 1987; Baker, 1993; Xu and Guo, 2003; Cheli *et al.*, 2006; Chen and Chen, 2010; Proppe and Wetzel, 2010). Almost all of them focus on searching the accident vehicle velocity directly, without exploring the progressive instability of a vehicle under crosswinds. The models of Baker (1986, 1987, and 1993), Xu and Guo (2003), and Cheli *et al.* (2006) were established in a fixed coordinate system coincident to the road. In these models, small angular displacements of the vehicle were assumed when the dynamic equations were derived. Moreover, the mass moments were kept constant as their initial values. In fact, when a vehicle approaches instability, angle displacements of the vehicle are quite large, and the small angular assumption and the constant mass moments are not valid any more. Although the model used in Chen and Chen (2010) was set up on the local coordinate system of the vehicle body, small displacement assumption remains in the dynamic equation. In all the vehicle models mentioned above, the effect of the attitude of the vehicle to wind loads was not included. It will affect the responses of the vehicle, particularly in the analysis of the progressive instability. A more rational vehicle model capable to demonstrate the progressive instability is thus required. Understanding the progressive instability of a moving vehicle is very important for avoiding possible dangerous situations and finding the true accident vehicle velocity.

Besides safety analysis of the road vehicle, ride comfort under both road conditions and crosswinds becomes an increasing concern for the public. Guo (2003) evaluated the ride comfort of a road vehicle with both random inputs of crosswinds and road roughness. The ride comfort was assessed based on the acceleration in both vertical and lateral directions. However, the vehicle moved forward without any lateral displacement and road roughness in a line was simulated to excite the vehicle model. Actually, vehicles can move in the lateral direction under crosswinds. The coherence of the road roughness in the lateral direction is important to the responses of the vehicle in addition to crosswinds, particularly for the rotating motion. Moreover, the tires always kept contact with the ground in their study, which may not be an actual situation. Therefore, the limitation of the vehicle movement in the lateral direction should be released after considering the driver behavior and the effects of road roughness on a plane. The jumping of tires from the ground should also be simulated to evaluate the ride comfort in a more accurate and natural sense.

In this chapter, an advanced vehicle model is presented. The dynamic equations of motion of the vehicle are established in the local coordinate system fixed on the vehicle body. The small displacement assumption commonly used in the previous vehicle model is no longer required. Some of the tires can lose contact with the ground. Through the transformation matrix with variables of Euler angle, the global velocity and acceleration responses of the vehicle are traced. Using this vehicle model, the progressive instability of a vehicle under extreme conditions can be analyzed. The traditional single-variable random method to model road surface roughness in a line is extended to model the surface roughness on a plane. After enforcing the aerodynamic forces considering the variation of the attitude of a moving vehicle in the analysis, the progressive instability of the moving vehicle is analyzed. The safety and ride comfort of the vehicle are finally investigated.

4.2 MODELING OF ROAD VEHICLE ON GROUND

4.2.1 Road Vehicle Model

A road vehicle is composed of a series of components (such as engine, tires, doors, windows, and wipers) that are connected in a complicated way. It is not easy to model the details of all components and connections numerically. Even if a detailed numerical model can be set up, it would be time-consuming work to solve its dynamics using a personal computer. A simplified model of a road vehicle is, therefore, used in this study. Moreover, the global information including displacements and accelerations is sufficient for safety and comfort analysis of a vehicle in crosswinds. In this regard, a simplified model of a two-axle lorry shown in Figure 4.1 is used in this chapter. It consists of a vehicle body, four pairs of wheel-tire, and four suspension systems connecting the wheel axles to the vehicle body.

4.2.2 Coordinate Systems

To effectively describe the motion of a road vehicle, different coordinate systems are required as described in SAEJ670 (2008). Earth-Fixed Coordinate System (ECS for short), Vehicle Coordinate System (VCS for short) and Wheel Coordinate System (WCS for short) are applied to represent the status of vehicle body and wheels in this study.

ECS is fixed on the ground plane to trace the global positions of a vehicle. It is defined in Figure 4.2 with three orthogonal axes: X, Y, and Z. Its origin is the starting position of the centre of gravity of the vehicle. XY plane is parallel to the ground plane with the X-axis along the centerline of the lane and the Y-axis perpendicular to the centerline. The Z-axis is upward and perpendicular to the XY plane using a right-handed system. The position of the centre of gravity of the vehicle body and the position of the axis of the ith wheel in ECS are (X_{vb}, Y_{vb} and Z_{vb}) and (X_{wi}, Y_{wi} and Z_{wi}), respectively. The subscripts vb and wi represent the vehicle body and the ith wheel, respectively.

VCS is defined in the reference frame of the vehicle body to describe the motion status of the vehicle body. It is also shown in Figure 4.2 with the orthogonal axes x, y and z. Its origin is attached to the gravity center of the vehicle body. xz plane is the vertical symmetry plane of the vehicle body; x-axis and y-axis are along the heading and horizontal directions while the vehicle is at rest; z-axis is vertical to xz plane in principle of a right-handed system. The translational velocity components of the vehicle body at its center along the three direction axes x, y and z are v_{vbx}, v_{vby} and v_{vbz}, respectively. The angular velocity components of the vehicle body around the three direction axes are ω_{vbx} (rolling), ω_{vby} (pitching) and ω_{vbz} (yawing), respectively. The position of the axis of ith wheel in VCS is represented as (x_{wi}, y_{wi}, z_{wi}).

WCS is attached on each wheel to identify the attitudes of wheels. Its origin is set on the center of the wheel axle as in Figure 4.2. x^*, y^* and z^* are the three coordinate axes. x^* and z^* axes are attached to the wheel plane with x^*-axis along the moving direction of the wheel and z^*-axis in the vertical direction; y^*-axis is in the lateral direction and identical to the spinning axle of the wheel.

4.2.3 Transformation between Coordinate Systems

4.2.3.1 ECS and VCS

In terms of coordinates, the relationship between XYZ-system (ECS) and xyz-system (VCS) can be expressed as

$$(x, y, z)^T = \mathbf{T}_{ve}(X - X_{vb}, Y - Y_{vb}, Z - Z_{vb})^T \tag{4.1a}$$

$$(X - X_{vb}, Y - Y_{vb}, Z - Z_{vb})^T = \mathbf{T}_{ev}(x, y, z)^T \tag{4.1b}$$

where (X_{vb}, Y_{vb}, Z_{vb}) is the location of the gravity center of the vehicle body in the XYZ-system; $\mathbf{T}_{ve}$ is the 3×3 transformation matrix from the XYZ-system to the xyz -system; $\mathbf{T}_{ev}$ is the 3×3 transformation matrix from the xyz-system to the XYZ -system; and the superscript T denotes a transpose operation of a vector or a matrix.

The relationship for any vector between the XYZ-system (ECS) and the xyz-system (VCS) can be expressed as follows:

$$\mathbf{V}_e = \mathbf{T}_{ev}\mathbf{V}_v \tag{4.2a}$$

$$\mathbf{V}_v = \mathbf{T}_{ve}\mathbf{V}_e \tag{4.2b}$$

where subscript e and v represent ECS and VCS respectively; $\mathbf{V}_e$ and $\mathbf{V}_v$ represent any column vector in ECS and VCS respectively.

Both ECS and VCS are orthogonal coordinate systems, satisfying

$$\mathbf{T}_{ev} = \mathbf{T}_{ve}^{-1} = \mathbf{T}_{ve}^{T} \tag{4.3}$$

Generally, a quaternion transformation, a direction cosine transformation, or a kinematics transformation in terms of Euler angles can be employed to locate the orientation of a local coordinate system of the body in a global coordinate system. Of them, kinematics transformation is widely used (Phillips, 2010) and introduced in SAEJ670 (2008). In the kinematics transformation between ECS and VCS, the vehicle Euler angles: yaw angle ψ, pitch angle θ, and roll angle ϕ are defined as the consecutive rational angles from ECS to VCS in a specific order, as follows:

(a) ECS is firstly rotated around its Z-axis with the yaw angle ψ in counterclockwise to get a transition coordinate system (x', y', z').

(b) The transition coordinate system (x', y', z') is then rotated around its y'-axis with the pitch angle θ in counterclockwise to get a new transition coordinate system (x'', y'', z'').

(c) The new transition coordinate system (x'', y'', z'') is rotated around its x''-axis with the roll angle ϕ in counterclockwise to get VCS finally.

As a result, the transformation matrix from ECS to VCS can be determined through the successive rotation transformation with angles ψ, θ, ϕ as follows:

$$
\begin{aligned}
\mathbf{T}_{ve} &= \begin{bmatrix} 1 & 0 & 0 \\ 0 & \cos(\phi) & \sin(\phi) \\ 0 & -\sin(\phi) & \cos(\phi) \end{bmatrix} \begin{bmatrix} \cos(\theta) & 0 & -\sin(\theta) \\ 0 & 1 & 0 \\ \sin(\theta) & 0 & \cos(\theta) \end{bmatrix} \begin{bmatrix} \cos(\psi) & \sin(\psi) & 0 \\ -\sin(\psi) & \cos(\psi) & 0 \\ 0 & 0 & 1 \end{bmatrix} \\
&= \begin{bmatrix} \cos(\theta)\cos(\psi) & \cos(\theta)\sin(\psi) & -\sin(\theta) \\ -\cos(\phi)\sin(\psi)+\sin(\phi)\sin(\theta)\cos(\psi) & \cos(\phi)\cos(\psi)+\sin(\phi)\sin(\theta)\sin(\psi) & \sin(\phi)\cos(\theta) \\ \sin(\phi)\sin(\psi)+\cos(\phi)\sin(\theta)\cos(\psi) & -\sin(\phi)\cos(\psi)+\cos(\phi)\sin(\theta)\sin(\psi) & \cos(\phi)\cos(\theta) \end{bmatrix}
\end{aligned}
\tag{4.4}
$$

Meanwhile, the angular velocities of the vehicle body in VCS can be expressed with the time derivatives of Euler angles ($\dot{\phi}, \dot{\theta}, \dot{\psi}$) and the corresponding rotation transformation matrix (Phillips, 2010) as follows:

$$
\begin{aligned}
\begin{Bmatrix} \omega_{vbx} \\ \omega_{vby} \\ \omega_{vbz} \end{Bmatrix} &= \begin{bmatrix} 1 & 0 & 0 \\ 0 & \cos(\phi) & \sin(\phi) \\ 0 & -\sin(\phi) & \cos(\phi) \end{bmatrix} \begin{Bmatrix} \dot{\phi} \\ 0 \\ 0 \end{Bmatrix} + \begin{bmatrix} 1 & 0 & 0 \\ 0 & \cos(\phi) & \sin(\phi) \\ 0 & -\sin(\phi) & \cos(\phi) \end{bmatrix} \begin{bmatrix} \cos(\theta) & 0 & -\sin(\theta) \\ 0 & 1 & 0 \\ \sin(\theta) & 0 & \cos(\theta) \end{bmatrix} \begin{Bmatrix} 0 \\ \dot{\theta} \\ 0 \end{Bmatrix} \\
&+ \begin{bmatrix} 1 & 0 & 0 \\ 0 & \cos(\phi) & \sin(\phi) \\ 0 & -\sin(\phi) & \cos(\phi) \end{bmatrix} \begin{bmatrix} \cos(\theta) & 0 & -\sin(\theta) \\ 0 & 1 & 0 \\ \sin(\theta) & 0 & \cos(\theta) \end{bmatrix} \begin{bmatrix} \cos(\psi) & \sin(\psi) & 0 \\ -\sin(\psi) & \cos(\psi) & 0 \\ 0 & 0 & 1 \end{bmatrix} \begin{Bmatrix} 0 \\ 0 \\ \dot{\psi} \end{Bmatrix} \\
&= \begin{bmatrix} 1 & 0 & -\sin(\theta) \\ 0 & \cos(\phi) & \sin(\phi)\cos(\theta) \\ 0 & -\sin(\phi) & \cos(\phi)\cos(\theta) \end{bmatrix} \begin{Bmatrix} \dot{\phi} \\ \dot{\theta} \\ \dot{\psi} \end{Bmatrix}
\end{aligned}
\tag{4.5}
$$

Through the inverse transformation of Equation 4.5, the time derivatives of Euler angles can be solved through the angular velocity of the vehicle body in VCS, solved in Equation 4.16 (see Section 4.2.4.1) as follows.

$$\begin{Bmatrix} \dot{\phi} \\ \dot{\theta} \\ \dot{\psi} \end{Bmatrix} = \begin{bmatrix} 1 & \sin(\phi)\tan(\theta) & \cos(\phi)\tan(\theta) \\ 0 & \cos(\phi) & -\sin(\phi) \\ 0 & \sin(\phi)/\cos(\theta) & \cos(\phi)/\cos(\theta) \end{bmatrix} \begin{Bmatrix} \omega_{vbx} \\ \omega_{vby} \\ \omega_{vbz} \end{Bmatrix} \tag{4.6}$$

By integrating $\dot{\phi}, \dot{\theta}$, and $\dot{\psi}$ numerically with respect to time, ϕ, θ, and ψ can be obtained to update the transformation matrix in Equation 4.4.

4.2.3.2 VCS and WCS

Camber angle and steer angle are defined between VCS and WCS in SAEJ670 (2008). As seen in Figure 4.3, camber angle γ is the angle between the z axis and the wheel plane (x^*z^* plane) about the x axis and it is related to the rotational displacement of the vehicle body in Equation 4.19. Steer angle δ is the angle between the x axis and the wheel plane (x^*z^* plane) about the z axis, and it is controlled by a driver (See Section 4.5). Besides camber angle around the x axis and steer angle around the z axis, angle about the y axis between the x axis and the x^*y^* plane is defined as β and can be integrated continuously through:

$$\beta = \int \omega_{vby} dt \tag{4.7}$$

Vectors such as displacement, velocity, acceleration and force are independent of the location of coordinate origins. The relationship of vector between the xyz-system (VCS) and the $x^*y^*z^*$-system (WCS) of the ith wheel can be expressed as

$$\mathbf{V}_{wi} = \mathbf{T}_{wiv}\mathbf{V}_{v} \tag{4.8a}$$

$$\mathbf{V}_{v} = \mathbf{T}_{vwi}\mathbf{V}_{wi} \tag{4.8b}$$

where $\mathbf{V}_{wi}$ and $\mathbf{V}_{v}$ represent the column vectors in the local coordinate system of the ith wheel and vehicle body, respectively; $\mathbf{T}_{wiv}$ is the 3×3 transformation matrix from the xyz-system to the $x^*y^*z^*$-system; $\mathbf{T}_{vwi}$ is the 3×3 transformation matrix from the $x^*y^*z^*$-system to the xyz-system; and the transformation matrices $\mathbf{T}_{wiv}$ can be determined through a successive rotation around x, y, z as:

$$\mathbf{T}_{wiv}=\begin{bmatrix}\cos(\delta) & \sin(\delta) & 0\\ -\sin(\delta) & \cos(\delta) & 0\\ 0 & 0 & 1\end{bmatrix}\begin{bmatrix}\cos(\beta) & 0 & -\sin(\beta)\\ 0 & 1 & 0\\ \sin(\beta) & 0 & \cos(\beta)\end{bmatrix}\begin{bmatrix}1 & 0 & 0\\ 0 & \cos(\gamma) & \sin(\gamma)\\ 0 & -\sin(\gamma) & \cos(\gamma)\end{bmatrix}$$

$$=\begin{bmatrix}\cos(\beta)\cos(\delta) & \cos(\gamma)\sin(\delta)+\sin(\gamma)\sin(\beta)\cos(\delta) & \sin(\gamma)\sin(\delta)-\cos(\gamma)\sin(\beta)\cos(\delta)\\ -\cos(\beta)\sin(\delta) & \cos(\gamma)\cos(\delta)-\sin(\gamma)\sin(\beta)\sin(\delta) & \sin(\gamma)\cos(\delta)+\cos(\gamma)\sin(\beta)\sin(\delta)\\ \sin(\beta) & -\sin(\gamma)\cos(\beta) & \cos(\gamma)\cos(\beta)\end{bmatrix} \tag{4.9}$$

Similarly, both WCS and VCS are orthogonal coordinate systems, satisfying

$$\mathbf{T}_{vwi}=\mathbf{T}_{wiv}^{-1}=\mathbf{T}_{wiv}^{T} \tag{4.10}$$

4.2.4 Governing Equations of Motion

4.2.4.1 Vehicle body

The vehicle body is treated as a rigid body with its mass and mass moments condensed on its center of gravity with a constant heading velocity. Figure 4.4 shows the forced-status of the vehicle body in VCS. f_{vbx}^{G}, f_{vby}^{G}, and f_{vbz}^{G} are the gravity components of the vehicle body along the *x*-axis, *y*-axis, and *z*-axis, respectively. f_{vz}^{W} and f_{vy}^{W} are the wind force components acting on the vehicle along the *z*-axis and *y*-axis, respectively. m_{vx}^{W}, m_{vy}^{W}, and m_{vz}^{W} are the wind moment components about the *x*-axis, *y*-axis, and *z*-axis, respectively. SP*i* (*i*=1, 2, 3, 4) represents the suspension location on the vehicle body corresponding to the *i*th wheel. f_{wiz}^{S} and f_{wiy}^{S} are the force components along the *z*-axis and *y*-axis caused by the suspension system connecting with the *i*th wheel. They are the functions of the displacement and velocity differences between SP*i* and the *i*th wheel axle as follows.

$$f_{wiz}^{S}=f(z_{SPi}-z_{wi},\dot{z}_{SPi}-\dot{z}_{wi}) \tag{4.11a}$$

$$f_{wiy}^{S}=f(y_{SPi}-y_{wi},\dot{y}_{SPi}-\dot{y}_{wi}) \tag{4.11b}$$

If linear springs and viscous dampers are employed, the above equations can be expressed as:

$$f(z_{SPi}-z_{wi},\dot{z}_{SPi}-\dot{z}_{wi})=k_{uz}(z_{SPi}-z_{wi})+c_{uz}(\dot{z}_{SPi}-\dot{z}_{wi}) \quad (4.12a)$$

$$f(y_{SPi}-y_{wi},\dot{y}_{SPi}-\dot{y}_{wi})=k_{uy}(y_{SPi}-y_{wi})+c_{uy}(\dot{y}_{SPi}-\dot{y}_{wi}) \quad (4.12a)$$

where k_{uz} and k_{uy} are the stiffness coefficients of the suspension system; c_{uz} and c_{uy} are the damping coefficients of the suspension system.

VCS is attached on the vehicle body. Newton's second law in the body-fixed system leads to the following dynamic formulation for the vehicle body in VCS (Phillips, 2010).

$$\frac{d}{dt}(m_{vb}\mathbf{v_{vb}})+\boldsymbol{\omega}_{\mathbf{vb}}\times(m_{vb}\mathbf{v_{vb}})=\mathbf{F}+\mathbf{G} \quad (4.13a)$$

$$\frac{d}{dt}([\mathbf{I}]\boldsymbol{\omega}_{\mathbf{vb}})+\boldsymbol{\omega}_{\mathbf{vb}}\times([\mathbf{I}]\boldsymbol{\omega}_{\mathbf{vb}})=\mathbf{M} \quad (4.13b)$$

where m_{vb} is the mass of the vehicle body; $\mathbf{v_{vb}}=v_{vbx}\mathbf{i}+v_{vby}\mathbf{j}+v_{vbz}\mathbf{k}$ and $\boldsymbol{\omega}_{\mathbf{vb}}=\omega_{vbx}\mathbf{i}+\omega_{vby}\mathbf{j}+\omega_{vbz}\mathbf{k}$ are the translational and angular velocity vectors of the vehicle body, with **i**, **j**, **k** being the unit vectors along the x, y, z axes in VCS; $\mathbf{G}=f_{vbx}^{G}\mathbf{i}+f_{vby}^{G}\mathbf{j}+f_{vbz}^{G}\mathbf{k}$ is the gravity vector of the vehicle body in VCS and can be transformed from the gravity vector in ECS by $\mathbf{T}_{ve}(0,0,m_{vb}g)^{T}$ with the gravity acceleration g; $\mathbf{F}=f_{vx}^{W}\mathbf{i}+f_{vy}^{W}\mathbf{j}+f_{vz}^{W}\mathbf{k}$ and $\mathbf{M}=m_{vx}^{W}\mathbf{i}+m_{vy}^{W}\mathbf{j}+m_{vz}^{W}\mathbf{k}$ are the wind induced force and moment vectors acting on the vehicle body in VCS; [**I**] is the inertia tensor with

$$[\mathbf{I}]=\begin{bmatrix} I_{xx} & -I_{xy} & -I_{xz} \\ -I_{xy} & I_{yy} & -I_{yz} \\ -I_{zx} & I_{zy} & I_{zz} \end{bmatrix} \quad (4.14)$$

where I_{xx}, I_{yy} and I_{zz} are the moments of inertia around the x-axis, y-axis, and z-axis, respectively; and I_{xy}, I_{yz}, I_{xz}, I_{yx}, I_{zx}, I_{zy} are the products of inertia. Since xz plane is symmetrical in terms of the mass distribution of the vehicle body, thus

$$I_{xy}=I_{yz}=I_{yx}=I_{zy}=0 \quad (4.15)$$

By extending the vector Equations 4.13 in scalar form, the dynamic equations of motion of the vehicle body with 5 DoFs, excluding the constant motion in the x direction, can be obtained as follows.

$$m_{vb}\dot{v}_{vby} + m_{vb}\omega_{vbz}v_{vbx} - m_{vb}\omega_{vbx}v_{vbz} = -\sum_{i=1}^{4} f_{wiy}^{S} - f_{vby}^{G} + f_{vy}^{W} \tag{4.16a}$$

$$m_{vb}\dot{v}_{vbz} - m_{vb}\omega_{vby}v_{vbx} + m_{vb}\omega_{vbx}v_{vby} = -\sum_{i=1}^{4} f_{wiz}^{S} - f_{vbz}^{G} + f_{vz}^{W} \tag{4.16b}$$

$$I_{xx}\dot{\omega}_{vbx} - I_{xz}\dot{\omega}_{vbz} + (I_{zz} - I_{yy})\omega_{vby}\omega_{vbz} - I_{xz}\omega_{vbx}\omega_{vby} = m_{vx}^{W} + \sum_{i=1,2} f_{wiz}^{S} b_1 - \sum_{i=3,4} f_{wiz}^{S} b_1 - \sum_{i=1}^{4} f_{wiy}^{S} h_1 \tag{4.16c}$$

$$I_{yy}\dot{\omega}_{vby} + (I_{xx} - I_{zz})\omega_{vbx}\omega_{vbz} - I_{xz}(\omega_{vbz}^{2} - \omega_{vbx}^{2}) = m_{vy}^{W} - \sum_{i=2,4} f_{wiz}^{S} L_2 + \sum_{i=1,3} f_{wiz}^{S} L_1 \tag{4.16d}$$

$$I_{zz}\dot{\omega}_{vbz} - I_{zx}\dot{\omega}_{vbx} + (I_{yy} - I_{xx})\omega_{vbx}\omega_{vby} + I_{xz}\omega_{vby}\omega_{vbz} = m_{vz}^{W} - \sum_{i=1,3} f_{wiy}^{S} L_1 + \sum_{i=2,4} f_{wiy}^{S} L_2 \tag{4.16e}$$

where b_1, h_1, l_1, and l_2 are the distances from the gravity center of the vehicle body to the wheel center in the y-direction, to the suspension system in the z-direction, to the front wheel center in the x-direction, and to the rear wheel center in the x-direction, respectively.

4.2.4.2 Wheel-tire

For the wheel-tire, it is assumed that the velocity of each wheel-tire at its center in the x direction is equal to the velocity of the vehicle body in the same direction:

$$v_{wix} = v_{vbx} \tag{4.17}$$

Figure 4.5 shows the forced status on the center of a wheel-tire viewed from the yz plane in VCS. f_{wiz}^{S} and f_{wiy}^{S} represent the forces transferred from the vehicle body through the suspension system to the wheel-tire along the z- and y-axis of VCS, respectively. G_w is the gravity force of the wheel-tire along the negative direction of the Z-axis of WCS. $f_{wiz^*}^{T}$ and $f_{wiy^*}^{T}$ are the normal and lateral forces received by the tire from the ground along the z*- and y*-axis of WCS, respectively. γ' is the angle between the wheel axle and the XY plane. It can be calculated using the coordinates of wheel centers at the same axle as:

$$\gamma' = \begin{cases} \arctan(\dfrac{Z_{w3} - Z_{w1}}{Y_{w3} - Y_{w1}}) & \text{for front wheels} \\ \arctan(\dfrac{Z_{w4} - Z_{w2}}{Y_{w4} - Y_{w2}}) & \text{for rear wheels} \end{cases} \tag{4.18}$$

and

$$\gamma' + \gamma = \int \omega_{vbx} dt \tag{4.19}$$

where Y_{wi}, Z_{wi} are the coordinate components of the center of the ith wheel-tire along the Y- and Z-axis, respectively.

Under normal driving conditions, the tire makes contact with the ground. The normal force $f_{wiz^*}^T$ is generated due to the deformation and damping effect of the tire in the vertical direction. It is taken that the function of the vertical position and velocity of the wheel axle are relative to the ground in ECS. It will become zero if the tire loses contact with the ground, as follows.

$$f_{wiz^*}^T = \begin{cases} f(Z_w - Z_g, \dot{Z}_w - \dot{Z}_g) & if(Z_w - Z_g < h_a) \\ 0 & else \end{cases} \tag{4.20}$$

where $Z_w - Z_g, \dot{Z}_w - \dot{Z}_g$ are the vertical positions and velocity differences of the wheel center and the contact point of the tire on the ground in ECS; $\dot{Z}_g$ is the changing rate of the contact points along the moving track; h_a is the allowed displacement difference between the wheel center and the contact point on the ground and approximated as the radius of the tire without deformation. If linear springs and viscous dampers are used, the first equation of Equation 4.20 becomes:

$$f(Z_w - Z_g, \dot{Z}_w - \dot{Z}_g) = k_{lz}(Z_w - Z_g) + c_{lz}(\dot{Z}_w - \dot{Z}_g) \tag{4.21}$$

where k_{lz} is the stiffness coefficients of the tire; c_{lz} is the damping coefficient of the tire.

The lateral force $f^T_{wiy^*}$ acting on the tire is related closely to the sideslip angle α and the vertical force $f^T_{wiz^*}$ of the tire as:

$$f^T_{wiy^*} = f(f^T_{wiz^*}, \alpha) \tag{4.22}$$

with the sideslip angle:

$$\alpha = \arctan \frac{v_{wiy^*}}{v_{wix^*}} \tag{4.23}$$

In the previous dynamic analysis of road vehicle in crosswinds (Baker, 1986; Xu and Guo, 2003, Chen and Chen, 2010), the lateral force on the tire is approximated using linear expression. To describe the possible large sideslip angle in the progressive stability of the vehicle, the Dugoff nonlinear lateral force model is employed in this study with

$$f(f^T_{wiz^*}, \alpha) = -C_y \tan(a) f(\lambda) \tag{4.24}$$

with

$$\lambda = \frac{\mu f^T_{wiz^*}}{2C_y \left|\tan(\alpha)\right|} \tag{4.25}$$

$$f(\lambda) = \begin{cases} (2-\lambda)\lambda & \lambda < 1 \\ 1 & \lambda \geq 1 \end{cases} \tag{4.26}$$

where C_y and μ are the cornering stiffness of the tire and the static friction coefficient between the tire and the ground.

According to Newton's second law, the wheel-tire has the following dynamic equations along the y and z directions in VCS:,

$$m_{wi}(\dot{v}_{wiy}, \dot{v}_{wiz})^T = (f_{wiy}, f_{wiz})^T \tag{4.27}$$

where m_{wi} is the mass of the ith wheel-tire; $\dot{v}_{wiy}$ and $\dot{v}_{wiz}$ are the acceleration components of the ith wheel-tire along the y- and z-axis in VCS, respectively; and $(f_{wiy}, f_{wiz})^T$ is the external force acting on the wheel-tire along the y- and z-axis in VCS and can be calculated as:

$$\begin{Bmatrix} f_{wix} \\ f_{wiy} \\ f_{wiz} \end{Bmatrix} = \begin{Bmatrix} f_{wix}^S \\ f_{wiy}^S \\ f_{wiz}^S \end{Bmatrix} + \mathbf{T}_{vwi} \begin{Bmatrix} f_{wix^*}^T \\ f_{wiy^*}^T \\ f_{wiz^*}^T \end{Bmatrix} + \mathbf{T}_{ve} \begin{Bmatrix} 0 \\ 0 \\ f_{wiZ}^G \end{Bmatrix} \tag{4.28}$$

where f_{wix}^S is the force transferred from the vehicle body through the suspension system along the *x*-axis, and it is not considered in the *yz* plane; $(f_{wix}^S, f_{wiy}^S, f_{wiz}^S)^T$ is the force vector in VCS transformed from the suspension system, and $f_{wix^*}^T$ is the force received by the tire from the ground in the *x**-axis, and is assumed to be neglected to the dynamic behavior of the wheel-tire in the *yz* plane; $(f_{wix^*}^T, f_{wiy^*}^T, f_{wiz^*}^T)^T$ is the force vector in WCS received by the tire from the ground; $(0, 0, f_{wiZ}^G)^T$ is the gravity of the wheel-tire in ECS.

4.3 WIND FORCES ON ROAD VEHICLE

Sudden change of crosswinds, such as when a vehicle enters to, or gets out of, a shielding body, is the main cause of wind-induced accidents of the vehicle. Commonly, wind forces caused by sudden crosswinds are generated to evaluate the accident resistance ability of the vehicle. To evaluate the ride comfort, wind forces due to fluctuating winds may lead to ride discomfort, and the fluctuating wind velocities should be therefore simulated.

4.3.1 Fluctuating Wind Velocity

Fluctuating winds are random processes with random characteristics in both the space and time domain. The statistical features including the cross- and auto-correlations should be used in numerical simulations. The spectral representation method proposed by Shinozuka (Shinozuko, 1971) is a typical technique to simulate the fluctuating winds. The method is further modified by Yang *et al.* (1997), Yang and Chang (1998), and Cao *et al.* (2000) to enhance the computational speed. For the simplified vehicle model, its dynamic behaviour along the *X*-axis is neglected (that is U_X=0). Only fluctuating winds U_Y and U_Z in the *Z*-

and *Y*-axis are generated. The time histories of U_Y and U_Z at the *j*th point in the *Z*- and *Y*-axis with an equal interval of length can be simulated by:

$$U_{Yj}(t) = \sqrt{2(\Delta\omega)}\sum_{m=1}^{j}\sum_{k=1}^{N}\sqrt{S_Y(\omega_{mk})}G_{jm}(\omega_{mk})\cos(\omega_{mk}t + \phi_{mk}) \tag{4.29a}$$

$$U_{Zj}(t) = \sqrt{2(\Delta\omega)}\sum_{m=1}^{j}\sum_{k=1}^{N}\sqrt{S_Z(\omega_{mk})}G_{jm}(\omega_{mk})\cos(\omega_{mk}t + \phi_{mk}) \tag{4.29b}$$

$$G_{jm}(\omega) = \begin{cases} 0, \, when \, 1 \le j < m \le n \\ C^{|j-m|}, \, when \, m = 1, m \le j \le n \\ C^{|j-m|}\sqrt{(1-C^2)}, \, when \, 2 \le m \le j \le n \end{cases} \tag{4.30}$$

$$\mathrm{C} = \exp\left(-\frac{\lambda\omega\Delta}{2\pi \mathrm{U_m}}\right) \tag{4.31}$$

$$\omega_{mk} = (k-1)\Delta\omega + \frac{m}{n}\Delta\omega, \qquad k=1,2,\ldots N \tag{4.32}$$

$$\Delta_{\mathrm{jm}} = \Delta|\mathrm{j} - \mathrm{m}| \tag{4.33}$$

where S_Y and S_Z are the auto-spectrums of fluctuating winds in the horizontal and vertical directions, respectively; *j*=1, 2,…. *n*; *n* is the total number of locations where wind speed time histories are simulated; *C* is the coherence function between wind velocities at point *j* and *m*; $\Delta\omega$ is the frequency interval, and *N* is the total number of frequency intervals to be simulated; ϕ_{mk} is a random variable uniformly distributed between 0 and 2π.

Kaimal spectrum (Kaimal *et al.*, 1972) is used as the auto-spectrums of the fluctuating wind velocity in the mean wind direction (*Y*-direction):

$$\frac{nS_Y(f)}{u_*^2} = \frac{200f}{[1+50f]^{5/3}} \tag{4.34a}$$

$$f = \frac{nz}{U(z)} \tag{4.34b}$$

$$u_* = \frac{KU(z)}{\ln\left(\frac{z}{z_0}\right)} \tag{4.34c}$$

where f is the dimensionless normalized frequency; n is the frequency in Hz; u_* is the shear velocity of the flow; $U(z)$ is the mean velocity at height z; z_0 is the roughness height of ground; and K is the Von Kármán number.

Lumley-Panofsky spectrum (Lumley and Panofsky, 1964) is used as the auto-spectrums of the fluctuating wind velocity in the vertical direction (Z-direction):

$$\frac{nS_Z(f)}{u_*^2} = \frac{3.36f}{\left[1+10f\right]^{5/3}} \tag{4.35}$$

4.3.2 Relative Wind Velocity and Direction

The generated sudden winds or fluctuating winds in ECS have to be transferred into VCS through the transformation matrix as:

$$\left\{U_x \quad U_y \quad U_z\right\}^T = \mathbf{T}_{ve}\left\{U_X \quad U_Y \quad U_Z\right\}^T \tag{4.36}$$

where U_x, U_y, and U_z are the wind velocity components in VCS.

Referred to the vehicle, the relative wind velocities can then be calculated as:

$$\left\{U_{xe} \quad U_{ye} \quad U_{ze}\right\}^T = \left\{U_x \quad U_y \quad U_z\right\}^T - \left\{v_{vbx} \quad v_{vby} \quad v_{vbz}\right\}^T \tag{4.37}$$

where U_{xe}, U_{ye}, and U_{ze} represent the relative wind velocity components to the vehicle along the x-, y- and z-axis in VCS, respectively.

Figure 4.6 shows the relative wind velocity and direction. The magnitude of the relative wind velocity is:

$$U_{re} = \sqrt{U_{xe}^2 + U_{ye}^2 + U_{ze}^2} \tag{4.38}$$

In Figure 4.6, ABCD is the plane coincident to the yz plane of VCS. A yaw angle α_w is formed between U_{re} and ABCD, with its value as:

$$\alpha_w = \arctan(\frac{\sqrt{U_{ye}^2 + U_{ze}^2}}{U_{xe}}) \tag{4.39}$$

An angle of incidence β_w is also formed in ABCD, with its magnitude as:

$$\beta_w = \arctan(\frac{U_{ze}}{U_{ye}}) \tag{4.40}$$

4.3.3 Wind Forces

The wind force components acting on the vehicle are obtained based on the quasi-steady assumption:

$$f_{vy}^W = \frac{1}{2}\rho U_{re}^2 A_f C_S(\alpha_w, \beta_w) \tag{4.41a}$$

$$f_{vz}^W = \frac{1}{2}\rho U_{re}^2 A_f C_L(\alpha_w, \beta_w) \tag{4.41b}$$

$$m_{vx}^W = \frac{1}{2}\rho U_{re}^2 A_f L_v C_R(\alpha_w, \beta_w) \tag{4.41c}$$

$$m_{vy}^W = \frac{1}{2}\rho U_{re}^2 A_f L_v C_P(\alpha_w, \beta_w) \tag{4.41d}$$

$$m_{vz}^W = \frac{1}{2}\rho U_{re}^2 A_f L_v C_Y(\alpha_w, \beta_w) \tag{4.41e}$$

where ρ is the density of air; A_f is a reference area; L_v is a reference length; C_S, C_L, M_P, M_Y, and M_R are the corresponding aerodynamic coefficients, which are the functions of α_w and β_w. The aerodynamic coefficients can be expanded at β_w=0 using Taylor's series as:

$$C_i(\alpha_w, \beta_w) \approx C_i(\alpha_w) + C_i'(\alpha_w)\beta_w \tag{4.42}$$

where $C_i(\alpha_w)$ and $C_i'(\alpha_w)$ (i=S, L, P, Y, R) are the aerodynamic coefficients and their derivative at β_w=0.

The aerodynamic coefficients $C_i(\alpha_w)$ of the moving vehicle at different yaw angles have been calculated in Chapter 3. All of them are fitted using 3-order polynomials of α_w:

$$C_i(\alpha_w) = C_{i0} + C_{i1}\alpha_w + C_{i2}\alpha_w^{\ 2} + C_{i3}\alpha_w^{\ 3} \tag{4.43}$$

where C_{ij} (i= S, L, P, Y, R and j=0, 1, 2, 3) are the fitting constants and listed in Table

4.1. The fitted curves for them are shown in Figure 4.7 and 4.8.

4.4 ROAD SURFACE ROUGHNESS

The roughness of the road surface is assumed as a homogeneous and ergodic random field satisfying a Gaussian distribution with a zero mean (Kamesh and Robson, 1978; Sun and Deng, 1998). Usually, it is described using a single point stochastic process (called "roughness in line" in this thesis).

4.4.1 Roughness in Line

The roughness in line can be represented by a series of stochastic roughness heights along a line through an inverse Fourier transform:

$$Z_g(X) = \sqrt{2(\Delta\Omega)} \sum_{k=1}^{N_r} \sqrt{G(\Omega_k)} \cos(\Omega_k X + \phi'_k) \tag{4.44}$$

where $Z_g(X)$ is the roughness height at the point X along the target line; $G(\Omega)$ is the power density spectrum (PSD) of the roughness in line at the spatial frequency Ω; $\Delta\Omega$ is the frequency interval and N_r is the total number of frequency intervals to be simulated; ϕ'_k is a random variable uniformly distributed between 0 and 2π.

The PSD of road roughness is selected as a one-parameter function in ISO 8608 as

$$G(\Omega) = G(\Omega_0)(\Omega / \Omega_0)^{-2} \tag{4.45}$$

At a fixed spatial frequency Ω_0 (Ω_0=1rad/m), different values of $G(\Omega_0)$ reflect the roughness grade. In ISO 8608, the road is classified into A, B, C, D, E, F, G and H. $G(\Omega_0)$ corresponding to these grades are 1×10^{-6}, 4×10^{-6}, 16×10^{-6}, 64×10^{-6}, 256×10^{-6}, 1024×10^{-6}, 4096×10^{-6} and 16384×10^{-6}, respectively.

4.4.2 Roughness in Plane

One way to consider the lateral correlation of road roughness (called roughness in plane in this thesis) is the isotropic model. The isotropic model was assessed and several new models were assessed (Kamash and Robson, 1978; Ammon, 1991;

Heath, 1989; Sun and Su, 2001). Bogsjö (2008) compared different coherence models between road roughness in the left and right wheel-paths and recommended an exponentially decreasing coherence model:

$$r(\Omega) = \exp(-\rho_r t_w \Omega) \tag{4.46}$$

where $r(\Omega)$ is the coherence coefficient for spatial frequency Ω; ρ_r is the parameter to be determined, and t_w is the lateral distance between the two paths.

After measuring 20 roads, the parameter ρ_r was founded in the range from 3.1 to 5.5 (Bogsjö, 2008). To generate a roughness plane of road surface, the exponential model of Bogsjö (2008) is extended into the whole plane in this study with:

$$r(\Omega) = \exp(-\rho_r c \Omega) \tag{4.47}$$

where c is the lateral distance.

The spectral representation method of generating fluctuating winds in 4.3.1 is employed to generalize the surface roughness in plane. The roughness height of X at the jth line in Y-direction is:

$$Z_{gj}(X) = \sqrt{2(\Delta\Omega)} \sum_{m=1}^{j} \sum_{k=1}^{N_1} \sqrt{G(\Omega_{mk})} R(\Omega_{mk}) \cos(\Omega_{mk} X + \phi'_{mk}) \tag{4.48}$$

$$R_{jm}(\Omega) = \begin{cases} 0, \, when\, 1 \le j < m \le n_1 \\ r^{|j-m|}, \, when\, m = 1, m \le j \le n_1 \\ r^{|j-m|}\sqrt{(1-r^2)}, \, when\, 2 \le m \le j \le n_1 \end{cases} \tag{4.49}$$

$$\Omega_{mk} = (k-1)\Delta\Omega + \frac{m}{n_1}\Delta\Omega, \qquad k=1,2,\ldots N_1 \tag{4.50}$$

$$\Delta_{\mathrm{jm}} = \Delta|\mathrm{j}-\mathrm{m}| \tag{4.51}$$

where j=1, 2, …. n_1 ; n_1 is the total number of lines in the Y-direction; N_1 is the total number of frequency intervals to be simulated; ϕ'_{mk} is a random variable uniformly distributed between 0 and 2π.

4.5 MODELING OF DRIVER BEHAVIOR

In most cases, the front wheels are steered by the driver while the rear wheels are driven by an engine. Driver models with different complexities have been developed in previous studies. Compared with the simple one as introduced in Baker (1988), more sophisticated driver models have several disadvantages. Firstly, more parameters are required to be determined. They depend on not only the reaction of the driver, both also the properties of the vehicle itself. For different vehicle type, different parameters should be provided, which make the selection of the driver parameters become difficult. Secondly, the parameters in the sophisticated driver model should be traced carefully, or they may lead to divergent results. Thirdly, simple vehicle model should be set up with the sophisticated driver model. With complex vehicle model, the calculation of the dynamic behavior of the vehicle may tend to diverge. Based on the above consideration, the simple vehicle model in Baker (1988) is adopted it this thesis. A simple and physically realistic model of driver behavior was used to control the steer angle δ of the front wheels, in which δ is proportional to the lateral displacement and velocity of the vehicle in ECS as:

$$\delta = -\lambda_1 Y_{vb}(t-\varepsilon) - \lambda_2 v_{vbY}(t-\varepsilon) \tag{4.52}$$

where v_{vbY} and Y_{vb} is the velocity and the displacement from the stable lane of the vehicle body at its center in the Y-direction; λ_1 and λ_2 are constants and required to be determined; ε is the driver reaction time taken as 0.25s.

4.6 ASSESSMENT OF SAFETY AND RIDE COMFORT

4.6.1 Safety

Generally, two types of wind-induced accidents may occur: one is overturning, and the other exceeds the lateral displacement (course deviation), which may involve a collision with a vehicle in the adjacent lane or equipment at the side of the road. Based on the assumption that drivers cannot alter the status of vehicles within 0.5s, Baker (1986) defined the accident’s critical standards for a vehicle entering an 0.5s sudden gust as: (a) the vertical reaction force of a tire reduces to zero; (b) the lateral deflection of vehicle exceeds 0.5m; (c) the yawing angular deflection of the vehicle exceeds 0.2. This standard was adopted in many studies (Cai and Chen, 2004; Guo and Xu, 2006; Chen and Wu, 2010). Cheli *et al.* (2006) took the so-called Load Transfer Ratio (LTR) on the same axle as the critical standard for the overturning risk:

for the front wheel-axle:

$$\mathrm{LTR}_f = \frac{f^T_{w3z^*} - f^T_{w1z^*}}{f^T_{w3z^*} + f^T_{w1z^*}} \tag{4.53a}$$

for the rear wheel-axle:

$$\mathrm{LTR}_r = \frac{f^T_{w4z^*} - f^T_{w2z^*}}{f^T_{w4z^*} + f^T_{w2z^*}} \tag{4.53b}$$

If the absolute value of $\mathrm{LTR_f}$ or $\mathrm{LTR_r}$ is larger than 0.9, the vehicle is regarded as overturning. Thus, if any tire loses contact with the ground, the vehicle is also accepted as overturning because $\mathrm{LTR_f}$ or $\mathrm{LTR_r}$ is a unit larger than 0.9. Actually, one tire may jump from, and restore, contact with the ground due to the roughness. The above $\mathrm{LTR_f}$ or $\mathrm{LTR_r}$ criteria may be too stringent. Another overturning criterion that allows two tires losing contact with the ground for a very short time is employed as the LTR of the whole vehicle, and it is defined as:

$$\mathrm{LTR}_v = \frac{f^T_{w3z^*} + f^T_{w4z^*} - f^T_{w1z^*} - f^T_{w2z^*}}{f^T_{w1z^*} + f^T_{w2z^*} + f^T_{w3z^*} + f^T_{w4z^*}} \tag{4.54}$$

where $\mathrm{LTR_v}$ means the LTR of the whole vehicle. Consistent with $\mathrm{LTR_f}$ or $\mathrm{LTR_r}$, if the absolute value of $\mathrm{LTR_v}$ is larger than 0.9, the vehicle is regarded as overturning.

To evaluate the safety of the vehicle, a sudden crosswind gust from zero to design wind speed with 0.5s duration will be enforced on the vehicle model. Within 0.5s, the maximum lateral deflection, yawing angle of the vehicle body and the $\mathrm{LTR_v}$ are assessed to decide whether a wind-induced accident occurs. A flow chart of the computer program for safety analysis is shown in Figure 4.9. The fourth-order Runge-kutta method is employed to solve the non-linear dynamic equations of the vehicle model. The first 5.0s allow the moving vehicle to achieve a stable status on the ground. A sudden crosswind gust acts on the vehicle from 5.0s to 5.5s.

4.6.2 Ride Comfort

ISO 2631-1(1997) proposes the evaluation standard for evaluating the human exposure to whole-body vibration. The ride comfort is then valued with an index named "frequency weighted root mean square acceleration" (FWRMSA for short, see Section 2.5.2). FWRMSA in each axis except the *x*-axis at the seat is combined as a final FWRMSA as:

$$a_v = (k_y^2 a_{wy}^2 + k_z^2 a_{wz}^2)^{\frac{1}{2}} \tag{4.55}$$

where k_y and k_z are the multiplying factors that can be taken as 1 for the seated drivers; a_{wy} and a_{wz} are the FWRMSA in *y*- and z-axis, respectively.

The flow chart of the computer program is shown in Figure 4.10. Steer angles of the front wheels are controlled through the drive model. The fourth-order Runge-Kutta method is employed to solve the non-linear dynamic equations of the vehicle model. The first 5.0s allows the moving vehicle to achieve a stable status on the ground. From 5.0s, the wind forces of fluctuating winds plus mean winds start to act on the vehicle model.

4.7 CASE STUDY

High-sided vehicles types are prone to sideslip or overturn under strong crosswinds. A two-axle road vehicle used in Guo and Xu (2003) is taken as a case study. The main parameters of the vehicle are listed in Table 4.2. With the advanced vehicle model established above, the progressive instability of the moving vehicle on the ground in a sudden crosswind gust can be simulated. The accident vehicle velocities and ride comfort of the vehicle can then be analyzed accurately.

4.7.1 Progressive Instability Analysis

A typical case considering road roughness in line without considering driver behavior is taken as an example to analyze the dynamic behavior of the vehicle under sudden crosswind gust. The applied crosswind gust suddenly changes from zero to 30m/s at 5.0s and then keeps 30m/s until 5.5s. The vehicle moves at a speed of 100km/h. Road surface roughness in line is generated according to Class B given in ISO8608.

Figure 4.11 shows the angular displacements of the vehicle body. Only pitching movement is excited by the road surface roughness before 5.0s. The rotating and yawing movements are excited by crosswinds after 5.0s. With the crosswind gust of 0.5s duration, the yaw angle increases until a maximum value of -0.044rad (-2.52°) at the end of gust at 5.5s. The roll angle first increases to a maximum value of -0.07rad (-4.01°) and then reduces to a relatively low value. Figure 4.12 shows the lateral positions of the vehicle body and the four wheels. W1 and W3 are the front wheels at the upwind and downwind sides, respectively. W2 and W4 are the rear wheels at the upwind and downwind sides, respectively. At initial status, the lateral positions of the vehicle body, W1, W2, W3, and W4 are 0.0, -1.1, -1.1, 1.1, and 1.1m, respectively, with reference to ECS in the horizontal plane. After 5.0s, both the vehicle body and wheels deviate from the heading course under crosswinds. Since the yaw angle is negative under crosswinds (see Figure 4.11), the derivations of the rear wheels (W2 and W4) exceed those of the front wheels (W1 and W3). Within the 0.5s gust wind period, the maximum lateral displacement of the vehicle body exceeds 0.5m, and thus it shall be regarded as unsafe (see Section 4.6.1). Figure 4.13 shows the vertical positions of the vehicle body and the wheel centers. At initial status, the vertical positions of the vehicle body, W1, W2, W3, and W4 are 1.2, 0.4, 0.4, 0.4, and 0.4m, respectively, with reference to ECS in the vertical plane. With the road roughness only in line, both wheels in the front axle (W1 and W3) or the rear axle (W2 and W4) have the same displacement in the vertical direction before crosswind gust is applied. Under crosswinds, the vertical displacements of the wheels in the same axle become different due to the rotating movement of the vehicle body. At about 5.119s, the vertical position of W1 is larger than 0.4m, which means the wheel jumps from the ground. About 5.148s, W2, on the same upwind side as W1, loses contact with the ground. Nevertheless, the two wheels jumping from the ground can still go back in touch with the ground. It can be seen that W1 contacts again with the ground at 5.234s, while W2 goes back to the ground at 5.380s. This progressive instability can also be seen from Figure 4.11, in which the maximum roll angle occurs when the two upwind wheels get rid of the ground. However, although both wheels lose contact with the ground, the maximum roll angle of the vehicle body is only -0.07rad (-4.01°) under the sudden gust. After the gust impact, the four wheels of the vehicle finally contact with the ground again. The above explanation can be further confirmed by Figure 4.14, which shows that the vertical contact forces of the two wheels reduce to zero from 5.119s to 5.380s for W1 and from 5.148s to 5.234s for W2. Figure 4.15 shows the LTR indexes for the wheel-axles and the whole vehicle. By definition, the LTR index becomes 1.0 when only one wheel jumps from the ground, while the LTR_v index reaches 1.0 when the two wheels lose contact with the ground. The LTR_f of LTR_r index may change from 1.0 to less than 1.0 if the off-ground wheel returns back to the ground. Similarly, the LTR_v index can also decrease from 1.0 as any one of the off-ground wheels comes back to the ground. The results presented in Figure 4.15 clearly demonstrate the contact condition between the four wheels of the vehicle and the ground during the gust period from 5.0s to 5.5s. The proposed model indeed can describe the progressive instability of the road vehicle under crosswind in detail. The vertical position of a wheel, the vertical contact force on a wheel, and the LTR index can be used to trace the contact condition of all the wheels with the ground. Clearly, the LTR_v index can describe the safety of the vehicle more realistically than the LTR_f/LTR_r index. Using the LTR_v index instead of the LTR_f/LTR_r index as the overturning criterion can remove a miss-judgment as one wheel jumps from the ground due to a large roughness block. For the vehicle of 100km/h speed under a 30m/s crosswind gust within the duration of 0.5s, even though both the wheels on the upwind side of the vehicle jump from the ground, they can still go back to the ground, as demonstrated in this study because the maximum roll angle is about

-4.01°only. If the LTR_f index is used in this case, the overturning occurs early and longer and this may be too conservative.

4.7.1.1 Effects of roughness in plane

The uneven roughness in the lateral direction is partly contributed to the rotational motion of the vehicle body. With the same class of roughness above, a plane roughness is generated at a lateral interval of 0.1m. A medium value of 4.0 is given to the cross-relation coefficient ρ_r. Figure 4.16 shows the simulated roughness along the road (X-direction) at the initial lateral positions of the wheels (Y=-1.1 and 1.1m).

By replacing the line roughness with the plane one, the dynamic responses of the vehicle moving at 100km/h under a 30m/s crosswind gust are solved. Figure 4.17 and Figure 4.18 show the lateral and vertical positions of the vehicle body. The vehicle moves slightly in the lateral direction on the road with plane roughness before 5.0s without crosswind. The lateral displacement of the vehicle in crosswinds is almost no change by considering the roughness plane with roughness height differences in the lateral direction. The vertical displacement of the vehicle, however, has slight changes due to the roughness plane. Figure 4.19 compares the angular displacements of the vehicle body with line and plane roughness. It can be seen that the rotating movement of the vehicle is affected by the plane roughness with and without crosswind gust. This can also be seen in the LTR_v index as shown in Figure 4.20. Nevertheless, the starting time and duration of the LTR_v index being 1.0 are not changed by the plane roughness, which means the roughness in plane has no additional contribution to the overturning compared with roughness in line.

4.7.1.2 Effects of roughness class

Class B of the road roughness in plane in 4.7.1.1 is now replaced with Class C to simulate the progressive instability of the vehicle. Figure 4.21 shows the angular displacements of the vehicle body. With the worse road roughness (Class C), the roll and pitch angle displacements of the vehicle increase. Figure 4.22 and Figure 4.23

show the lateral and vertical positions of the vehicle body. Similarly, the worse road roughness leads to larger displacements. Figure 4.24 shows the LTR values. The LTR values become larger for the roughness Class C than the roughness Class B in general. Particularly, W3 jumps from the ground, leading the LTR_f index reaching 1.0 at about 4.2s even without crosswinds. Nevertheless, although W3 loses contact with the ground, the vehicle can still run in safe in terms of LTR_v. This indicates again that using the LTR_v index as the criterion of overturning can exclude the occasional jump of one wheel from the ground compared with the criterion of using the vertical reaction force of a wheel or the LTR value for one wheel-axle.

4.7.1.3 Effects of driver behavior

To consider the effects of driver behavior, the parameter pair (λ_1, λ_2) is required to be determined first. A very simple and rational way is adopted here to decide the parameters. Generally, the skill of changing lanes on roads is a basic training subject for one to get a driving license. Physically, the purpose of this step is to train the active reaction of one to the lateral movement of vehicles. The parameter pair (λ_1, λ_2) is exactly the mathematical measure of the active reflection. Therefore, numerical simulation of the process of changing lanes is employed to determine the drive model parameters.

Assuming that the width of a lane is 3.75m, the driver needs to change lanes of the moving vehicle through rotating the steering wheel of a vehicle without crosswinds. The driver parameters λ_1 and λ_2 are distributed with values independently from 0.2 to 1.0 with an interval of 0.2. 25 cases are simulated to observe the lateral displacement of the vehicle and the steer angle of the driver. Two initial criteria are judged for the rational driver behavior: (a) the lateral displacement convergences to the target lane (Y=3.75m); and (b) the steer angle cannot exceed 90°. The simulated results meet the two criteria with the driver parameter pairs (0.2, 0.4), (0.2, 0.6), (0.2, 0.8), and (0.2, 1.0). Figure 4.25 shows the corresponding steer angles and the lateral displacements. At a high value λ_2 of 1.0, the driver controls the steering wheel with high frequency leading to a relative perfect curve of the lateral displacement without any fluctuation. At a low value λ_2 of 0.4, the driver adjusts the steering wheel with a longer period leading to much fluctuation of the lateral displacement around the target lane. It is meaningful to relate the driver model parameter with the skill level of a driver. The driver model with parameters (0.2, 1.0) represents the driver with high-level skill, while driver model with parameters (0.2, 0.4) represents the driver with low-level skill. Actually, from Figure 4.25(b), the lateral displacement of the driver with low-level skill (0.2, 0.4) exceeds the safety criteria (3.75+0.5m), which may cause an accident. Two driver parameter pairs (0.2, 1.0) and (0.2, 0.45) representing high and low level driving skill are adopted to study the effects of the driver behavior on the dynamic behavior of the vehicle in crosswinds.

The vehicle moving on the road with plane roughness Class B is investigated under control of a high and low-level skill driver with control parameter pairs (0.2, 1.0) and (0.2, 0.45), respectively. Figures 4.26, 4.27, and 4.28 show the angular, lateral and vertical displacements of the vehicle body. Figure 4.29 shows the various LTR indexes. Since the crosswind gust period is so short that the driver could not react to the change immediately, all the displacements and the LTR indexes are not affected by the driver at the beginning of the gust wind, but there are slight changes at the end of the 0.5s gust wind, which can be seen from Figure 4.29 in particular.

4.7.2 Accident Vehicle Speed under Sudden Crosswind Gust

To assess the accident vehicle speed, the road vehicle under a crosswind gust of different speeds is investigated. The gust speed is arranged from 10m/s to 30m/s at an interval of 5m/s. At each gust speed, the vehicle runs at different speeds from 20km/h to 150km/h with an interval of 5km/h. The critical vehicle speeds are then determined throughout the assessment of the responses of the vehicle against the safety criteria. From the assessment results, it is found that overturning always occurs before the course deviation, which is consistent with the results of Xu and Guo (2003). Figure 4.30 shows the accident vehicle speeds of the vehicle due to overturning, evaluated against different criteria and compared with the results obtained by Xu and Guo (2003). In the study of Xu and Guo (2003), the vehicle with one wheel of zero contact force was regarded as overturning, which is the same as the LTR_f/LTR_r equal to one. Since the aerodynamic coefficients used in Xu and Guo (2003) are moderately larger than those used in this study, the accident speeds calculated in this study are larger than those of Xu and Guo (2003) in terms of zero vertical force on any tire. Nevertheless, in terms of the LTR_v index proposed in this study, the accident vehicle speeds could be increased considerably within a wide range of wind speed.

4.7.3 Ride Comfort Analysis

The fluctuating winds are simulated with a time interval of 0.05s. The generated fluctuating wind speed time-histories at the gravity center of the vehicle for different mean wind speeds (5.0, 10.0, and 15.0 m/s) are shown in Figures 4.31 and 4.32 for 60s duration. The acceleration responses of the vehicle controlled by a middle-level skilful driver of the parameter pair (0.2, 0.7) are computed. To be consistent with the running distance of the vehicle moving on the bridge with a length of 1376m (in Chapter 6), the vehicle moves for a total of 2376m (142.56s for the vehicle with a speed of 60km/h). The first 1000m is for the purpose of stabilizing the vehicle motion, and the last 1376m is used to evaluate the ride comfort. The effects of road roughness in plane are also explored. The ride comfort of the vehicle is finally evaluated.

4.7.3.1 Acceleration responses under fluctuating crosswinds

The vehicle moving at a velocity of 60km/h under fluctuating winds of a 10m/s mean value with a driver's control is first considered. Roughness in line generated with Class B is taken as input. Figure 4.33 and Figure 4.34 display the acceleration responses in the vertical and lateral directions respectively at the location of the driver for the last 1376m. The acceleration response in the vertical direction is much larger than that in the lateral direction in general. Through the FFT translation, the acceleration spectra of the vehicle at the driver's location are obtained and shown in Figures 4.35 and 4.36. Since the lowest natural frequencies of the vehicle in the vertical and rotating directions are 1.94Hz and 2.54Hz respectively, the acceleration responses in the vertical and lateral direction at the corresponding natural frequencies reach their peak values. For the acceleration response in the lateral direction, the spectral components at very low frequency around 0.25Hz are also excited by the steer angle input from the driver (see the amplitude spectrums of the steer angle in Figure 4.37). Since the frequency weighting factor W_d in the lateral direction is relatively large in the low frequency range (see Figure 2.2), the behavior of the driver has a significant effect on the ride comfort beside the crosswinds.

4.7.3.2 Effect of roughness in plane

By replacing the line roughness in 4.7.3.1 with the plane one, the dynamic responses of the vehicle are re-calculated. Figures 4.38 and 4.39 show the amplitude spectrums of the acceleration responses at the location of the driver seat in the lateral and vertical directions, respectively. Compared with the amplitude spectrums of the acceleration responses for the vehicle moving on the road with roughness in line (see Section 4.7.3.1), the vertical acceleration changed very slightly. However, the spectral amplitudes of the lateral acceleration response rise around the natural frequency in the rotating direction. Therefore, road roughness in plane should be considered in the evaluation of the ride comfort, particularly in the lateral direction.

4.7.3.3 Ride comfort evaluation

The ride comfort of the vehicle under crosswinds, on the road roughness in plane, and under the control of driver is evaluated in terms of the FWRMSA introduced in Section 4.6.2. The crosswind is fluctuating wind speeds with a mean speed of 10m/s. The dynamic responses of the vehicle with different moving speeds from 20km/h to 100km/h at an interval of 10km/s are computed. The FWRMSA results from each case are shown in Figure 4.40. It can be seen that the total FWRMSA and FWRMSA in the vertical direction increase with the increase of the vehicle speed in general, while the FWRMSA in the lateral direction increases first and then keeps a relatively stable level. For the chosen roughness level, the ride comfort level is between fairly uncomfortable and uncomfortable at a low vehicle velocity of 20km/h and between very uncomfortable and extremely uncomfortable at a high vehicle velocity of 100km/h.

4.8 SUMMARY

In this chapter, an advanced vehicle model able to simulate its progressive instability under crosswinds has been developed. In this model, the dynamic equations are established in the local coordinate system fixed on the vehicle body disregarding small displacement assumption. No contact of the tires of the vehicle with the road surface can be simulated in a natural way. The wind loads on the vehicle are updated with the consideration of the time-varying attitude of the vehicle. The lateral movement of the vehicle is controlled by a driver through a driver's model. By using this vehicle model, the progressive instability, the accident vehicle speed, and the ride comfort of a high-sided road vehicle have been analyzed. The major conclusions are summarized as follows:

- The progressive instability of the high sided vehicle under a sudden crosswind gust has been analyzed in terms of the criteria of course deviation and overturning. For the vehicle of 100km/h speed under a 30m/s crosswind gust within the duration of 0.5s, the front wheel at the upwind side jumps from the ground first at 0.119s, and the rear wheel at the upwind side loses contact with the ground at 0.148s. Even though both the wheels on the upwind side of the vehicle jump from the ground, they can still go back to the ground because the maximum roll angle is about -4.01°only.

- As a criterion to judge the overturning of the high-sided vehicle, the LTR_v index can describe the safety of the vehicle more realistically than the LTR_f/LTR_r index. Using the LTR_v index instead of the LTR_f/LTR_r index as the overturning criterion can remove the misjudgment as one wheel jumps from the ground due to a large roughness block.

- Roughness in plane changes the lateral displacement of the high-sided vehicle only slightly, compared with roughness in line. Although the consideration of roughness in plane would increase the rotating movement of the vehicle, it has no significant contribution to the overturning of the vehicle in terms of LTR_v.

- With the worse road roughness of Class C, the displacements of the high-sided vehicle in both the vertical and lateral directions increase compared with the good road condition of Class B. This increasing trend is the same for the roll and pitch angle as well as the LTR_v of the vehicle. The wheels of the vehicle may jump from the ground as the vehicle moves across the worse road roughness without crosswinds.

- By simulating the process of changing lanes of the high-sided vehicle under the control of a driver, the parameters in the driver model are determined. It is found that λ_2 has a close relation with the skill level of a driver. With large λ_2, the driver adjusts the steer angle in high frequency, leading a relative perfect curve of the lateral displacement without any fluctuation. The displacements and LTR value of the high-sided vehicle are hard to be controlled in a 0.5s crosswind gust due to the time delay of the reaction of the driver.

- The accident vehicle speeds of the high-sided vehicle under crosswind gust are determined in terms of overturning and course deviation. Overturning occurs before the course deviation for different gust velocities. With reference to the LTR_v index, using zero vertical force on any one wheel or the LTR_f/LTR_r index to evaluate the critical vehicle speed due to the overturning is conservative.

- For the vehicle moves on the rough road of Class B in fluctuating crosswinds, the acceleration response at the driver's seat in the vertical direction is larger than that in the lateral direction. The vertical acceleration at the driver's seat is mainly excited by the vertical movement of the vehicle, due to road roughness. The lateral acceleration at the driver's seat is mainly excited by the rotating movement, due to the crosswinds and the steer angle controlled by the driver. In the low frequency domain, the behavior of the driver has a significant effect on the ride comfort in the lateral direction in addition to the fluctuating crosswinds.

- Compared with the road roughness in line, the vertical acceleration at the driver's seat changes very slightly with road roughness in plane in terms of the amplitude spectrum. However, the lateral acceleration response at the driver's seat rises significantly around the natural frequency of rotating movement. As a result, road roughness in plane has to be considered in the evaluation of the ride comfort, particularly in the lateral direction.

- The ride comfort of the vehicle under fluctuating crosswinds, on the road roughness in plane, and under the control of the driver is evaluated in terms of the FWRMSA. The total FWRMSA and FWRMSA in the vertical direction increase with the increase of the vehicle speed in general, while the FWRMSA in the lateral direction increases first, and then keeps a relatively stable level.

Table 4.1 Fitted constants of aerodynamic coefficients

j=	C_{Sj}	C_{Lj}	C_{Pj}	C_{Yj}	C_{Rj}
0	0.005	-0.177	-0.076	-1.11E-16	-1.67E-16
1	0.11837	0.10532	0.00664	-0.01144	-0.00796
2	-5.71E-04	-0.00218	-8.89E-05	1.33E-04	1.16E-04
3	-1.43E-06	1.16E-05	2.47E-07	-8.83E-07	-5.86E-07

Table 4.2 Parameters of a two-axle vehicle model

Parameter	Unit	Value
Mass of vehicle body (m_{vb})	kg	4480
Pitching moment of inertia (I_{yy})	kg·m^2	5516
Rolling moment of inertia (I_{xx})	kg·m^2	1349
Yawing moment of inertia (I_{zz})	kg·m^2	10^5
Cross moment of inertia (I_{xz})	kg·m^2	1000
Mass of the front wheel - tire (m_w)	kg	800
Mass of the rear wheel - tire (m_w)	kg	710
Linear stiffness coefficient of suspension in vertical (k_{uz})	kN/m	399
Linear stiffness of suspension system in lateral (k_{uy})	kN/m	299
Damping coefficient of suspension in vertical (c_{uz})	kN·s/m	23.21
Damping coefficient of suspension system in lateral (c_{uy})	kN·s/m	23.21
Stiffness of tire in vertical (k_{lz})	kN/m	351
Damping coefficient of tire in vertical (c_{lz})	kN·s/m	0.80
Static friction coefficient (μ)	1	0.60
Corning stiffness (C_y)	N/rad	108.9
Distance (l_1)	m	3.00
Distance (l_2)	m	5.00
Distance (l_3)	m	2.50
Distance (b_1)	m	1.10
Distance (b_2)	m	0.00
Distance (h_1)	m	0.80
Distance (h_2)	m	1.00
Reference area (A_f)	m^2	10.50
Reference length (L_v)	m	13.45

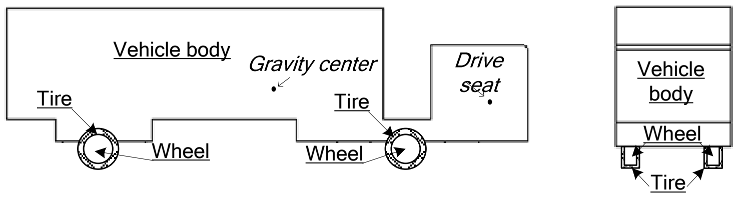

Figure 4.1 Simplified model of a two-axle lorry

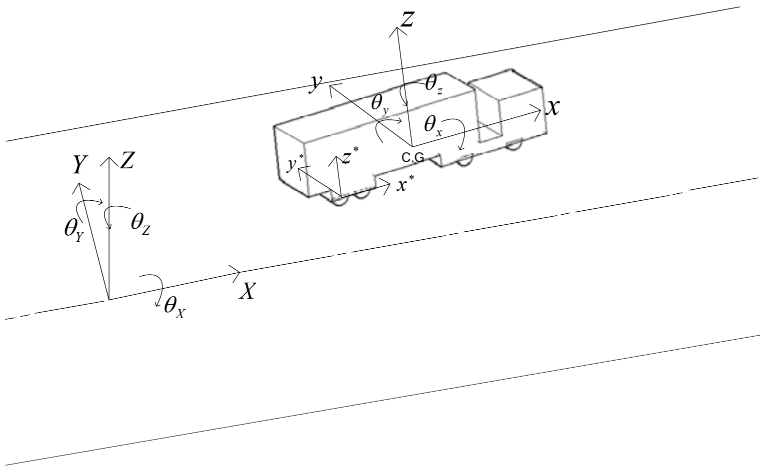

Figure 4.2 Coordinate systems

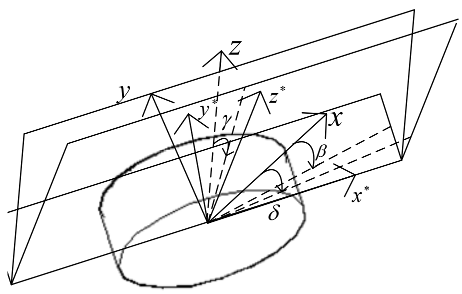

Figure 4.3 VCS and WCS

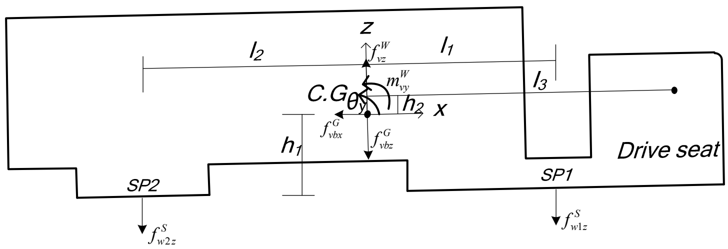

(a) *xy* plane

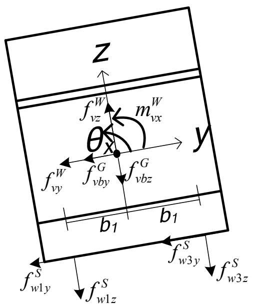

(b) *yz* plane

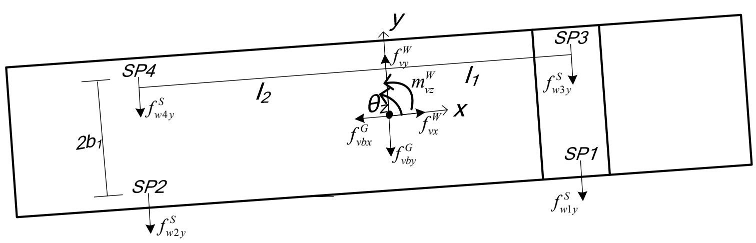

(c) *xz* plane

Figure 4.4 Force diagrams of the vehicle body

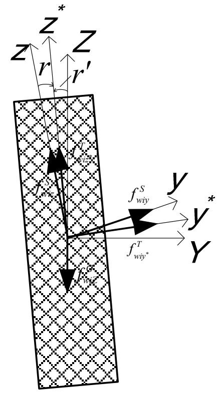

Figure 4.5 Force diagram of the *i*th wheel–tire

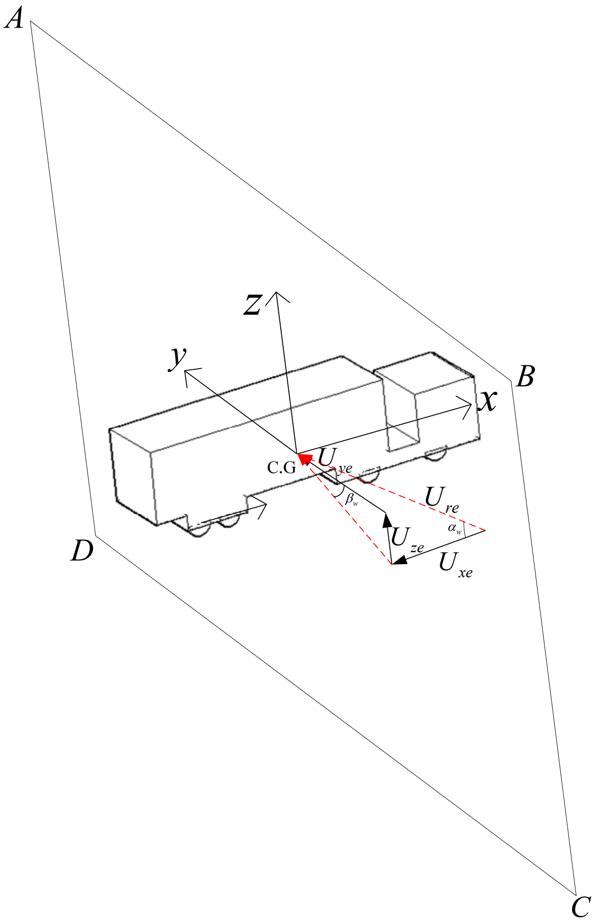

Figure 4.6 Relative wind velocity and direction

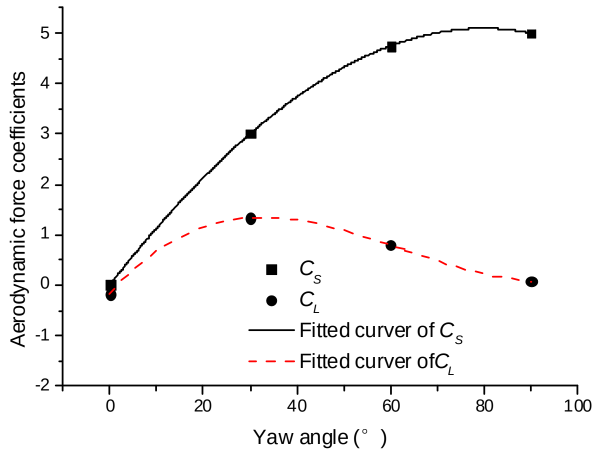

Figure 4.7 Fitted curves for aerodynamic force coefficients

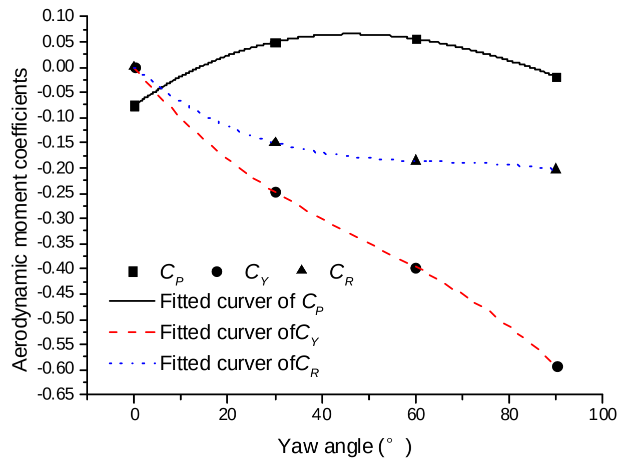

Figure 4.8 Fitted curves for aerodynamic moment coefficients

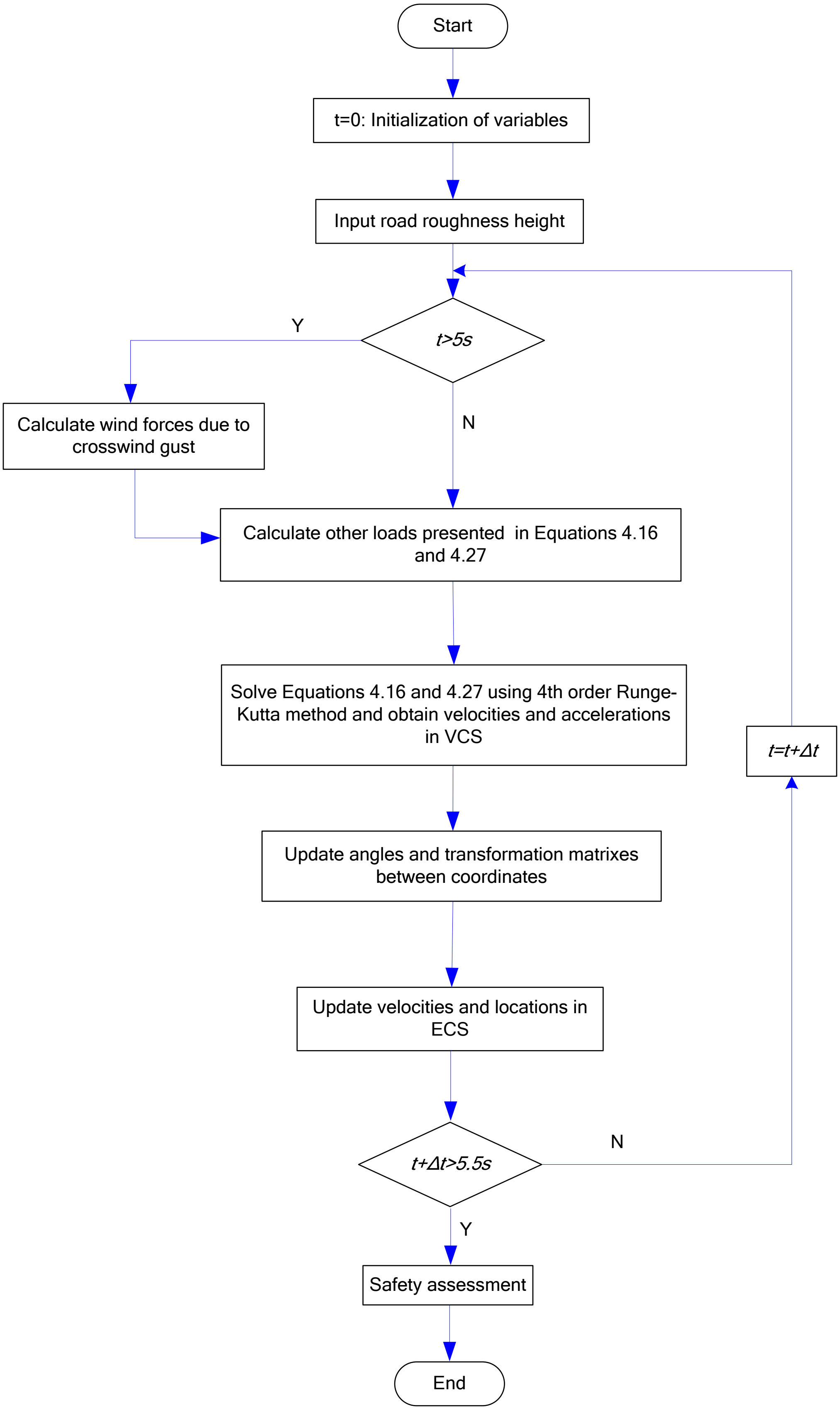

Figure 4.9 Flowchart for the safety analysis of the vehicle

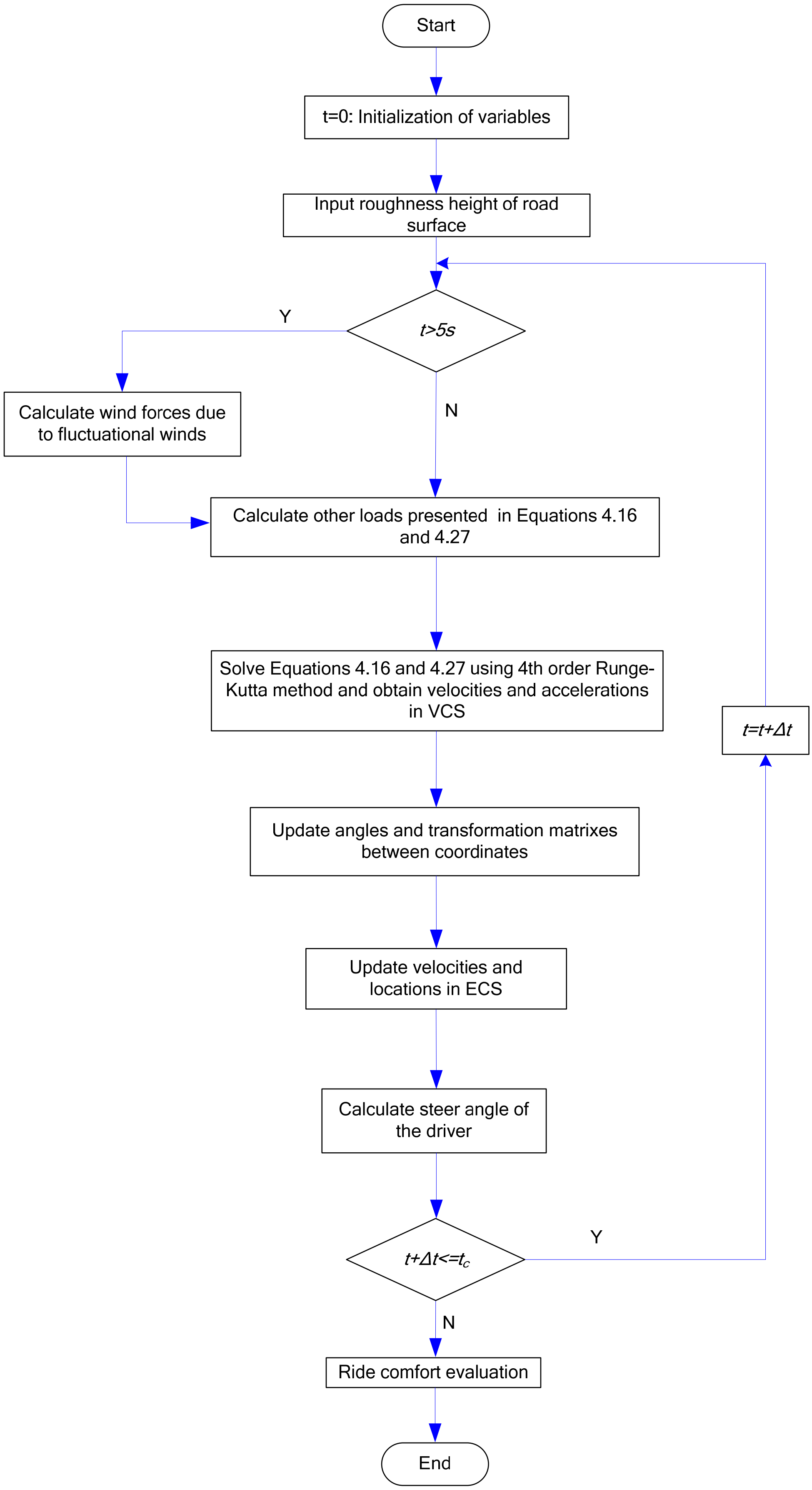

Figure 4.10 Flowchart for the ride comfort analysis of the vehicle

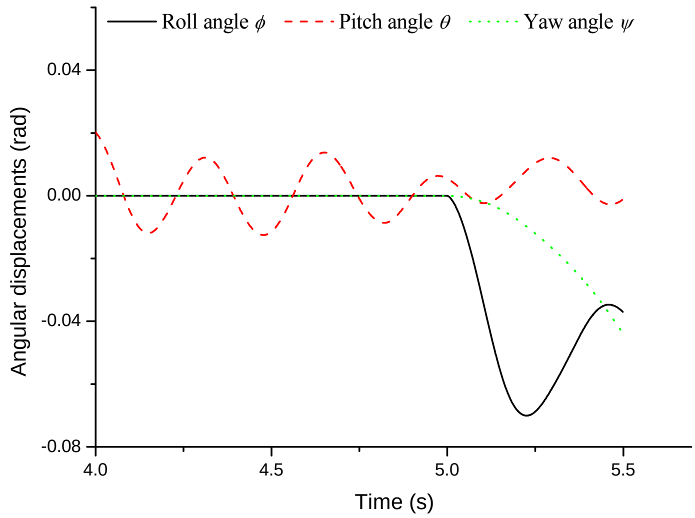

Figure 4.11 Angular displacements of the vehicle body

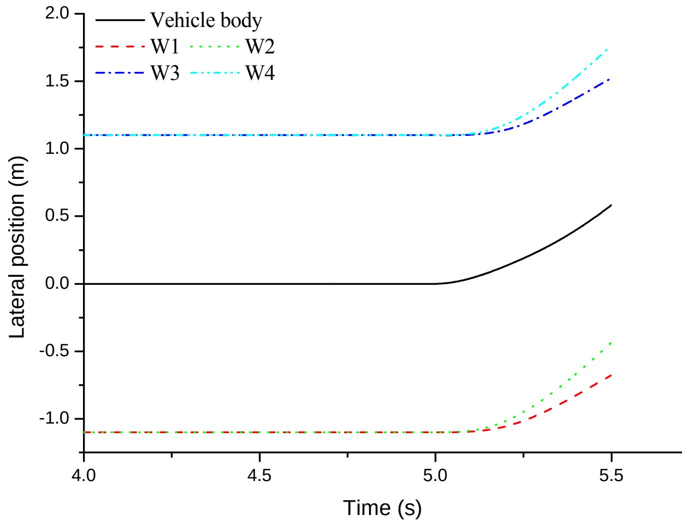

Figure 4.12 Lateral positions of the vehicle body and the wheels

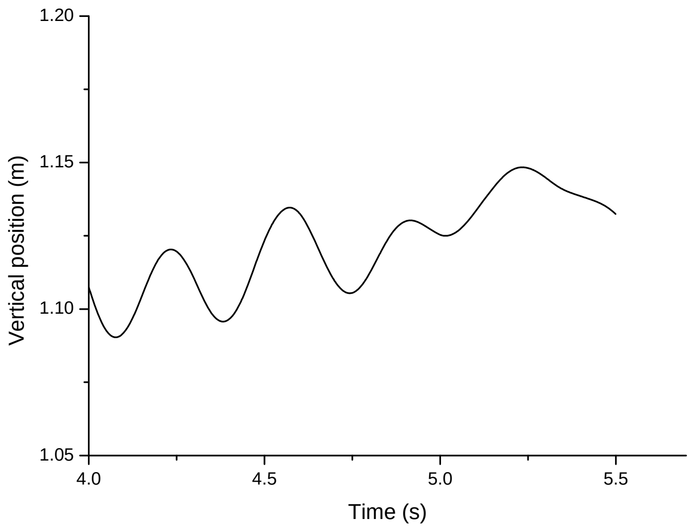

(a) Vehicle body

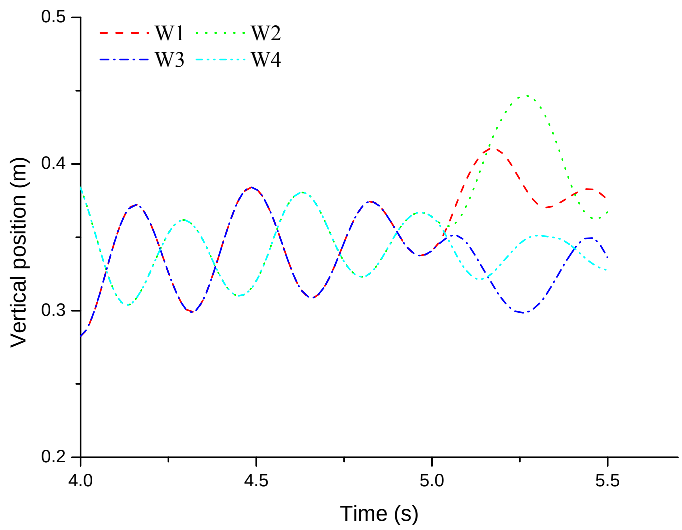

(b) Wheels

Figure 4.13 Vertical positions

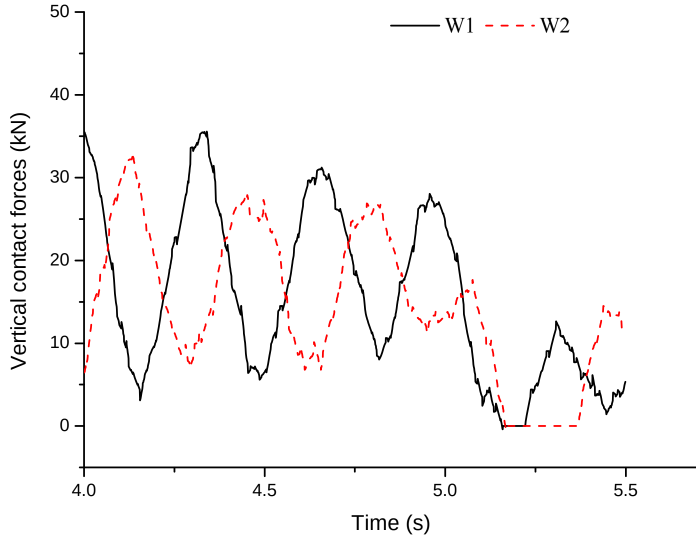

(a) W1 and W2 (upwind side)

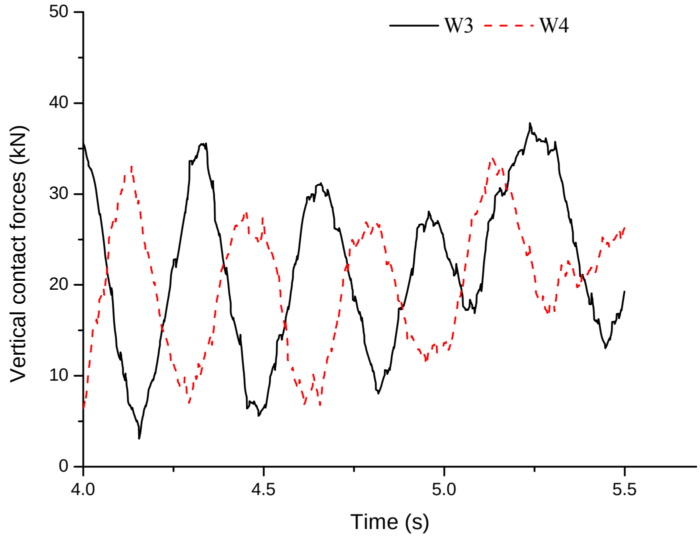

(b) W3 and W4 (downwind side)

Figure 4.14 Vertical contact forces of the tires

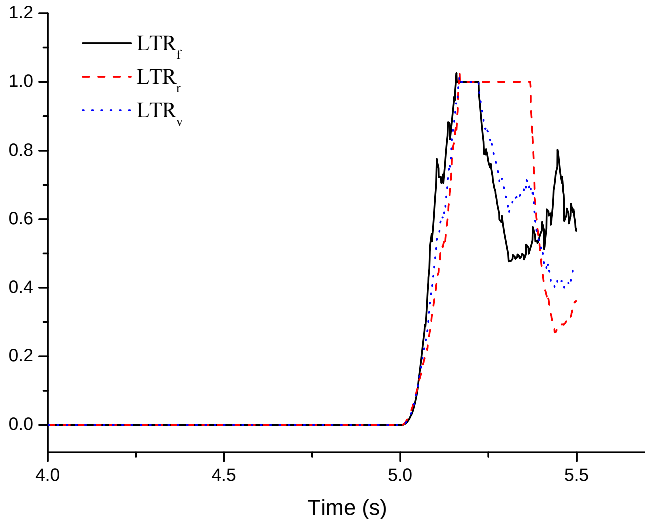

Figure 4.15 LTR indexes for the vehicle

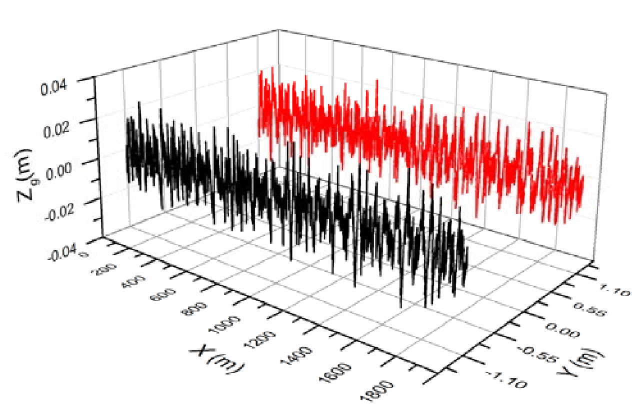

Figure 4.16 Simulated roughness heights in plane

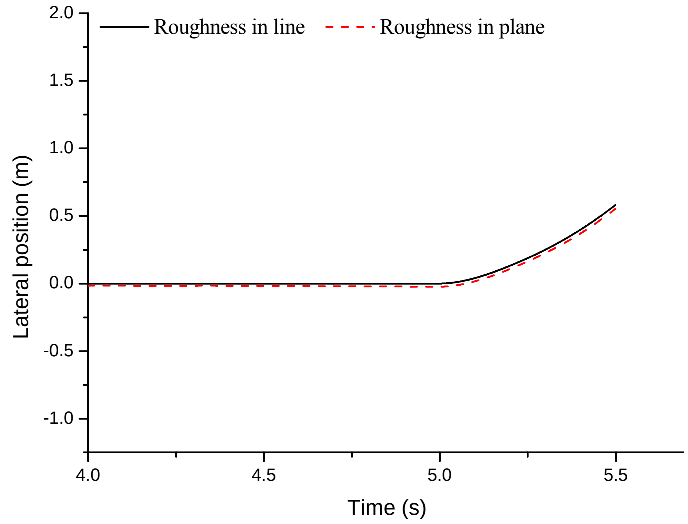

Figure 4.17 Lateral positions of the vehicle body

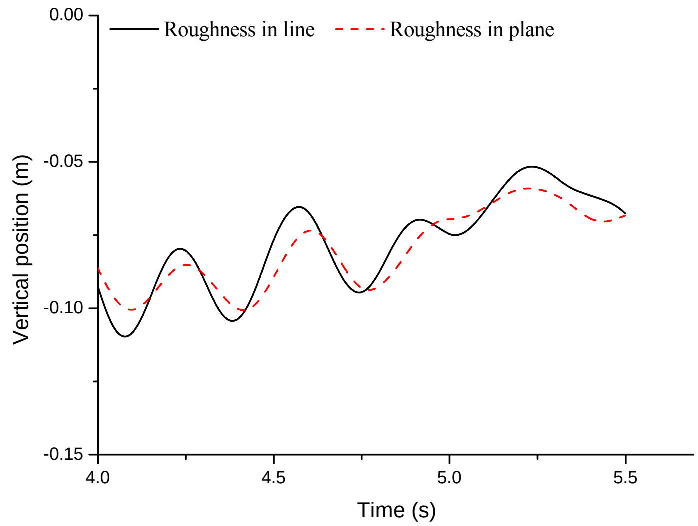

Figure 4.18 Vertical positions of the vehicle body

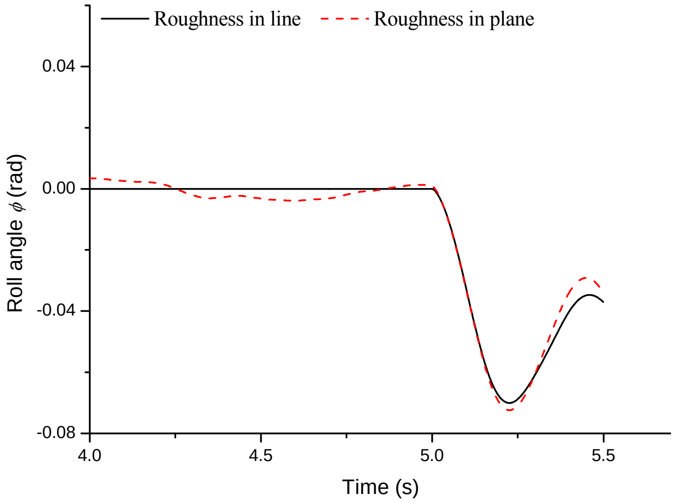

(a) Roll angle

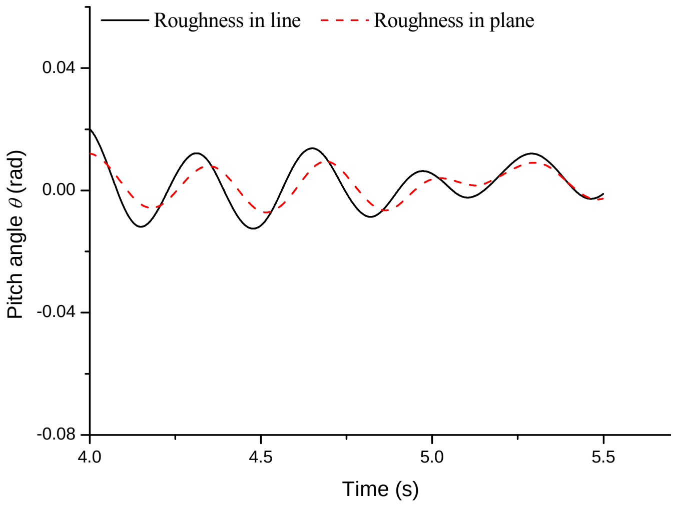

(b) Pitch angle

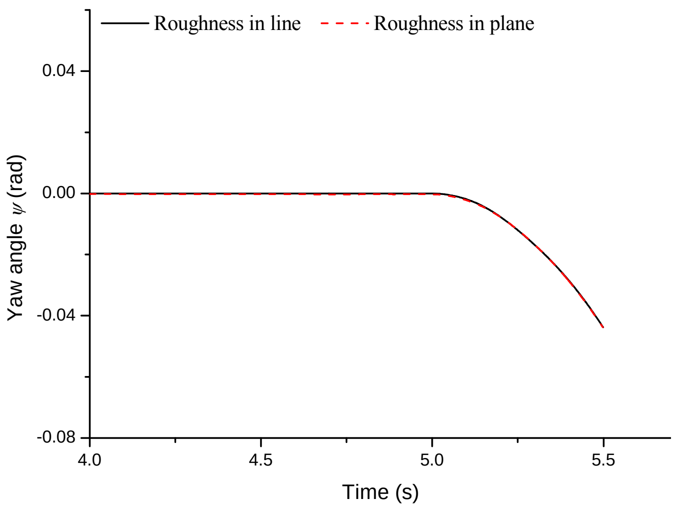

(c) Yaw angle

Figure 4.19 Angular displacements of the vehicle body

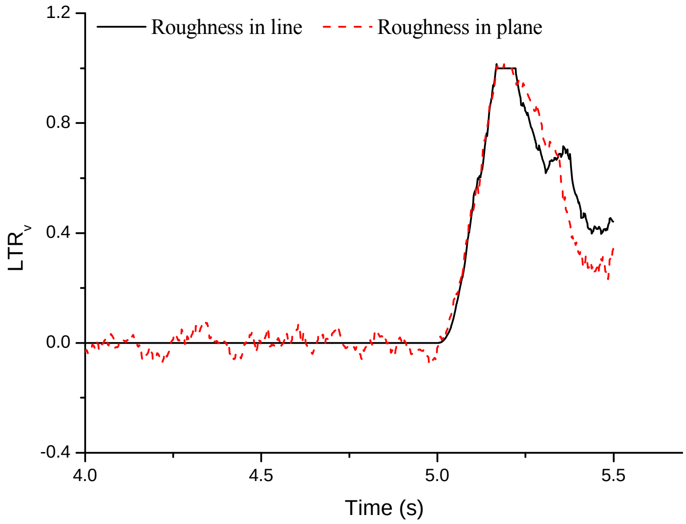

Figure 4.20 LTRv index

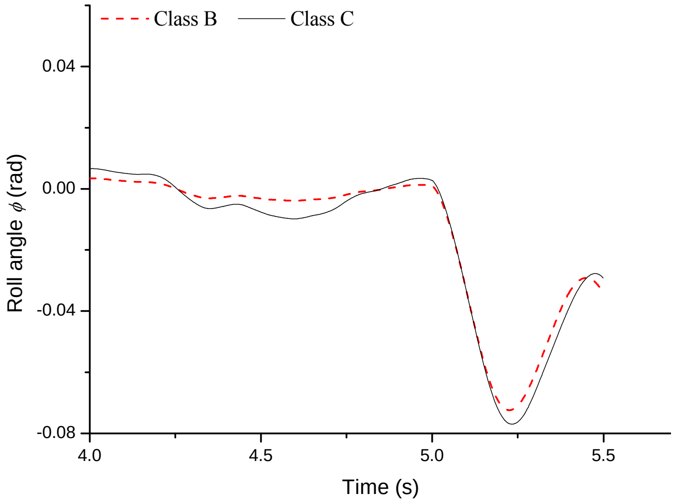

(a) Roll angle

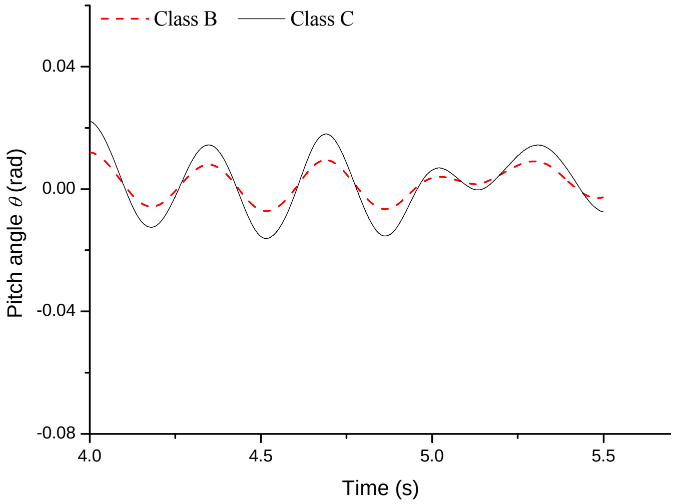

(b) Pitch angle

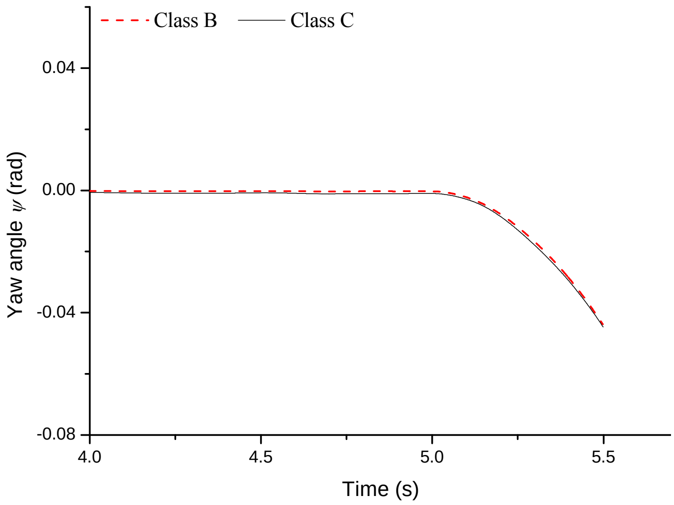

(c) Yaw angle

Figure 4.21 Angular displacements of the vehicle body

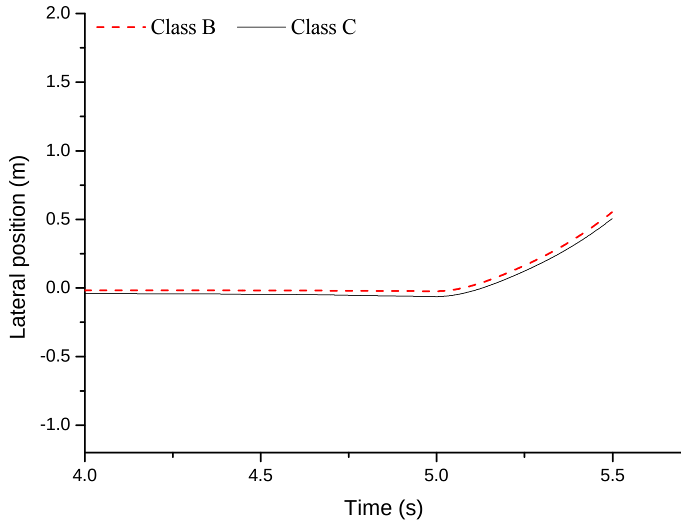

Figure 4.22 Lateral positions of the vehicle body

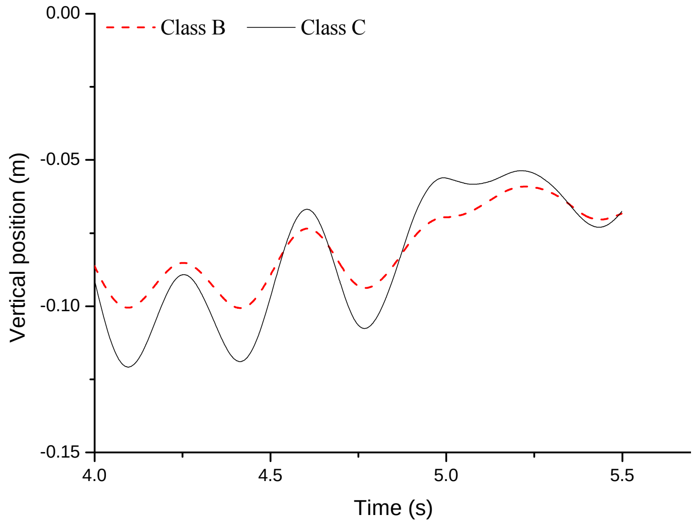

Figure 4.23 Vertical positions of the vehicle body

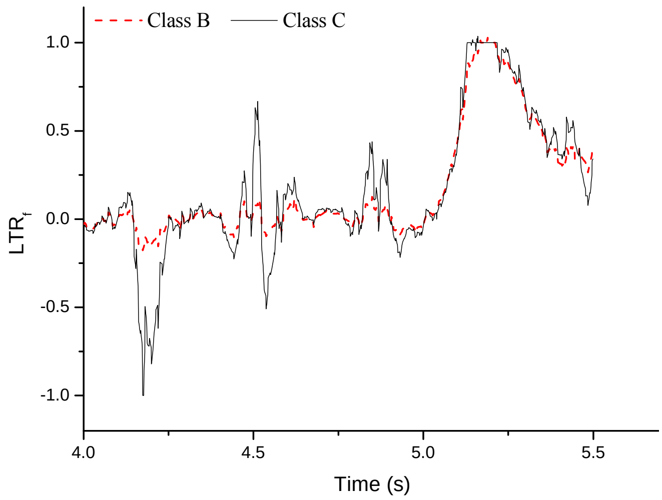

(a) LTR_f index

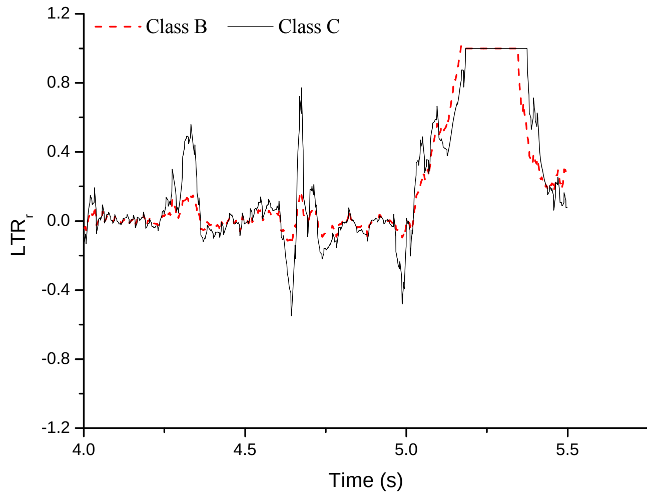

(b) LTR_r index

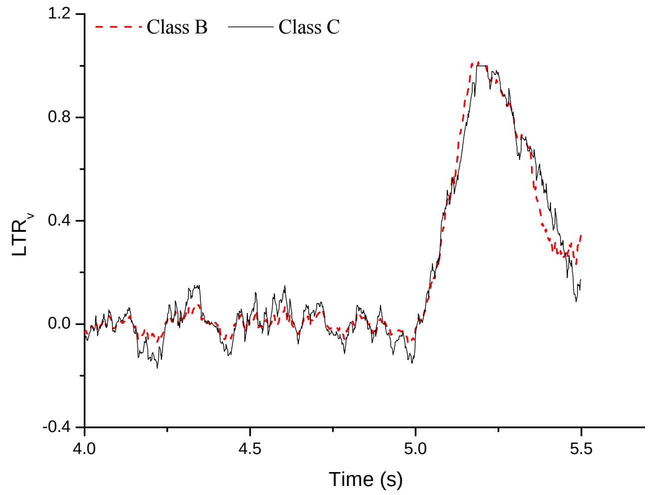

(c) LTR_v index

Figure 4.24 Various LTR indexes

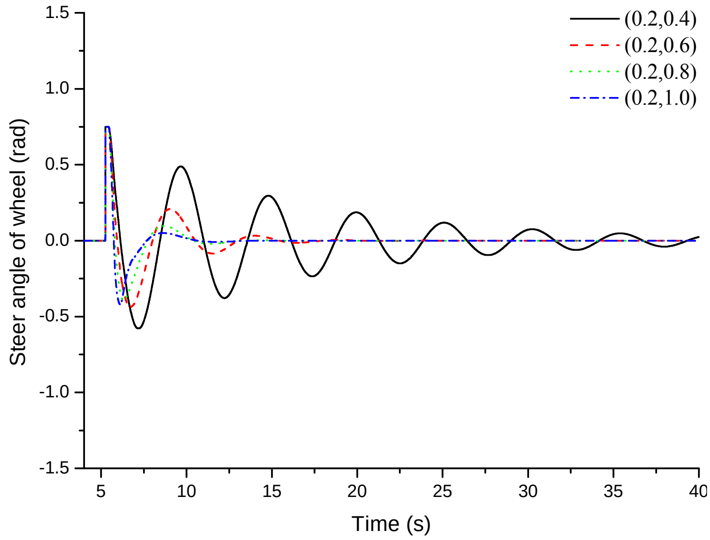

(a) Steer angle

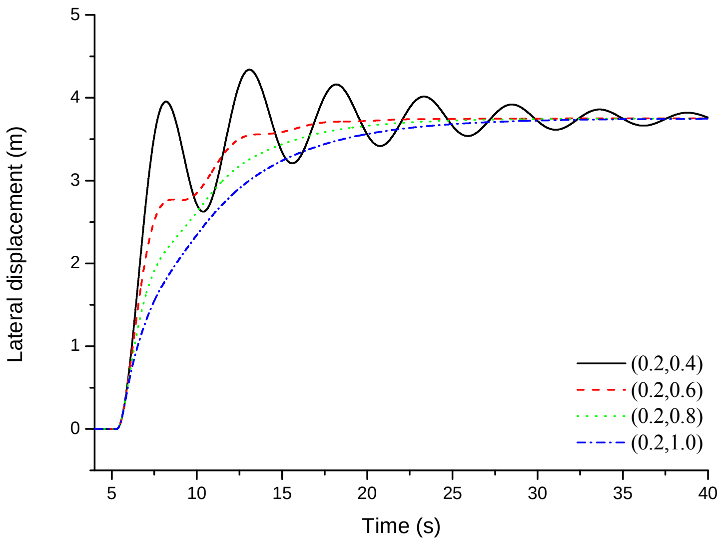

(b) Lateral displacement

Figure 4.25 Steer angle and lateral displacement for parameter selection

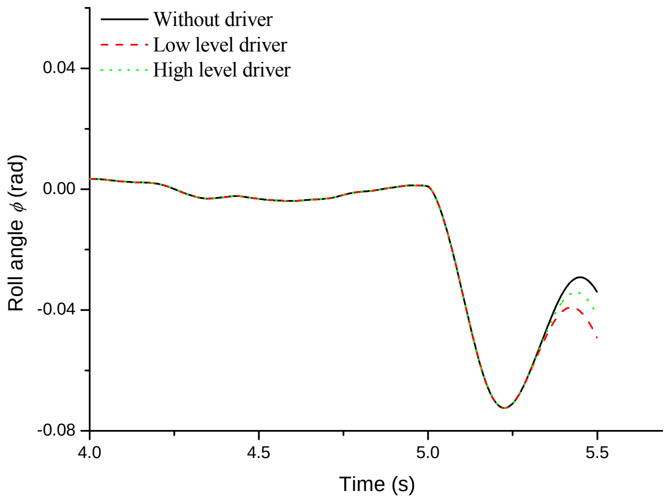

(a) Roll angle

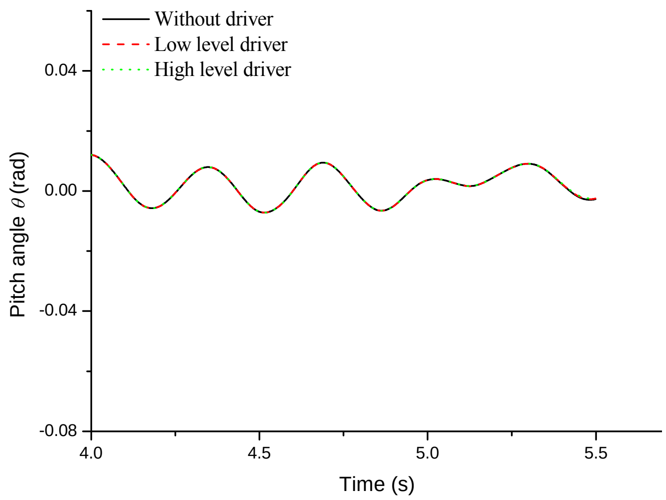

(b) Pitch angle

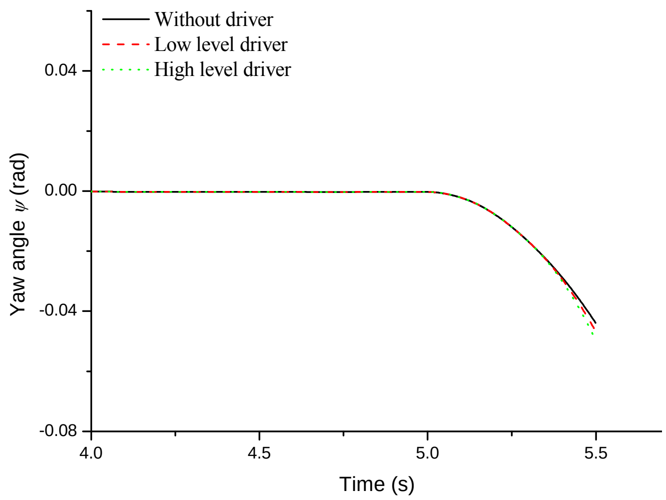

(c) Yaw angle

Figure 4.26 Angular displacements of the vehicle body

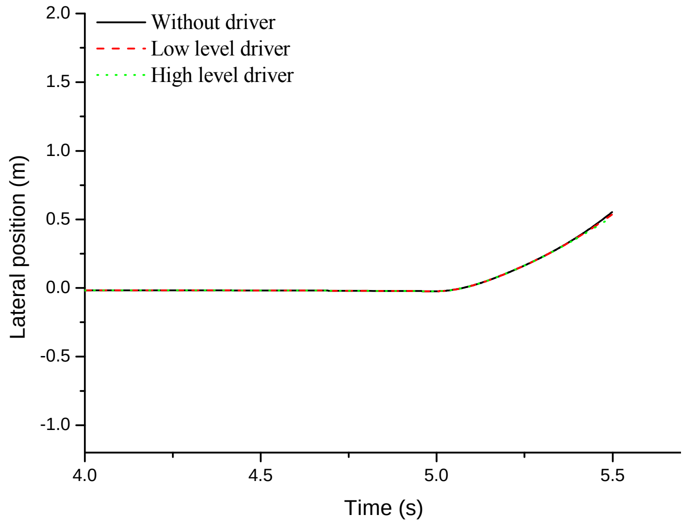

Figure 4.27 Lateral positions of the vehicle body

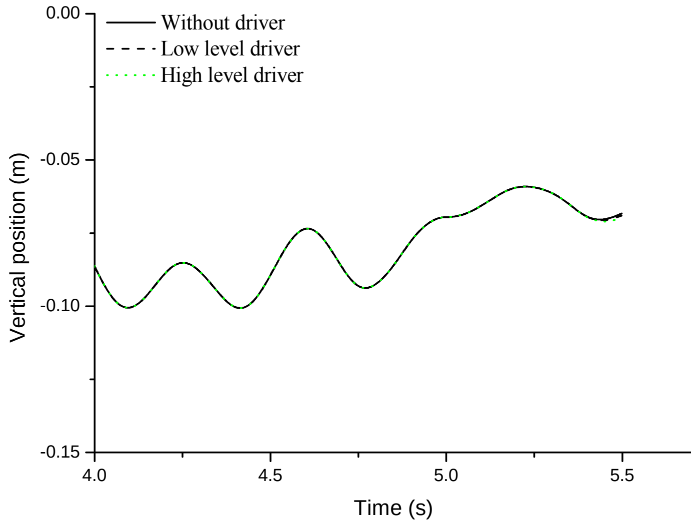

Figure 4.28 Vertical positions of the vehicle body

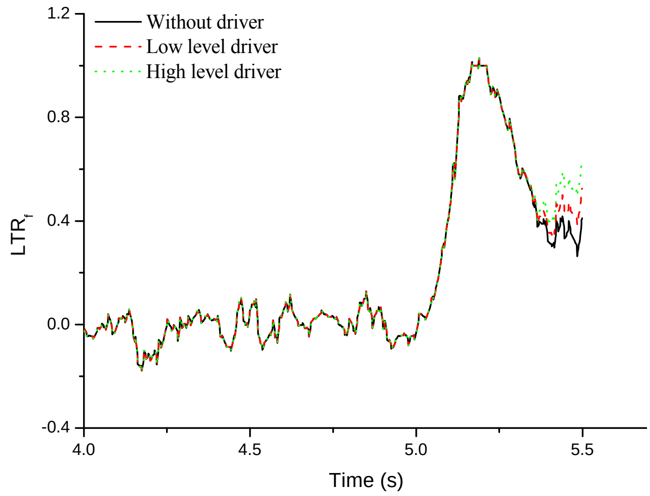

(a) LTR_f

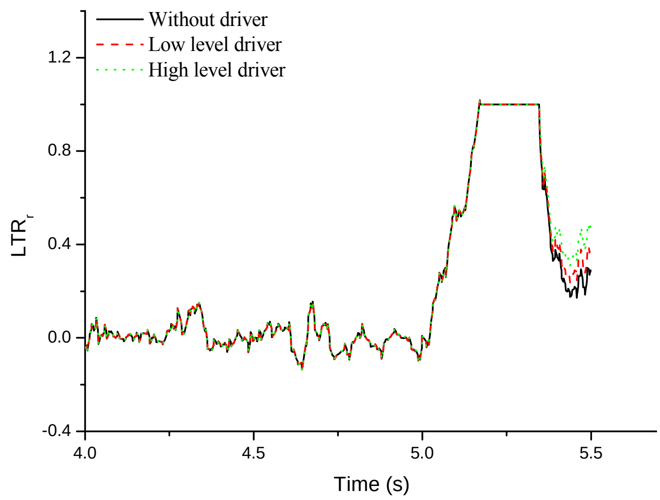

(b) LTR_r

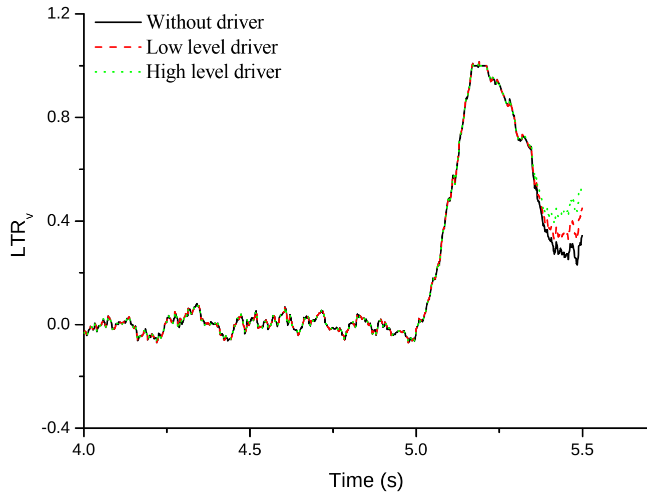

(c) LTR_v

Figure 4.29 Various LTR indexes

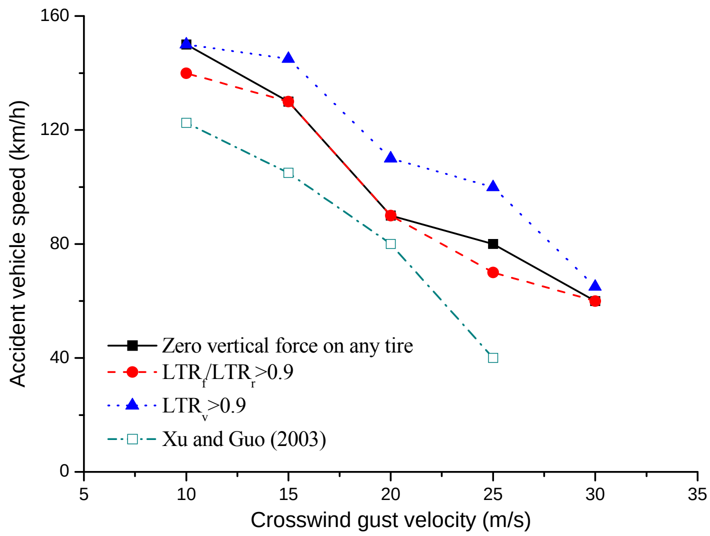

Figure 4.30 Accident vehicle speeds

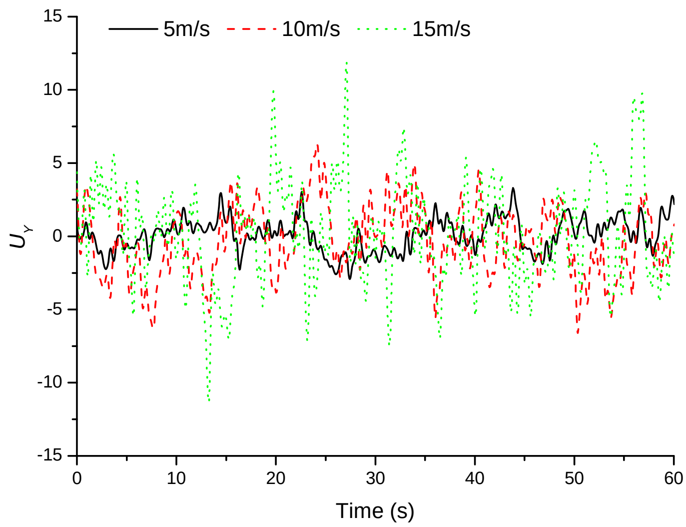

Figure 4.31 Simulated fluctuating wind velocity in the horizontal direction

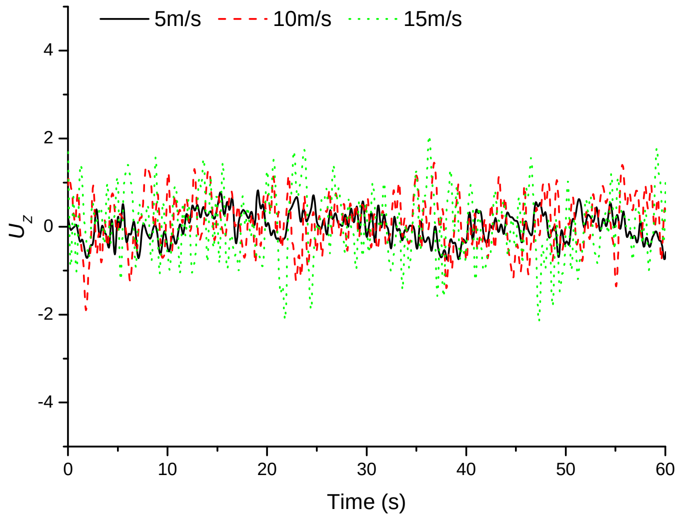

Figure 4.32 Simulated fluctuating wind velocity in the vertical direction

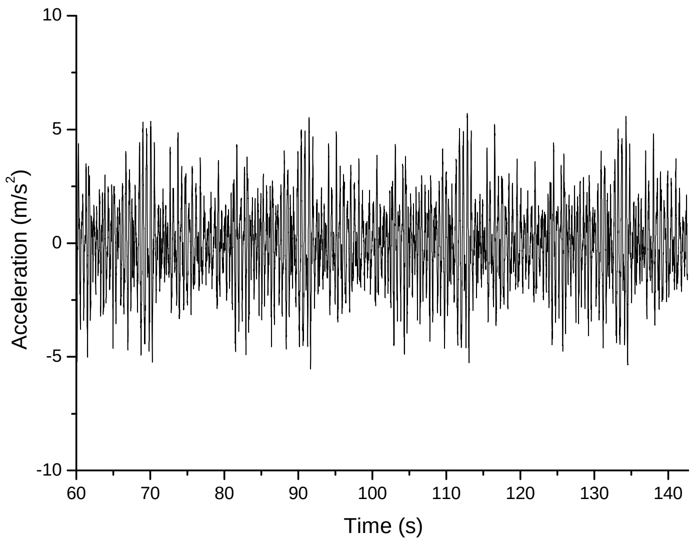

Figure 4.33 Acceleration responses in the vertical direction

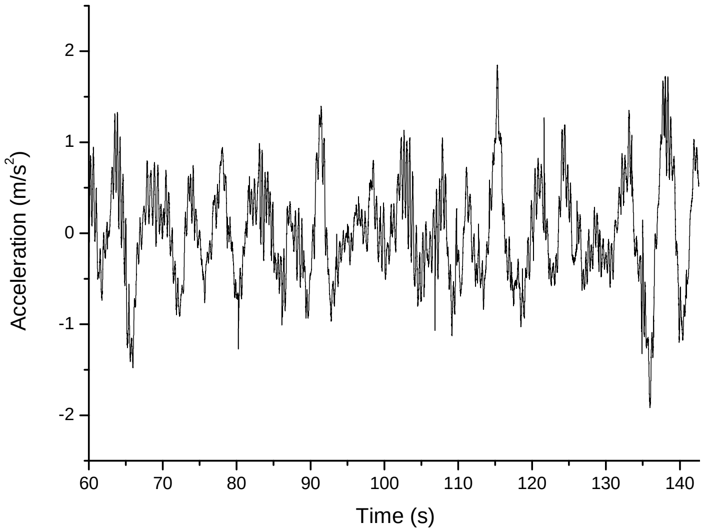

Figure 4.34 Acceleration responses in the lateral direction

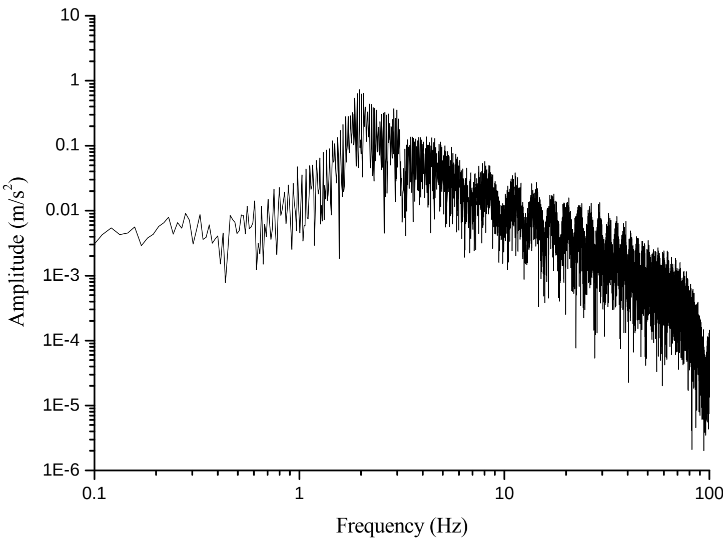

Figure 4.35 Amplitude spectrum of acceleration in the vertical direction

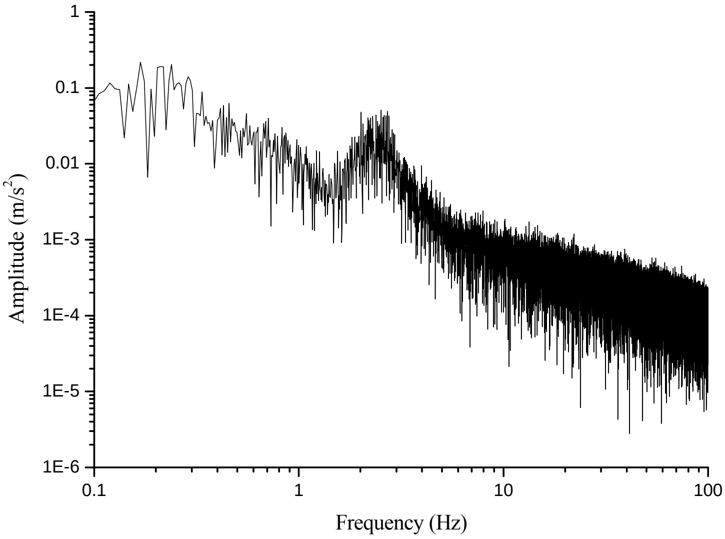

Figure 4.36 Amplitude spectrum of acceleration in the lateral direction

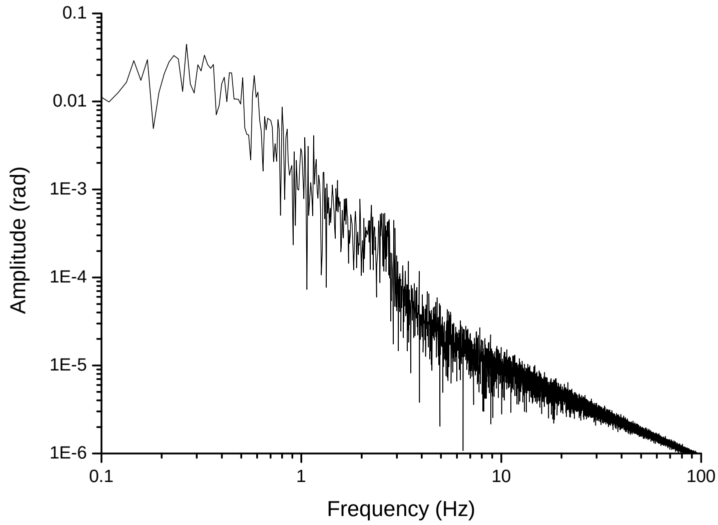

Figure 4.37 Amplitude spectrums of the steer angle

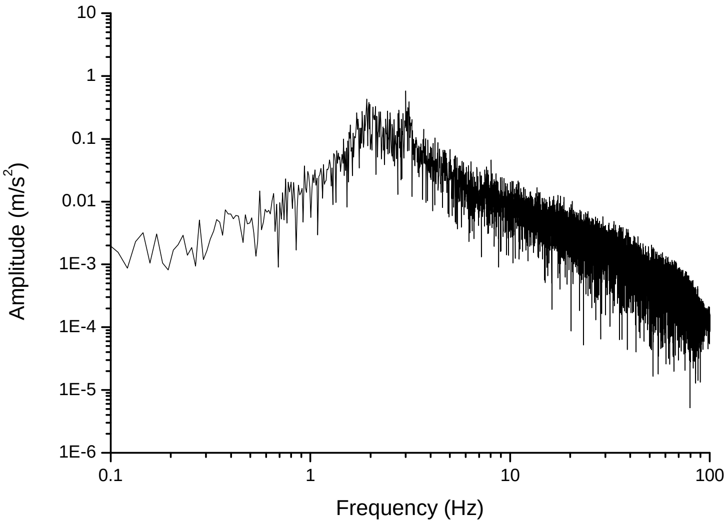

Figure 4.38 Amplitude spectrum of the acceleration in the vertical direction

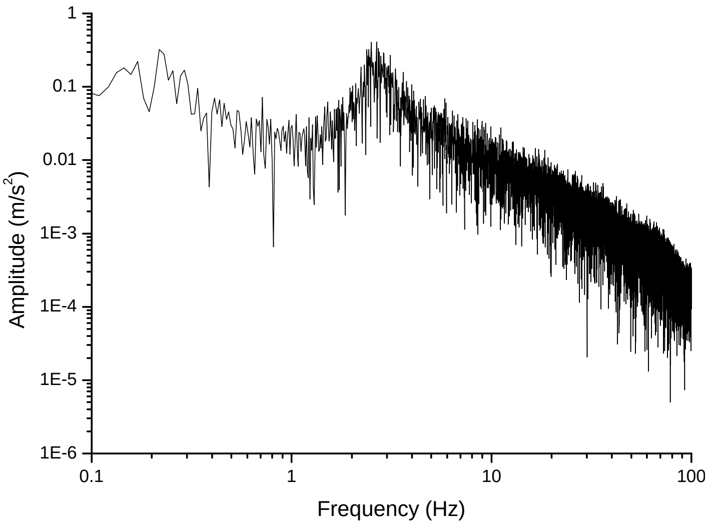

Figure 4.39 Amplitude spectrum of the acceleration in the lateral direction

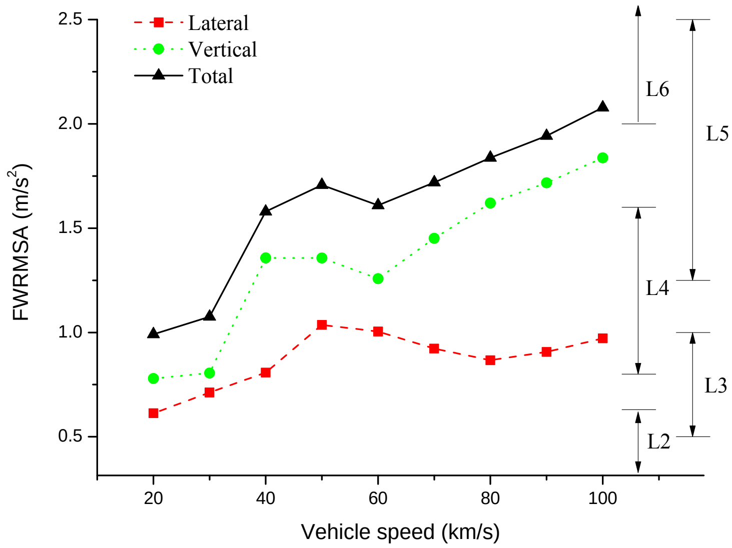

Figure 4.40 FWRMSA (Comfort Index)

CHAPTER 5

AERODYNAMIC INTERFERENCES BETWEEN A MOVING VEHICLE AND A BRIDGE DECK UNDER CROSSWINDS

5.1 INTRODUCTION

The aerodynamic interferences between a moving vehicle and the ground under crosswinds have been explored using Computational Fluid Dynamics (CFD) in Chapter 3. The aerodynamic interferences between a moving vehicle and a bridge deck under crosswinds will be analyzed using CFD in this Chapter. The computed aerodynamic forces will be then applied to the moving vehicle on the bridge deck to investigate its ride comfort and explained in Chapter 6.

In the previous studies about the coupled Road Vehicle-Bridge-Wind (RVBW) system (Xu and Guo, 2003a; Cai and Chen, 2004; Cheung and Chan, 2010), the aerodynamic forces on the moving vehicle were approximated with those on the stationary vehicle on the ground, and the aerodynamic forces on the bridge deck were also approximated without considering the influences of the vehicles moving on. In fact, the aerodynamic forces on the vehicle are influenced considerably by the local environment, such as the geometric shape of the bridge deck and the layout of the rails in front of the vehicles. In return, the motion of the vehicle alters the aerodynamic forces acting on the deck naturally. Therefore, it is necessary to obtain the aerodynamics of both the moving vehicle and the deck, considering the interference between them.

The wind tunnel test is a common way of determining the aerodynamic forces on a vehicle-bridge system. Coleman and Baker (1990, 1994) conducted wind tunnel tests to measure the aerodynamic forces on a high-sided vehicle in which the vehicle model was fixed on a box girder, but no detailed information was given about the box girder. Zhou and Ge (2008) investigated the vortex-induced vibration of a bridge deck with the presence of vehicles in a wind tunnel, with vehicles fixed on the deck. They showed that the presence of vehicles had significant effects on the vortex-induced vibration of the bridge deck. Zhu *et al*. (2012) also measured the aerodynamic forces on road vehicles in the different lanes of a bridge deck in a wind tunnel; but in their case, the vehicles were stationary and the aerodynamic forces on the bridge deck with the presence of the vehicle were not measured.

The CFD technique can also be employed as an alternative wind tunnel test to obtain aerodynamic forces. Many studies have been devoted to simulating the aerodynamics of bridge decks using CFD with different numerical methods (Fujiwara *et al*., 1993; Larsen and Walther, 1997; Ge *et al*., 2002; Jeong and Kwon, 2003; Li and Wang, 2004; Zhu *et al*., 2007; Taylor and Vezza, 2009; Zhou and Ma, 2010; Huang and Liao, 2011). The aerodynamic forces of both stationary and moving bridge decks have also been analyzed numerically. Recently, the aerodynamic characteristics of vehicles on the ground under crosswinds have been simulated using CFD methods (Krajnovic *et al*., 2012). When a vehicle stays on a bridge deck, the situation is more complex than with a single bridge deck case or a single vehicle case. Bettle *et al*. (2003) made an attempt to use CFD to explore the aerodynamic characteristics of a stationary vehicle-bridge system. A truck on a bridge deck was simulated using the steady Reynolds Averaged Navier-Stokes (RANS) method, from which the aerodynamic lift, drag and moment coefficients were obtained. The motion of the vehicle on the bridge deck has not yet been investigated.

In this chapter, a numerical model is formed to simulate the flows around and the aerodynamic forces on a vehicle-deck system under crosswinds using CFD. The unsteady RANS method with the SST k-ω turbulence model will be used to compute the time-averaged aerodynamic coefficients of the stationary vehicle on the bridge deck. The computed aerodynamic coefficients will be compared with the measured ones to validate the numerical simulation. The aerodynamic characteristics of the moving vehicle on the first lane of the bridge deck will then be studied numerically using a relative velocity method, and the results will be compared with those of the stationary vehicle-bridge deck system to explore the effects of vehicle movement on the aerodynamic coefficients of both the vehicle and the bridge deck.

5.2 VEHICLE-BRIDGE DECK MODEL AND AERODYNAMIC FORCES

A vehicle-bridge system, composed of the deck section of a long-span cable-stayed bridge and a typical high-sided articulated vehicle, is selected. The same model of vehicle described in Section 3.2 is re-used in this chapter. The deck is a flat box girder with side fairing, as shown in Figure 5.1. The cross section of the prototype bridge deck is 34.0m wide and 3.5m high, carrying a dual two-lane highway on its upper surface. Two lines of hand rails, four lines of protection rails, and two lines of I-shape maintenance traces are mounted on the bridge deck. Both the deck and the vehicle are scaled with a ratio of 1:25.

For the bridge deck, the hand and protection rails are continuously horizontal bars supported by vertical poles in the prototype. It will be time-consuming and not absolutely necessary to model both the horizontal bars and the vertical poles numerically. Therefore, in this numerical simulation, the vertical poles are not simulated, but the blockage areas (the projected areas along the wind direction) of the vertical poles are taken into account, based on the principle that the heights of the rails and the ventilation ratio are identical to the deck model used in the wind tunnel tests. In other words, the horizontal continuous bars are enlarged so that their final projected areas along the wind direction are equal to the projected areas of the rails containing vertical poles in the same direction. All other components of the bridge deck, including the maintenance traces, are modeled in the light of the principle of geometric similarity. The bridge deck model used in the numerical simulation is shown in Figure 5.2. The vehicle is arranged on the first lane of the bridge deck.

By integrating the pressures and the shear stress over all the surfaces, the aerodynamic forces and moments on the bridge deck and the vehicle can be obtained. The aerodynamic coefficients of the vehicle are defined in Section 3.2. For the deck model, only three aerodynamic forces/moments are required: drag force (F_{HB}); lift force (F_{VB}), and moment (M_B) (see Figure 5.3). The drag force and lift force are along the deck width (x) and the deck height (y), respectively. The reference point of the moment is set as the centroid of the deck. The dimensionless aerodynamic coefficients of the bridge deck are defined by:

$$C_{HB} = \frac{F_{HB}}{q_B B_B L_B}; C_{VB} = \frac{F_{VB}}{q_B B_B L_B}; C_{MB} = \frac{M_B}{q_B B_B^{\ 2} L_B} \tag{5.1}$$

$$q_B = 0.5 \rho U_B^{\ 2} \tag{5.2}$$

where C_{HB}, $C_{VB,}$ and C_{MB} are the drag coefficient, lift coefficient, and moment coefficient of the bridge deck; B_B and L_B are the width and length of the deck, respectively; and U_B is the wind velocity viewed from the deck.

5.3 TESTED AERODYNAMIC FORCES ON STATIONARY SYSTEM

Wind tunnel tests of the stationary vehicle-bridge deck system were carried out in the TJ-3 wind tunnel of the State Key Laboratory for Disaster Reduction in Civil Engineering at Tongji University in Shanghai, China. The wind tunnel is closed-circuit with a test section 15m wide, 2m high, and 14m long. The bridge deck model was installed on the turning table of the wind tunnel at a height of 1.14 m above the tunnel floor, and the vehicle model was then mounted in different lanes of the deck model via a six-component high-frequency force balance, which was used to measure the aerodynamic forces acting on the vehicle. By rotating the turning table, winds of different yaw angles to the vehicle-bridge system could be realized. The wind generated in the tunnel was a uniform smooth wind with a speed of 10m/s.

More details about the wind tunnel tests can be found in Zhu *et al*. (2012). No aerodynamic coefficients of the bridge deck with the presence of the vehicle were measured. The measured aerodynamic coefficients of the vehicle on the upwind first lane are shown in Figure 5.4.

5.4 NUMERICAL SIMULATION OF STATIONARY VEHICLE-BRIDGE DECK SYSTEM

5.4.1 Simulation Scheme

The unsteady RANS method supplemented with the SST k-ω turbulence model described in Section 3.4.1 is employed. The governing equations are discretized using the QUICK scheme based on the finite volume method. The SIMPLEC algorithm is employed for the coupling of velocity and pressure. The time integration is performed using the second-order implicit method. The CFD code Fluent is employed to solve the parameters of flow field. The results are accepted as convergence after 30 iterations at each time step.

5.4.2 Computational Domain and Boundary Conditions

A cubic computational domain enclosed by the six outer boundaries is formed around the vehicle-bridge system, as shown in Figure 5.5. The six outer boundaries are named as *b_left*, *b_right*, *b_head*, *b_tail*, *b_up,* and *b_down*. The outer boundary *b_left* is the inflow face from which the wind blows in. *b_right* is parallel to *b_left* with an offset of X. The boundaries *b_up* and *b_down* are parallel to the lower surface of the deck with a distance of Y between the two boundaries. *b_head* and the *b_tail* are the outer boundaries of the domain with *b_head* near the vehicle head and *b_tail* near the vehicle tail. The distance between *b_head* and *b_tail* is Z. The total size of the domain is: X=15B_B, Y=11H_{vd} and Z=7L (H_{vd} is the total height of the vehicle-deck system, B_B is the width of the deck, and L is the length of the vehicle). The vehicle-bridge system model is located in the middle of the domain in the y direction while the vehicle is in the middle of the domain in the z-direction. For this study, in the x direction (wind direction), an upstream length of 3.5B_B and a downstream length of $10.5B_B$ are assigned between the vehicle-bridge system model and the corresponding outer boundaries. All the flow boundaries, including both the outer boundaries and the surfaces of the vehicle and the bridge deck, are enforced with mathematical boundary conditions to approximate the real situations. For instance, Figure 5.5 shows the vehicle-bridge system with a 90° yaw angle (the upcoming wind is perpendicular to the bridge deck). *b_left* is the source of the upcoming wind; a uniform wind speed of 10m/s, turbulence kinetic energy k of 0.05 and special dissipation ratio ω of 2 are assigned to this boundary. Generally, after passing the vehicle-bridge system, wind blows out of the domain through the outer boundary *b_right*. Thus, *b_right* is specified for this study as a flow outlet with zero pressure. In Figure 5.5 the outer boundaries *b_up*, *b_down*, *b_head* and *b_tail* are parallel to the direction of the upcoming wind; in this study the flows at these boundaries are assumed to be uniform, but the gradients of flow variables (including both wind velocity and pressure) normal to the boundary are zero. The flow generally cannot penetrate the surfaces of a vehicle or a deck, and therefore no-slip walls are assigned to these surfaces.

5.4.3 Meshing

Three meshing schemes M1, M2 and M3 with different grid sizes are generated to check the independence of the numerical results on grid sizes. The grid distributions over the vehicle surfaces and the height of the first layer grids over all the walls are kept consistent for the three meshing schemes but the densities of the grids in the other parts of the computational domain vary. The height of the first layer grids near the surfaces of the vehicle is 1×10^{-5}m, thus ensuring that the corresponding y^+ is below 1 in the simulation. The height of the first layer grids near the surfaces of the deck is 1×10^{-4}m, leading to the corresponding y^+ being smaller than 7. The grid distributions over the surfaces of the vehicle are shown in Figure 5.6 from different directions. A total of about 56 thousand grids are generated over the vehicle surfaces. Of the three meshing schemes, M1 is the coarsest one, with 4.8 million grids. Its grid distribution is shown in Figure 5.7. M2 and M3 are identified as the refined meshing systems based on M1. M2 refines the grid distributions in the planes parallel to the cross section of deck (the *xy* plane in Figure 5.5a) with 10.7 million grids, while M3 refines the grid distributions in the direction perpendicular to the cross section of the bridge deck (in the *yz* plane in Figure 5.5b), with 8.1 million grids.

The computed six aerodynamic coefficients of the vehicle, using different meshing schemes, are listed in Table 5.1. The results from the three meshing schemes are very similar, except for the life force coefficient, which has a very small value. The maximum difference among all the coefficients between the schemes M1 and M3 is only about 0.043. The computed three aerodynamic coefficients of the bridge deck along its length, using different meshing schemes, are shown in Figure 5.8. They can be seen to be consistent for the three meshing schemes in general. In consideration of both the accuracy of the results and the computational effort required, the meshing scheme M1 is finally accepted for the following numerical simulations.

5.4.4 Time Step and Length

The time step and length used in the simulation are decided based on the characteristic time t^* defined in Equation 3.7. Two time steps, $0.1t^*$ and $0.05t^*$, are used in the simulation to check the influence of time steps on the numerical results. For all the cases, the first $60t^*$ is treated as a converging time period, and the corresponding results are not used. The next $60t^*$ is taken as the normal time length for the simulation results. The following results, including the aerodynamic coefficient, averaging velocity, and pressure coefficient, represent all the values averaged over the last $60t^*$.

The aerodynamic coefficients of the vehicle and the bridge deck obtained using the two time steps are shown in Table 5.2 and Figure 5.9, respectively. The results show that there are almost no differences between the results from the two time steps. Therefore, the time step $0.1t^*$ can be accepted in the following numerical simulations.

5.4.5 Simulation Cases

In addition to the 90° yaw angle, three other yaw angles (0°, 30° and 60°) are also considered in exploring the effects of the yaw angle on the aerodynamic characteristics of the stationary vehicle-bridge system. The boundary conditions of the numerical simulation domain for the other yaw angles are adjusted appropriately, compared with the 90° yaw angle case. For a yaw angle $0° < \alpha_{wv} < 90°$, as shown in Figure 5.10, the upcoming wind is assigned with the angle α for the boundary *b_left*. The boundaries *b_head* and *b_tail* are then assigned with periodic conditions so that the flow entering the boundary *b_head* is identical to the flow exiting the boundary *b_tail*. The boundary *b_right* is still specified as a flow outlet with zero pressure. For the 0° yaw angle, *b_head* becomes the input boundary of upcoming winds; *b_tail* becomes the flow outlet with zero pressure; both *b_left* and *b_right* boundaries become symmetric and the gradients of flow variables at these boundaries are set as zero. In the next section the computed aerodynamic coefficients of the vehicle under crosswinds of different yaw angles will be compared with the measured ones from the wind tunnel.

5.4.6 Numerical simulation results and analysis

The computed aerodynamic coefficients of the vehicle are plotted in Figure 5.11 and compared with the wind tunnel test results. Only the cases of high yaw angles from 60° and 90° were tested in the wind tunnel. It can be seen that, within this range, the varying patterns of all the six computed aerodynamic coefficients with the yaw angle are similar to those of the wind tunnel test results. The drag coefficients and the rotating moment coefficients are almost the same for the computation simulations and the wind tunnel tests. The maximum difference of the aerodynamic force coefficients is found to be about 1.06 from the lift coefficient at the 60° yaw angle. The lift coefficient represents the pressure difference between the bottom and the top surface of the vehicle. However, the flows beneath the vehicle are very complex mainly due to the following two reasons: (a) the space beneath the vehicle is very narrow; (b) the existed wheels disturb the flows among the narrow space. In this narrow region, serious separation and possible reattachment of flows exist, which is a typical challenge for the CFD to predict with a high accuracy. Moreover, there is an additional 1mm gab left between the low boundary of the wheels and the top surface of the deck in the wind tunnel tests, which may lead the flows under the vehicle showing different effects on the vehicle. Therefore, the calculated C_L is hard to satisfy the wind tunnel results for the complex flow under the vehicle and the artificial 1mm additional gap in a high accuracy, which can also be reflected in C_p. The difference of C_p at 90° yaw angle is the maximum one among all the differences of the aerodynamic moment coefficients. In consideration of many uncertainties involved in both the wind tunnel tests and the numerical simulations, the numerical simulation scheme used in this study can be considered acceptable.

The variations of the aerodynamic coefficients of the vehicle from 0° to the 90° yaw angle can be seen from the simulation results. The side coefficient increases with the yaw angle and reaches the maximum value at the high yaw angle of 90°. The lift coefficient and the pitching moment coefficient increase first and decrease later, with a maximum value around 30° yaw angle. The drag coefficient decreases first and increases later, with a minimum value also around 30° yaw angle. The yawing moment coefficient decreases with the increasing yaw angle. The rotating moment coefficient decreases first and then becomes flat beyond 60° yaw angle. In brief, the aerodynamic coefficients of the stationary vehicle on the bridge deck are found to vary with wind yaw angle.

At the 90° yaw angle, the upcoming winds become perpendicular to the bridge deck. The aerodynamic coefficients of the bridge deck along its length direction at this particular angle are shown in Figure 5.12. It can be seen that, with the presence of the vehicle, the aerodynamic coefficients of the bridge deck change abruptly. Compared with the bridge deck without the vehicle, the drag coefficient of the bridge deck can be seen to reduce significantly with the presence of the vehicle, while the moment coefficient of the bridge deck shows a remarkable increase with the existence of the vehicle. The maximum differences are about 0.025 for the drag coefficient and 0.045 for the moment coefficient. The lift coefficient of the bridge deck shows rapid changes at the two ends of the vehicle with two peak values about 0.054 higher than the lift coefficient of the bridge deck without the vehicle. The lift coefficient of the bridge deck in the middle part of the vehicle appears to be slightly smaller than that of the deck without the vehicle. The drag force on the rails in front of the vehicle can be seen to decrease greatly leading to the decrease of the drag coefficients at the location of the vehicle. Thus the presence of the vehicle does affect the aerodynamic forces and moment on the bridge deck.

5.5 NUMERICAL SIMULATION OF MOVING VEHICLE-DECK SYSTEM

5.5.1 Relative Velocity Method

If one observes both the upcoming wind and the moving vehicle by standing on the bridge deck, the upcoming wind $\mathbf{u_W}$ is perpendicular to the bridge deck and the vehicle moves on the deck at a velocity of $\mathbf{u_V}$, as shown in Figure 5.13. However, if one observes both the upcoming wind and the moving vehicle by standing on the vehicle, the bridge deck actually moves at a velocity of $\mathbf{u_{BV}}$ and the upcoming wind becomes the relative wind velocity $\mathbf{u_{WV}}$, as shown in Figure 5.14. The vector relations between these two sets of velocities can be given by

$$\mathbf{u_{BV}}=-\mathbf{u_V}; \quad \mathbf{u_{WV}} = \mathbf{u_W}-\mathbf{u_V} \tag{5.3}$$

The yaw angle between the velocity $\mathbf{u_{WV}}$ and the longitudinal direction of the vehicle is given by

$$a_{WV} = \arctan(\frac{|\mathbf{u}_w|}{|\mathbf{u}_v|}) \tag{5.4}$$

Compared with Figure 5.10, it can be seen that the outer boundaries of the computational domain for the moving vehicle-bridge deck system are the same as those for the stationary vehicle-bridge deck system under the equal yaw angle, except that the bridge deck is now defined with a velocity $\mathbf{u_{BV}}$. This relative velocity method was also used by Krajnović and Davidson (2005) to obtain the aerodynamic forces of a moving vehicle, but in this case it was on the ground; the vehicle was fixed but the ground was enforced a moving velocity. In this study, the vehicle is fixed while the bridge deck is assigned a moving velocity. The upcoming crosswind velocity and the velocity of the deck constitute the relative velocity to the vehicle. In the computation simulation, the magnitude of $\mathbf{u}_{\mathbf{WV}}$ is selected as 10m/s and the four cases with different angles α_{WV} (0°, 30°, 60° and 90°) are considered to compute the aerodynamic coefficients of the system so that the effects of the vehicle's movement can be found.

5.5.2 Flow Fields and Comparison with Stationary Cases

The flow field around the stationary vehicle-bridge deck system (for the case of the 90° yaw angle) is shown in Figure 5.15 in terms of the averaged velocity. It can be seen that the flows separate at the ridges of the upwind side-surface while the other surfaces are totally immersed in the separated flow region. The flow field viewed from the driver on the moving vehicle for the case of the 30° yaw angle (the vehicle velocity is 8.66m/s and the crosswind velocity is 5m/s) is shown in Figure 5.16. It can be seen that the flows separate at the ridges of both the upwind side-surface and the front surface. An inclined wake structure is also evident along the direction of the combined velocity of the vehicle and the crosswind. The flow impacts on the front surface of the vehicle and then its velocity decrease dramatically, indicating that the front surface of the vehicle is pushing the air away if viewed by a person standing on the bridge deck. The inclined wake structure is the result of the vehicle dragging the air if viewed by a person standing on the bridge deck. A similar flow field can also be found around the stationary vehicle-bridge deck system under the crosswind velocity of a 30° yaw angle, as shown in Figure 5.17.

The averaged flow velocity distribution beneath the stationary vehicle is shown in Figure 5.18. This shows clearly that the flows separate at the corner of the bottom surface of the vehicle and accelerate near the deck surface. The averaged flow velocity distribution beneath the moving vehicle is shown in Figure 5.19. The flows beneath the moving vehicle are more complicated than those beneath the stationary vehicle. Flows separation and acceleration repeat lengthwise along the vehicle. The averaged flow velocity distribution beneath the stationary vehicle under the crosswind velocity of 30° yaw angle is shown in Figure 5.20. The flows shown in Figure 5.20 are similar to those shown in Figure 5.19, indicating that the aerodynamic coefficient of the moving vehicle is similar to the aerodynamic coefficient of the stationary vehicle under the crosswind velocity of the same yaw angle.

5.5.3 Aerodynamic Coefficients

The computed aerodynamic coefficients of the moving vehicle with the equal angle α_{WV} are shown in Figure 5.21 and are compared with the computed aerodynamic coefficients of the stationary vehicle. It can be seen that the computed aerodynamic coefficients of the moving vehicle are similar to those of the stationary vehicle under the equal yaw angle. Under such a condition, the vehicle motion (or the deck motion) has a slight influence on the aerodynamic coefficients of the vehicle. Therefore, the aerodynamic coefficients of the stationary vehicle under can be used for those of the moving vehicle with the equal yaw angle.

The computed aerodynamic coefficients of the bridge deck along its length are shown in Figure 5.22 for the yaw angle of 30°, 60° and 90° with the same relative wind speed to the vehicle. The angle of 0° implies that there was no wind perpendicular to the bridge deck, and therefore this case is excluded. The yaw angle of 90° means that the vehicle stayed on the deck without movement. It can be seen that the influence of the vehicle on the aerodynamic coefficients of the deck depends on the moving velocity of the vehicle. Compared with the 90° case, the aerodynamic coefficients of the bridge deck in the 30° and 60° yaw angle cases change significantly, not only within the vehicle location but also in the adjacent regions. These types of changes appear to be more significant in the 30° yaw angle case than in the 60° yaw angle case, that is, more significant with high vehicle speeds than with low vehicle speeds.

5.6 SUMMARY

In this Chapter, a numerical model is generated to compute the aerodynamic forces in terms of aerodynamic coefficients of and the flows around a stationary vehicle-bridge deck system are computed using CFD with unsteady RANS method and validated with the results from wind tunnel tests. Then the model is extended to solve the aerodynamic coefficients of and the flows around the moving vehicle-bridge deck system through a relative velocity method. The major procedures and conclusions are summarized as follows:

- A cubic computational domain enclosed by the six outer boundaries is formed around the vehicle-bridge system with mathematical boundary conditions. Three meshing schemes with different grid sizes are generated to check the independence of the numerical results on the grid sizes. The grid numbers of the three meshing schemes are 4.8, 8.1, and 10.1 million respectively. The aerodynamic coefficients of both the vehicle and the deck are in consistent for the three meshing schemes. In consideration of both the accuracy of the results and the computational effort required, the meshing scheme with 4.8 million grids is finally accepted for the further numerical simulations. A time step of $0.1t^*$ is accepted compared with a shorter time step.

- The flows around the stationary vehicle-deck system are simulated with different yaw angles. Compared with the tested aerodynamic coefficients of the stationary vehicle, the varying patterns of all the six computed aerodynamic coefficients with the yaw angle are similar to those of the wind tunnel test results. The drag coefficients and the rotating moment coefficients are almost the same for the computation simulations and the wind tunnel tests. The maximum difference of the aerodynamic force coefficients is about 1.06 from the lift coefficient at the 60° yaw angle. The maximum difference of the aerodynamic moment coefficients is about 0.16 from the pitching moment coefficient at the 90° yaw angle. In consideration of many uncertainties involved in both the wind tunnel tests and the numerical simulations, the numerical simulation scheme used in this study can be considered acceptable.

- The aerodynamic coefficients of the stationary vehicle on the bridge deck vary with wind yaw angle. The side coefficient increases with the yaw angle and reaches the maximum value at the high yaw angle of 90°. The lift coefficient and the pitching moment coefficient increase first and decrease later, with a maximum value around 30° yaw angle. The drag coefficient decreases first and increases later, with a minimum value also around 30° yaw angle. The yawing moment coefficient decreases with the increasing yaw angle.

- The presence of the vehicle does affect the aerodynamic forces and moment on the bridge deck. With the presence of the vehicle, the aerodynamic coefficients of the bridge deck change abruptly. Compared with the bridge deck without the vehicle, the drag coefficient of the bridge deck reduce significantly with the presence of the vehicle, while the moment coefficient of the bridge deck shows a remarkable increase with the existence of the vehicle. The lift coefficient of the bridge deck shows rapid changes at the two ends of the vehicle.

- Through the relative velocity method, the flows around the moving vehicle-deck system are simulated. Viewed from the driver's seat on the moving vehicle, the flows separate at the ridges of the both the upwind side-surface and the front surface, and the corner of the bottom surface of the vehicle. They accelerate near the deck surface. An inclined wake structure is generated along the direction of the combined velocity of the vehicle and the crosswind. A similar flow field can also be found around the stationary vehicle-bridge deck system. The flows beneath the moving vehicle are more complicated than those beneath the stationary vehicle.

- The computed aerodynamic coefficients of the moving vehicle are similar to those of the stationary vehicle under the equal yaw angle. The vehicle motion (or the deck motion) has a slight influence on the aerodynamic coefficients of the vehicle. Therefore, the aerodynamic coefficients of the stationary vehicle can be used for those of the moving vehicle with the given yaw angle.

Table 5.1 Computed aerodynamic coefficients of the vehicle under different meshing schemes

Meshing	C_S	C_L	C_D	C_P	C_Y	C_R
M1	4.439	-0.003	0.254	-0.123	-0.627	-0.229
M2	4.458	0.001	0.239	-0.120	-0.627	-0.228
M3	4.396	0.040	0.267	-0.113	-0.622	-0.230

Table 5.2 Computed aerodynamic coefficients of the vehicle at different time steps

Time step	C_S	C_L	C_D	C_P	C_Y	C_R
$0.1t^*$	4.439	-0.003	0.254	-0.123	-0.627	-0.229
$0.05t^*$	4.437	-0.003	0.254	-0.123	-0.626	-0.229

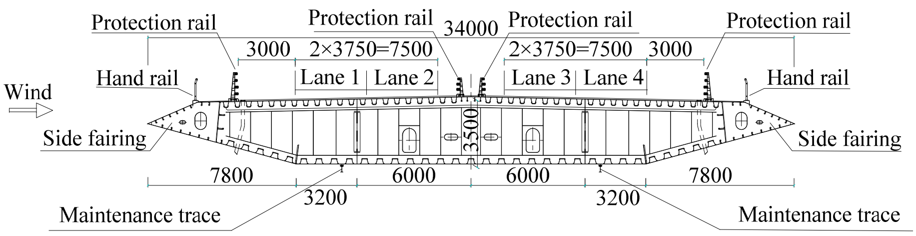

Figure 5.1 Cross section of the prototype bridge deck (unit: mm)

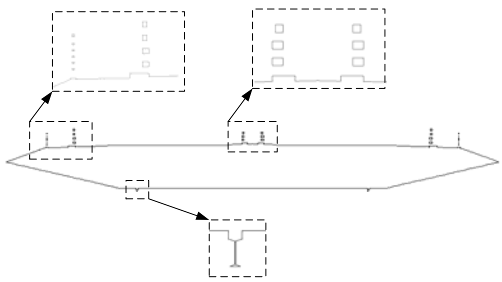

Figure 5.2 Numerical model of the bridge deck

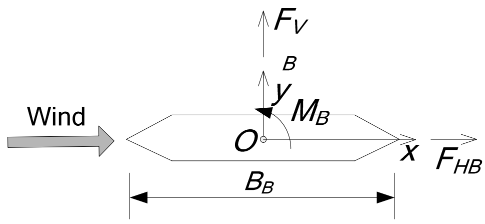

Figure 5.3 Aerodynamic forces on the bridge deck

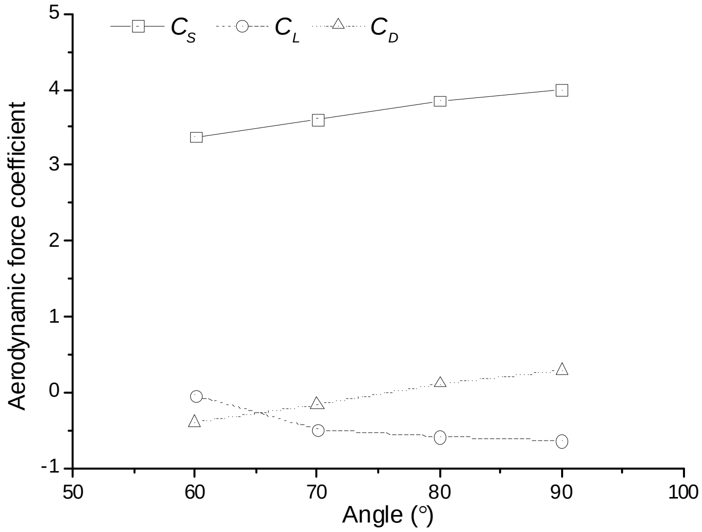

(a) Aerodynamic force coefficients

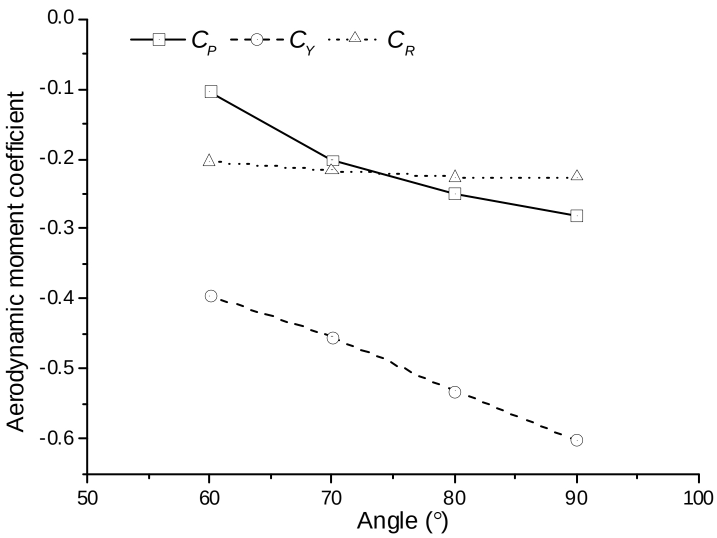

(b) Aerodynamic moment coefficients

Figure 5.4 Measured aerodynamic coefficients of the vehicle

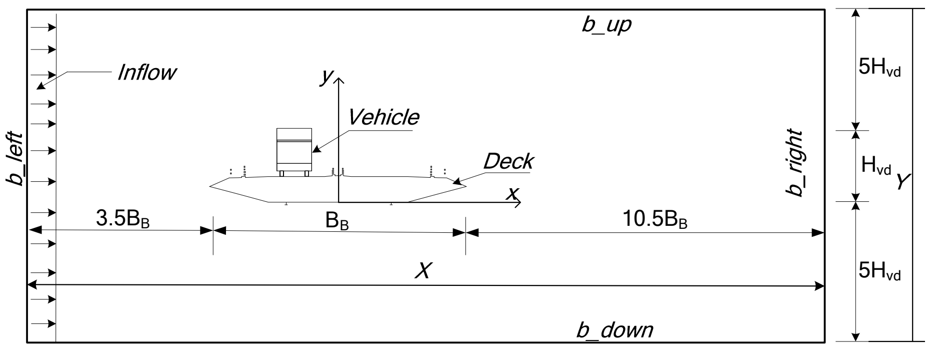

(a) *xy* section

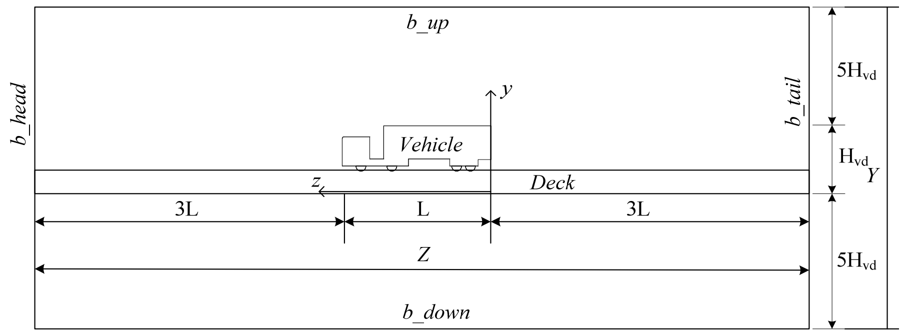

(b) *yz* section

Figure 5.5 Computational domain sketch: vehicle-bridge system

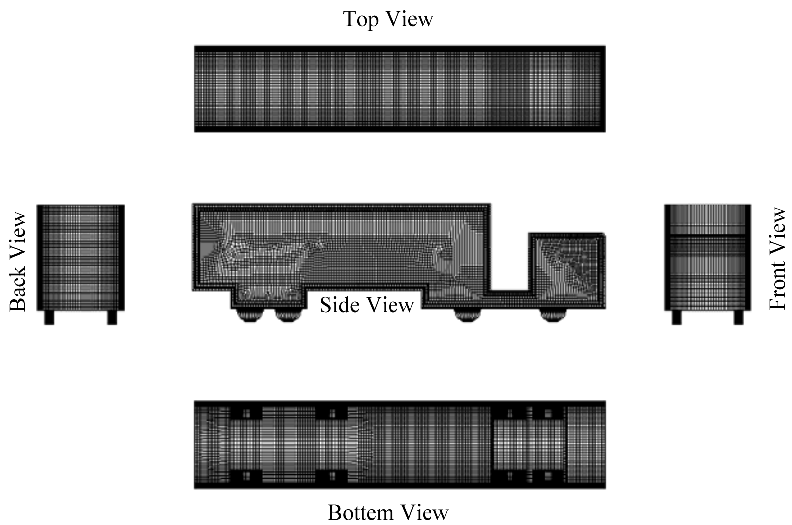

Figure 5.6 Grid distributions over the vehicle surfaces

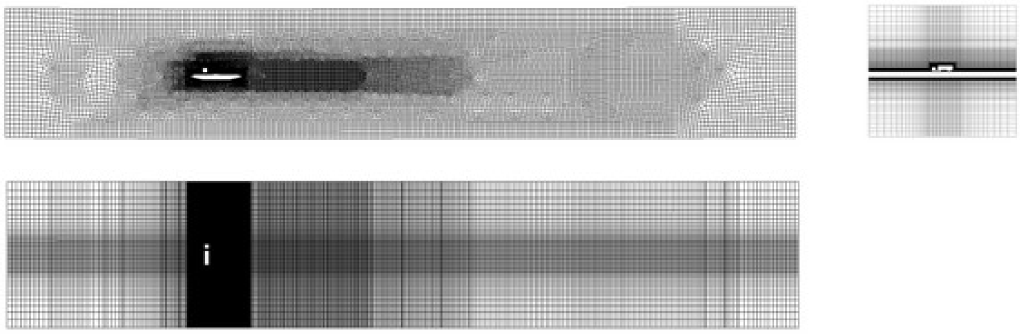

(a) Global grid distributions

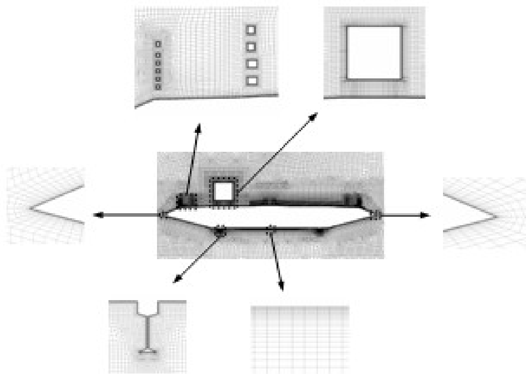

(b) Local grid distributions near the deck

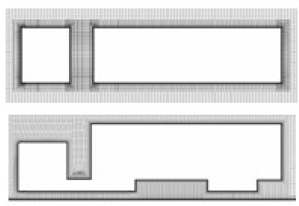

(c) Local grid distributions near the vehicle

Figure 5.7 Grid distributions in the meshing scheme M1

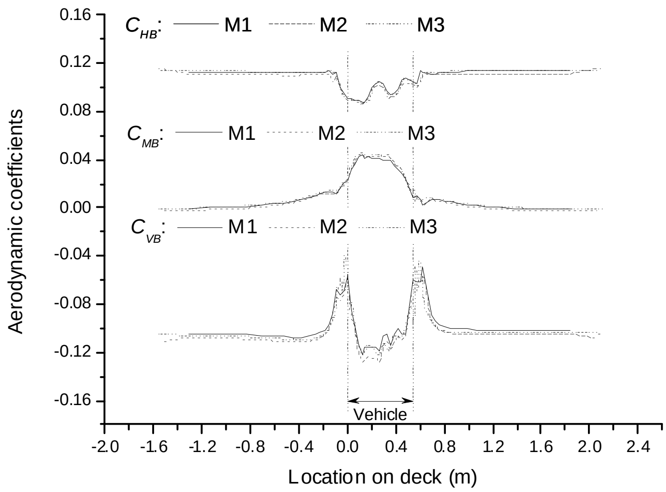

Figure 5.8 Computed aerodynamic coefficients of the bridge deck under different meshing schemes

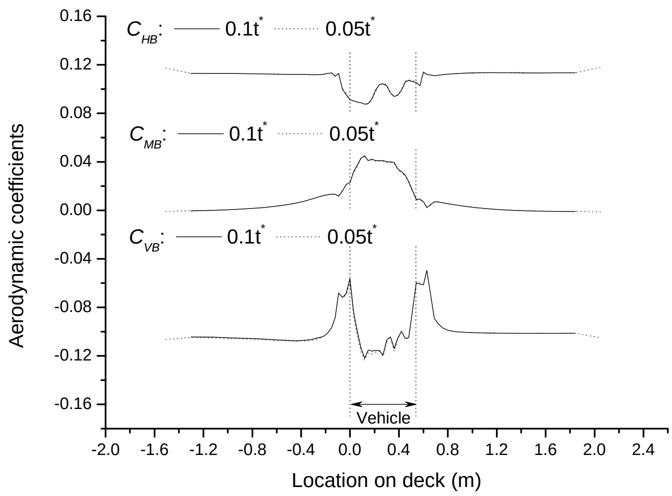

Figure 5.9 Computed aerodynamic coefficients of the bridge deck with different time steps

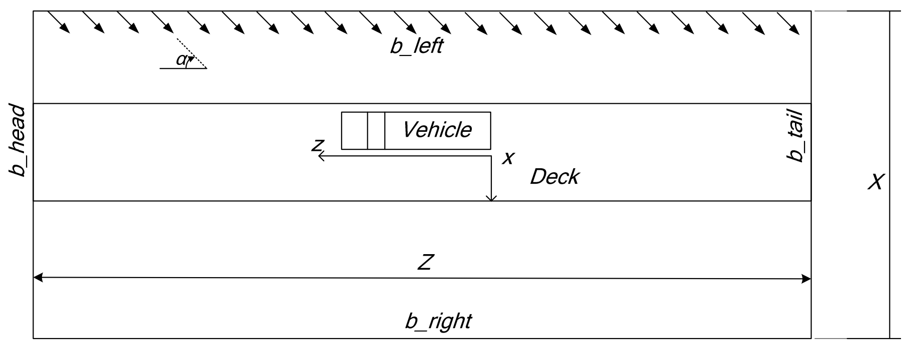

Figure 5.10 Computational domain for yaw angle cases

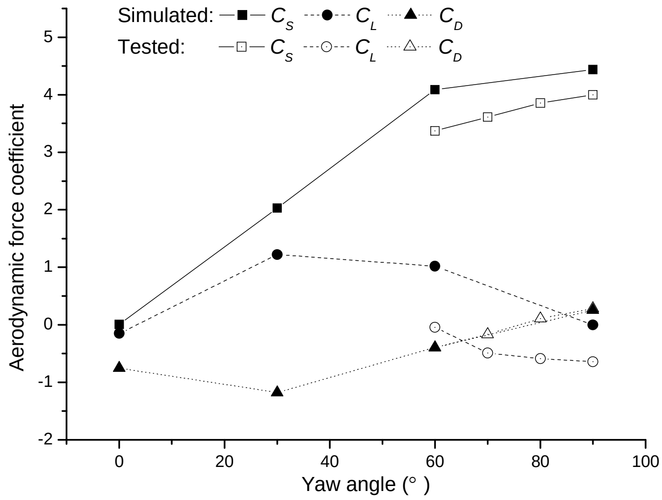

(a) Aerodynamic force coefficients

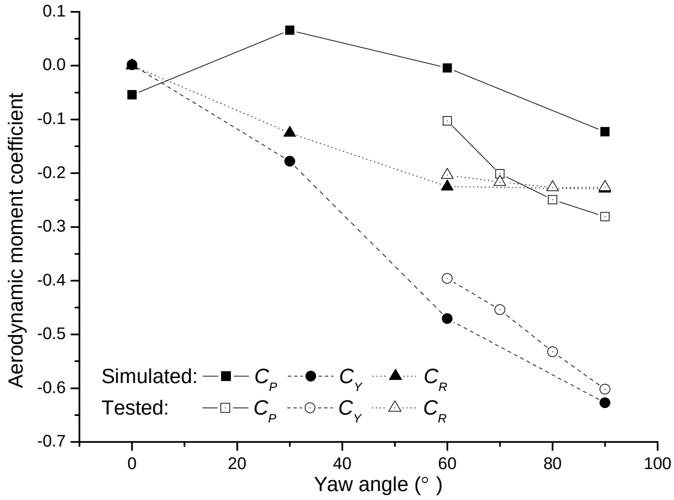

(b) Aerodynamic moment coefficients

Figure 5.11 Computed aerodynamic coefficients of the vehicle at different yaw angles

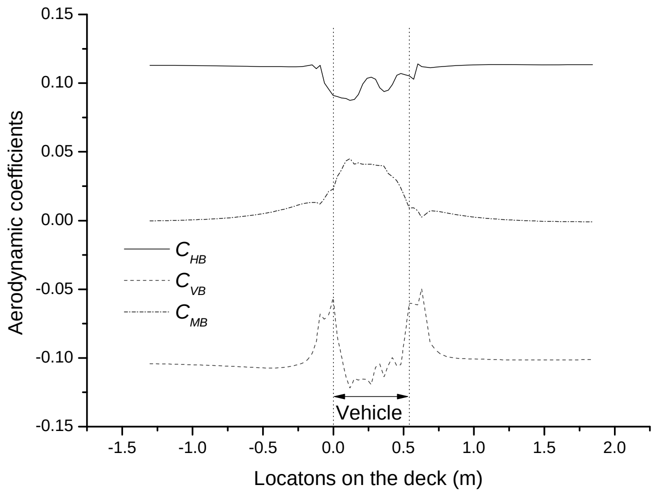

Figure 5.12 Aerodynamic coefficients of the bridge deck with the stationary vehicle

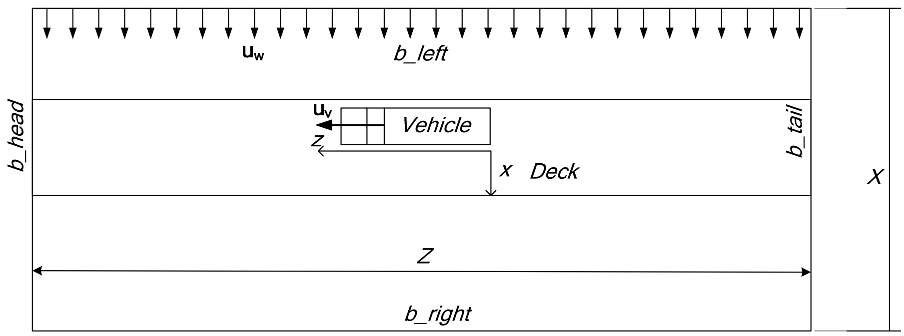

Figure 5.13 Moving vehicle-bridge deck system (see on the deck)

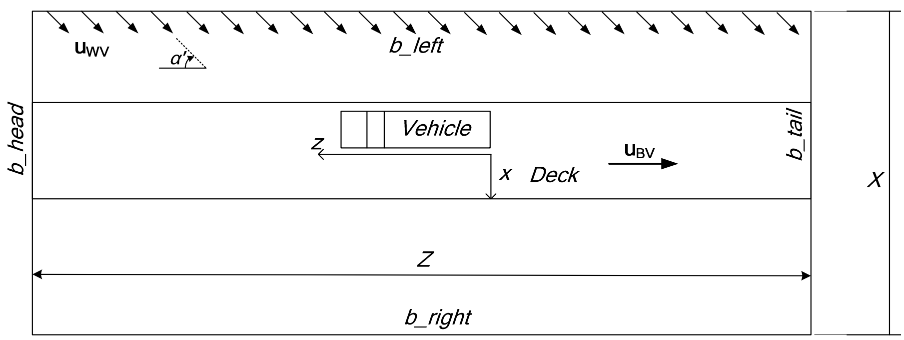

Figure 5.14 Moving vehicle-bridge deck system (see on the vehicle)

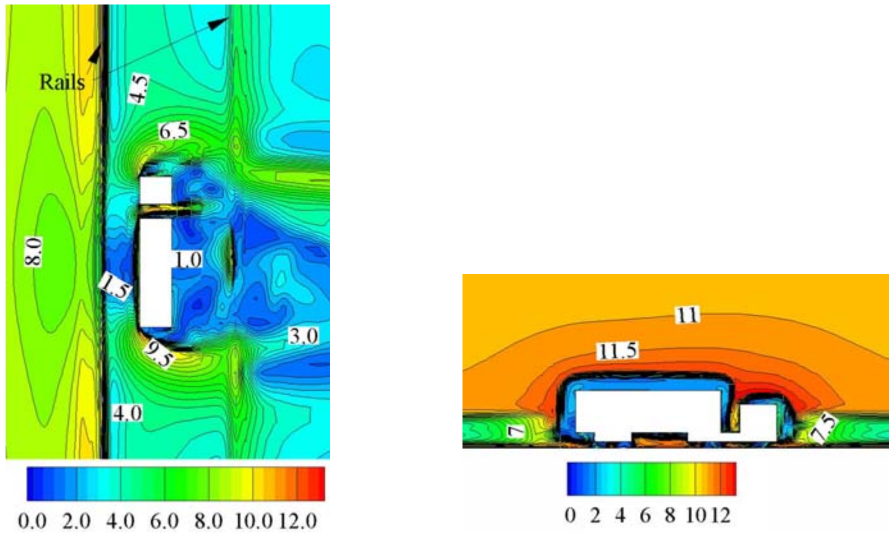

(a) Horizontal plane (m/s)   (b) Vertical plane (m/s)

Figure 5.15 Averaged flow velocity distribution around the stationary vehicle (90° yaw angle)

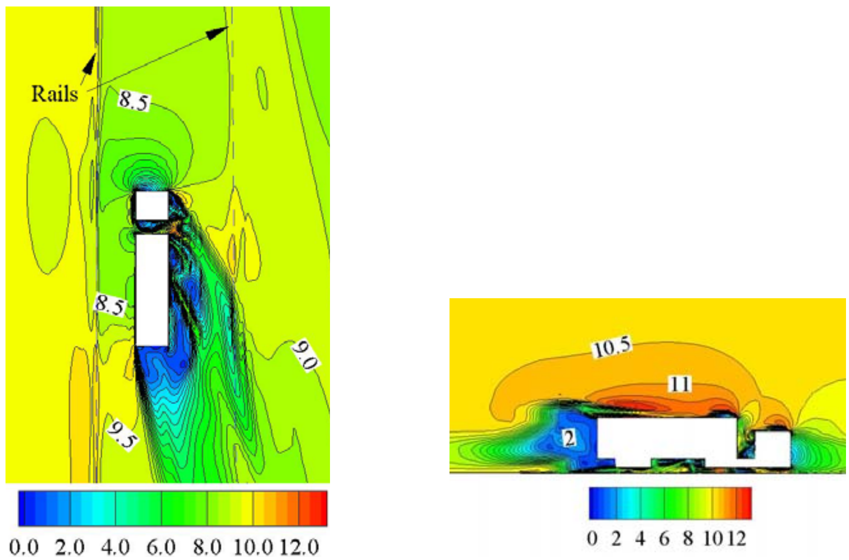

(a) Horizontal plane (m/s)   (b) Vertical plane (m/s)

Figure 5.16 Averaged flow velocity distribution around the moving vehicle (30° yaw angle)

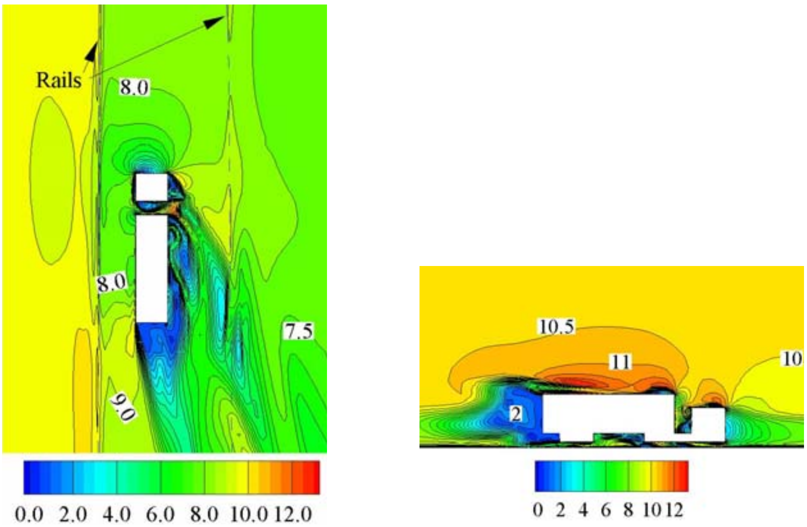

(a) Horizontal plane (m/s) (b) Vertical plane (m/s)

Figure 5.17 Averaged flow velocity distribution around the stationary vehicle under the crosswind velocity of 30° yaw angle

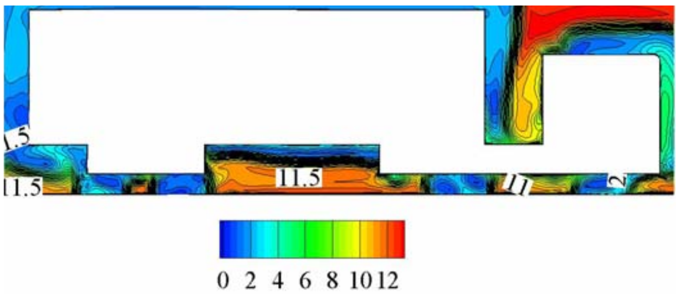

(a) Lengthwise vertical plane (m/s)

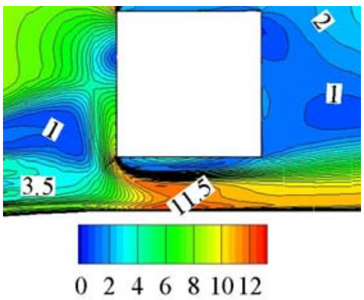

(b) Vertical plane perpendicular to length (m/s)

Figure 5.18 Averaged flow velocity distribution beneath the stationary vehicle (90° yaw angle)

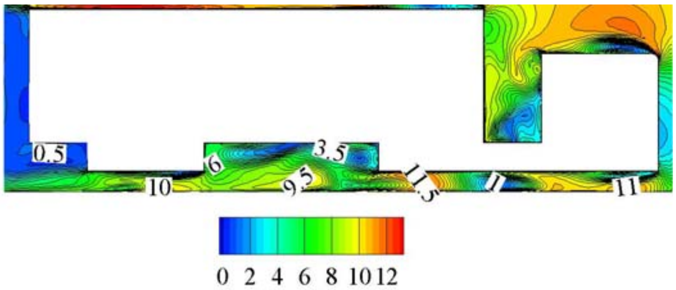

(a) Lengthwise vertical plane (m/s)

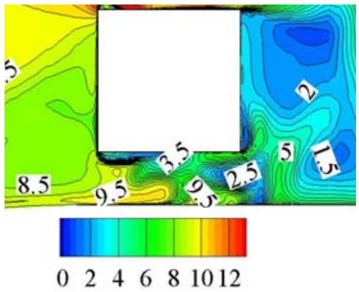

(b) Vertical plane perpendicular to length (m/s)

Figure 5.19 Averaged flow velocity distribution beneath the moving vehicle (30° yaw angle)

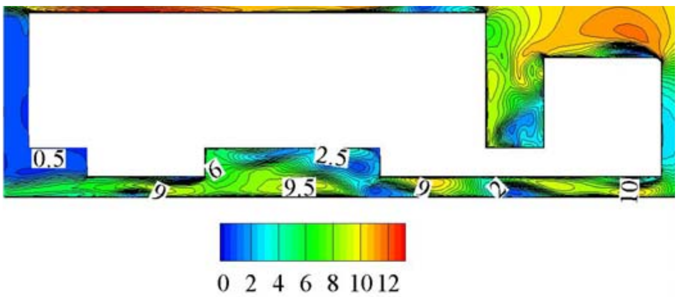

(a) Lengthwise vertical plane (m/s)

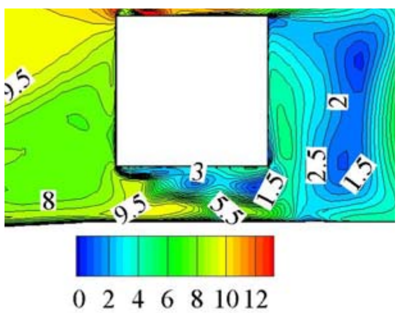

(b) Vertical plane perpendicular to length (m/s)

Figure 5.20 Averaged flow velocity distribution under the stationary vehicle under the crosswind velocity of 30° yaw angle

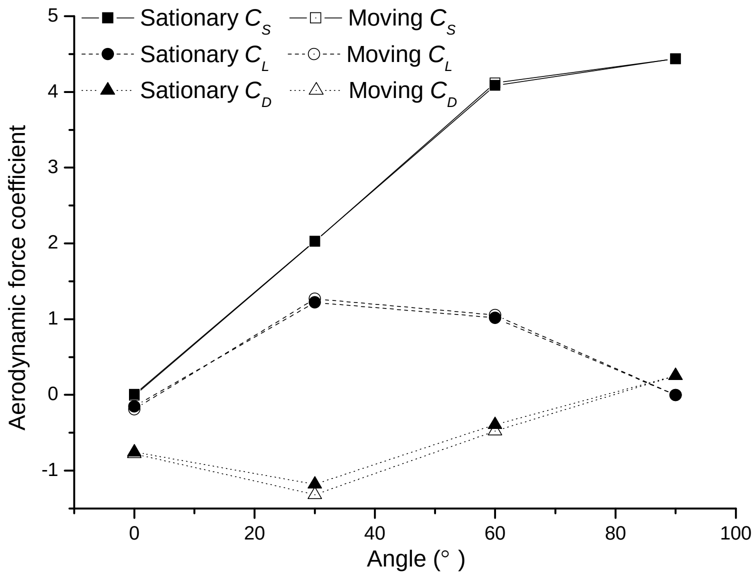

(a) Aerodynamic force coefficient

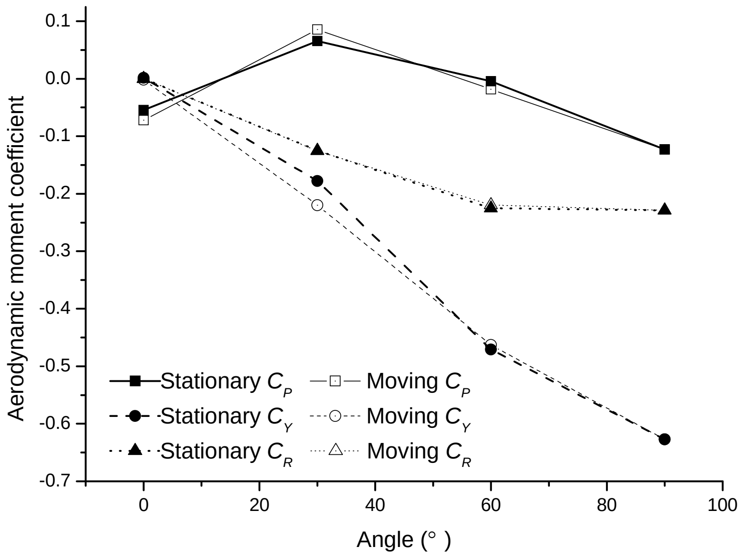

(b) Aerodynamic moment coefficient

Figure 5.21 Comparison of computed aerodynamic coefficients of the vehicle with and without movement

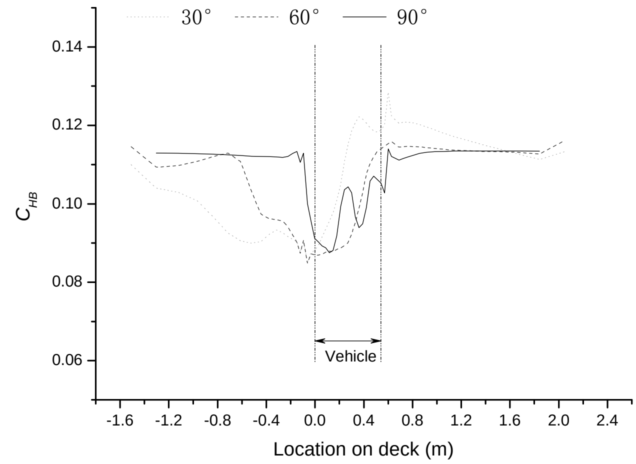

(a) Drag coefficient

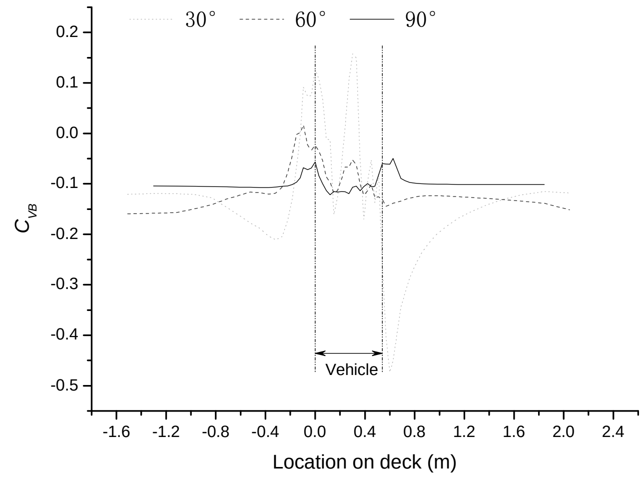

(b) Lift coefficient

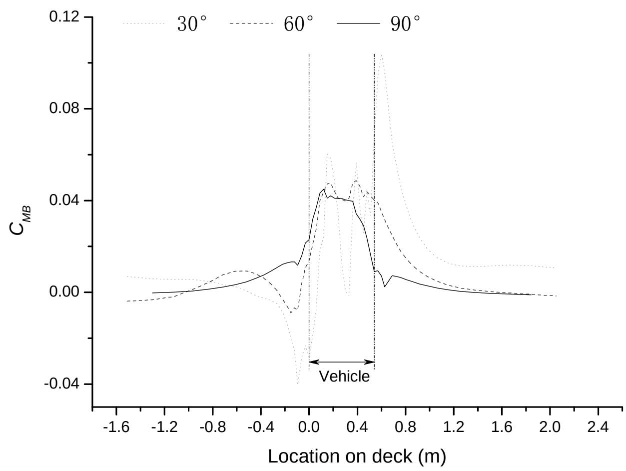

(c) Moment coefficient

Figure 5.22 Computed aerodynamic coefficients of the bridge deck

CHAPTER 6

RIDE COMFORT OF A MOVING VEHICLE ON A BRIDGE DECK

6.1 INTRODUCTION

An advanced road vehicle model able to simulate the lateral motion of the moving vehicle on the ground under the combined action of fluctuating crosswinds and driver has been established in Chapter 4. The results show that road roughness in plane considerably influences the ride comfort of the vehicle in the lateral direction. In this chapter, the advanced road vehicle model will be incorporated into the framework of the Road Vehicle-Bridge-Wind (RVBW) system with emphasis on the effects of the lateral motion of the road vehicle on the ride comfort. Moreover, the aerodynamic coefficients of a high-sided road vehicle and a bridge deck as the vehicle moves on the deck have been computed in Chapter 5. It is found that the movement of the vehicle does affect the aerodynamic coefficients of the bridge deck. Based on these newly computed aerodynamic coefficients, the ride comfort of the moving vehicle on a bridge deck will be analyzed in this chapter.

Several frameworks of the RVBW system were presented in the previous studies. Xu and Guo (2003a) constructed a coupled wind-road vehicle-bridge system using a fully computerized approach. In this system, vehicles were modeled as mass-spring-damper systems while bridges were modelled by the Finite Element Method (FEM). Random crosswinds were simulated and the corresponding wind forces were applied to both vehicles and bridges. Road roughness was also simulated in random and attached on the surface of the bridge deck. Cai and Chen (2004) presented a framework for the dynamic analysis of the coupled RVBW system. The simulated vehicle responses including the vertical, rolling, and pitching responses and the lateral acceleration of the bridge were then input to a separated vehicle model to find the lateral responses of vehicle (Chen and Cai, 2004). Cheung and Chan (2010) considered three aspects for the coupled RVBW system: the wind-bridge interaction, the wind-vehicle interaction and the vehicle-bridge interaction.

Based on the dynamic analysis framework, the ride comfort of vehicles on the bridge has been studied in Xu and Guo (2004). It was concluded that the crosswinds affected the ride comfort of the vehicle in the lateral direction while the bridge motion affected the ride comfort of the vehicle in the vertical direction. In the ride comfort analysis of Xu and Guo (2004), the road vehicle was assumed to be moving on the deck without any lateral motion, and the road roughness differences between the wheels on the two sides were neglected, and the driver's behavior was also not considered. A new framework is thus required to evaluate the ride comfort in considering the road roughness in plane, the lateral motion of the vehicle and the driver's behavior.

In the frameworks of the RVBW systems mentioned above in the previous studies, wind loads acting on a vehicle were formed based on the aerodynamic coefficients of a stationary vehicle on the ground. The wind loads acting on the bridge deck were also generated without considering the influences of the vehicles. Actually, the aerodynamic forces on vehicles moving on the bridge deck are different from those on vehicles moving on the ground. They are influenced considerably by the local environment such as the geometric shape of the bridge deck and the layout of the rails in front of the vehicles. As vehicles move on the bridge deck and the flows around the pure deck are altered naturally by the passing of the vehicles, the aerodynamic forces on the bridge deck are, therefore, changed by the movement of the vehicles (See Chapter 5). Thus, it is more rational to evaluate the ride comfort of the vehicles moving on the bridge deck by considering the effects of movement of the vehicles and the mutual influences between the bridge deck and the vehicles in terms of aerodynamic forces.

In this chapter, the advanced road vehicle model established in Chapter 4 considering the road roughness in plane, lateral motion of the vehicle, and driver's behavior will be incorporated into the framework of the coupled RVBW system. The computed aerodynamic coefficients of both the moving vehicle and the bridge deck with mutual interference included in Chapter 5 will then be used to evaluate the ride comfort of the moving road vehicle on the long span cable-stayed bridge.

6.2 FRAMEWORK OF RVBW SYSTEM

In this study, the moving road vehicle and the long span cable-stayed bridge are treated as two subsystems under crosswinds. They are coupled through the contact forces and the geometric compatibility between the vehicle wheels and the surface of the bridge deck. In the vehicle subsystem, the vehicle model is represented using a lumped mass vehicle model with a series of springs and dashpots, and the equation of motion is established on the local coordinate system of the vehicle body so that it can simulate the progressive instability of the vehicle under extreme conditions. The vehicle can move laterally, and the wheels can lose contact with the road surface in a physically rational way under the action of crosswinds, drivers, and the road roughness in plane. The equations of motion of the road vehicle on the ground (see Chapter 4) in the local coordinates of the vehicle body (VCS) are rearranged and repeated here to have a complete picture of the RVBW system:

$$m_{vb}\dot{v}_{vby} + m_{vb}\omega_{vbz}v_{vbx} - m_{vb}\omega_{vbx}v_{vbz} = f_{vby}^{S} - f_{vby}^{G} + f_{vy}^{W} \tag{6.1a}$$

$$m_{vb}\dot{v}_{vbz} - m_{vb}\omega_{vby}v_{vbx} + m_{vb}\omega_{vbx}v_{vby} = f_{vbz}^{S} - f_{vbz}^{G} + f_{vz}^{W} \tag{6.1b}$$

$$I_{xx}\dot{\omega}_{vbx} - I_{xz}\dot{\omega}_{vbz} + (I_{zz} - I_{yy})\omega_{vby}\omega_{vbz} - I_{xz}\omega_{vbx}\omega_{vby} = m_{vbx}^{S} + m_{vx}^{W} \tag{6.1c}$$

$$I_{yy}\dot{\omega}_{vby} + (I_{xx} - I_{zz})\omega_{vbx}\omega_{vbz} - I_{xz}(\omega_{vbz}^{2} - \omega_{vbx}^{2}) = m_{vby}^{S} + m_{vy}^{W} \tag{6.1d}$$

$$I_{zz}\dot{\omega}_{vbz} - I_{zx}\dot{\omega}_{vbx} + (I_{yy} - I_{xx})\omega_{vbx}\omega_{vby} + I_{xz}\omega_{vby}\omega_{vbz} = m_{vbz}^{S} + m_{vz}^{W} \tag{6.1e}$$

$$m_{wi}\dot{v}_{wiy} = f_{wiy}^{S} + f_{wiy}^{G} + f_{wiy}^{T} \tag{6.1f}$$

$$m_{wi}\dot{v}_{wiz} = f_{wiz}^S + f_{wiz}^G + f_{wiz}^T \tag{6.1g}$$

where the subscript v, vb, and wi represent the vehicle, vehicle body and the ith wheel, respectively; the subscript x, y, and z are the three orthogonal directions of the VCS; the superscript S, G, and W represent the suspension system, gravity, and wind, respectively; m_{vb} and m_{wi} is the mass of the vehicle body and the ith wheel, respectively; I_{xx}, I_{yy}, and I_{zz} are the moments of inertia of the vehicle body around the x-axis, y-axis, and z-axis, respectively; I_{xz} is the product of inertial of the vehicle body in the xz plane; v_{vby} and v_{vbz} are the transitional velocities of the vehicle body along the y-axis and z-axis, respectively; ω_{vbx}, ω_{vby}, and ω_{vbz} are the angular velocities of the vehicle body around the x-axis, y-axis, and z-axis, respectively; v_{wiy} and v_{wiz} are the transitional velocities of the ith wheel along the y-axis and z-axis, respectively; f_{vy}^W and f_{vz}^W are the wind forces on the vehicle along the y-axis and z-axis, respectively; m_{vx}^W, m_{vy}^W, and m_{vz}^W are the wind moments on the vehicle about the x-axis, y-axis and z-axis, respectively; f_{vby}^G and f_{vbz}^G are the gravity components of the vehicle body along the y-axis and z-axis, respectively; f_{wiy}^G and f_{wiy}^G are the gravity components of the ith wheel along the y-axis and z-axis, respectively; f_{vby}^S and f_{vbz}^S are the forces on the vehicle body due to the deformation of the suspension system along the y-axis and z-axis, respectively; m_{vbx}^S, m_{vby}^S, and m_{vbz}^S are the moments due to the deformation of the suspension system about the x-axis, y-axis, and z-axis, respectively; f_{wiy}^S and f_{wiz}^S are the forces on the ith wheel due to the deformation of the suspension system along the y-axis and z-axis, respectively; f_{wiy}^T and f_{wiy}^T are the forces received by the ith tire from the deck.

The forces (f_{vby}^S, f_{vbz}^S) and moments ($m_{vbx}^S, m_{vby}^S, m_{vby}^S$) acting on the vehicle body due to the deformation of the suspension are integrated from the corresponding forces on each wheel and have the following formations:

$$f_{vby}^{S} = -\sum_{i=1}^{4} f_{wiy}^{S} \tag{6.2a}$$

$$f_{vbz}^{S} = -\sum_{i=1}^{4} f_{wiz}^{S} \tag{6.2b}$$

$$m_{vbx}^{S} = \sum_{i=1,2} f_{wiz}^{S} b_1 - \sum_{i=3,4} f_{wiz}^{S} b_1 - \sum_{i=1}^{4} f_{wiy}^{S} h_1 \tag{6.2c}$$

$$m_{vby}^{S} = -\sum_{i=2,4} f_{wiz}^{S} L_2 + \sum_{i=1,3} f_{wiz}^{S} L_1 \tag{6.2d}$$

$$m_{vbz}^{S} = -\sum_{i=1,3} f_{wiy}^{S} L_1 + \sum_{i=2,4} f_{wiy}^{S} L_2 \tag{6.2e}$$

where b_1, h_1, l_1, and l_2 are the distances from the gravity center of the vehicle body to the wheel center in the y-direction, to the suspension system in the z-direction, to the front wheel center in the x-direction and to the rear wheel center in the x-direction, respectively.

The forces (f_{wiy}^{S}, f_{wiz}^{S}) on the ith wheel due to the deformation of the suspension system are the functions of the relative displacement and velocity between the ith wheel center and its corresponding suspension point SPi on the vehicle body as:

$$f_{wiz}^{S} = f(z_{SPi} - z_{wi}, \dot{z}_{SPi} - \dot{z}_{wi}) \tag{6.3a}$$

$$f_{wiy}^{S} = f(y_{SPi} - y_{wi}, \dot{y}_{SPi} - \dot{y}_{wi}) \tag{6.3b}$$

The forces (f_{wiy}^{T}, f_{wiy}^{T}) received by the ith tire from the deck in VCS are transformed from the local coordinated system of the ith wheel as:

$$f_{wiy}^{T} = \mathbf{T}_{vwi}(2,:)(f_{wix^*}^{T}, f_{wiy^*}^{T}, f_{wiz^*}^{T})^{T} \tag{6.4a}$$

$$f_{wiz}^{T} = \mathbf{T}_{vwi}(3,:)(f_{xiy^*}^{T}, f_{wiy^*}^{T}, f_{wiz^*}^{T})^{T} \tag{6.4b}$$

Where $\mathbf{T}_{vwi}(j,:)$ with j (=2, 3) represent the vector of the jth row of the transformation matrix $\mathbf{T}_{vwi}$ from WCS of the ith wheel to VCS; $f_{wix^*}^T$, $f_{wiy^*}^T$, and $f_{wiz^*}^T$ are the forces received by the tire from the deck along the x*-, y*-, and z*-axis of WCS. In the expression of $\mathbf{T}_{vwi}$, steer angle δ is an input to model the behavior of a driver as:

$$\delta = -\lambda_1 Y_{vb}(t-\varepsilon) - \lambda_2 v_{vbY}(t-\varepsilon) \tag{6.5}$$

where v_{vbY} and Y_{vb} is the velocity and the displacement from the stable lane of the vehicle body at its center in the global system on the bridge; λ_1 and λ_2 are two constants; ε is the driver reaction time. $f_{wix^*}^T$ is approximated as zero since it has little contribution to the dynamic behavior of the wheel-tire in the plane with limited steer angle of the driver. $f_{wiy^*}^T$ is related to the sideslip angle α and $f_{wiz^*}^T$ as:

$$f_{wiy^*}^T = f(f_{wiz^*}^T, \alpha) \tag{6.6}$$

α is defined as:

$$\alpha = \arctan \frac{v_{wiy^*}}{v_{wix^*}} \tag{6.7}$$

where v_{wix^*} and v_{xiy^*} are the relative velocities of the ith wheel center to the contact point on the bridge deck and can be expressed as:

$$\begin{aligned} v_{wix^*} &= \mathbf{T}_{wiv}(1,:)(v_{wix} - v_{dix}, v_{wix} - v_{diy}, v_{wiz} - v_{diz})^T \\ &= \mathbf{T}_{wiv}(1,:)(v_{wix}, v_{wix}, v_{wiz})^T - \mathbf{T}_{wiv}(1,:)\mathbf{T}_{ve}(v_{diX}, v_{diY}, v_{diZ})^T \end{aligned} \tag{6.8}$$

Similarly,

$$v_{wiy^*} = \mathbf{T}_{wiv}(2,:)(v_{wix}, v_{wix}, v_{wiz})^T - \mathbf{T}_{wiv}(2,:)\mathbf{T}_{ve}(v_{diX}, v_{diY}, v_{diZ})^T \tag{6.9}$$

where $\mathbf{T}_{wiv}(j,:)$ with j (=1, 2) represent the vector of the jth row of the transformation matrix $\mathbf{T}_{wiv}$ from VCS to WCS of the ith wheel; $\mathbf{T}_{ve}$ is the transformation matrix from ECS (ECS is identical to the global system of the bridge) to VCS; v_{diX}, v_{diY}, and v_{diZ} are the velocity of the contact point of the ith wheel on the deck along X-, Y-, and Z-axis in ECS and should be solved from the bridge subsystem.

$f_{wiz^*}^{T}$ is expressed as the rational function of the relative displacement and velocity along z^* between the center of the ith wheel and the corresponding contact point on the deck as:

$$f_{wiz^*}^{T} = \begin{cases} f(Z_{wi} - Z_{pi}, Z_{wi} - \dot{Z}_{pi}) & if(Z_{wi} - Z_{pi} < h_a) \\ 0 & else \end{cases} \quad (6.10)$$

where h_a is the allowed displacement difference between the wheel center and the contact point on the ground and approximated as the radius of the tire without deformation. Z_{pi} and $\dot{Z}_{pi}$ are the actual surface profiles of the bridge deck under the ith tire and should be solved from the bridge subsystem.

The bridge subsystem is presented using the conventional Finite Element Method (FEM) in the global system. The equations of motion of a long span cable-stayed bridge in FEM in the global system are expressed as:

$$\mathbf{M_b}\ddot{\boldsymbol{\delta}}_\mathbf{b} + \mathbf{C_b}\dot{\boldsymbol{\delta}}_\mathbf{b} + \mathbf{K_b}\boldsymbol{\delta}_\mathbf{b} = \mathbf{F}_b^W + \mathbf{F}_b^V \quad (6.11)$$

where the subscript b represent the bridge; $\boldsymbol{\delta}_\mathbf{b}$, $\dot{\boldsymbol{\delta}}_\mathbf{b}$, and $\ddot{\boldsymbol{\delta}}_\mathbf{b}$ are the vectors of the nodal displacement, velocity and acceleration of all the elements; $\mathbf{M_b}$, $\mathbf{K_b}$, and $\mathbf{C_b}$ are the matrixes of mass, stiffness, and damping; $\mathbf{F}_b^W$ is the vector of wind loads acting on the nodes of the bridge; and $\mathbf{F}_b^V$ is the vector of contact forces transformed from the vehicle subsystem.

6.3 MODELLING OF LONG SPAN CABLE-STAYED BRIDGE

FEM is employed to model the long span bridge (Xu and Guo, 2003a; Cai and Chen, 2004; Cheung and Chan, 2010). Typically, spatial beam elements of six DoFs at each end node are adopted to build the decks, towers, and piers numerically. Bar elements with three translational DoFs at each end node are used for the cables of the cable-stayed bridge. For each element, an element stiffness matrix in its local coordinate system can be generated based on the virtual work principle or other methods to describe its load resistance property. All the element stiffness matrixes are assembled eventually in the global coordinate system as $\mathbf{K_b}$. The mass matrix $\mathbf{M_b}$ is formed using the lumped or consistent mass method. The structural damping matrix $\mathbf{C_b}$ is assumed as Reyleigh damping and expressed as follows:

$$\mathbf{C_b} = a_0\mathbf{M_b} + a_1\mathbf{K_b} \tag{6.12}$$

with

$$a_0 = \frac{2\omega_i\omega_j\left(\omega_i\xi_j - \omega_j\xi_i\right)}{\omega_i^2 - \omega_j^2}, \quad a_1 = \frac{2\left(\omega_i\xi_i - \omega_j\xi_j\right)}{\omega_i^2 - \omega_j^2} \tag{6.13}$$

where ω_i and ω_j are the frequencies of the *i*th and *j*th order modal, respectively; ξ_i and ξ_j are the damping ratios of the *i*th and *j*th order modal, respectively. The detailed process and formation of $\mathbf{M_b}$ and $\mathbf{K_b}$ can be found in many textbooks related to the application of the FEM to structures of linear elements, such as Xu and Xia (2012).

6.4 WIND LOADS ON BRIDGE

As a vehicle moves on the bridge deck, the wind loads acting on the bridge deck are more dominant to affect the ride comfort of the vehicle compared with the wind loads on other parts of the bridge such as towers. Therefore, wind loads acting on only the deck of the bridge are considered in the framework of the RVBW system as in Xu and Guo (2003), Cai and Chen (2004), and Cheung and Chan (2010). This approximation is also taken in this study and wind loads on only the bridge deck are applied. The wind loads on a bridge deck are usually decomposed according to the nature of wind induced forces as three components: static wind loads, buffeting loads and self-excited loads:

$$\mathbf{F}_b^W = \mathbf{F}_{bst}^W + \mathbf{F}_{bfl}^W + \mathbf{F}_{bse}^W \tag{6.14}$$

where $\mathbf{F}_{bst}^W$, $\mathbf{F}_{bfl}^W$, and $\mathbf{F}_{bse}^W$ represent the vector of the static wind loads, buffeting loads and self-excited loads acting on the nodes of the bridge deck, respectively. In this study, the wind loads on the each node are integrated from the wind loads on the section of deck along half length/lengths of the element/elements possessing the node.

6.4.1 Static Wind Loads

Static wind loads are the forces due to the mean winds. Figure 6.1 illustrates the cross section on a pure deck (pure deck in this study means deck without vehicles on it). A local coordinate system $x_d o_d y_d$ is attached on the deck cross section with its origin on the centriod of the deck cross section, the x_d-axis and y_d-axis along the horizontal and vertical directions of the deck cross section. The static wind loads on the deck cross section are composed by the drag force F_{Dst}^{W} along the x_d-axis, lift force F_{Lst}^{W} along the y_d-axis and the moment F_{Mst}^{W} around o_d. They can be expressed as:

$$F_{Dst}^{W} = \frac{1}{2}\rho U^2 C_D\left(\alpha_{wd}\right)B \tag{6.15a}$$

$$F_{Lst}^{W} = \frac{1}{2}\rho U^2 C_L\left(\alpha_{wd}\right)B \tag{6.15b}$$

$$F_{Mst}^{W} = \frac{1}{2}\rho U^2 C_M\left(\alpha_{wd}\right)B^2 \tag{6.15c}$$

where ρ is the air density; U is the mean wind velocity; B is the width of deck; C_D, C_L, and C_M are the non-dimensional static aerodynamic coefficients of drag, lift, and moment on the pure deck, respectively. The aerodynamic coefficients of the deck are the function of wind angle of attack, α_{wd} , to the deck.

In the previous RVBW analyses (Xu and Guo, 2003; Cai and Chen, 2004; and Cheung and Chan, 2010), the aerodynamic coefficients of a pure deck without taking into account the effects of the moving road vehicle were adopted. In Chapter 5, the aerodynamic coefficients of a bridge deck under a road vehicle are computed. They vary with not only the locations of the vehicle d_v on the deck, but also the relative angle between the velocity of the vehicle and the winds α_{vw}. The aerodynamic loads acting on the deck have to be rewritten to include the effects of the moving vehicle as follows:

$$F_{ist}^{W} = \frac{1}{2}\rho U^2 C_{iv}\left(\alpha_{wd}, \alpha_{wv}, d_v\right)B \qquad i=D, L, M \tag{6.16}$$

where C_{iV} is the modified static aerodynamic coefficient, considering the effects of the moving vehicle on the bridge deck. It is assumed that the effects of the moving vehicle on the static aerodynamic coefficients of the deck alter very slightly with the attack angle of wind. C_{iV} can thus be approximated as:

$$C_{iv}\left(\alpha_w,\alpha_{vw},d_v\right)\approx C_i\left(\alpha_{wd}\right)R_i\left(\alpha_{wv},d_v\right) \tag{6.17}$$

where R_i can be denoted as the influence factor of the moving vehicle on the static aerodynamic coefficients of the deck and it is the function of d_v and α_{wv}.

Figure 5.22 shows the calculated C_{iV} of the deck under a moving vehicle of different moving speeds. It is very difficult to draw an explicit expression for C_{iv}. A simple way is used to identify the influence factor R_i through a process of Standardization and Segmental Averaging (SSA for short). This procedure involves the following steps.

(a) Dividing segments

The aerodynamic coefficients of the bridge deck under and near the vehicle actually vary with location. The deck under the vehicle is, therefore, divided into several segments. Three equal segments are set for the deck right under the vehicle. The length of each segment is $L_v/3$ (with L_v is the length of the vehicle). Since the influenced range of the vehicle on the aerodynamic coefficients of the deck is mainly within a length about 7 times the length of the vehicle, thus, totally 21 segments are set for the deck influenced by the vehicle. The segments are numbered with j=-10, -9…9, 10 from left to right and j=-1, 0 and 1 are the position of the vehicle (see Figure 6.2 for the drag coefficients at α_{wv}=60°).

(b) Averaging aerodynamic coefficients

The averaged aerodynamic coefficient of the jth segment C_{iVj} is to represent the coefficient of the entire segment, and it can be obtained by averaging:

$$C_{ivj}=\frac{3}{L_v}\int_j C_{iv}dz \tag{6.18}$$

As an example, the solid line in Figure 6.2 shows C_{Dvj} at α_{wv}=60°.

(c) Standardization

The aerodynamic coefficient C_i of the bridge deck being not influenced by the vehicle can be taken as the average value of the aerodynamic coefficients of the two end segments as:

$$C_i = \frac{1}{2}(C_{iVj}\big|_{j=-10} + C_{iVj}\big|_{j=10}) \tag{6.19}$$

The influence factor R_i of the jth segment can thus be calculated as:

$$R_{ij} = \frac{C_{iVj}}{C_i} \tag{6.20}$$

Through the process of SSA, the aerodynamic coefficients of the bridge deck varying with the location of the vehicle can be obtained for each relative yaw angle α_{wv}. For each segment, the influence factor R_i is fitted with α_{wv} based on the CFD results at 30°, 60°, and 90° using the second order polynomials as follows:

$$R_{ij}\left(\alpha_{wv}\right) = C_{ij0} + C_{ij1}\alpha_{wv} + C_{ij2}\alpha_{wv}{}^2 \tag{6.21}$$

where C_{ij0}, C_{ij1}, and C_{ij2} are the fitting constants and listed in Tables 6.1 to 6.3. For illustration, R_{D0} at α_{wv} =30°, 60°, and 90° and the fitted curve are shown in Figure 6.3.

6.4.2 Buffeting Loads

Buffeting loads are the forces induced by the fluctuations of incoming winds. Corresponding to the three directions of the local coordinate system of the deck , the buffeting loads are decomposed as the buffeting drag force F^W_{Dbl} along the x_d-direction, buffeting lift force F^W_{Lbl} along the y_d-direction, and the moment F^W_{Mbl} around the origin o_d. Based on the quasi-steady theory, they are expressed as (Scanlan, 1978b):

$$F^W_{Dbl}(t) = \frac{1}{2}\rho U^2 B\left[2C_D(\alpha_{wd})\chi_{Du}\frac{u(t)}{U} + C_D^{'}(\alpha_{wd})\chi_{Dw}\frac{w(t)}{U}\right] \tag{6.22a}$$

$$F_{Lbl}^{W}(t)=\frac{1}{2}\rho U^{2}B\left[2C_{L}(\alpha_{wd})\chi_{Lu}\frac{u(t)}{U}+\left(C_{L}^{'}(\alpha_{wd})+C_{D}(\alpha_{wd})\right)\chi_{Lw}\frac{w(t)}{U}\right] \quad (6.22b)$$

$$F_{Mbl}^{W}(t)=\frac{1}{2}\rho U^{2}B^{2}\left[2C_{M}(\alpha_{wd})\chi_{Mu}\frac{u(t)}{U}+C_{M}^{'}(\alpha_{wd})\chi_{Mw}\frac{w(t)}{U}\right] \quad (6.22c)$$

where $C_{i}^{'}(\alpha_{wd})$ (i=D, L, and M) is the slope of $C_{i}(\alpha_{wd})$; $u(t)$ and $w(t)$ are the fluctuating wind speeds along, and perpendicular to, the mean wind direction and can be simulated using the modified spectral representation method (see Section 4.3.1); χ_{Lu}, χ_{Lw}, χ_{Pu}, χ_{Mu}, χ_{Mw} are the aerodynamic admittance functions.

The aerodynamic coefficients in Equation 6.22 are for a pure deck without the influence of vehicles. If considering the aerodynamic coefficients of the deck under moving vehicles, $C_{i}(\alpha_{wd})$ shall be replaced by $C_{i}\left(\alpha_{wd}\right)R_{i}\left(\alpha_{wv},d_{v}\right)$. As a result, the fluctuating loads expressed by Equation 6.22 are updated as follows:

$$F_{Dbl}^{W}(t)=\frac{1}{2}\rho U^{2}BR_{i}\left(\alpha_{wv},d_{v}\right)\left[2C_{D}(\alpha_{wd})\chi_{Du}\frac{u(t)}{U}+C_{D}^{'}(\alpha_{wd})\chi_{Dw}\frac{w(t)}{U}\right] \quad (6.23a)$$

$$F_{Lbl}^{W}(t)=\frac{1}{2}\rho U^{2}BR_{i}\left(\alpha_{wv},d_{v}\right)\left[2C_{L}(\alpha_{wd})\chi_{Lu}\frac{u(t)}{U}+\left(C_{L}^{'}(\alpha_{wd})+C_{D}(\alpha_{wd})\right)\chi_{Lw}\frac{w(t)}{U}\right] (6.23b)$$

$$F_{Mbl}^{W}(t)=\frac{1}{2}\rho U^{2}B^{2}R_{i}\left(\alpha_{wv},d_{v}\right)\left[2C_{M}(\alpha_{wd})\chi_{Mu}\frac{u(t)}{U}+C_{M}^{'}(\alpha_{wd})\chi_{Mw}\frac{w(t)}{U}\right] \quad (6.23c)$$

6.4.3 Self-Excited Loads

Self-excited loads are the forces induced by the movement of the deck. Similar to the static and fluctuating wind loads, the self-excited loads on the cross section of a pure deck can be decomposed as three components: self-excited drag force F_{Dse}^{W} along the x_d-direction, self-excited lift force F_{Lse}^{W} along the y_d-direction, and self-excited moment F_{Mse}^{W} around the origin o_d. They can be expressed in the form of convolution integrals (Bucher and Lin, 1988) as follows:

$$F_{Dse}^{W}(t)=\int_{-\infty}^{t} f_{Dh}(t-\tau)h(\tau)\mathrm{d}\tau+\int_{-\infty}^{t} f_{Dp}(t-\tau)p(\tau)\mathrm{d}\tau+\int_{-\infty}^{t} f_{D\alpha}(t-\tau)\alpha(\tau)\mathrm{d}\tau \tag{6.24a}$$

$$F_{Lse}^{W}(t)=\int_{-\infty}^{t} f_{Lh}(t-\tau)h(\tau)\mathrm{d}\tau+\int_{-\infty}^{t} f_{Lp}(t-\tau)p(\tau)\mathrm{d}\tau+\int_{-\infty}^{t} f_{L\alpha}(t-\tau)\alpha(\tau)\mathrm{d}\tau \tag{6.24b}$$

$$F_{Mse}^{W}(t)=\int_{-\infty}^{t} f_{Mh}(t-\tau)h(\tau)\mathrm{d}\tau+\int_{-\infty}^{t} f_{Mp}(t-\tau)p(\tau)\mathrm{d}\tau+\int_{-\infty}^{t} f_{M\alpha}(t-\tau)\alpha(\tau)\mathrm{d}\tau \tag{6.24c}$$

where $h(\tau)$, $p(\tau)$, and $\alpha(\tau)$ are the vertical, lateral, and rotational displacements of the bridge deck at time τ; f_{ij} ($i = D, L, M$; $j = p, h, \alpha$) are the response functions of unit impulse displacement of j and can be calculated from the flutter derivatives of the pure deck as in Section 2.3.1.3. This chapter aims to evaluate the ride comfort, where the vehicle moves with a speed lower than vehicle accident velocity and wind speed is much smaller than the critical wind velocity. As a result, the resulted bridge responses are not large. Therefore, the self-excited loads on the bridge deck are also limited. In this regard, the effects of the moving vehicle on the flutter derivatives are neglected.

6.5 WIND LOADS ON A MOVING VEHICLE

Wind loads on a moving vehicle have been derived based on the quasi-steady assumption in Section 4.3 and rewritten as:

$$f_{vy}^{W}=\frac{1}{2}\rho U_{re}^{2}A_{f}[C_{S}(\alpha_{w})+C_{S}'(\alpha_{w})\beta_{w}] \tag{6.25a}$$

$$f_{vz}^{W}=\frac{1}{2}\rho U_{re}^{2}A_{f}[C_{L}(\alpha_{w})+C_{L}'(\alpha_{w})\beta_{w}] \tag{6.25b}$$

$$m_{vx}^{W}=\frac{1}{2}\rho U_{re}^{2}A_{f}L_{v}[C_{R}(\alpha_{w})+C_{R}'(\alpha_{w})\beta_{w}] \tag{6.25c}$$

$$m_{vy}^{W}=\frac{1}{2}\rho U_{re}^{2}A_{f}L_{v}[C_{P}(\alpha_{w})+C_{P}'(\alpha_{w})\beta_{w}] \tag{6.25d}$$

$$m_{vz}^{W}=\frac{1}{2}\rho U_{re}^{2}A_{f}L_{v}[C_{Y}(\alpha_{w})+C_{Y}'(\alpha_{w})\beta_{w}] \tag{6.25e}$$

with

$$U_{re}=\sqrt{U_{xe}^{2}+U_{ye}^{2}+U_{ze}^{2}} \tag{6.26a}$$

$$\alpha_w = \arctan(\frac{\sqrt{U_{ye}^2 + U_{ze}^2}}{U_{xe}}) \tag{6.26b}$$

$$\beta_w = \arctan(\frac{U_{ze}}{U_{ye}}) \tag{6.26c}$$

where ρ is the density of air; A_f is a reference area; U_{xe}, U_{ye}, and U_{ze} represent the relative wind components to the vehicle along the x-, y- and z-axis in the VCS coordinate, respectively; C_S, C_L, C_P, C_Y, and C_R are the corresponding aerodynamic coefficients. The aerodynamic coefficients of a moving vehicle on a bridge deck at different relative yaw angles have been calculated in Chapter 5. They are fitted using 3-order polynomials of α_w:

$$C_i(\alpha_w) = C_{i0} + C_{i1}\alpha_w + C_{i2}\alpha_w{}^2 + C_{i3}\alpha_w{}^3 \tag{6.27}$$

where C_{ij} (i= S, L, P, Y, R and j=0, 1, 2, 3) are the fitting constants and listed in Table 6.4. The fitted curves for the aerodynamic coefficients of the moving vehicle are shown in Figures 6.4 and 6.5.

6.6 INTERACTION OF SUBSYSTEMS

The bridge subsystem and vehicle subsystem are coupled through the contact forces and the displacement compatibility between the vehicle wheels and the bridge deck surface. The contact forces both in the vertical and lateral directions from the tires imposed on the bridge deck, causing the dynamic responses of the bridge. The displacements of the bridge deck change the moving traces of the tires, in return.

6.6.1 Contact Forces Transformed from Vehicle to Bridge

During the movement of the vehicle, the contract forces on the ith tire $(f_{wix^*}^T, f_{wiy^*}^T, f_{wiz^*}^T)^T$ counteract on the deck at the location of the tire of the magnitude $(-f_{wix^*}^T, -f_{wiy^*}^T, -f_{wiz^*}^T)^T$ in the WCS coordinate system. Through the following transformation, they are enforced on the bridge subsystem in the global system.

$$(F_{bwiX}^V, F_{bwiY}^V, F_{bwiZ}^V)^T = -\mathbf{T}_{ev}\mathbf{T}_{vwi}(f_{wix^*}^T, f_{wiy^*}^T, f_{wiz^*}^T)^T \tag{6.28}$$

where $(F_{bwiX}^{V}, F_{bwiY}^{V}, F_{bwiZ}^{V})^{T}$ is the contact forces transformed from the vehicle to the deck along the *X*-, *Y*- and *Z*-axes in the global system, respectively. The contact forces on all the tires can be assembled as $\mathbf{F}_{b}^{V}$ in Equation 6.11.

6.6.2 Geometric Compatibility between Bridge and Vehicle

The geometric contact boundaries of the moving vehicle are formed from the superposition of the displacements of the bridge deck and the road roughness. The actual surface profile Z_p under the tires can then be expressed as follows:

$$Z_{p}(X,Y) = Z_{b}(X,Y) + Z_{g}(X,Y) \tag{6.29}$$

where (*X*, *Y*) is the plane coordinate on the bridge deck with *X* points to the longitudinal direction and *Y* points to the lateral direction; Z_g is the road roughness generated, using the way described in Section 4.4; Z_b is the vertical displacement of the bridge deck, and it is expressed as the function of the vertical displacement Z_{bc} and the rotational displacement θ_{Xbc} around the *X*-axis at the central axis of the bridge deck as:

$$Z_{b}(X,Y) = Z_{bc}(X) + Y\theta_{Xbc}(X) \tag{6.30}$$

At any *X*, the displacements vector of the central axis of the bridge deck can be interpolated from the geometric displacements of the two end nodes of corresponding elements through the interpolation in terms of element shape functions as:

$$Z_{bc}(X) = \mathbf{N}_{Z}^{e}(\xi_{eX}) \begin{Bmatrix} \boldsymbol{\delta}_{bl}^{eX} \\ \boldsymbol{\delta}_{br}^{eX} \end{Bmatrix} \tag{6.31a}$$

$$\theta_{Xbc}(X) = \mathbf{N}_{\theta X}^{e}(\xi_{eX}) \begin{Bmatrix} \boldsymbol{\delta}_{bl}^{eX} \\ \boldsymbol{\delta}_{br}^{eX} \end{Bmatrix} \tag{6.31b}$$

where *eX* represents the element of the deck at the designated location *X*; ξ_{eX} is the coordinate of the location *X* referred to the node of the element *eX*; $\mathbf{N}_{Z}^{e}$ and $\mathbf{N}_{\theta X}^{e}$ are the element shape functions for the vertical and rotational displacements; $\boldsymbol{\delta}_{bl}^{eX}$

and $\boldsymbol{\delta}_{br}^{eX}$ are the left and right end nodes of the element *eX*.

The time deviation of the surface profile thus becomes

$$\dot{Z}_p(X,Y) = [\dot{Z}_{bc}(X) + Y\dot{\theta}_{Xbc}(X) + \frac{\partial Z_g}{\partial X}]\dot{X} + (\theta_{Xbc}(X) + \frac{\partial Z_g}{\partial Y})\dot{Y} \tag{6.32}$$

with

$$\dot{Z}_{bc}(X) = \frac{\partial \mathbf{N}_Z^e}{\partial X}\begin{Bmatrix} \boldsymbol{\delta}_{bl}^{eX} \\ \boldsymbol{\delta}_{br}^{eX} \end{Bmatrix}\dot{X} + \mathbf{N}_Z^e(\xi_{eX})\begin{Bmatrix} \dot{\boldsymbol{\delta}}_{bl}^{eX} \\ \dot{\boldsymbol{\delta}}_{br}^{eX} \end{Bmatrix} \tag{6.33a}$$

$$\dot{\theta}_{Xbc}(X) = \frac{\partial \mathbf{N}_{\theta X}^e}{\partial X}\begin{Bmatrix} \boldsymbol{\delta}_{bl}^{eX} \\ \boldsymbol{\delta}_{br}^{eX} \end{Bmatrix}\dot{X} + \mathbf{N}_{\theta X}^e(\xi_{eX})\begin{Bmatrix} \dot{\boldsymbol{\delta}}_{bl}^{eX} \\ \dot{\boldsymbol{\delta}}_{br}^{eX} \end{Bmatrix} \tag{6.33b}$$

The velocities of the contact point (v_{dX}, v_{dY}, v_{dZ}) at the coordinate (X, Y, Z) on the bridge deck to generate the lateral force on the tires of the vehicle (Equation 6.8) can also be determined from the responses of the deck as follows:

$$v_{dX} = \dot{X}_{bc}(X) + d_Z\dot{\theta}_{Ybc}(X) + d_Y\dot{\theta}_{Zbc}(X) \tag{6.34a}$$

$$v_{dY} = \dot{Y}_{bc}(X) + d_Z\dot{\theta}_{Xbc}(X) \tag{6.34b}$$

$$v_{dZ} = \dot{Z}_{bc}(X) + d_Y\dot{\theta}_{Xbc}(X) \tag{6.34c}$$

where d_Y, and d_Z is the relative position of the contact point to the centroid of the deck section at X; $\dot{X}_{bc}$ and $\dot{Y}_{bc}$ are the velocity of the centroid of the deck section along the X- and Y-axis, respectively; $\dot{\theta}_{Ybc}$, and $\dot{\theta}_{Zbc}$ are the angular velocity of the deck section around the Y-, and Z-axis, respectively. Similar to $\dot{Z}_{bc}$ and $\dot{\theta}_{Xbc}$ in Equation 6.33, $\dot{X}_{bc}$, $\dot{Y}_{bc}$, $\dot{\theta}_{Ybc}$, and $\dot{\theta}_{Zbc}$ can also be interpolated from the element shape function and the nodal displacement.

6.7 NUMERICAL SOLUTION

The RVBW system is seen as the combination of the vehicle subsystem and the bridge subsystem in crosswinds. Interactions occur between the two subsystems through the contact forces transformed from the vehicle and the displacement compatibility. An iterative scheme is required for the two subsystems and their coupling effects. It is summarized as follows.

1. Update the positions and attitudes of the vehicle body and wheels at the current time step $t+\Delta t$ based on their positions and velocities at the last time t. Provide the road roughness under each tire based on its position at the current time step $t+\Delta t$.
2. Calculate the vertical displacement of the bridge deck under each tire using Equation 6.31 at the iteration k. Combine the road roughness and the vertical displacement of the deck under each tire as the profile of the tire at the current iteration k+1 using Equation 6.29. Calculate the velocity of the contact point on the deck using Equation 6.34.
3. Calculate the forces received by the tires from the deck using the status of the wheels at the current iteration k+1; Produce the fluctuating crosswinds and generate wind loads on the vehicle at the current iteration k+1.
4. Update the forces on the vehicle body and wheels due to their gravity and the suspension system. Solve the equations of motion of the vehicle (Equation 6.1) using the fourth-order Runge-Kutta method to find the status of the vehicle body and tires at the iteration k+1.
5. Repeat steps 3 to 4 until the convergence for Equation 6.1 is reached.
6. Generate the forces transformed from the vehicle to the deck using Equation 6.28. Provide the wind velocity time histories and generate wind loads on the bridge deck using Equation 6.14. Solve the equations of motion of the bridge (Equation 6.11) using the Newmark-β method to find the responses of the bridge.
7. Repeat steps 2 to7 until the convergence for Equation 6.14 is reached. After this step, the procedure can be continued from step 1 for a new time step.

6.8 CASE STUDY

A long span highway cable-stayed bridge built in Mainland China is taken as an example bridge. Its elevation is shown schematically in Figure 6.6. It was designed with two towers and a main span of 688m. The cross section of the bridge (see Figure 6.7) is 34.0m wide and 3.5m high, carrying a dual two-lane highway on its upper surface. The static aerodynamic coefficients C_D, C_L, and C_M of the pure deck are computed also using CFD in Xu (2013) and shown in Figure 6.8. The aerodynamic admittance functions between the buffeting forces and the fluctuating winds are assumed as a unit. Since the geometric section of the pure deck is in a streamline form with a high ratio of width to height, the flutter derivatives of the pure deck are approximated using those of an ideal thin plate derived by Theodorsen (1935).

To compare the ride comfort of a vehicle moving on the ground, the high-sided road vehicle used in Chapter 4 is used again, but this time, it moves over the bridge deck. Generally, wind velocity on the first upwind lane is larger than that on the other lanes. The high-sided vehicle is thus located in Lane 1 (see Figure 6.7) in the upwind direction. The vehicle moves with a moderate speed of 60km/h under the crosswinds of a 10m/s mean speed. To obtain stable responses, the vehicle starts at 277.8m away from the left end of the bridge (see Figure 6.9). It then moves on the bridge deck at 16.668s, reaches the middle span of the bridge at 57.947s, and finally gets out of the bridge deck at 99.227s. The road roughness is Class B and simulated in plane. The constant pair (λ_1, λ_2) for the driver model in Equation 6.5 is determined in Section 4.7.1.3 and the moderate value of (0.2, 0.7) is used. The first and second modes of vibration of the bridge are used to determine the damping constants in Equation 6.13 for the bridge with the mode damping ratio ξ_1=ξ_2=1%. Figures 6.10 to 6.12 show the first mode shape of the bridge in the lateral bending (0.196Hz), vertical bending (0.243HZ) and torsion (1.024Hz), respectively. In the dynamic responses calculation of the RVBW system, the time is advanced with a time step of 0.001s.

6.8.1 Dynamic Responses of Bridge

Figure 6.13 shows the lateral and vertical displacements of the middle span of the bridge deck. Since the drag coefficient of the deck and the side coefficient of the moving vehicle are positive, the lateral wind forces (including the mean wind force) acting on the deck and transformed from the vehicle, and accordingly the resulted lateral displacements, are all positive. It can be seen from Figure 6.13 that as the vehicle moves to the middle span (about 57.9s), the vertical displacement of the bridge deck at the middle span reaches the maximum value (the absolute value) while it reaches the minimum value when the vehicle moves at the middle positions of the two side spans. The predominant frequency of the translational displacement response in the lateral and vertical direction is consistent with the first natural frequency in the lateral bending and vertical bending, respectively. Figure 6.14 shows the torsional angle of the section at the middle span of the bridge deck. As the vehicle approaches the middle span, the torsional angle reaches the maximum value (absolute value). The negative angle of the bridge deck at the middle span is due to the location of the vehicle being on the first lane of the bridge. The predominant frequency of the torsional angle is consistent with the first natural frequency of torsional vibration of the bridge. For a single vehicle passing over the bridge, all the maximum displacements of the bridge at its middle span are small.

6.8.1.1 Effects of Vehicle Aerodynamic Coefficients

In the previous study of the RVBW system, the aerodynamic coefficients of the road vehicle on the ground were used. It is meaningful to compare the dynamic responses of the bridge deck using the aerodynamic coefficients of the vehicle on the ground computed in Chapter 3 and the aerodynamic coefficients of the moving vehicle on the deck computed in Chapter 5. Figure 6.15 and Figure 6.16 show the comparative results of the translational displacements and torsional angle of the bridge at the middle span. It can be seen that there are only slight differences in both the translational and angular displacements for the bridge at the middle span by using the two types of aerodynamic coefficients. Of course, it is noted that only one vehicle is considered here.

6.8.1.2 Effects of Deck Coefficients Influenced by Vehicle

In the previous study of the RVBW system, the aerodynamic coefficients of the bridge under moving vehicles were approximated using those of the pure deck. The uncertainty analysis of this approximation has not been investigated. It is necessary to compare the dynamic responses of the bridge deck using the aerodynamic coefficients of the pure deck and the aerodynamic coefficients with the influence of moving vehicles. Figure 6.17 and Figure 6.18 show the translational displacements and torsional angle of the bridge at the middle span, respectively. Again, there are only slight differences in the translational displacements for the bridge at the middle span by using the two types of aerodynamic coefficients. However, if the aerodynamic coefficients of the deck under a moving vehicle instead of those of the pure deck are used, the torsional angle of the bridge deck at the middle span becomes much larger and vibrates when the vehicle approaches the middle span. This is mainly because the moment coefficient of the deck under a moving vehicle is larger than that of the pure deck.

6.8.1.3 Combined Effects of Aerodynamic Coefficients of Both Deck and Vehicle

In the previous study of the RVBW system, the aerodynamic coefficients of the bridge under moving vehicles were approximated using these of the pure deck, and at the same time, the aerodynamic coefficients of the vehicle were approximated using those of the vehicle on the ground. The actual aerodynamic coefficients of both the bridge deck and the moving vehicle are studied in this thesis, and therefore, the uncertainty analysis of the approximation can be investigated. Figure 6.19 and Figure 6.20 show the translational displacements and torsional angle of the deck at the middle span, respectively. Again, there are only slight differences in the translational displacements for the bridge at the middle span by using the two types of aerodynamic coefficients. However, if the actual aerodynamic coefficients of both the deck and the moving vehicle are used, the torsional angle of the bridge deck at the middle span becomes much larger and vibrates when the vehicle approaches the middle span.

6.8.2 Dynamic Responses of Vehicle

By using the aerodynamic coefficients of the moving vehicle on the bridge deck and those of the deck with the influence of the moving vehicles, the dynamic responses of the high-sided vehicle moving on the bridge deck are calculated. Figure 6.21 and Figure 6.22 show the lateral displacement and yaw angle, respectively, of the vehicle body in the ECS coordinate system as the vehicle moves on the bridge deck. Obvious lateral and yawing motions of the vehicle can be observed for the vehicle under the combined action of crosswinds, driver, and bridge motion.

Figure 6.23 shows the vertical displacement of the gravity centre of the vehicle body in the ECS coordinate system as the vehicle moves on the bridge deck. Apart from the fluctuating components, the vertical displacement of the vehicle is consistent with the vertical displacement of the bridge deck under the vehicle. Generally, the vertical displacement of the deck reaches valleys when the vehicle moves on the middle section of each span. This can be observed in the vertical displacement of the vehicle body at about 27s, when the vehicle moves to the middle section of the left side span, at about 57.9s, when the vehicle moves to the middle section of the main span, and at about 88.9s, when the vehicle moves to the middle section of the right side span.

Figures 6.24 and 6.25 show the roll and pith angles, respectively, of the vehicle body as the vehicle moves on the bridge deck. Although their magnitudes are very small, they vary in high frequency mainly due to the road roughness and the crosswinds. Figure 6.26 and Figure 6.27 display the acceleration responses at the seat of the driver in the lateral and vertical directions, respectively, as the vehicle moves on the deck. The fluctuating magnitude of acceleration in the lateral direction is similar to that in the vertical direction. Figure 28 and Figure 6.29 show the amplitude spectrums of the acceleration responses at the seat of the driver. Similar to the vehicle moving on the ground, peaks occur at the natural rotating frequency and steer angle frequency in the lateral direction while peaks occur at the natural vertical frequency in the vertical direction. Moreover, small bulges can be found in the amplitude spectrum of acceleration response in the lateral direction in low frequency range, which corresponds to the natural frequency of the bridge in the lateral direction.

6.8.2.1 Effects of Vehicle Aerodynamic Coefficients

This chapter mainly concentrates on the ride comfort analysis of the high-sided road vehicle moving on the bridge. Therefore, the focus is on the acceleration responses at the driver's seat. Figure 6.30 and Figure 6.31 show the rms acceleration responses at the driver's seat in both lateral and vertical directions on octave third band. The two types of aerodynamic coefficients are used, and their results are compared with each other: one uses the aerodynamic coefficients of the vehicle on ground, and the other uses the aerodynamic coefficients of the vehicle moving on the deck. In both the lateral and vertical directions, the rms acceleration responses obtained using the aerodynamic coefficients of the moving vehicle on the deck are at the same level with those using the aerodynamic coefficients of the stationary vehicle on the ground.

6.8.2.2 Effects of Deck Coefficients Influenced By Vehicle

Similar to Section 6.8.1.2, Figure 6.32 and Figure 6.33 show the rms acceleration responses at the driver's seat in both lateral and vertical directions on octave third band by using the two types of aerodynamic coefficients of the bridge deck: one uses the aerodynamic coefficients of the deck under the moving vehicles and the other uses the aerodynamic coefficients of the pure deck. It can be seen from the figures that there are no obvious differences between the two cases.

6.8.2.3 Combined Effects of Aerodynamic Coefficients of Both Deck and Vehicle

Parallel to Section 6.8.1.3, Figure 6.34 and Figure 6.35 show the rms acceleration responses at the driver's seat in both lateral and vertical directions on octave third band by using the two types of aerodynamic coefficients: one uses the aerodynamic coefficients of the deck under the moving vehicles and the aerodynamic coefficients of the moving vehicle with the influence of the bridge deck; the other uses the aerodynamic coefficients of the pure deck and the aerodynamic coefficients of the vehicle on the ground, as done in the previous studies. It can be seen that in both lateral and vertical directions, the rms acceleration responses obtained using the actual aerodynamic coefficients of both the moving vehicle and the deck are at the same level with those using the approximate aerodynamic coefficients at a few dominant frequencies.

6.8.3 Ride Comfort Evaluation and Comparison with Ground Condition

By employing the proposed dynamic analysis system of the RVBW with the actual aerodynamic coefficients of the moving vehicle on the deck and the deck under the moving vehicle, the ride comfort of the high-sided vehicle is evaluated and compared with that of the same vehicle moving on the ground, as discussed in Chapter 4. The vehicle moves with speeds from 20km/h to 100km/h at an interval of 10km/h under the fluctuating crosswinds of a mean speed of 10m/s. Figure 6.36 shows the FWRMSA results of the vehicle in the lateral direction, the vertical direction and the results for the two cases: the vehicle on the bridge and the vehicle on the ground. It can be seen that in the vertical direction, the ride comfort of the vehicle gets worse with the increase of the speed of the vehicle moving on either ground or bridge, in general. Compared with the vertical direction, in the lateral direction, the ride comfort of the vehicle gets worse with the increasing vehicle speed until about 50km/h, and then the ride comfort becomes relatively stable with the further increase of vehicle speed. The total ride comfort has the same tendency as the vertical one, indicating that the vertical acceleration response of the vehicle dominates the ride comfort. Slight differences exist in the ride comfort of the single vehicle moving on the ground and the bridge deck.

6.9 SUMMARY

In this chapter, the advanced road vehicle model, considering the road roughness in plane, the lateral motion of the vehicle and the driver's behavior, is incorporated into the framework of the coupled RVBW system for the ride comfort analysis. The wind loads on both the moving vehicle and the bridge deck are updated with the computed aerodynamic coefficients, considering mutual interference between the bridge deck and the moving vehicle, in order to more realistically evaluate the ride comfort of the moving road vehicle on the bridge. Based on the results from the case studies of the high-sided road vehicle on the first upwind lane moving over a long span bridge, the conclusions in this chapter can be summarized as follows:

- The feasibility of the established framework of the RVBW system for the response analysis of a bridge is confirmed in terms of a case study. The lateral and vertical displacements and the torsional angle of the bridge deck at the middle span reach their maximum/minimum values as the high-sided vehicle moves at the middle span. The predominant frequencies of the bridge responses are consistent with the corresponding natural frequencies of the bridge.

- For a single high-sided road vehicle passing by a long span bridge, there are only slight differences in the vertical and lateral responses of the bridge deck when either using the aerodynamic coefficients of the moving vehicle on the deck or using the aerodynamic coefficients of the moving vehicle on the ground. The torsional angular response of the bridge deck becomes larger when using the actual aerodynamic coefficients of the deck under the moving vehicle instead of those of the pure deck.

- The adoption of the aerodynamic coefficients of a road vehicle on the ground and the aerodynamic coefficients of the pure bridge deck for a single vehicle passing over the bridge deck may lead to an underestimation of the torsional angular response of the bridge. This will hamper the safety and ride comfort of the road vehicle, particularly if a group of road vehicles moving on a bridge is considered.

- The feasibility of the established framework of the RVBW system for the ride comfort analysis is also confirmed through the case study. Apart from the fluctuating components, the vertical displacement of the vehicle is consistent with the vertical displacement of the bridge deck under the moving vehicle. Obvious lateral and yaw motions of the vehicle occur under the combined action of winds, driver, and bridge motion. In the amplitude spectrums of the lateral acceleration responses at the driver's seat, spectral peaks occur at the natural rotational frequency of the vehicle as well as with the steer angle frequency of the driver; whereas in the vertical direction, spectral peaks occur at the natural vertical frequency of the vehicle. Moreover, small bulges can be found in the amplitude spectrums of the acceleration responses in a low frequency range, which corresponds to the natural frequencies of the bridge.

- As a single high-sided road vehicle passes over a long span bridge, the predicted rms accelerations at the driver's seat on octave third band are at the same level if the aerodynamic coefficients of the moving vehicle on the deck are usedas compared with the use of the aerodynamic coefficients of the road vehicle on the ground. No obvious differences in the rms accelerations responses of the vehicle are found when using the aerodynamic coefficients of the deck under a moving vehicle rather than those of the pure deck.

- The adoption of the aerodynamic coefficients of a road vehicle on the ground and the aerodynamic coefficients of the pure bridge deck for a single vehicle passing over the bridge deck may lead to the same level of the rms accelerations of the vehicle as compared with the actual aerodynamic coefficients in the situation of the moving vehicle on the deck.

- By employing the proposed dynamic analysis system of the RVBW with the actual aerodynamic coefficients of the moving vehicle on the deck and the deck under the moving vehicle, the ride comfort of the high-sided vehicle is evaluated and compared with that of the same vehicle moving on the ground. With the increase of vehicle speed, the ride comfort becomes worse. Slight differences exist in the ride comfort of the single vehicle moving on the ground and the bridge deck.

Table 6.1 Fitted coefficients for the standardized drag coefficients of the deck

j	C_{Dj0}	C_{Dj1}	C_{Dj2}
-10	0.97056	0.00067	0.00000
-9	0.88887	0.00190	-0.00001
-8	0.83544	0.00361	-0.00002
-7	0.74486	0.00647	-0.00005
-6	0.60329	0.01068	-0.00007
-5	0.47785	0.01392	-0.00010
-4	0.67574	0.00461	-0.00002
-3	0.94876	-0.00699	0.00008
-2	0.96325	-0.00876	0.00009
-1	1.01161	-0.00709	0.00005
0	1.52412	-0.02199	0.00016
1	1.27201	-0.00789	0.00004
2	1.14986	-0.00303	0.00000
3	1.21421	-0.00537	0.00003
4	1.19117	-0.00516	0.00003
5	1.14783	-0.00422	0.00002
6	1.10891	-0.00325	0.00002
7	1.07836	-0.00248	0.00001
8	1.04787	-0.00173	0.00001
9	1.02482	-0.00128	0.00001
10	1.02944	-0.00067	0.00000

Table 6.2 Fitted coefficients for the standardized lift coefficients of the deck

j	C_{Lj0}	C_{Lj1}	C_{Lj2}
-10	0.99047	1.39E-03	-1.38E-05
-9	0.89922	0.00533	-4.83E-05
-8	0.92613	0.00449	-4.19E-05
-7	1.09974	-0.0031	2.16E-05
-6	1.51699	-0.01894	1.47E-04
-5	2.3607	-0.04797	3.66E-04
-4	3.60036	-0.08547	6.31E-04
-3	3.68844	-0.09723	7.47E-04
-2	-0.86447	0.01196	6.15E-05
-1	-0.16527	0.00781	6.03E-05
0	-2.15844	0.05686	-2.34E-04
1	1.07631	-0.01442	1.46E-04
2	7.11412	-0.16767	1.07E-03
3	5.30212	-0.12675	8.68E-04
4	3.39788	-0.07581	5.41E-04
5	2.34201	-0.04584	3.39E-04
6	1.79647	-0.02983	2.28E-04
7	1.48375	-0.02039	1.62E-04
8	1.23626	-0.01256	1.06E-04
9	1.06785	-0.00652	5.91E-05
10	1.00953	-1.39E-03	1.38E-05

Table 6.3 Fitted coefficients for the standardized moment coefficients of the deck

j	C_{Mj0}	C_{Mj1}	C_{Mj2}
-10	-1.29942	0.08594	-0.00068
-9	-3.09053	0.15933	-0.00136
-8	-2.44463	0.13080	-0.00116
-7	1.17936	-0.02281	0.00004
-6	5.58286	-0.21568	0.00156
-5	9.14692	-0.37716	0.00276
-4	1.50112	-0.04778	-0.00031
-3	-17.35694	0.76042	-0.00753
-2	-26.33193	1.04345	-0.01013
-1	18.40458	-0.46866	-0.00142
0	20.47724	-0.58365	-0.00046
1	44.24917	-1.55251	0.00862
2	65.82788	-2.32117	0.01671
3	32.29070	-1.10253	0.00762
4	14.18559	-0.47326	0.00321
5	8.01115	-0.25586	0.00177
6	6.48207	-0.19848	0.00142
7	6.08941	-0.18264	0.00134
8	5.69563	-0.16792	0.00125
9	4.82348	-0.13791	0.00105
10	3.29942	-0.08594	0.00068

Table 6.4 Fitted coefficients for the aerodynamic coefficients of the vehicle

j	C_{Sj}	C_{Lj}	C_{Pj}	C_{Yj}	C_{Rj}
0	-0.00632	-0.18802	-0.07229	-0.00175	-3.32E-04
1	0.04622	0.0857	0.01254	-0.00572	-0.0041
2	0.00106	-0.00139	-2.90874E-4	-7.10E-05	-1.25E-05
3	-1.13524E-5	5.14395E-6	1.61415E-6	6.38E-07	3.31E-07

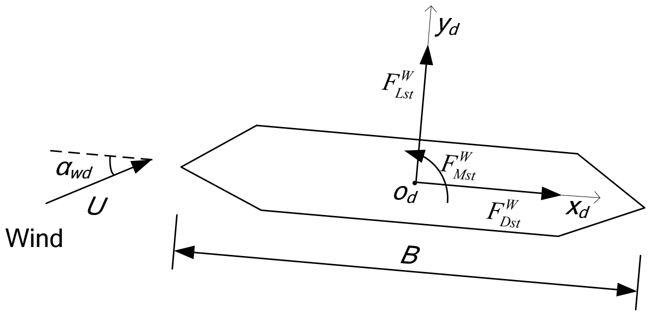

Figure 6.1 Static wind loads on the cross section of deck

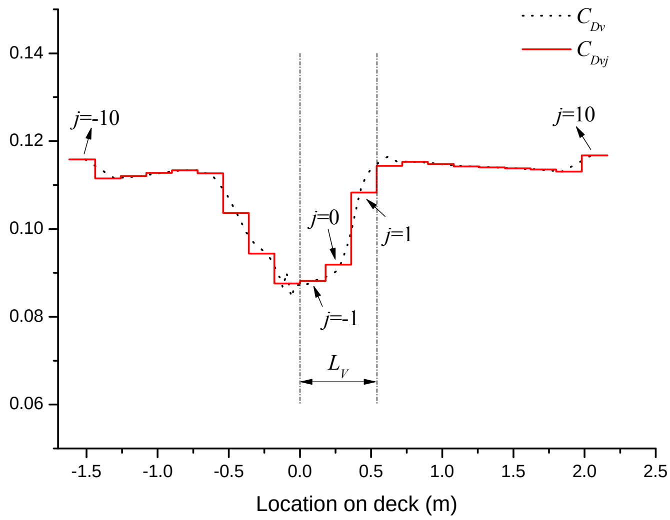

Figure 6.2 Dividing segment and averaging aerodynamic coefficient

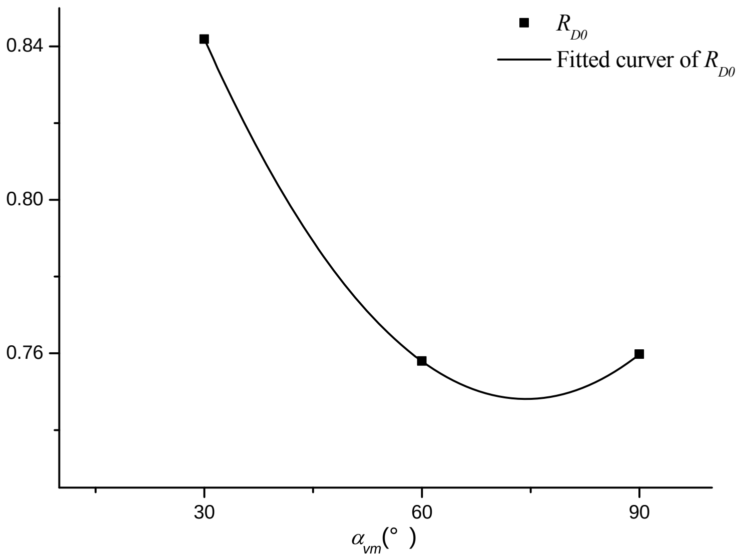

Figure 6.3 Fitted influence factor R_{D0}

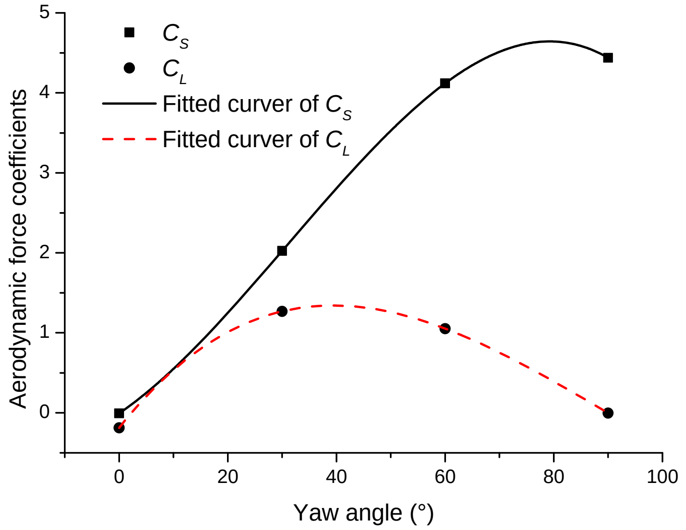

Figure 6.4 Fitted curves of the aerodynamic force coefficients

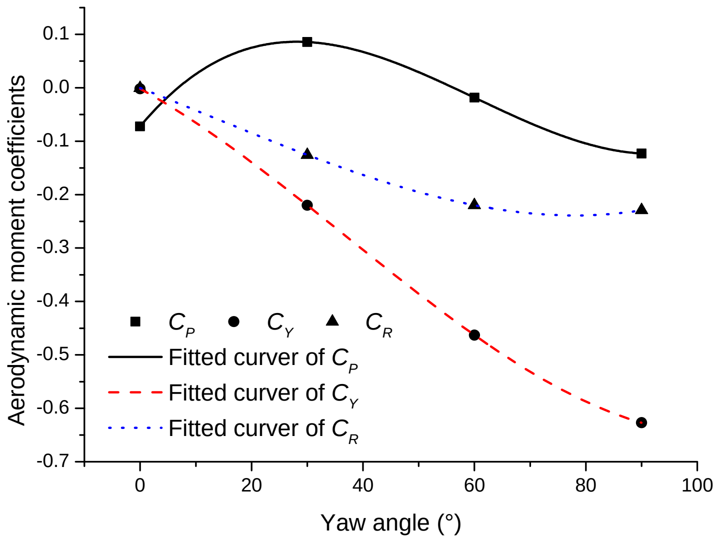

Figure 6.5 Fitted curves of the aerodynamic moment coefficients

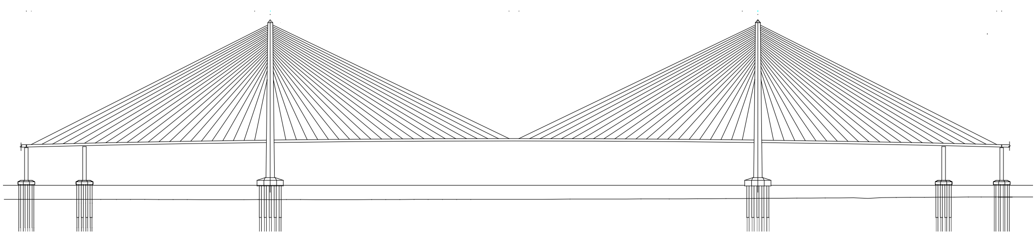

Figure 6.6 Elevation of a long span cable-stayed bridge (unit: cm)

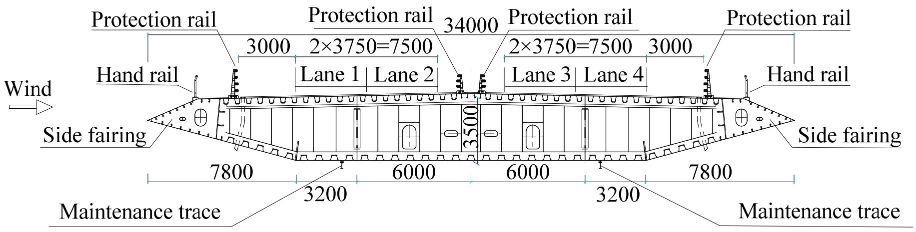

Figure 6.7 Cross section of the prototype bridge deck (unit: mm)

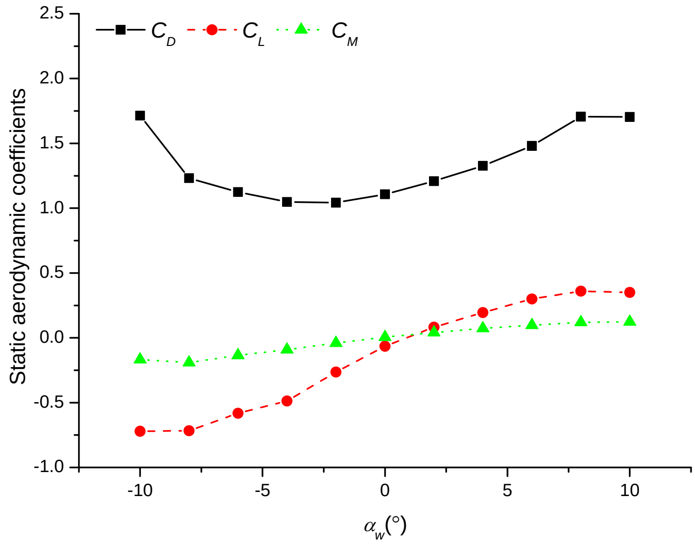

Figure 6.8 Static aerodynamic coefficients of the pure deck

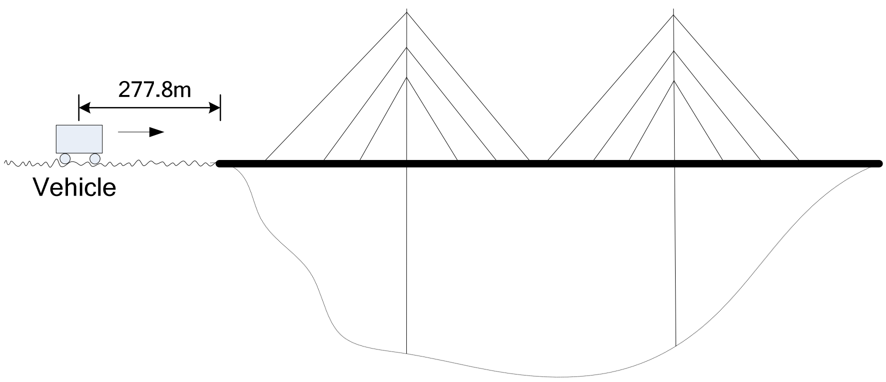

Figure 6.9 Starting position of the vehicle moving over the bridge

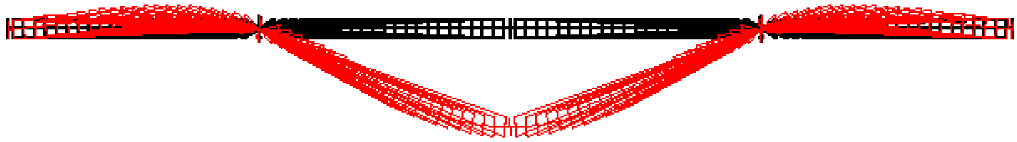

Figure 6.10 First mode shape of the lateral bending

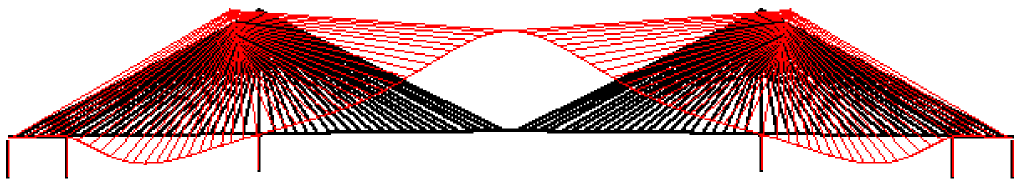

Figure 6.11 First mode shape of the vertical bending

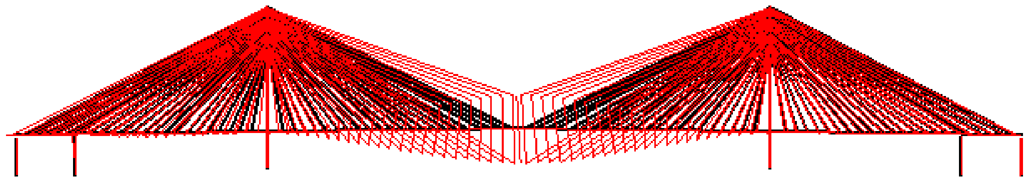

Figure 6.12 First mode shape of the torsional vibration

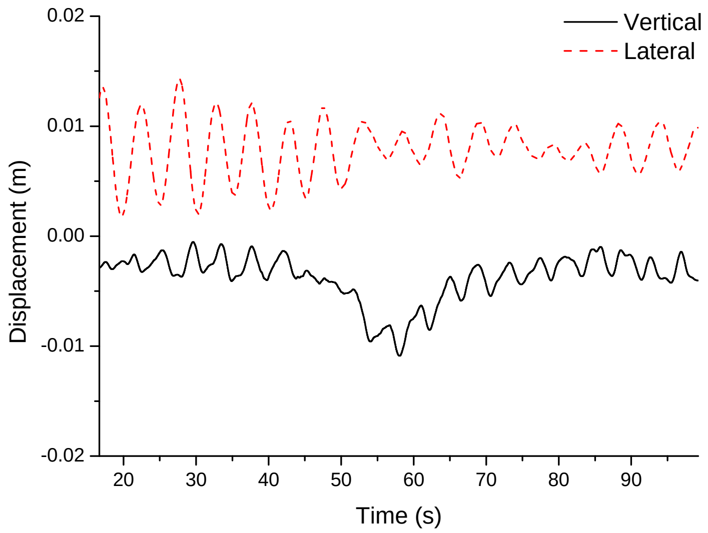

Figure 6.13 Translational displacements of the bridge in the middle span

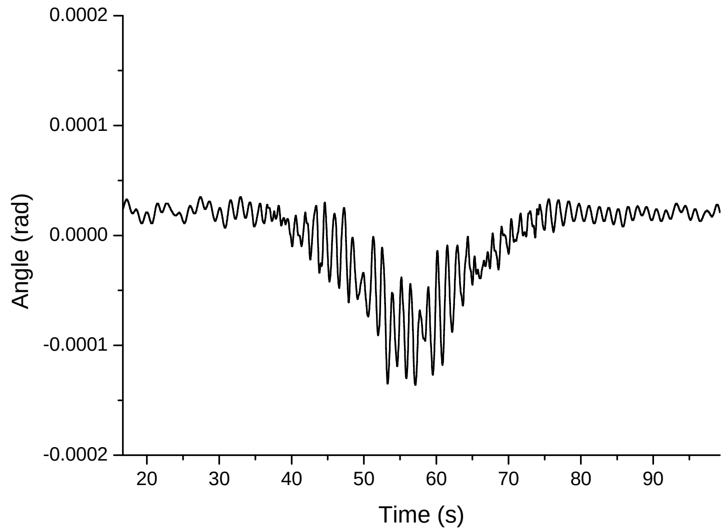

Figure 6.14 Torsional angle of the bridge in the middle span

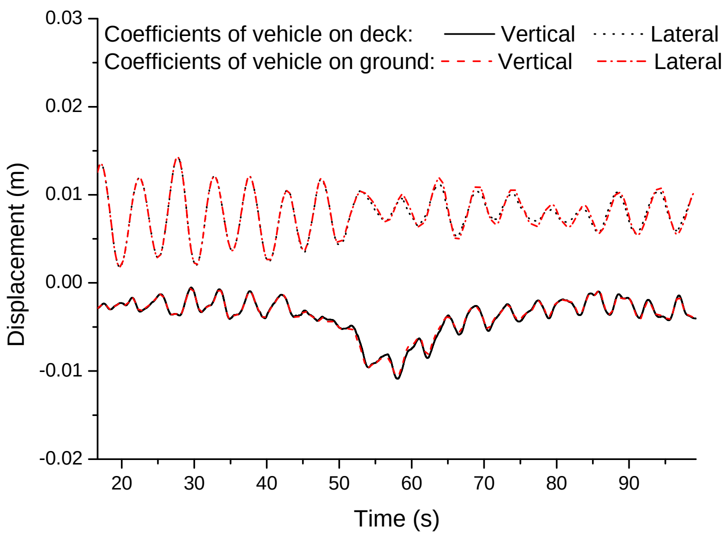

Figure 6.15 Comparison of the translational displacements of the bridge in the middle span (changing vehicle coefficients)

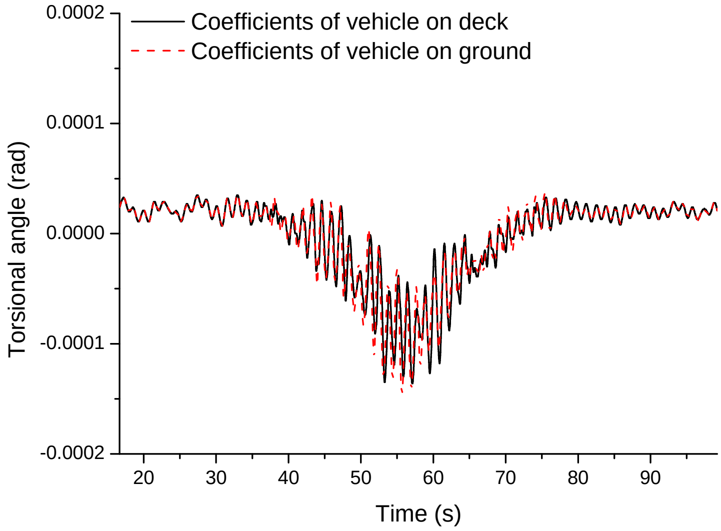

Figure 6.16 Comparison of the torsional angle of the bridge in the middle span (changing vehicle coefficients)

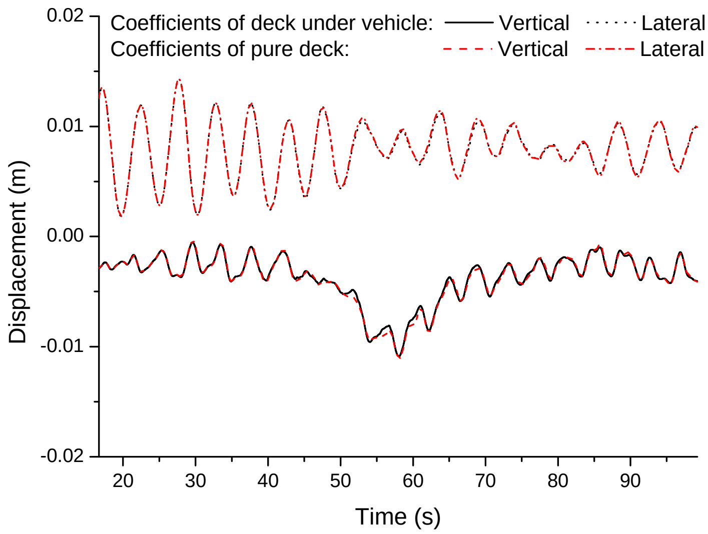

Figure 6.17 Comparison of the translational displacements of the bridge in the middle span (changing deck coefficients)

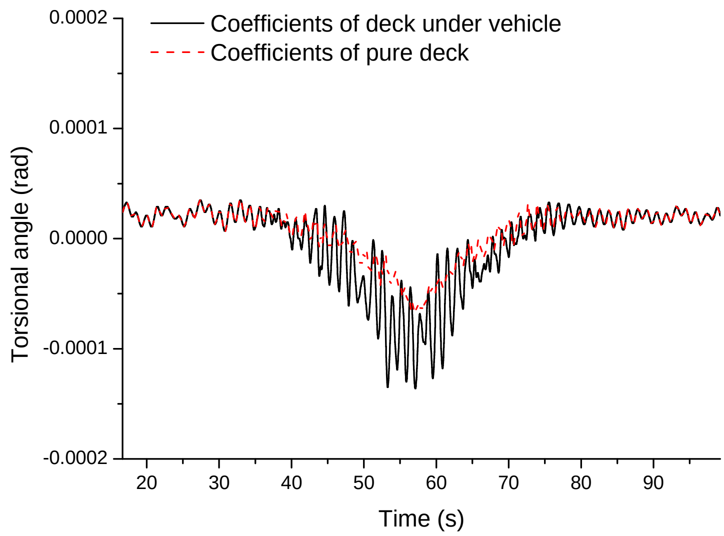

Figure 6.18 Comparison of the torsional angle of the bridge in the middle span (changing deck coefficients)

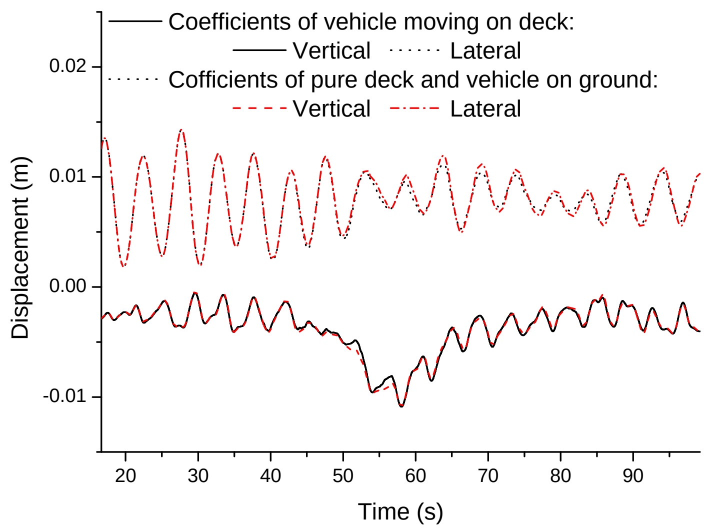

Figure 6.19 Comparison of the translational displacements of the bridge in the middle span (changing both vehicle and deck coefficients)

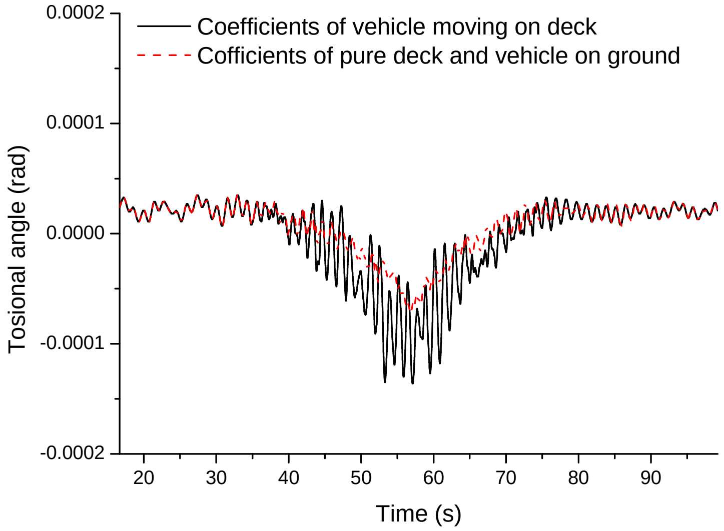

Figure 6.20 Comparison of the angular displacements of the bridge in the middle span (changing both vehicle and deck coefficients)

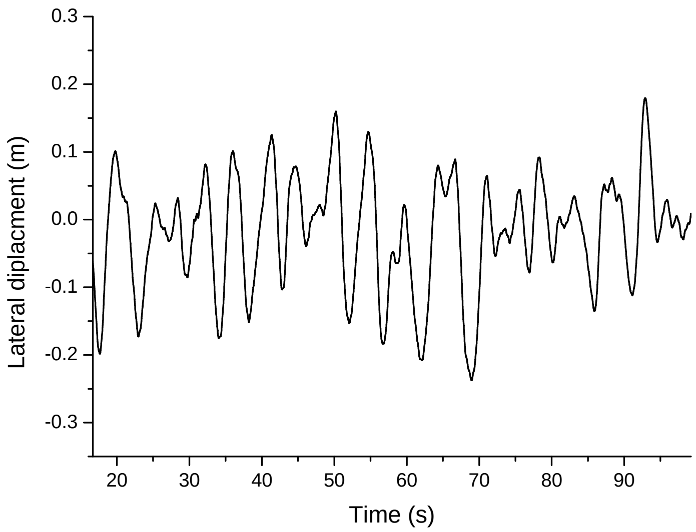

Figure 6.21 Lateral displacement of the vehicle on the deck

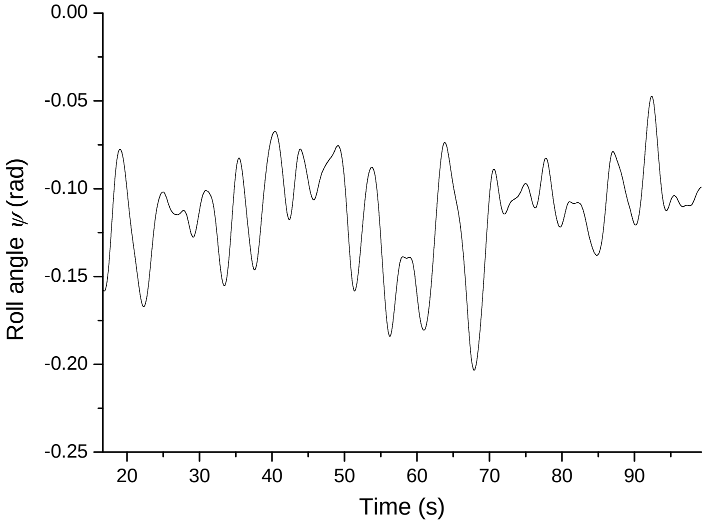

Figure 6.22 Yaw angle of the vehicle on the deck

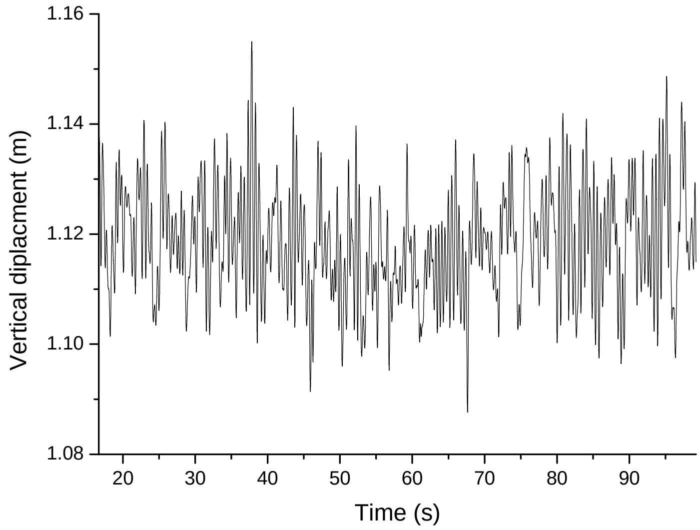

Figure 6.23 Vertical displacement of the vehicle on the deck

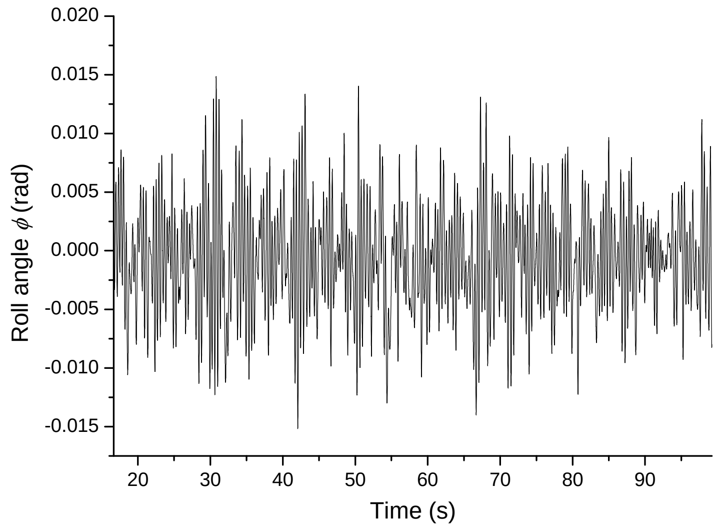

Figure 6.24 Roll angle of the vehicle on the deck

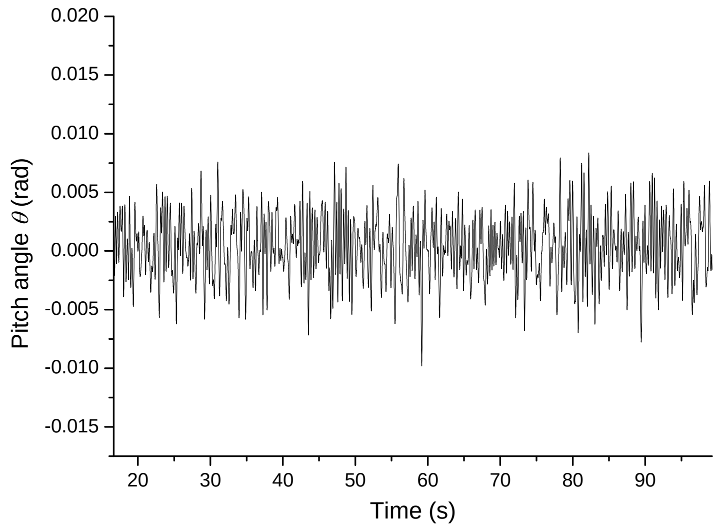

Figure 6.25 Pitch angle of the vehicle on the deck

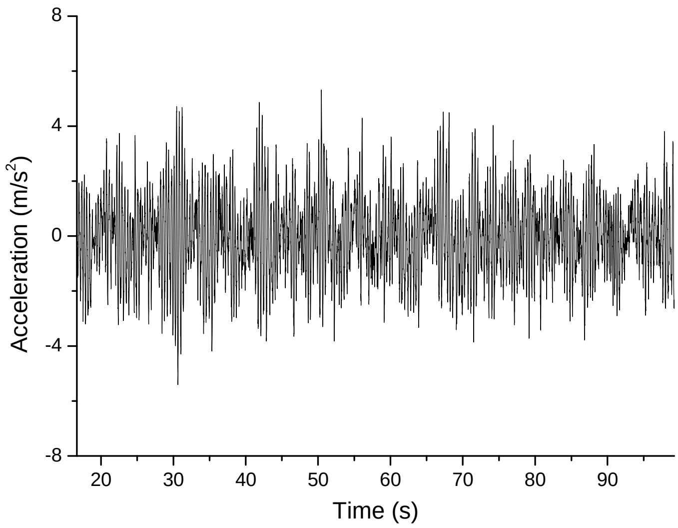

Figure 6.26 Acceleration at the driver's seat in the lateral direction

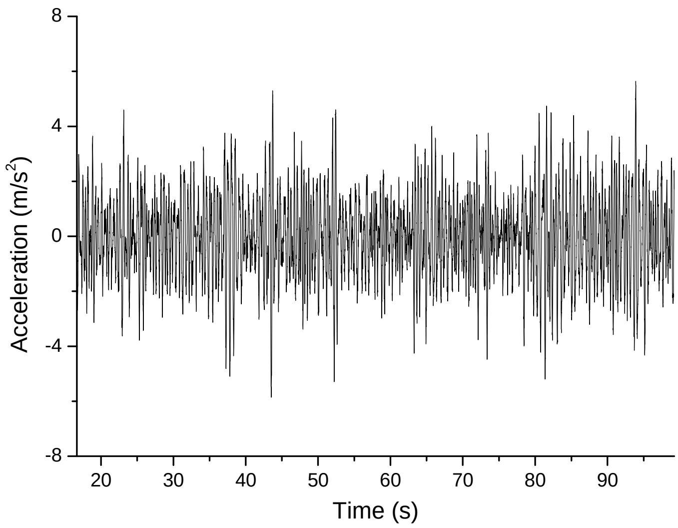

Figure 6.27 Acceleration at the driver's seat in the vertical direction

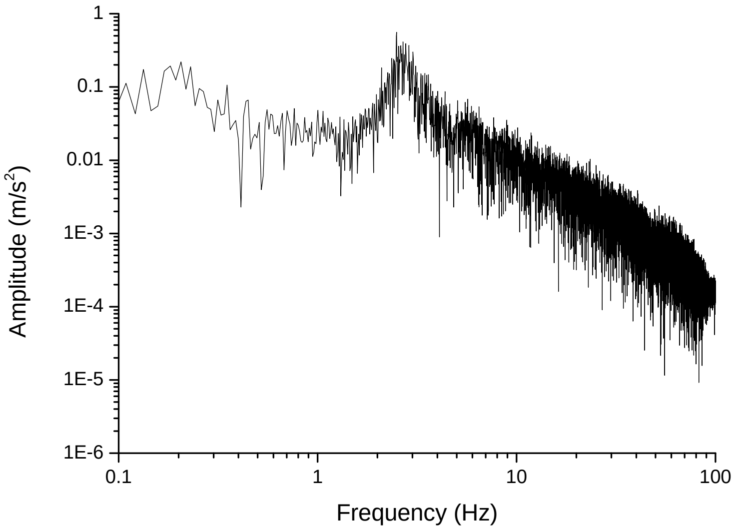

Figure 6.28 Amplitude spectrum of the acceleration at the driver's seat in the lateral direction

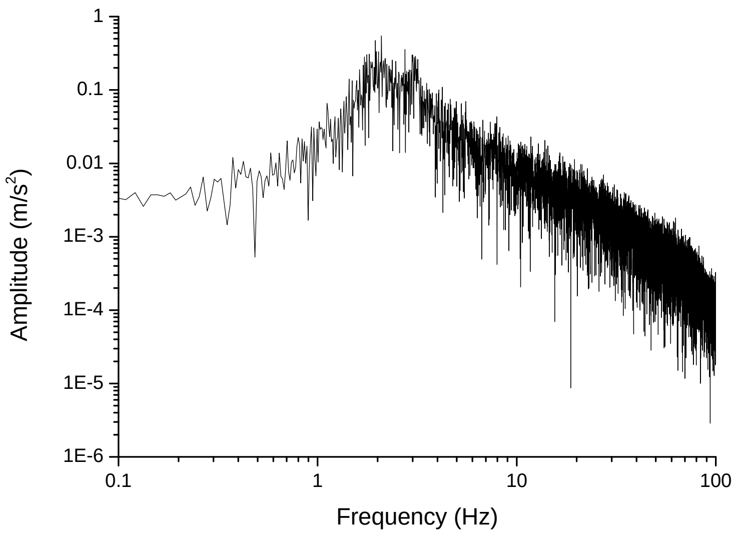

Figure 6.29 Amplitude spectrum of the acceleration at the driver's seat in the vertical direction

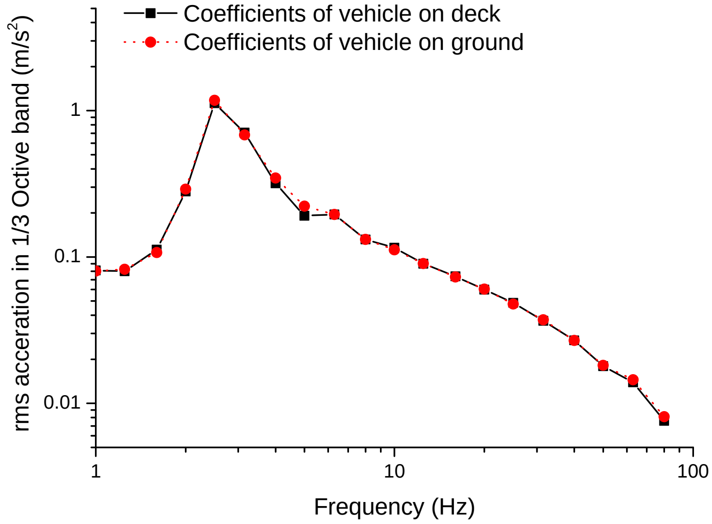

Figure 6.30 rms acceleration of the vehicle at the seat in the lateral direction

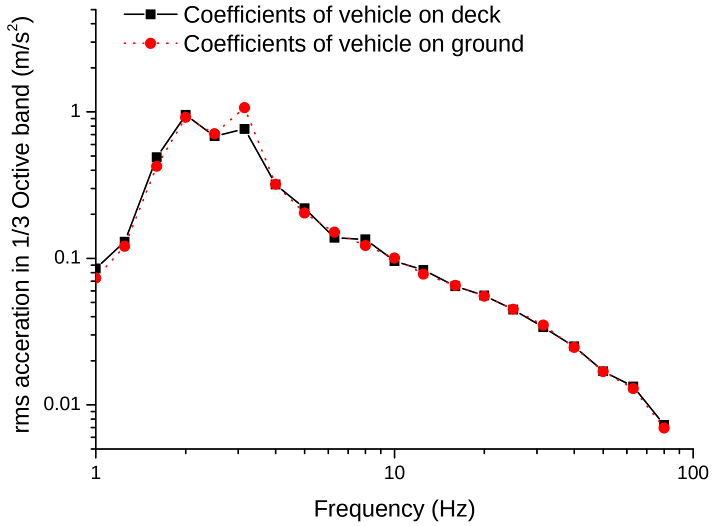

Figure 6.31 rms acceleration of the vehicle at the seat in the vertical direction

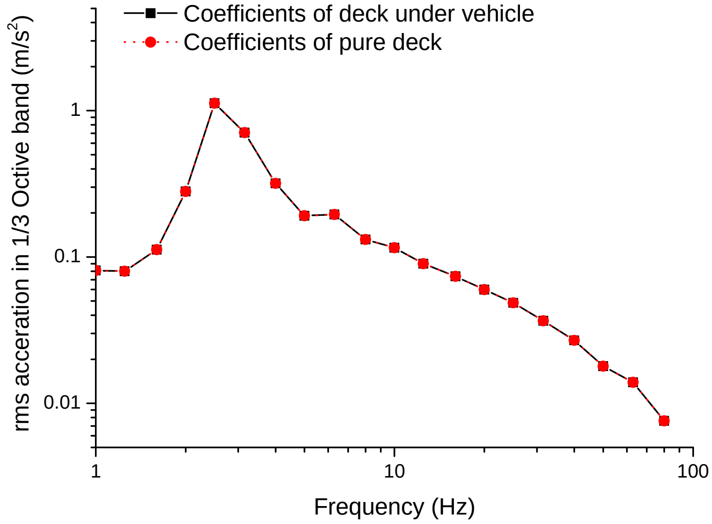

Figure 6.32 rms acceleration of the vehicle at the seat in the lateral direction

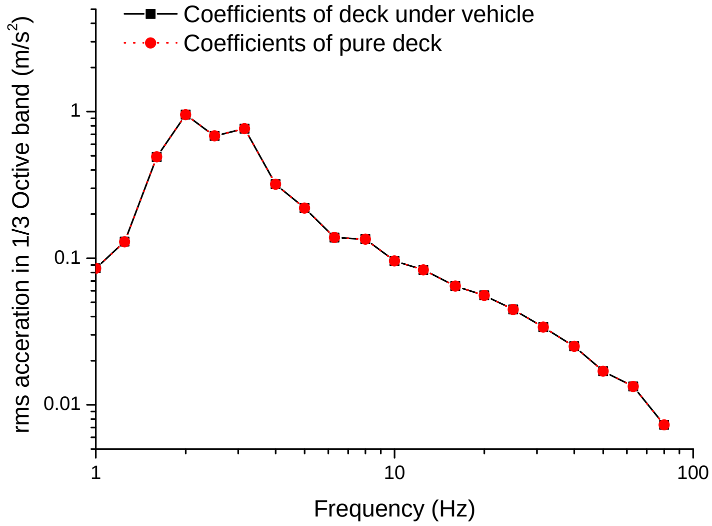

Figure 6.33 rms acceleration of the vehicle at the seat in the vertical direction

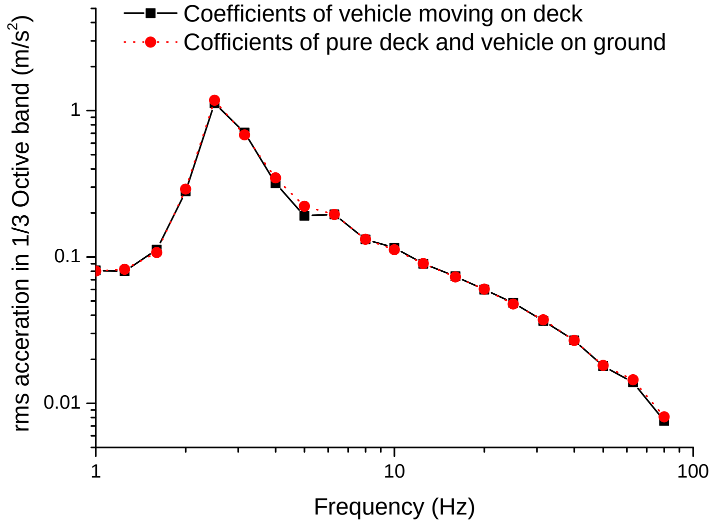

Figure 6.34 rms acceleration of the vehicle at the seat in the lateral direction

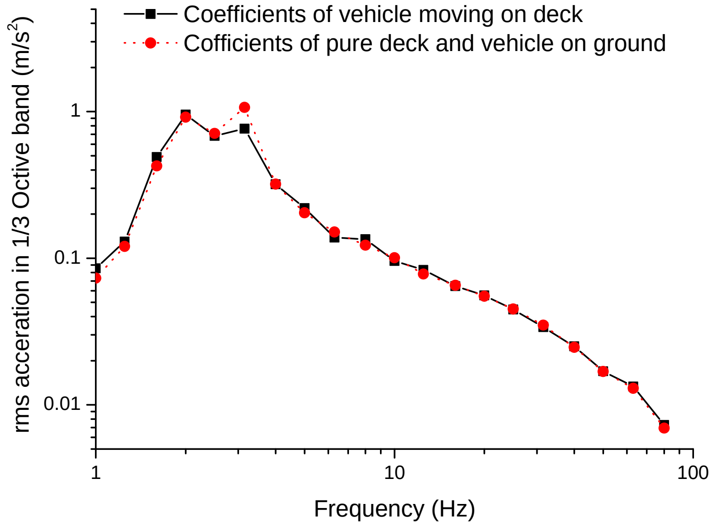

Figure 6.35 rms acceleration of the vehicle at the seat in the vertical direction

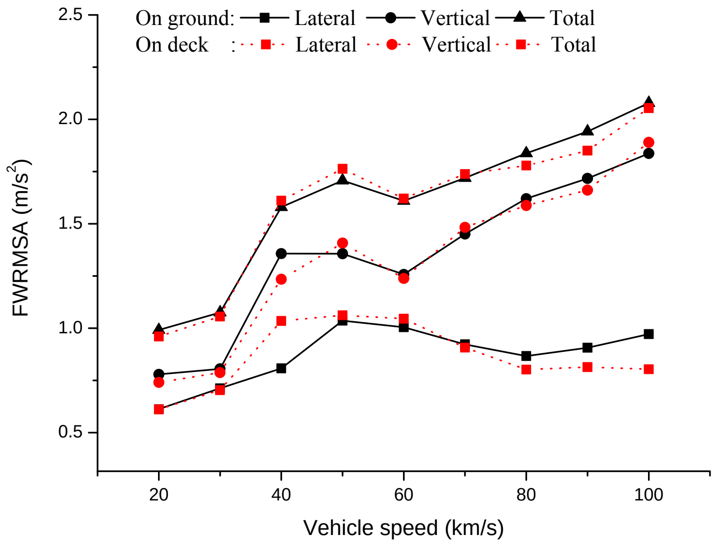

Figure 6.36 FWRMSA of the moving vehicle on bridge deck

CHAPTER 7

AERODYNAMIC FORCES ON A MOVING VEHICLE PASSING BY A BRIDGE TOWER UNDER CROSSWINDS

7.1 INTRODUCTION

The aerodynamic interferences between a moving vehicle and the ground or a bridge deck are numerically computed using Computational Fluid Dynamics (CFD) in Chapter 3 and in Chapter 5, respectively. Different from the situations on the ground and the deck, the vehicle will be shielded briefly from the crosswinds as it passes by a bridge tower. In this chapter, the varying aerodynamic forces on the moving vehicle passing by a bridge tower under crosswinds will be computed using CFD. The solved aerodynamic forces in terms of aerodynamic coefficients will be applied on the moving vehicle to study its safety as it is passing by bridge towers and be presented in Chapter 8.

As a road vehicle passes by a bridge tower under crosswinds, the vehicle will be briefly shielded from the crosswinds by the tower within a very short period of time, but when it passes out of the shelter, it enters a sharp-edged crosswind gust with the obvious danger of turning over or course deviation. However, in the previous studies about the safety of coupled road vehicle-bridge systems in crosswinds (Xu and Guo, 2003a; Cai and Chen, 2004), the aerodynamic forces on a vehicle were assumed as ideally sudden loads, without considering the real wake environment of a bridge tower as well as the interferences between the moving vehicle and the bridge tower. The aerodynamic forces on a vehicle in the wake of the bridge tower should be investigated in order to have a reliable assessment of the running safety of the vehicle.

Charuvisit *et al*. (2004) carried out wind tunnel tests to measure the side force and yawing moment of both a stationary vehicle and a moving vehicle in the wake of bridge tower models. Argentini *et al.* (2011) also performed wind tunnel tests to measure the aerodynamic forces and surface pressures on a stationary vehicle at different locations of the wake of a bridge tower. Smoke visualization was used to observe the flow patterns around the vehicle. The side coefficient, rotating moment coefficient and yawing moment coefficient were presented.

In this chapter, a lower level numerical model is applied to explore this special engineering problem as the vehicle is passing by a bridge tower using CFD for the first time. The RANS method, supplemented with SST k-ω turbulence model, is employed to investigate the aerodynamic forces (coefficients) on, flow fields around, and surface pressure distribution over, a stationary/moving vehicle passing by a bridge tower. A stationary vehicle immerged in the wake of a bridge tower is first simulated and compared with wind tunnel test results. By using the dynamic mesh method, the moving of the vehicle passing by a bridge tower is then simulated.

7.2 MODELS AND TESTED AERODYNAMIC FORCES

A vehicle-deck-tower system, composed of a deck section, a bridge tower of a long-span cable-stayed bridge (see Figure 7.1) and a high-sided articulated vehicle, is selected. The same model of the vehicle as described in Section 3.2 is adopted. The bridge deck of a flat box girder with side fairing shown in Section 5.2 is used here again. The bridge tower contains a pair of legs side by side (see Figure 7.2). The two legs are inclined from the bridge deck to both their ends with a chamfered rectangle cross section. The ratio of the vehicle length to the tower width is 1.35.

The wind tunnel tests were carried out in the TJ-3 wind tunnel of the State Key Laboratory for Disaster Reduction in Civil Engineering at Tongji University in China. The deck sectional model of a width of 1.36m and a length of 5m was manufactured for wind tunnel tests. A uniform upcoming wind was generated perpendicular to the length of the deck. The aerodynamic forces on the stationary vehicle model were measured by a force balance for three positions of the vehicle on the first upstream deck lane: Z_V=0, L_V and $2L_V$ (Z_V is the distance from the right bound of the tower to the head surface of the vehicle as shown in Figure 7.3). A gap of 1 mm was left between the vehicle model and the upper surface of the deck model to prevent the contact of vehicle wheel sets to the deck surface during tests. The details of the tests can be found in Li (2009).

As defined in Section 3.2, the measured averaged aerodynamic coefficients of the vehicle are listed in Table 7.1. From Z_V=0 to Z_V=$2L_V$, the vehicle departs from the bridge tower more and more (see Figure 7.3). The side coefficient increases, but the pitching moment coefficient decreases. The lift coefficient and the rotating moment coefficient decrease first, and then increase slightly; whereas, the drag coefficient and the yawing moment coefficient increase first, and then decrease slightly. All coefficients show a high gradient from Z_V=0 to Z_V=L_V. It is worthwhile to mention that both the side coefficient and the yawing moment coefficient have the same trend as the test results presented by Charuvisit *et al.* (2004).

7.3 NUMERIC SIMULATION OF STATIONARY VEHICLE

7.3.1 Simulation Scheme

In consideration of the complexity of the problem, this chapter considers only the averaged aerodynamic forces on the vehicle. Owing to the lower computation effort required when using RANS to solve the averaged flow, this method is used to compute the flow field numerically around the vehicle-deck-tower system. The governing equations of the unsteady RANS method have been introduced in Section 3.4.1. If the first term in Equation 3.6 is neglected, it is then called the steady RANS method with the following governing equations:

$$\frac{\partial \overline{u}_i}{\partial x_i} = 0 \tag{7.1}$$

$$\rho \overline{u}_j \frac{\partial \overline{u}_i}{\partial x_j} = -\frac{\partial \overline{p}}{\partial x_i} + \mu \nabla^2 \overline{u}_i - \frac{\partial \rho \overline{u_i' u_j'}}{\partial x_j} \tag{7.2}$$

where t is the time; x_i is the coordinate in the i^{th} axis in the Cartesian coordinate system; ρ and μ are the density and dynamic viscosity coefficient of air, respectively; u_i is the velocity component along the x_i-axis; u'_i is the fluctuation part of u_i; p is the pressure; the over bar represents the mean value; $-\rho u'_i u'_j$ is the so-called Reynolds stress represented by the SST k-ω turbulence model in this study.

In this chapter, the unsteady RANS method is used in all of the computation simulations, except for the determination of the meshing scheme, in which the steady RANS method is used to reduce the extremely demanding computational time. The governing equations are discretized using the QUICK scheme, based on the finite volume method. The SIMPLEC algorithm is employed for the coupling of velocity and pressure. The time integration is performed using the first-order implicit method. The CFD code Fluent is employed to solve these governing equations. The numerical simulation provides the pressure and shear stress distribution over the surfaces of the vehicle. The aerodynamic forces acting on the vehicle could then be acquired by integrating the pressures and the shear stresses over the surfaces. The results are accepted as convergence after 30 iterations at each time step.

7.3.2 Computational Domain and Boundary Condition

The vehicle-deck-tower model is enclosed in a computational domain with a shape of cube as shown in Figure 7.4. The sizes of the domain are identified as *Dx* along the wind direction, *Dy* vertical to the ground and *Dz* along the length direction of the bridge deck. In order to obtain the same blockage ratio (the ratio of the blockage area of the models to the cross section area of upcoming winds) as it is in the wind tunnel, the cross section perpendicular to the upcoming wind direction of the computational domain is equal to the wind tunnel, that is, *Dy*=2m and *Dz*=15m. B_d is the width of the deck. L_V and L_D are the lengths of the vehicle and the deck, respectively. They are equal to the corresponding size in the wind tunnel tests. z_V is the relative distance of vehicle to the tower. All boundaries, including the six outer boundaries and the surfaces of the vehicle, the deck and the tower are enforced with mathematic boundary conditions to approximate the experimental situation. *b_left* is the source of upcoming wind; a uniform wind speed of 10m/s, turbulence kinetic energy k of 0.05 and special dissipation ratio ω of 2 are assigned to this boundary. After the flow passes the vehicle, wind blows out of the domain through the outer boundary *b_right*. Thus, *b_right* is specified as flow outlet with zero pressure. The outer boundaries *b_head* and *b_tail* are parallel to the direction of the upcoming wind. The flows at these boundaries are assumed to be uniform and the gradients of flow variables (including wind velocity and pressure) normal to the boundaries are zero. The boundaries *b_up* and *b_down* are set as no-slip wall boundaries. The flow cannot penetrate the ground and the vehicle surfaces; hence the no-slip wall is also assigned to the deck, the tower and the vehicle surfaces.

7.3.3 Meshing

The characteristic sizes of the components of the vehicle-deck-tower system vary to a great extent, from the small size of the rails to the large size of the tower. The complex geometric shape and the large variation in the characteristic size lead to a complicated flow field around the system in both time and space domains. In order to obtain a relative adequate spatial discretization grid system corresponding to the ability of the computer, the grid optimization is performed. Since the simulation with the unsteady RANS method is time-consuming for the flow around the three-dimensional complex geometric body, the steady RANS equations enclosed with the SST two-equation turbulence model are solved during the process of grid optimization. Four meshing schemes with different grid sizes are generated for the vehicle to have a relative distance $z_V=L_V$ from the tower. In the four meshing schemes, the grid distributions over the vehicle surfaces and the height of the first layer grid near the walls remain consistent, and the grid density in the left flow regions becomes the focus. The height of the first layer grid near the vehicle's surfaces is 1×10^{-5} m, which ensured that the y^+ of the first layer grid near the walls is below 1 in the simulation. The grid distributions over the surfaces of the vehicle are shown in Figure 7.5. Totally, about 56 thousand grids are used for the vehicle surfaces. Meshing scheme 1 is the coarsest case, with 15.5 million grids, as shown in Figure 7.6. Meshing scheme 2 is generated through the refinement of the grid sizes along the direction of the deck length, while meshing scheme 3 is meshed through the refinement of the grid sizes in the plane perpendicular to the direction. Meshing scheme 4 is the result of refining the grid sizes along and perpendicular to the direction. As a result， meshing schemes 2, 3 and 4 have the grid numbers of 20.6, 22.7 and 31.8 million, respectively. The maximum y^+ on the walls of the tower, the deck and the up and down boundary faces are about 2, 5, and 5, respectively.

The steady RANS method is utilized to obtain the numerical results for the four grid systems. The mean aerodynamic coefficients obtained from the 1000 iterations after the first computation of 2000 iterations are presented in Table 7.2. The relative differences of the side coefficient and the rotating moment coefficient are within 5% for different meshing schemes. The maximum relative difference is the lift coefficient among all of these aerodynamic coefficients. For the lift coefficient, the space underneath the bottom of the vehicle is very small and the geometric shape of the bottom surface is very complex. As a result, the flows underneath the vehicle bottom and the pressure on the bottom surface are hard to predict with a high degree of accuracy in the computation simulation. The lift force, or the lift coefficient, is also hard to predict because it is caused mainly by the pressure difference between the top and bottom surfaces of the vehicle. Fortunately, lift force is less significant to the behavior of the vehicle under crosswinds compared with other force components such as side force, yawing and rotating moment. Therefore, it can be concluded that the computed aerodynamic coefficients are not too sensitive to the mesh size within the range selected; hence meshing scheme 1 is adopted with the least computational effort.

7.3.4 Time Step and Length

The time step and length for the calculation are set based on the dimensional time t^* defined in Section 3.4.4. For the case z_V=L_V, two time steps 0.1t^* and 0.05t^* are simulated to check the influence of time step on the simulation results. For all the cases of the stationary vehicle, the first 60t^* is treated as a converging process and the corresponding results are not taken into account. The next 60t^* is accepted as the time length for the normal computational results. The following results, including the aerodynamic coefficients, are all the averaged values on the last 60t^*. The streamlines, velocity contour and pressure coefficients are taken from the time at 120t^*.

The simulated aerodynamic coefficients from different time steps (0.1t^* and 0.05t^*) using the unsteady RANS method can be seen in Table 7.3. It can be seen that a time step of 0.1t^* is accurate enough compared with a shorter time step. 0.1t^* is thus selected as the time step to be used in the computation of aerodynamic forces on the stationary vehicle.

7.3.5 Numerical Simulation Results and Analysis

7.3.5.1 Flow field and surface pressure

The flow field around the vehicle is illustrated in two main planes: section 1-1 and section 2-2 as shown in Figure 3.2. Cross section 1-1 is located at the middle length of the vehicle's trailer, while cross section 2-2 is in the middle height of the vehicle. The velocity vectors in the plane are first extracted from the original 3D flow field. The contours of the 2-norms of these velocity vectors and the streamlines of the projected vehicle vectors on the plane are taken to show the flow field. At Z_V=0, the vehicle is just behind the bridge tower, and the projected streamlines and velocity contours of the vehicle-deck-tower system in the two selected main planes are displayed in Figure 7.7. Although the ratio of the vehicle length to the tower width in this thesis is smaller, an obvious suction region can be observed between the vehicle and the tower. This region is also observed from the smoke visualization done by Argentini *et al*. (2011). From Figure 7.7, it is also noted that a large vortex is generated near the up boundary. This is the byproducts of the combination of strong separation flows from the vehicle and the flow drag from the up wall that should not exist in real situation. Nevertheless, it can also be seen from Figure 7.7 that the flow velocities involved in the large vortex are very small and, therefore, the large vortex is expected to have slight effects on the computed aerodynamic forces on the vehicle. At $Z_V=L_V$ and $Z_V=2L_V$, the vehicle moves out of the tower. The projected streamlines and velocity contours of the vehicle-deck-tower system are shown in Figures 7.8 and 7.9 for $Z_V=L_V$ and $Z_V=2L_V$, respectively. Clearly, the flow fields shown in Figures 7.8 and 7.9 are quite different from those shown in Figure 7.7. The location of the vehicle relative to the tower affects the flow field around the vehicle significantly. In view of section 1-1, the wake region around the vehicle-deck is much higher for the $Z_V=0$ case compared with the $Z_V=L_V$ case. The effects of the tower on the flow around the vehicle are limited for the $Z_V=2L_V$ case in view of section 2-2.

At the position $Z_V=0$ and $Z_V= L_V$ of the vehicle, the pressure coefficient distributions are displayed in Figure 7.10. The pressure coefficient is defined as the ratio of the pressure to the dynamic pressure. Since the length of the vehicle is slightly longer than the width of the tower, the tail part of the vehicle is not shielded by the tower at the position $Z_V=0$. High positive pressures occur on the tail part of the windward side surface of the vehicle as in Figure 7.10. From the case $Z_V=0$ to the case $Z_V= L_V$, the positive pressures extend to most parts of the windward side surface of the vehicle.

7.3.5.2 Aerodynamic coefficients

The simulated aerodynamic coefficients of the vehicle and their comparisons with wind tunnel results are listed in Table 7.4. The maximum relative difference between them is the yawing moment coefficient. The simulated side coefficient, lift coefficient and absolute yawing moments are larger than the measured ones while the rotating moment coefficients are close to the measured ones. An initial explanation about the differences is that the velocities perpendicular to the lane in the wake of the tower are overestimated, leading to a high side force and yawing moment, but the velocities along the lane are underestimated, leading to a low drag force and pitching moment. The differences in aerodynamic coefficients between the simulations and wind tunnel tests are expected in the current study if considering the complexity of the problem and uncertainties involved in wind tunnel tests and numerical simulations, but a further study is required to examine reducing these differences when both experimental and numerical simulation techniques are developed to a mature level for the problem concerned. Nevertheless, it will be conservative from the practical viewpoint of the vehicle safety under crosswinds if the simulated aerodynamic forces are used.

7.4 NUMERICAL SIMULATION OF MOVING VEHICLE

7.4.1 Simulation Scheme

The dynamic meshing method implemented in the software Fluent is activated to simulate the movement of the vehicle. The total computational domain is divided into two regions, as seen in Figure 7.11(a). The one surrounding the vehicle is a dynamic mesh region, where the meshes move with the same velocity as the vehicle moves. The other region is a stationary mesh region without the motion of meshes. The interface defined in Fluent is assigned to the contact faces between the two regions. For the flow in the stationary region, the common governing equations (Equations 3.5 and 3.6) are applied. In the region of the dynamic mesh, the conservation equation for a general scale ϕ, which represents the flow velocity component $\overline{u}_i$, turbulence kinetic energy k or special turbulence dissipation rate ω for the turbulence model used in this study, on an arbitrary grid volume V can be written as (Ansys 13.0 help):

$$\frac{d}{dt}\int_V \rho\phi dV + \int_{\partial V} \rho\phi(\overline{\mathbf{u}} - \mathbf{u}_\mathbf{g}) \cdot d\mathbf{A} = \int_{\partial V} \Gamma\nabla\phi \cdot d\mathbf{A} + \int_V S_\phi dV \tag{7.3}$$

where $\overline{\mathbf{u}}$ is the flow velocity vector; $\mathbf{u}_\mathrm{g}$ is the velocity vector of the moving mesh; Γ is the diffusion coefficient; S_ϕ is the source term of ϕ; ∂V is the boundary face of the control volume; and $\boldsymbol{A}$ is the area vector of ∂V. The discretization methods are the same as used in Section 7.3.1.

It can be seen from Figure 7.11(a) that the dynamic mesh region is enclosed by the contact faces with the stationary mesh region and a part of the deck surface. After each time step, offsets of the meshes occur at the contact faces between the stationary and dynamic mesh regions. The locations of the meshes in the dynamic mesh region are updated using the dynamic layering model. The layer split factor and layer collapse factor are both set as 0.5. The detailed information about the dynamic layering model can be found in the help document of Fluent. Moreover, the part of the deck surface moved together with the dynamic mesh region in the numerical simulation, but at the same time, the moving velocity of the vehicle is oppositely set on the part of the deck surface to keep the deck stationary.

7.4.2 Computational Cases

To ensure the proper simulation of flows around the moving vehicle when it passes by the tower, the length of the bridge deck has to be increased from 5m to 15m, as shown in Figure 7.11b. The vehicle then moved from the left to the right. A distance of 10m is arranged at the left side of the tower so that it is long enough for developing a rational flow around the moving vehicle before it passes by the tower. The increase of the deck length results in a higher blockage ratio. To keep the blockage ratio unchanged, the height of the computational domain is also increased, from 2m to 4.43m. As a result, the number of grids increases to 20.7 million, with the same grid distribution around the vehicle-deck-tower surfaces as the stationary case. The outer boundary settings of the computational domain are the same as those used in the stationary case except for the surfaces of the vehicle and the wind inflow boundary *b_left*. The surfaces of the vehicle are also non-slip wall boundaries, but with a moving velocity V_V along the deck. The vehicle is positioned at Z_V = -8.52m originally and then accelerated to the designated velocity at a distance of 2.7m (equal to $5L_V$). A yaw angle α_{WV} is defined to reflect the relative magnitude of wind velocity to vehicle velocity:

$$\alpha_{WV} = \arctan(\frac{V_W}{V_V}) \tag{7.4}$$

where V_W and V_V are the designated wind velocity and the designated vehicle velocity, respectively. Three moving cases of α_{WV} =0° (V_W=0, V_V=10m/s), 30° (V_W=5m/s, V_V=8.66m/s) and 60° (V_W=8.66m/s, V_V=5m/s) are computed. Therefore, different wind velocities are assigned to the inflow boundary *b_left*. For each case, the time step is set as 0.01m/ V_V.

7.4.3 Flow Field and Surface Pressure

The projected streamlines and velocity contours of the vehicle-deck-tower system in the two selected planes (see Section 7.3.5.1) of the vehicle when it enters behind the tower are displayed in Figures 7.12 to 7.14. At 0°, it is obvious that the head of the vehicle pushes the air away and the air then converges at the tail of the vehicle. At other angles, the air near the surfaces of the vehicle is driven by both the motion of the vehicle and the crosswind. For section 1-1, air circulations are generated at the upper, bottom and leeward side surfaces of the vehicle at 30°, and the flow separates at the windward corners of the vehicle at 60°. This indicates that the flow around the vehicle changes from the lengthwise feature to the crosswise feature as the yaw angle increases. For section 2-2, the flow around the vehicle interacts with the wake of the windward tower and the symmetric wake feature behind the windward tower is disturbed by the motion of the vehicle. The developing direction of the wake behind the trail of the vehicle is along the direction of the resultant velocity of the crosswind and the vehicle velocity. The pressure coefficient distributions over the vehicle surfaces at the location Z_V=L_V are displayed in Figure 7.15. At 0°, positive pressures exist only on the head surface. Positive pressures extend to the windward side surface at 30° and further to the leeward side surface, the roof and the bottom surface at 60°.

7.4.4 Aerodynamic Coefficients

The simulated aerodynamic coefficients of the vehicle during the period of passing by the tower are shown in Figure 7.16, from Z_V= -3.78m to Z_V= 3.78m for the three velocity cases. At 0°, there is no action of crosswind. The influences of the tower on the aerodynamic forces of the vehicle are thus limited. The side coefficient, the yawing moment coefficient and the rotating moment coefficient are almost zero. The negative lift coefficient of the vehicle at 0° indicates that the vehicle's ability to attach to the ground is enhanced.

When the vehicle is at the location without the influence of the tower (e.g. Z_V=-3.78), its side coefficient, yawing moment coefficient and rotating moment coefficient increase with the increase of crosswind velocity. Different from these coefficients, the lift and pitching moment coefficients are related not only to the crosswind velocity but also to the vehicle running velocity. Therefore, they do not show a monotonic relationship with α. Intuitively, the drag force decreases with the decrease of vehicle velocity. However, a large drag force occurs at the front surface of the trailer at a low yaw angle, which makes the drag force at 30° larger than those at 0° and 60°.

At Z_V=-B_T in Figure 7.16, the head surface of the vehicle is aligned with the left boundary of the tower, which means the vehicle is entering the tower region. At Z_V=0, the head surface of the vehicle is aligned with the right boundary of the tower, which means the vehicle is exiting the tower region. At Z_V=L_V, the tail surface of the vehicle is aligned with the right edge of the tower, and the entire vehicle is just out of the tower region. The aerodynamic coefficients of the moving vehicle at positions Z_V =0, L_V and 2L_V are compared with those of the stationary vehicle at the same positions in Table 7.5. It can be seen that the side coefficient of the moving vehicle and the absolute value of the yawing moment coefficient of the moving vehicle increase with the relative angle and are lower than those of the stationary vehicle at the same positions. There are no obvious magnitude relations for other aerodynamic coefficients between the moving and stationary vehicles.

The shielding effects of the tower on the aerodynamic forces of the vehicle are significant in the cases where α_{WV}=30° and α_{WV} =60°. As the vehicle approaches the tower, the absolute values of the side coefficient, the yawing moment coefficient and the rotating moment coefficient increase continuously to their respective peak values due to the accelerated flow at the side of the tower. The side coefficient and the rotating moment coefficient then decrease to the lowest values as the vehicle is totally immerged by the tower (about Z_V=0) because the flows are shielded by the tower. These two coefficients reach peak values again as the vehicle moves out of the tower, because the flow is accelerated at the right side of it. The value of the right peak is higher than that of the left peak, which is the same as the test results presented by Charuvisit *et al*. (2004). The situation becomes different for the yawing moment coefficient. The side forces act mainly on the trail part of the vehicle as it enters the tower region and on the head part of the vehicle as it moves out of the tower region. Therefore, the yawing moment reaches a maximum value when the side force decreases at the location near $-B_T$, and it then reduces and increases again. The accelerated flows at the sides of the tower also yield peak values for the lift and pitching moment. At the position of the vehicle directly behind the tower (about Z_V=0), the lift and the pitching moment are small. At the two sides of the tower, the accelerated flows lead to a higher yaw angle of wind to the vehicle. As a result, the drag force decreases at these positions. The drag force approaches to the same value as the case of no crosswind if the vehicle is just behind the tower. This is why the drag coefficient decreases at 30° and increases at 60° when the vehicle is behind the tower.

7.5 SUMMARY

In this chapter, a numerical model has been used to obtain the aerodynamic forces acting on a moving vehicle as the vehicle passes by a bridge tower using CFD. The RANS method, supplemented with SST k-ω turbulence model, is employed. A stationary vehicle immerged in the wake of a bridge tower is first simulated and compared with wind tunnel test results. By using the dynamic mesh method, the moving of the vehicle passing by a bridge tower is then simulated. The major conclusions are summarized as follows:

- A cubic computational domain enclosed by the six outer boundaries is formed around the vehicle-deck-tower system with mathematical boundary conditions. Four meshing schemes with different grid sizes are generated to obtain a relative adequate grid system corresponding to the ability of the computer. The grid numbers of the four meshing schemes are 15.5, 20.6, 22.7, and 31.8 million. The relative differences of the side coefficient and the rotating moment coefficients are within 5% for different meshing schemes. Since the flows underneath and the pressure on the vehicle bottom surface are hard to predict with a high degree of accuracy, the maximum relative difference is the lift coefficient among all of these aerodynamic coefficients. Fortunately, lift force is less significant to the behavior of the vehicle under crosswinds compared with other force components. The meshing scheme with 15.5 million grids are selected for the simulation of the stationary vehicle immerged into the wake of the bridge tower. A time step of $0.1t^*$ is accepted compared with a shorter time step for the stationary cases.

- The flows around the stationary vehicle immerged into the wake of the bridge tower with different relative position refer to the tower (Z_V=0, L_V, and $2L_V$). At Z_V=0, an obvious suction region can be observed between the vehicle and the tower, which is also observed from the previous experiment by Argentini *et al.* (2011). The location of the vehicle relative to the tower affects the flow field around the vehicle significantly.

- The simulated aerodynamic coefficients of the stationary vehicle in the wake of the tower are compared with the wind tunnel results. The maximum relative difference between them is the yawing moment coefficient, while the maximum absolute difference occurs on the side coefficient. The simulated side coefficient, lift coefficient, and absolute yawing moments are larger than the measured ones while the rotating moment coefficients are close to the measured ones. The differences in aerodynamic coefficients between the simulations and wind tunnel tests are expected in the current study, if considering the complexity of the problem and uncertainties involved in wind tunnel tests and numerical simulations. Nevertheless, it will be conservative from the practical viewpoint of the vehicle safety under crosswinds if the simulated aerodynamic forces are used.

- The dynamic meshing method is activated to simulate the movement of the vehicle passing by the bridge tower. A dynamic mesh region surrounding the vehicle is formed while the left computation domain is defined as the stationary region. Interface defined in Fluent is assigned to the contact faces between the two regions. In the region of the dynamic mesh, locations of the meshes in the dynamic mesh region are updated using the dynamic layering model. The moving velocity is taken into considered in the governing equations for the flows in the dynamic mesh region.

- To have a deck with enough length for the vehicle moving on, the bridge deck is lengthened compared with the stationary cases. To keep the blockage ratio unchanged as in the stationary cases, the height of the computational domain also increases. The final number of grids for the moving vehicle cases increases to 20.7 million, with the same grid distribution around the vehicle-deck-tower surfaces as in the stationary cases. For each case, the time step is set as 0.01m/ V_V.

- The flows around the moving vehicle-deck-tower system are simulated with different yaw angles. At 0°, it is obvious that the head of the vehicle pushes the air away and the air then converges at the tail of the vehicle. At other angles, the air near the surfaces of the vehicle is driven by both the motion of the vehicle and the crosswind. The flow around the vehicle changes from the lengthwise feature to the crosswise feature as the yaw angle increases.

- The aerodynamic coefficients of the moving vehicle passing by the bridge tower are computed with different yaw angles. At 0°, there is no action of crosswind. The side coefficient, the yawing moment coefficient and the rotating moment coefficient are almost zero. At positions Z_V =0, L_V and $2L_V$, the side coefficient of the moving vehicle and the absolute value of the yawing moment coefficient of the moving vehicle increase with the relative angle and are lower than those of the stationary vehicle at the same positions. There are no obvious magnitude relations for other aerodynamic coefficients between the moving and stationary vehicles.

- The shielding effects of the tower on the aerodynamic forces of the vehicle are significant in the cases where α_{WV} =30° and α_{WV} =60°. As the vehicle approaches the tower, the absolute values of the side coefficient, the yawing moment coefficient and the rotating moment coefficient increase continuously to their respective peak values. The side coefficient and the rotating moment coefficient then decrease to the lowest values as the vehicle is totally immerged by the tower. These two coefficients reach peak values again as the vehicle moves out of the tower. The yawing moment reaches a maximum value when the side force decreases at the location near $-B_T$, and it then reduces and increases again. The lift and pitching moment also yield peak values at the sides of the tower; and they are small, as the vehicle is directly behind the tower. The drag force decreases at the two sides of the tower and approaches to the same value as in the case of no crosswind if the vehicle is just behind the tower.

Table 7.1 Measured aerodynamic coefficients of the vehicle

	C_S	C_L	C_D	C_P	C_Y	C_R
Z_V=0	1.145	0.112	-0.136	-0.062	-0.670	-0.129
Z_V= L_V	4.120	-0.939	0.499	-0.225	-0.371	-0.251
Z_V=2L_V	4.494	-0.837	0.490	-0.248	-0.473	-0.236

Table 7.2 Simulated aerodynamic coefficients of the vehicle with different meshing schemes

Meshing scheme	C_S	C_L	C_D	C_P	C_Y	C_R
1	4.986	-0.070	0.378	-0.138	-0.611	-0.255
2	4.996	-0.089	0.347	-0.130	-0.623	-0.254
3	5.071	-0.137	0.339	-0.113	-0.567	-0.249
4	4.958	-0.185	0.349	-0.116	-0.577	-0.246

Table 7.3 Simulated aerodynamic coefficients of the vehicle with different time steps

Time step	C_S	C_L	C_D	C_P	C_Y	C_R
0.1t*	5.006	-0.116	0.350	-0.130	-0.626	-0.256
0.05t*	4.998	-0.111	0.355	-0.130	-0.623	-0.256

Table 7.4 Simulated aerodynamic coefficients of the vehicle and compared with test results

		C_S	C_L	C_D	C_P	C_Y	C_R
Z_V=0	SIM	2.005	0.164	-0.017	-0.030	-0.707	-0.108
	RD(%)	75	46	88	52	-6	16
Z_V= L_V	SIM	5.006	-0.116	0.350	-0.130	-0.626	-0.256
	RD(%)	22	88	-30	42	-69	-2
Z_V=2L_V	SIM	6.241	0.030	0.058	-0.181	-1.005	-0.303
	RD(%)	39	104	-88	27	-113	-28

SIM: Simulation value; RD: Relative Difference: (Value of SIM.-Value of test)/| Value of test| *100%

Table 7.5 Comparison of aerodynamic coefficients of the vehicle in moving and stationary status

		C_S	C_L	C_D	C_P	C_Y	C_R
Z_V=0	0°	-0.043	-0.224	-0.735	-0.066	0.005	0.000
	30°	0.889	0.516	-1.036	0.069	-0.243	-0.059
	60°	1.671	0.302	-0.268	-0.022	-0.492	-0.264
	Stationary	2.005	0.164	-0.017	-0.030	-0.707	-0.108
$Z_V= L_V$	0°	0.021	-0.212	-0.746	-0.066	-0.011	0.000
	30°	2.742	1.405	-1.241	0.065	-0.210	-0.179
	60°	5.361	1.668	-0.407	0.098	-0.620	-0.283
	Stationary	5.006	-0.116	0.350	-0.130	-0.626	-0.256
$Z_V=2L_V$	0°	0.003	-0.217	-0.748	-0.067	-0.001	0.000
	30°	2.785	1.342	-1.274	0.091	-0.284	-0.159
	60°	5.160	0.766	-0.441	-0.080	-0.556	-0.096
	Stationary	6.241	0.030	0.058	-0.181	-1.005	-0.303

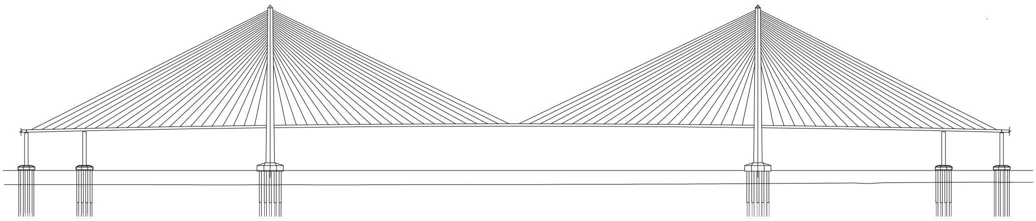

Figure 7.1 Elevation of the long-span cable-stayed Bridge (unit: cm)

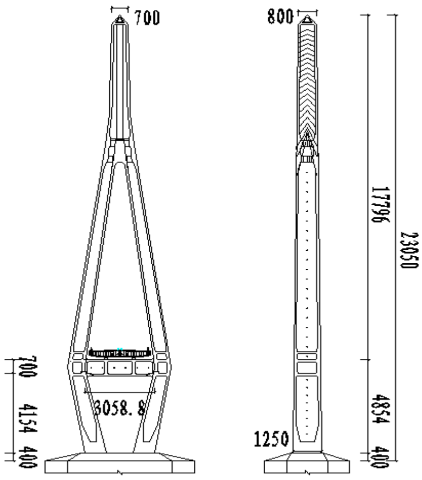

Figure 7.2 Dimensions of the bridge tower (unit: cm)

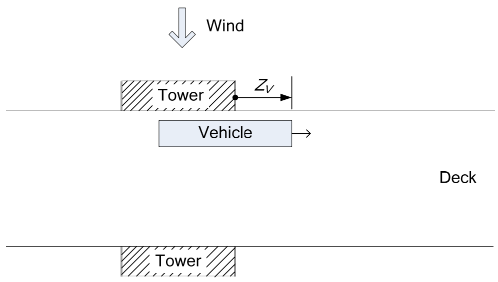

Figure 7.3 Illustration of the vehicle location

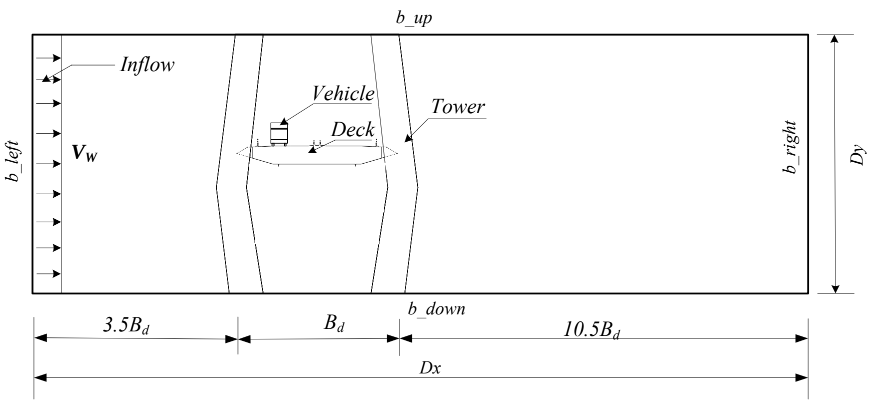

(a) Section in wind direction

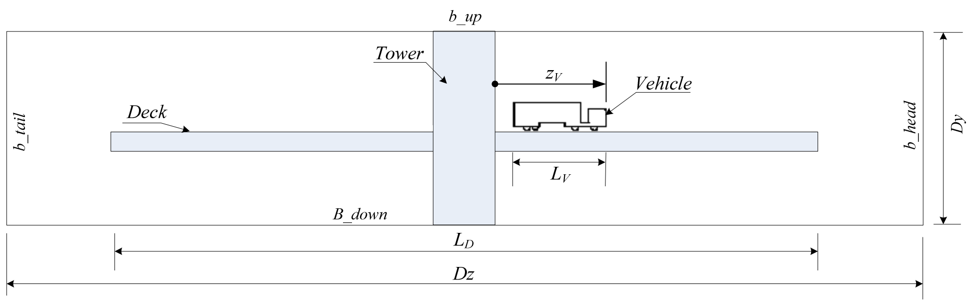

(b) Section perpendicular to wind direction

Figure 7.4 Computational domain sketch: vehicle-deck-tower system

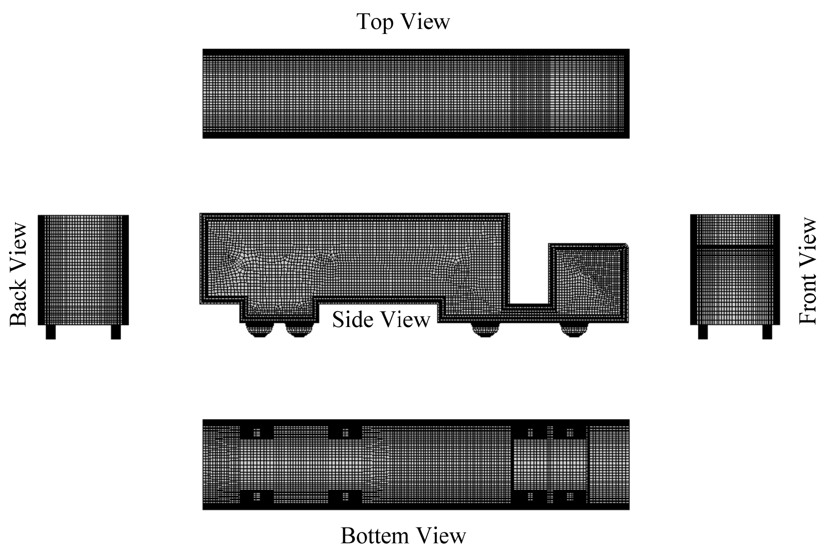

Figure 7.5 Grid distributions on the vehicle surfaces

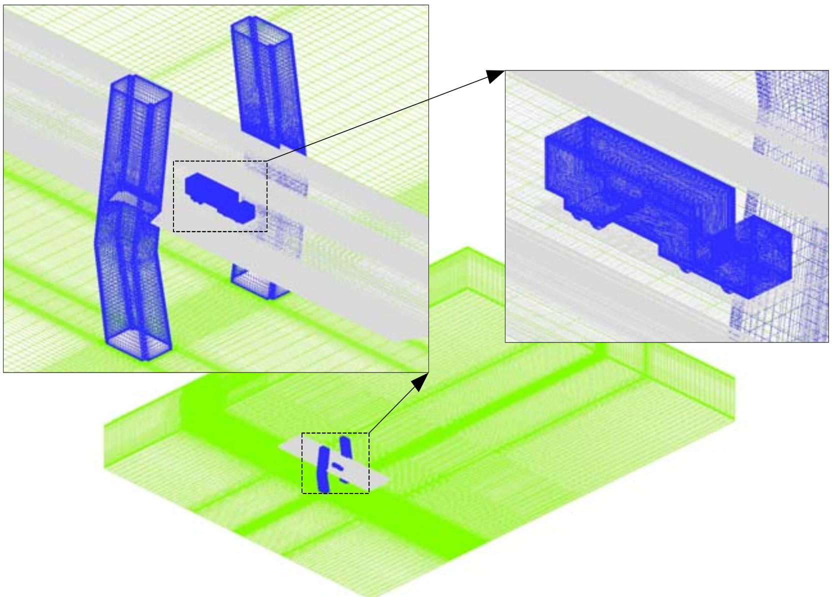

Figure 7.6 Meshing scheme 1

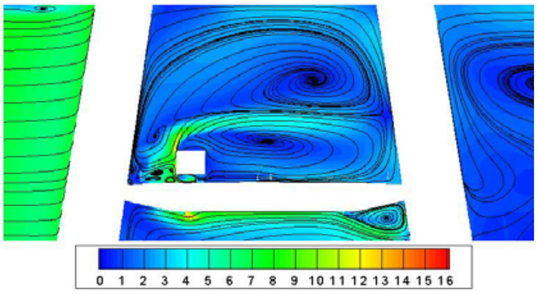

(a) Section 1-1

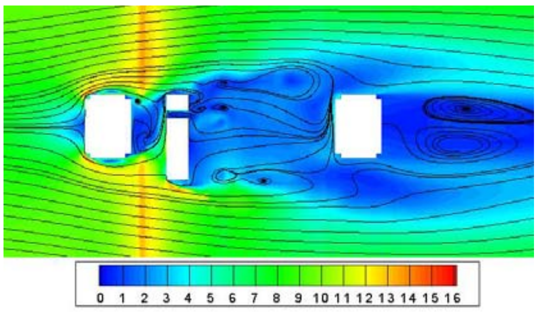

(b) Section 2-2

Figure 7.7 Projected streamlines and velocity contours
(Z_V=0, unit: m/s)

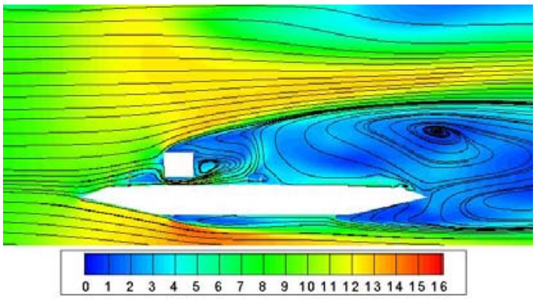

(a) Section 1

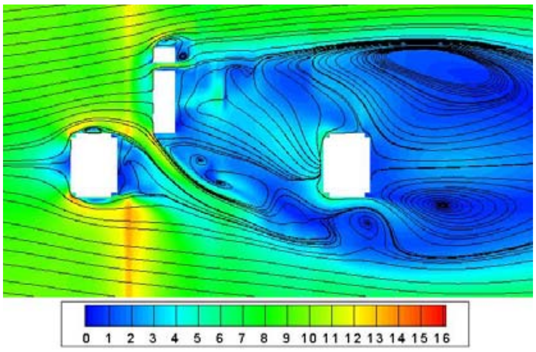

(b) Section 2

Figure 7.8 Projected streamlines and velocity contours ($Z_V = L_V$, unit: m/s)

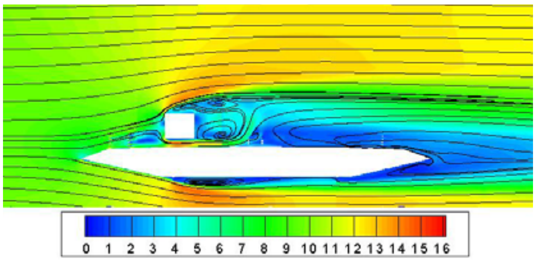

(a) Section 1

Figure 7.9 Projected streamlines and velocity contours (to be continued)

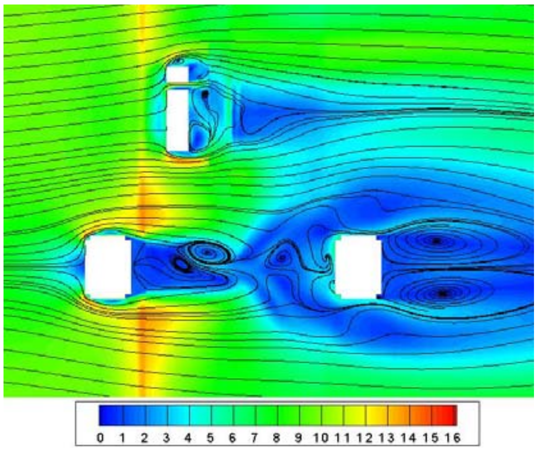

(b) Section 2

Figure 7.9 Projected streamlines and velocity contours (Z_V=2L_V, unit: m/s)

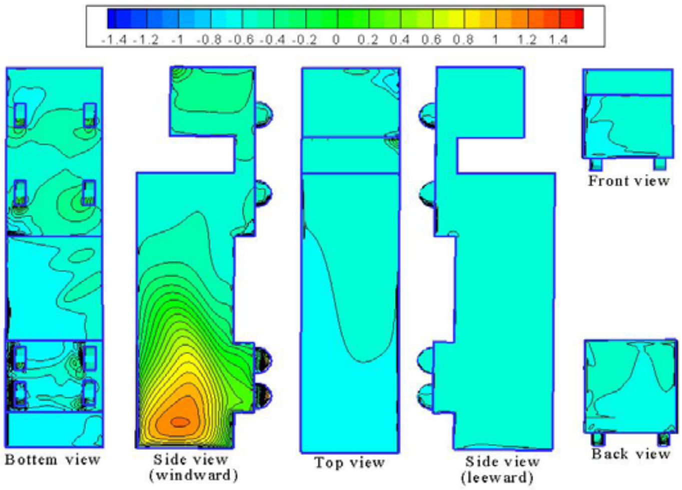

(a) Z_V=0

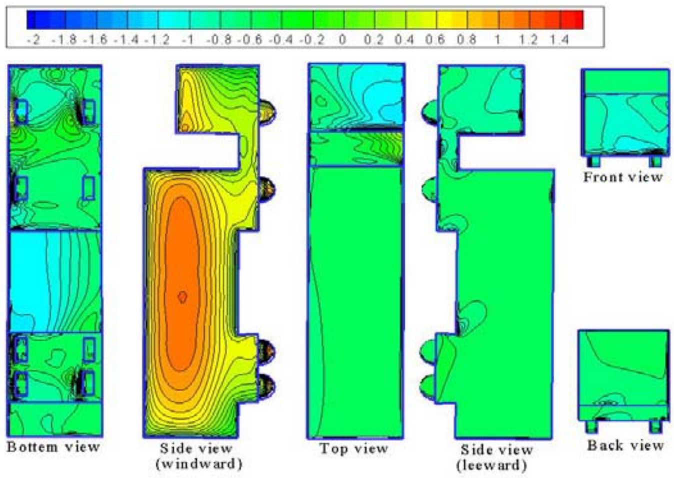

(b) Z_V= L_V

Figure 7.10 Pressure distributions on the surfaces of the vehicle

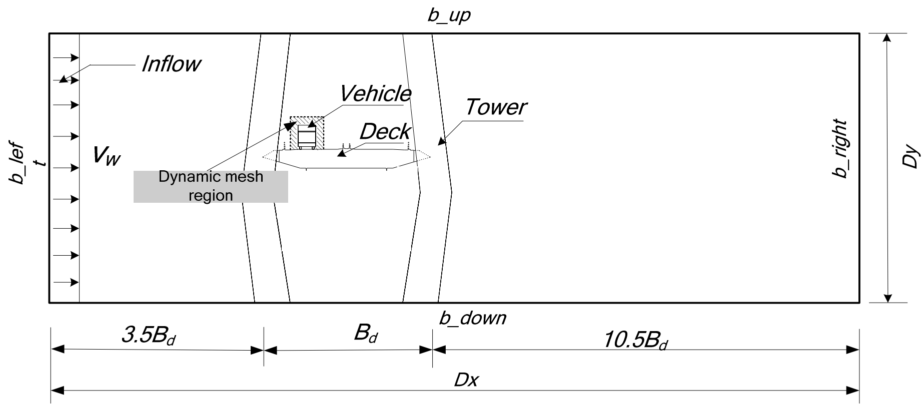

(a)

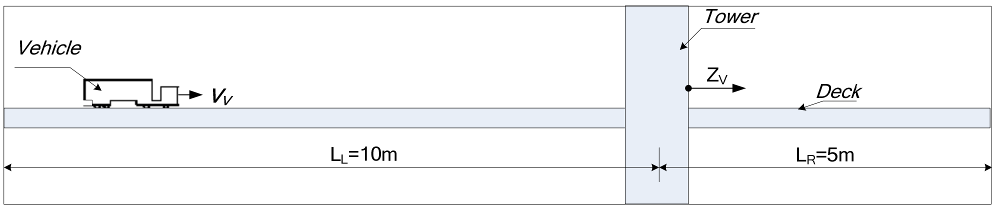

(b)

Figure 7.11 Computational domain for the moving vehicle-deck-tower system

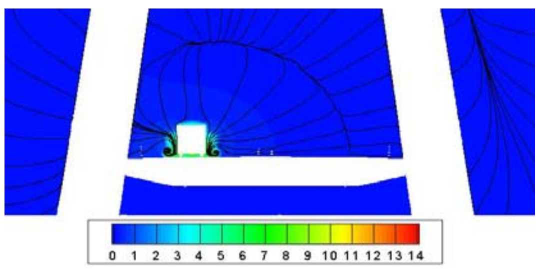

(a) Section 1-1

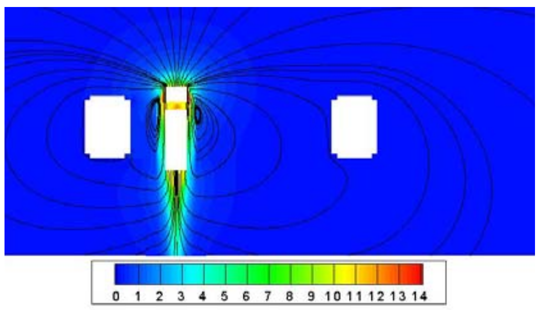

(b) Section 2-2

Figure 7.12 Flow velocity contour and projected streamlines (α_{wv}=0°, unit: m/s)

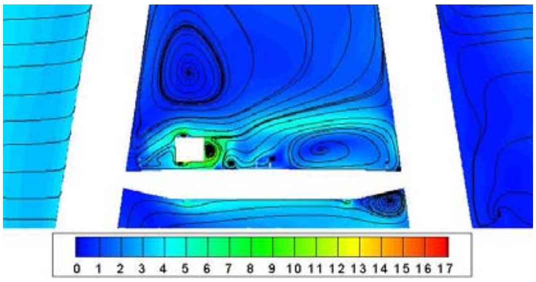

(a) Section 1-1

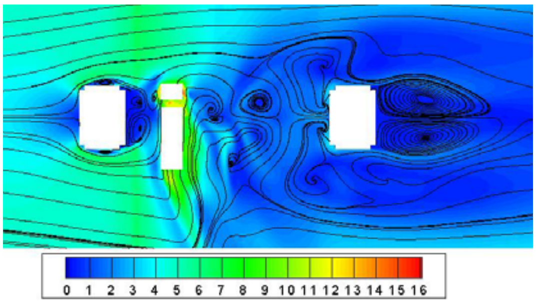

(b) Section 2-2

Figure 7.13 Flow velocity contour and projected streamlines (α_{wv}=30°, unit: m/s)

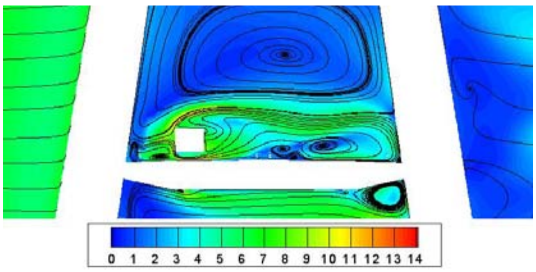

(a) Section 1-1

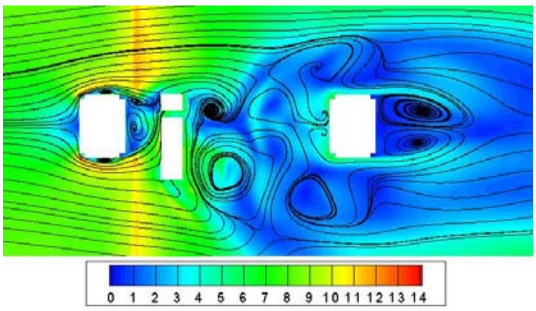

(b) Section 2-2

Figure 7.14 Flow velocity contour and projected streamlines (α_{wv}=60°, unit: m/s)

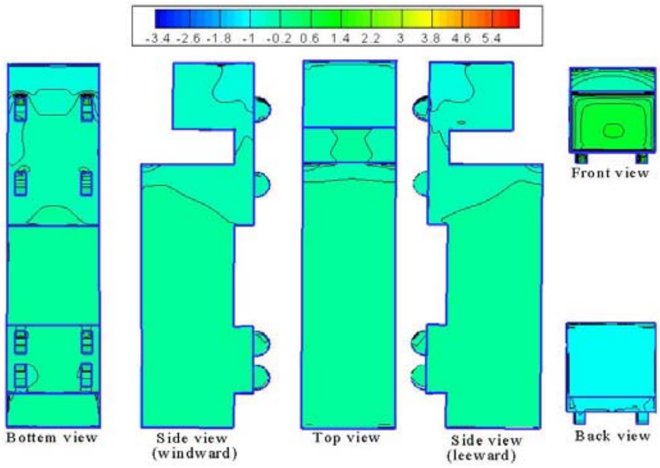

(a) 0°

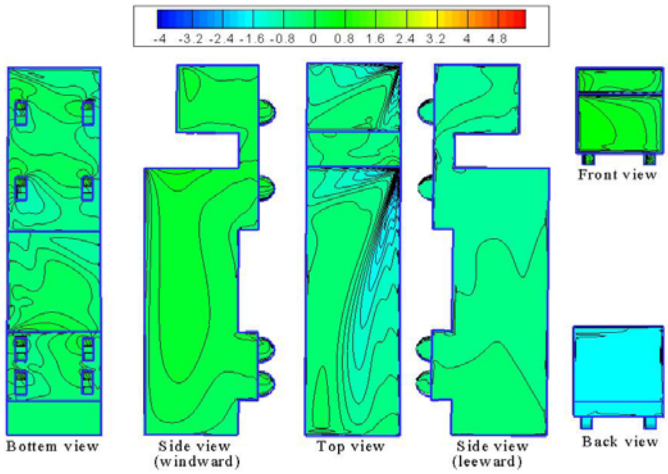

(b) 30°

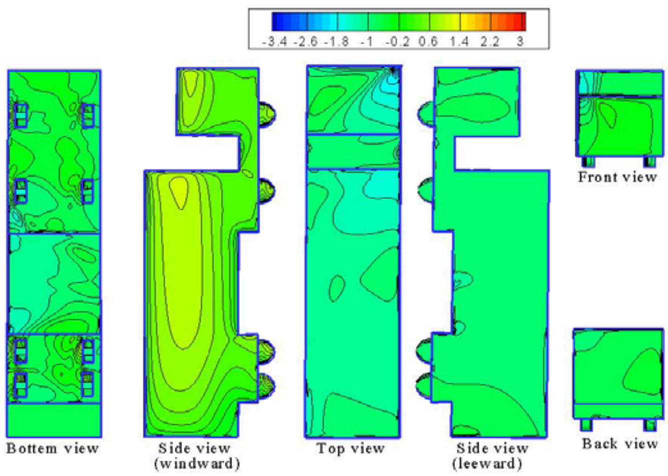

(c) 60°

Figure 7.15 Mean pressure distributions over the surfaces of the vehicle (Z_V=L_V)

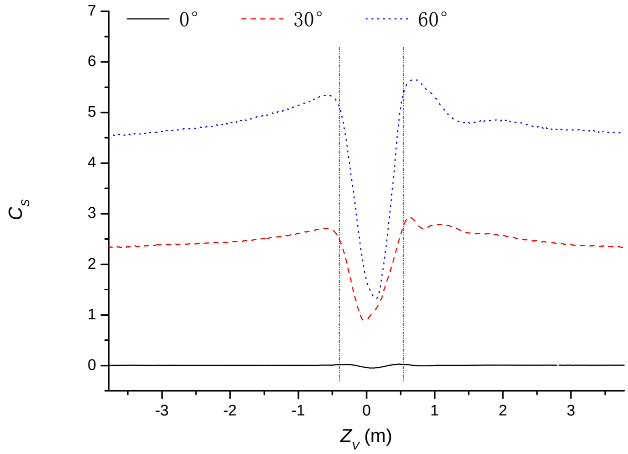

(a) Side coefficient

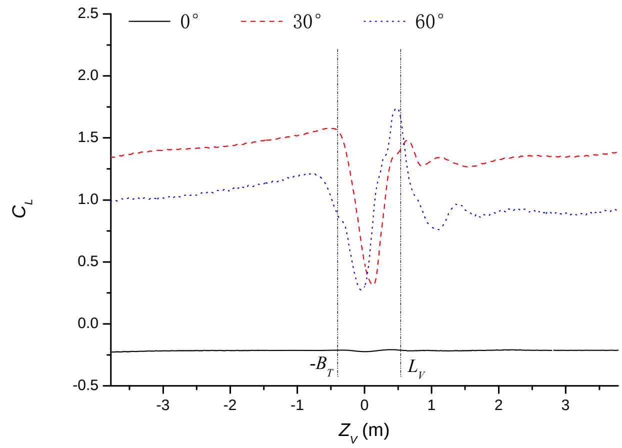

(b) Lift coefficient

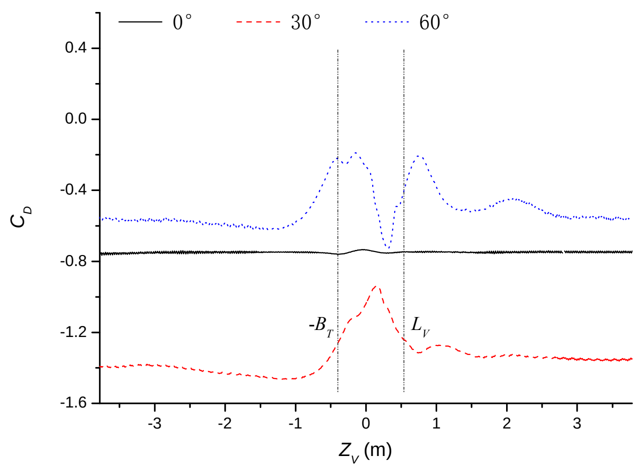

(c) Drag coefficient

Figure 7.16 Aerodynamic coefficients of the moving vehicle (to be continued)

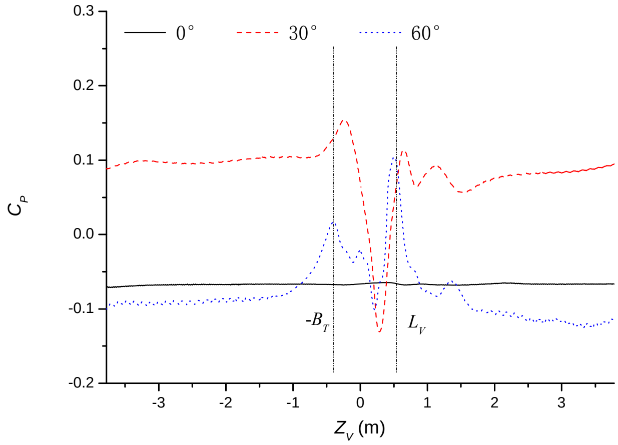

(d) Pitching moment coefficient

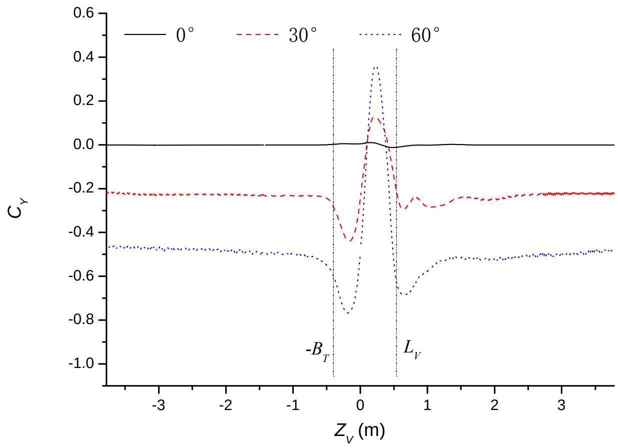

(e) Yawing moment coefficient

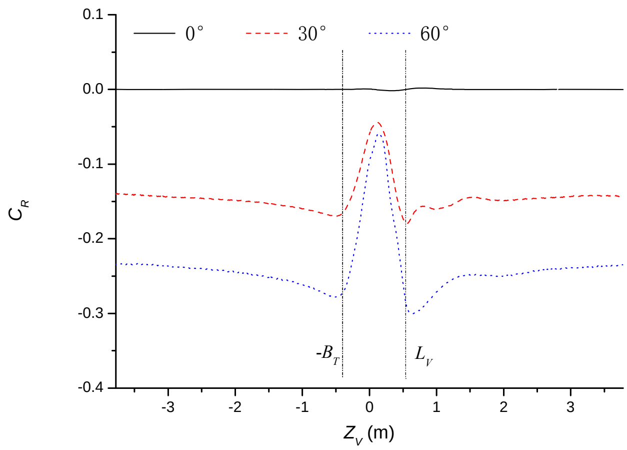

(f) Rotating moment coefficient

Figure 7.16 Aerodynamic coefficients of the moving vehicle

CHAPTER 8
SAFETY ANALYSIS OF A VEHICLE PASSING BY BRIDGE TOWER

8.1 INTRODUCTION

An advanced road vehicle model able to simulate the progressive instability of a vehicle moving on the ground under the crosswind gust has been established in Chapter 4. The vehicle model has been incorporated into the framework of the Road Vehicle-Bridge-Wind (RVBW) system with the Computational Fluid Dynamics (CFD)-simulated aerodynamic coefficients of both the moving vehicle and the bridge deck with mutual influence and is included in Chapter 5. Based on the RVBW system, the ride comfort of a moving road vehicle on a bridge has been assessed in Chapter 5. Nevertheless, moving vehicles on a bridge may be in danger as they pass by a bridge tower, since the aerodynamic forces acting on the vehicle will be suddenly sheltered by the tower. The safety analysis of a vehicle passing by a bridge tower shall be carried out in addition to the comfort analysis. In Chapter 7, the aerodynamic coefficients of a road vehicle passing by a bridge tower have been computed using CFD. In this chapter, the progressive instability and safety of the road vehicle passing by a bridge tower under the combined action of crosswind and driver will be analyzed.

In the previous studies, a sudden crosswind gust of 0.5s duration was enforced on a vehicle to evaluate the safety of the vehicle moving on a long span bridge. In Chen and Cai (2004), the vehicle responses in the vertical, rolling and pitching directions were first solved from the RVBW system. A local accident vehicle model separated from the RVBW system was then set to evaluate the safety of the vehicle moving on the bridge, based on the vehicle responses obtained from the RVBW system. The safety of the vehicle passing by a bridge tower was evaluated in terms of a sudden wind action. In Guo and Xu (2006), the safety of a vehicle moving on a bridge had been assessed using their framework of the RVBW system without any supplemented accident vehicle model. Similarly, a sudden crosswind gust was applied on the road vehicle. In fact, a much more complicated wind condition than a sudden crosswind gust of 0.5s duration is confronted by the vehicle when it is passing by a bridge tower. The vehicle is first shielded from the crosswinds by the tower within a very short time, and then it enters into the crosswinds within another very short period. This wind condition also depends on the size and shape of the tower cross section, and it is different from a sudden crosswind gust of 0.5s duration, as currently assumed. The time duration of the vehicle passing by a bridge tower is particularly important for the behavior of the driver. Therefore, the actual wind loads acting on the vehicle passing by the bridge tower should replace the assumed sudden crosswind gust to have a more realistic assessment of vehicle safety. Furthermore, most of the previous studies focused on the safety of a vehicle running on the ground without considering the effect of RVBW interaction. The effects of the dynamic responses of the bridge on the safety assessment of the vehicle running on the bridge should also be investigated.

In this chapter, the framework of the RVBW system incorporated with the advanced road vehicle model, considering the road roughness in plane, vehicle lateral motion, and driver's behavior, and established in Chapter 6, is employed to assess the safety of the road vehicle passing by a bridge tower. The varying aerodynamic coefficients of the moving vehicle passing by a bridge tower, obtained by using CFD in Chapter 7, are used to analyze the progressive instability and safety of the road vehicle passing by a bridge tower and are described in this chapter. The effects of the dynamic responses of the bridge on the vehicle safety are discussed. The accident velocity of a single vehicle passing by the bridge tower is finally assessed.

8.2 BRIEF DESCRIPTION OF ANALYSIS METHOD

Figure 8.1 illustrates a road vehicle passing by a bridge tower under crosswinds. During the passage, four main positions of the vehicle in the lateral direction of the bridge (see S1, S2, S3, and S4 in Figure 8.1) are concerned. In the position S1, the vehicle moving on the bridge deck is far from the bridge tower. The aerodynamic forces on the vehicle are influenced by the deck, but not the tower. Meanwhile, the aerodynamic forces on the deck vary with the location of the vehicle. This is a normal case that has been considered in the RVBW system described in Chapter 6. Since the vehicle is under lateral wind forces due to crosswinds, it tends to move downwind, and the driver will thus steer the wheels to get the vehicle back to the original lane. As the vehicle approaches the tower gradually, the crosswinds on the vehicle will be shielded by the bridge tower. This position of the vehicle is denoted as S2. At this position, the aerodynamic forces on the vehicle reduce as the vehicle moves behind the tower, which can be observed from the aerodynamic coefficients computed in Chapter 7 for the vehicle passing by the tower. As a result, the vehicle departs from the moving lane in the counter-direction of the crosswinds due to the reduced aerodynamic forces. Accordingly, if there is enough time, the driver will steer so that the vehicle can be controlled back to the moving lane. As the vehicle gets out of the way of the tower, the crosswinds restore to the normal ones within a very short time. This position is characterized as S3. In this position, the wind loads on the vehicle increase and lead to the lateral motion of the vehicle downwind. The lateral motion of the vehicle may not be balanced by the steer angle due to the time delay of the driver system. Consequently, the vehicle departs from the original moving lane again, but in the opposite direction to the case of S2. The vehicle will go back to the original lane eventually under the action of the driver, which is designated as S4.

During the entire procedure of the vehicle passing by a bridge tower as described above, the responses of the vehicle are induced by the wind loads with the interference of both the deck and the tower, the dynamic response of the bridge, and the action of driver. To analyze the behavior and safety of the road vehicle passing by the bridge deck in a natural way, two aspects shall be taken into account. One is that the RVBW system used in the analysis shall be able to include the lateral motion of the vehicle and consider the aerodynamic interference between the deck and the moving vehicle. This system has been established already in Chapter 6. The other is that the varying aerodynamic coefficients of the vehicle passing by a bridge tower shall be available for considering the shielding effects of the tower. In summary, under the normal positions of the vehicle without influence from the tower (S1 and S4 positions), the responses of the vehicle are simulated directly using the RVBW analysis system used in Chapter 6. While the vehicle moves into the shielding positions of the tower, the varying aerodynamic coefficients of the vehicle passing by the bridge tower should be used together with the RVBW analysis system.

8.3 BASIC EQUATIONS OF MOTION

For the sake of easy understanding, the basic equations of motion of a RVBW system, which will be used in this chapter, are provided again. The RVBW system is comprised of two subsystems: one is the moving vehicle under crosswinds, and the other is the long span bridge under crosswinds.

In the bridge subsystem, the bridge is modeled using the conventional Finite Element Method (FEM) in the global system. For a cable-stayed bridge, the deck, towers, and piers are modeled with spatial beam elements with six Degree of Freedoms (DoFs) at each end node, and cables are modeled with bar elements with three translational DoFs at each end mode. The assembled dynamic property matrixes for the cable-stayed bridge in the global coordinate system are the mass matrix $\mathbf{M_b}$**,** the stiffness matrix $\mathbf{K_b}$ and the Rayleigh damping matrix $\mathbf{C_b}$. The basic equations of motion of a long span cable-stayed bridge in the RVBW system are expressed as:

$$\mathbf{M_b}\ddot{\boldsymbol{\delta}}_\mathbf{b} + \mathbf{C_b}\dot{\boldsymbol{\delta}}_\mathbf{b} + \mathbf{K_b}\boldsymbol{\delta}_\mathbf{b} = \mathbf{F}_{bst}^{W} + \mathbf{F}_{bfl}^{W} + \mathbf{F}_{bse}^{W} + \mathbf{F}_{b}^{V} \tag{8.1}$$

where the subscript b represents the bridge; $\boldsymbol{\delta}_\mathbf{b}$, $\dot{\boldsymbol{\delta}}_\mathbf{b}$, and $\ddot{\boldsymbol{\delta}}_\mathbf{b}$ are the vector of the nodal displacement, velocity and acceleration of all the elements of the bridge; $\mathbf{F}_{bst}^{W}$, $\mathbf{F}_{bfl}^{W}$, and $\mathbf{F}_{bse}^{W}$ represent the vectors of the static wind loads, buffeting loads and self-excited loads acting on the nodes of the bridge deck, respectively; and $\mathbf{F}_{b}^{V}$ is the vector of contact forces transformed from the vehicle subsystem.

In the vehicle subsystem, the vehicle model is established on its own local coordinate system with lumped masses and a series of springs and dampers. The vehicle can move laterally with the wheels contacting with the road surface under the action of crosswinds, driver, and road roughness in plane. The vehicle model is able to simulate the progressive instability of the vehicle under extreme conditions. The basic equations of motion of the road vehicle in the local coordinates of the vehicle body (VCS) are expressed as:

$$m_{vb}\dot{v}_{vby} + m_{vb}\omega_{vbz}v_{vbx} - m_{vb}\omega_{vbx}v_{vbz} = f_{vby}^{S} - f_{vby}^{G} + f_{vy}^{W} \tag{8.2a}$$

$$m_{vb}\dot{v}_{vbz} - m_{vb}\omega_{vby}v_{vbx} + m_{vb}\omega_{vbx}v_{vby} = f_{vbz}^{S} - f_{vbz}^{G} + f_{vz}^{W} \tag{8.2b}$$

$$I_{xx}\dot{\omega}_{vbx} - I_{xz}\dot{\omega}_{vbz} + (I_{zz} - I_{yy})\omega_{vby}\omega_{vbz} - I_{xz}\omega_{vbx}\omega_{vby} = m_{vbx}^{S} + m_{vx}^{W} \tag{8.2c}$$

$$I_{yy}\dot{\omega}_{vby} + (I_{xx} - I_{zz})\omega_{vbx}\omega_{vbz} - I_{xz}(\omega_{vbz}^{2} - \omega_{vbx}^{2}) = m_{vby}^{S} + m_{vy}^{W} \tag{8.2d}$$

$$I_{zz}\dot{\omega}_{vbz} - I_{zx}\dot{\omega}_{vbx} + (I_{yy} - I_{xx})\omega_{vbx}\omega_{vby} + I_{xz}\omega_{vby}\omega_{vbz} = m_{vbz}^{S} + m_{vz}^{W} \tag{8.2e}$$

$$m_{wi}\dot{v}_{wiy} = f_{wiy}^{S} + f_{wiy}^{G} + f_{wiy}^{T} \tag{8.2f}$$

$$m_{wi}\dot{v}_{wiz} = f_{wiz}^{S} + f_{wiz}^{G} + f_{wiz}^{T} \tag{8.2g}$$

where the subscripts v, vb, and wi represent the vehicle, vehicle body and the ith wheel, respectively; the subscripts x, y, and z are the three orthogonal directions of the VCS; the superscripts S, G, and W represent the suspension system, gravity, and wind, respectively; m_{vb} and m_{wi} are the masses of the vehicle body and the ith wheel, respectively; I_{xx}, I_{yy}, and I_{zz} are the moments of inertia of the vehicle body around the x-axis, y-axis, and z-axis, respectively; I_{xz} is the product of inertia of the vehicle body in the xz plane; v_{vby} and v_{vbz} are the transitional velocities of the vehicle body along the y-axis and z-axis, respectively; ω_{vbx}, ω_{vby}, and ω_{vbz} are the angular velocities of the vehicle body around the x-axis, y-axis, and z-axis, respectively; v_{wiy} and v_{wiz} are the transitional velocities of the ith wheel along the y-axis and z-axis, respectively; f_{vy}^{W} and f_{vz}^{W} are the wind forces on the vehicle along the y-axis and z-axis, respectively; m_{vx}^{W}, m_{vy}^{W}, and m_{vz}^{W} are the wind moments on the vehicle about the x-axis, y-axis and z-axis, respectively; f_{vby}^{G} and f_{vbz}^{G} are the gravity components of the vehicle body along the y-axis and z-axis, respectively; f_{wiy}^{G} and f_{wiy}^{G} are the gravity components of the ith wheel along the y-axis and z-axis, respectively; f_{vby}^{S} and f_{vbz}^{S} are the forces on the vehicle body due to the deformation of the suspension system along the y-axis and z-axis, respectively; m_{vbx}^{S}, m_{vby}^{S}, and m_{vbz}^{S} are the moments due to the deformation of the suspension system about the x-axis, y-axis, and z-axis, respectively; f_{wiy}^{S} and f_{wiz}^{S} are the forces on the ith wheel due to the deformation of the suspension system along the y-axis and z-axis, respectively; f_{wiy}^{T} and f_{wiy}^{T} are the forces received by the ith tire from the deck.

Through the transformation of interaction force vector $\mathbf{F}_{b}^{V}$ in Equation 8.1 and f_{wiy}^{T} and f_{wiy}^{T} in Equation 8.2, the two subsystems are coupled together. The detailed framework of the RVBW system is already introduced in Chapter 6. In the RVBW system presented in Chapter 6, the wind loads considering the mutual interference between the moving vehicle and the bridge deck are considered and can be employed to find the behavior of the vehicle in the positions S1 and S4. As the vehicle moves into the positions S2 and S4, the wind loads on the vehicle influenced by the tower are required to consider the shielding effects of the bridge tower.

8.4 WIND LOADS ON VEHICLE INFLUENCED BY TOWER

8.4.1 Wind Loads on Vehicle

The wind loads acting on the road vehicle considering the fluctuating winds and the attitude of the vehicle are rewritten as:

$$f_{vy}^{W} = \frac{1}{2}\rho U_{re}^{2} A_f [C_S(\alpha_w) + C_S'(\alpha_w)\beta_w] \tag{8.3a}$$

$$f_{vz}^{W} = \frac{1}{2}\rho U_{re}^{2} A_f [C_L(\alpha_w) + C_L'(\alpha_w)\beta_w] \tag{8.3b}$$

$$m_{vx}^{W} = \frac{1}{2}\rho U_{re}^{2} A_f L_v [C_R(\alpha_w) + C_R'(\alpha_w)\beta_w] \tag{8.3c}$$

$$m_{vy}^{W} = \frac{1}{2}\rho U_{re}^{2} A_f L_v [C_P(\alpha_w) + C_P'(\alpha_w)\beta_w] \tag{8.3d}$$

$$m_{vz}^{W} = \frac{1}{2}\rho U_{re}^{2} A_f L_v [C_Y(\alpha_w) + C_Y'(\alpha_w)\beta_w] \tag{8.3e}$$

with

$$U_{re} = \sqrt{U_{xe}^2 + U_{ye}^2 + U_{ze}^2} \tag{8.3f}$$

$$\alpha_w = \arctan(\frac{\sqrt{U_{ye}^2 + U_{ze}^2}}{U_{xe}}) \tag{8.3g}$$

$$\beta_w = \arctan(\frac{U_{ze}}{U_{ye}}) \tag{8.3h}$$

where ρ is the density of air; A_f is a reference area; U_{xe}, U_{ye}, and U_{ze} represent the relative wind velocity components to the vehicle along the x-, y- and z-axis in the VCS coordinate system, respectively; and C_i (i= S, L, P, Y, R) is the corresponding aerodynamic coefficient.

Different from the wind loads on the moving vehicle in the framework of RVBW in Chapter 6, wind loads on the moving vehicle passing by a bridge tower vary not only with the relative angle between the wind velocity and the vehicle velocity, but also the location of the vehicle relative to the tower center. Consequently, the wind loads shall be rewritten as:

$$f_{vy}^{W} = \frac{1}{2}\rho U_{re}^{2} A_f [C_{St}(\alpha_w, z_{vt}) + C_{St}'(\alpha_w, z_{vt})\beta_w] \tag{8.4a}$$

$$f_{vz}^{W} = \frac{1}{2}\rho U_{re}^{2} A_f [C_{Lt}(\alpha_w, z_{vt}) + C_{Lt}'(\alpha_w, z_{vt})\beta_w] \tag{8.4b}$$

$$m_{vx}^{W} = \frac{1}{2}\rho U_{re}^{2} A_f L_v [C_{Rt}(\alpha_w, z_{vt}) + C'_{Rt}(\alpha_w, z_{vt})\beta_w] \quad (8.4c)$$

$$m_{vy}^{W} = \frac{1}{2}\rho U_{re}^{2} A_f L_v [C_{Pt}(\alpha_w, z_{vt}) + C'_{Pt}(\alpha_w, z_{vt})\beta_w] \quad (8.4d)$$

$$m_{vz}^{W} = \frac{1}{2}\rho U_{re}^{2} A_f L_v [C_{Yt}(\alpha_w, z_{vt}) + C'_{Yt}(\alpha_w, z_{vt})\beta_w] \quad (8.4e)$$

where C_{it} (i= S, L, P, Y, R) are the corresponding varying aerodynamic coefficients of the moving vehicle as it passes by the bridge tower; and z_{vt} is the distance from the right boundary of the tower to the head surface of the vehicle.

8.4.2 Formulation of Varying Aerodynamic Coefficients

The varying aerodynamic coefficients C_{it} of a moving vehicle passing by a bridge tower have been computed and shown in Chapter 7. However, since the computation time to obtain these coefficients is tremendous, only a few cases with several yaw angles have been simulated. Moreover, the computed coefficients are discrete with the positions of the vehicle. The varying aerodynamic coefficients are thus required to be presented in a general formulation so as to be applied to the vehicle with different relative yaw angles.

8.4.2.1 Aerodynamic Coefficient Factorization

The effects of the tower on the aerodynamic coefficients of the vehicle are presented with an index named as aerodynamic shielding ratio SR_i (i = S, L, P, Y, R) in this thesis. It is defined as the ratio of the varying aerodynamic coefficients to the aerodynamic coefficients of the moving vehicle on the deck without the tower. Accordingly, the varying aerodynamic coefficients can be factorized as:

$$C_{it}(\alpha_w, z_{vt}) = C_i(\alpha_w) SR_i(\alpha_w, z_{vt}) \quad (8.5)$$

Since the position of the vehicle corresponding to the two ends of the computed curve for C_{it} in Chapter 7 is far enough from the tower, $C_i(\alpha_w)$ is taken as the mean value of C_{it} at the two ends.

$$C_i(\alpha_w) = \left(C_{it}^{l}(\alpha_w) + C_{it}^{r}(\alpha_w)\right)/2 \quad (8.6)$$

where $C_{it}^{l}(\alpha_w)$ and $C_{it}^{r}(\alpha_w)$ are the computed value of C_{it} at the left and right ends of the computed aerodynamic coefficients. The shielding ratios for the aerodynamic coefficients $\alpha_w = 30°$ and $60°$ are then calculated and shown in Figures 8.2 to 8.6.

8.4.2.2 Aerodynamic Shielding Ratio

The aerodynamic shielding ratios are functions of both the relative yaw angle and the relative location of the vehicle to the tower. A linear expression is adopted to express the shielding ratio of aerodynamic coefficients with the yaw angle as follows:

$$SR_i(\alpha_w, z_{vt}) = SR_{i0}(z_{vt}) + SR_{i1}(z_{vt})\alpha_w \tag{8.7}$$

where SR_{i0} and SR_{i1} are the function of the relative location of the vehicle to the tower. They can be approximated using the least squares method on each Z_{vt} for α_w=30° and 60°. As an example, SR_{S0} and SR_{S1} are shown in Figures 8.7 to 8.16.

SR_{i0} and SR_{i1} of the aerodynamic shielding ratio vary with the relative locations of the vehicle to the tower. They change rapidly around the tower with several peaks. The Gaussian multi-peak function is therefore employed to formulize SR_{i0} and SR_{i1}. They are expressed with offset values and peak functions in Gaussian functions as:

$$SR_{ik}(z_{vt}) = SR_{ik}^0 + \sum_{i=1}^{Np} \frac{A_i}{w_i\sqrt{\pi/(4\ln 2)}} \exp(-4\ln 2\frac{(z_{vt}-z_{ci})^2}{w_i^2}) \tag{8.8}$$

where i=S, L, P, Y, R; k=0, 1; SR_{ik}^0 is the offset value of SR_{ik}; A_i, x_{ci}, and w_i are the amplitude, centric position, and peak width of the ith peak, respectively; Np is the number of the peaks. Np for SR_{i1} is decided with the minimum value of the best fitting. For illustration, the SR_{i0} and SR_{i1} expressed in Gaussian multi-peak function are presented in Figures 8.7 to 8.16.

8.5 SAFETY CRITERIA

As the vehicle passes by a bridge tower, two types of wind-induced accidents, course deviation and overturning, may occur. Consistent with the safety criteria used for the vehicle on the ground, the vehicle is regarded as course deviation if its lateral displacement exceeds 0.5m. As already discussed in Chapter 4, using the Load Transfer Ratio of the entire vehicle body (LTR_v) as the overturning criterion is better than using the Load Transfer Ratio on a single wheel axel or employing the zero vertical contact force on any wheel. The LTR_v is thus adopted here to assess the overturning of the vehicle passing by the tower. If the absolute value of LTR_v is larger than 0.9, the vehicle will be considered overturning. The critical wind speed is defined as the maximum gust wind within a length range around the location of the tower when the vehicle is regarded as overturning or course derivation. In this thesis, the length range is adopted as 3 times the tower width. Within this range, the peak aerodynamic coefficients computed in Chapter 7 have been included.

8.6 CASE STUDY

Based on the RVBW framework and the varying aerodynamic coefficients, the progressive instability and accident velocity of a road vehicle passing by a tower of a long span bridge are studied. The road vehicle is taken as the two-axel high-sided vehicle on the ground investigated in Chapter 4, and also on the deck studied in Chapter 6. The long span bridge is taken as the highway cable-stayed bridge with a main span of 688m studied in Chapter 6. The bridge deck carries a dual two-lane highway on its upper surface. The damping properties, static aerodynamic coefficients, aerodynamic admittance functions, and flutter derivatives have been explained in Section 6.8. The road vehicle moves along the upwind first lane of the deck with an 80km/h velocity under the crosswinds of a 15m/s mean speed. The road roughness level used is Class B, and it is presented in plane. The constant pair (λ_1 , λ_2) for the driver model is determined in Section 4.7.1.3, and the moderate value of (0.2, 0.7) is used here. The vehicle starts 277.8m away from the left end of the bridge to achieve stable movement before embarking on the deck. At 12.501s, 27.981s, 58.941s, and 74.421s, it moves on the bridge deck, reaches the center of the left tower, reaches the center of the right tower, and moves out of the bridge, respectively. In the dynamic response calculation of the RVBW system, the time is advanced with a time step of 0.001s.

8.6.1 Behaviour of Vehicle Passing by Bridge Tower

Figure 8.17 shows the instantaneous wind velocity experienced by the moving vehicle on the bridge in the lateral direction. LT and RT denote the centre line of the left and right tower of the bridge, respectively, and the length range of 3 times the tower width is also indicated in Figure 8.17. The instantaneous wind velocities in the lateral direction are 15.9 and 19.22m/s at LT and RT, respectively, due to randomness of fluctuating winds. In Figure 8.17, the middle span of the bridge deck is selected as zero distance as a reference, for the sake of easy understanding. Figure 8.18 and Figure 8.19 show the vertical displacement and the pitch angle of the vehicle body. These responses are not influenced by the existence of the tower, for they are mainly attributed to the vehicle and bridge interaction including road roughness effect in the vertical direction. Figure 8.20 shows the roll angle. A clear peak of the roll angle occurs when the vehicle just moves out of the right tower. Corresponding to the peaks of roll angle, there are also the peaks in $LTR_{v,}$ as shown in Figure 8.21. Nevertheless, the maximum LTR_v does not exceed 0.9, and the vehicle is regarded as safe in terms of overturning. Under the crosswinds, the driver continues to adjust the steer angle to keep the vehicle moving in the right lane. Figure 8.22 shows the variation of steer angle as the vehicle moves forward. It can be seen that the quick action with a high steer angle is taken by the driver at the location of the right tower to resist the wind shielding effects of the tower. The steer angle reaches the maximum value as the vehicle moves out of the tower. Large lateral displacement occurs at the large steer angle, as shown in Figure 8.23. Although the vehicle can be taken back to the right lane finally, the lateral displacement of the vehicle exceeds 0.5m (see Figure 8.23) at the location of the right tower, and the vehicle is regarded in danger due to sideslip.

8.6.2 Effects of Varying Aerodynamic Forces

The road vehicle passing by the bridge tower without considering the influence of the tower on the aerodynamic coefficients of the vehicle is also simulated, and the results are compared with these presented in Section 8.6.1. Figure 8.24 shows the comparison of the LTR_v that denotes the tendency of the overturning of the vehicle. It can be seen that around the locations of both towers, disregarding the influence of the tower on the aerodynamic forces on the vehicle would lead to an underestimation of the magnitude of the LTR_v. It can also be deduced that neglecting varying aerodynamic coefficients induced by the tower would result in an underestimation of the overturning risk of the vehicle passing by the bridge tower. Figure 8.25 shows the lateral displacement of the vehicle body for the two cases. At the locations of both towers, the lateral displacement is also underestimated if the influence of the tower on the aerodynamic forces of the vehicle is not considered, so does the risk of accident caused by the exceeded course deviation.

8.6.3 Effects of Dynamic Responses of Bridge

The responses of the bridge under a single moving vehicle in crosswinds are very small (see Chapter 6). With this consideration, assessing the safety of a single vehicle passing by a bridge tower may be approximated in order to assess the safety of the single vehicle moving on the ground, but the varying aerodynamic coefficients of the vehicle induced by the tower would need to be considered. To validate this approximation, a supplemented case is calculated here with the vehicle moving on the ground with the same road surface and crosswinds. The varying aerodynamic coefficients are applied on the vehicle by assuming that the towers are on the ground with the same positions as they are on the bridge. Figure 8.26 and Figure 8.27 show the comparison of the LTR_v value and the lateral displacement, respectively, of the vehicle on the ground and on the bridge. From the results presented in these figures, one may see that considering the ground condition with the existence of the tower is feasible to assess the safety of a single vehicle passing by a bridge tower. In this regard, the safety of a single vehicle passing by a tower can be predicted in a practical way using the ground condition with the existence of the tower to save the computational efforts without losing accuracy.

8.6.4 Accident Vehicle Speed and Comparison with Ground Condition

As the vehicle passes by the tower, the accident vehicle speed occurs if the vehicle is found either overturning or course derivation within a length range around the location of the tower. In this study, the length range is adopted as 3 times the width of the tower. Within this range, the peak aerodynamic coefficients are included (see the aerodynamic coefficients computed in Chapter 7). For the calculated 80km/h vehicle passing by the bridge tower in Section 8.6.1, the accident gust wind speed within the concerned length range is 23.36 m/s. Through a series simulation of the single vehicle passing by the tower using the practical way without considering the responses of the bridge as concluded in Section 8.6.3, the accident vehicle speeds are calculated. It is found that for the single vehicle passing by the tower, the course deviation occurs before the overturning, which is different from the conclusion for the vehicle moving on the ground without the effects of the tower. The calculated accident vehicle speeds and the comparisons with these on the ground condition are shown in Figure 8.28. Under the same crosswind gust, it is more dangerous for the vehicle passes by the bridge tower than it moves on the ground.

8.7 SUMMARY

In this chapter, the varying aerodynamic coefficients of the moving vehicle on the bridge influenced by the tower are used in the framework of RVBW to consider the safety of the road vehicle passing by the bridge tower. The shielding ratios are defined to describe the influence of the tower on the aerodynamic coefficients of the moving vehicle. These coefficients change with the relative angle and a linear expression is used to describe this relationship. These coefficients also vary with the location from the tower, and Gaussian multi-peak functions are used to fit the relationship. After extensive studies on a single vehicle passing by a bridge tower, the major points can be summarized as follows:

- As the road vehicle passes by the bridge tower, its vertical displacement and the pitch angle are not influenced obviously by the existence of the tower. However, its roll angle, LTR_v index, and lateral displacement are influenced significantly due to the shielding effects of the tower. To keep the right course of the vehicle, the driver needs to take quick action with a high steer angle.

- Neglecting the varying aerodynamic coefficients induced by the tower would lead one to underestimate both overturning and course deviation risk of the vehicle passing by the bridge tower.

- The influence of the dynamic responses of the bridge on the safety of the single vehicle passing by the bridge tower under crosswinds is insignificant. It can be a practical way to assess the safety of the single vehicle passing by the bridge tower by considering the vehicle on the ground, but with the varying aerodynamic coefficients induced by the tower.

- The accident vehicle speeds of a single road vehicle passing by the bridge tower are calculated using the practical way. It is found that course deviation occurs before overturning as the vehicle passes by the bridge tower. This finding is different from that for the moving vehicle on the ground, where overturning occurs first. It is also found that the accident vehicle speeds of the vehicle passing by the bridge tower are lower than those for the vehicle moving on the ground.

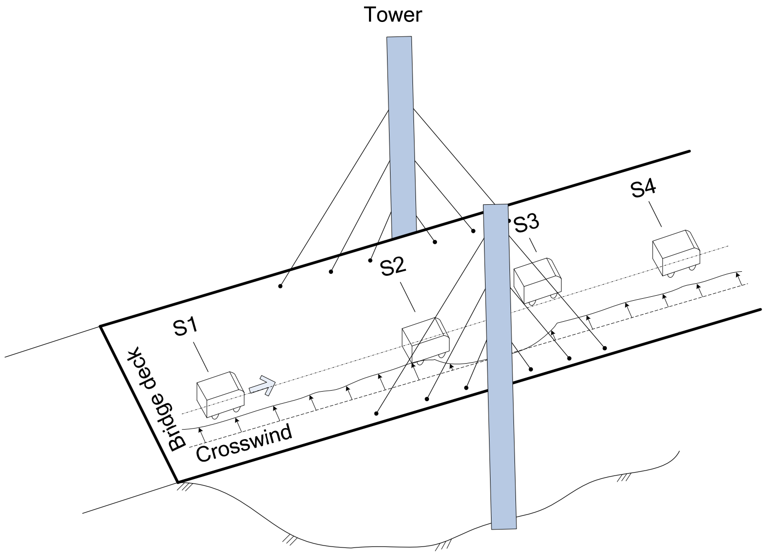

Figure 8.1 Schematic diagram of a vehicle passing by a bridge tower under crosswinds

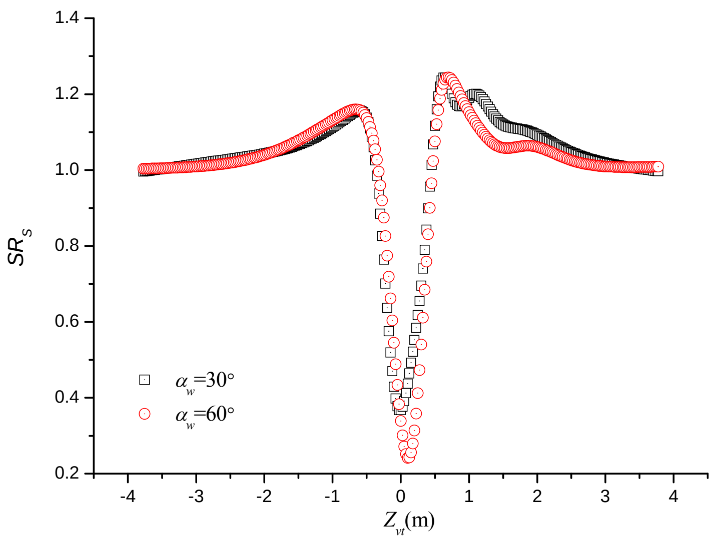

Figure 8.2 Shielding ratio of the side coefficient SR_S

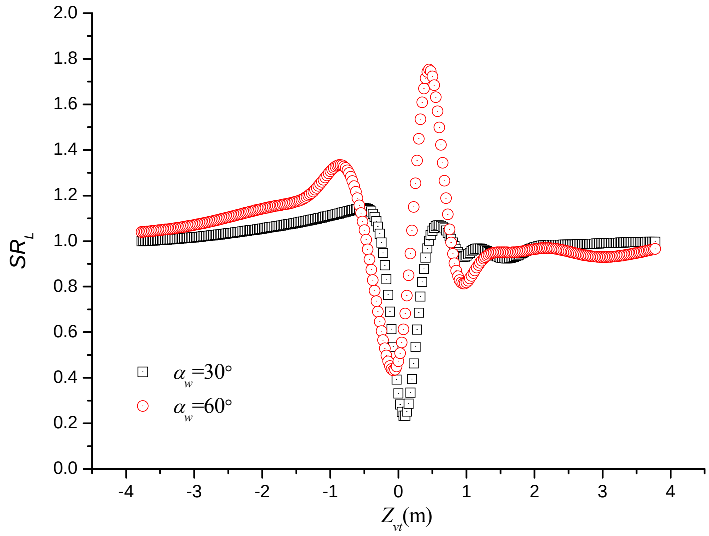

Figure 8.3 Shielding ratio of the lift coefficient SR_L

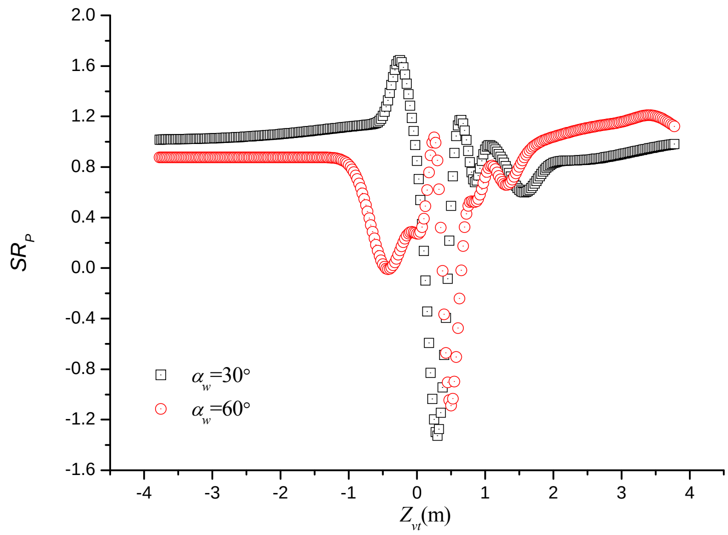

Figure 8.4 Shielding ratio of the pitching moment coefficient SR_P

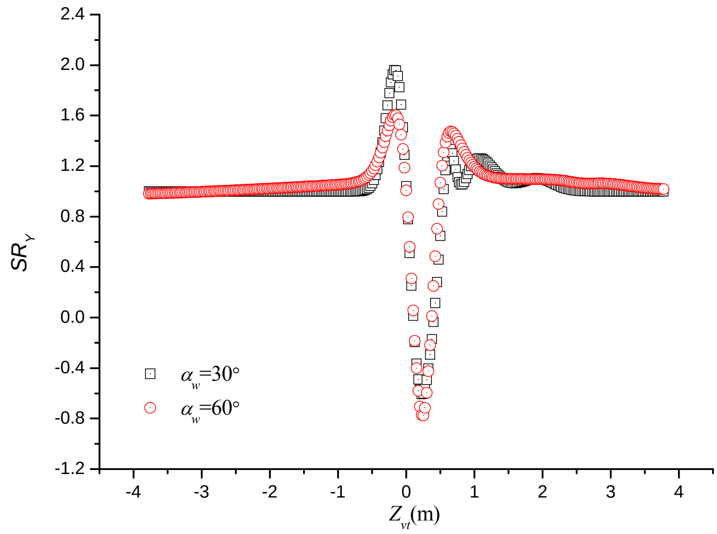

Figure 8.5 Shielding ratio of the yawing moment coefficient SR_Y

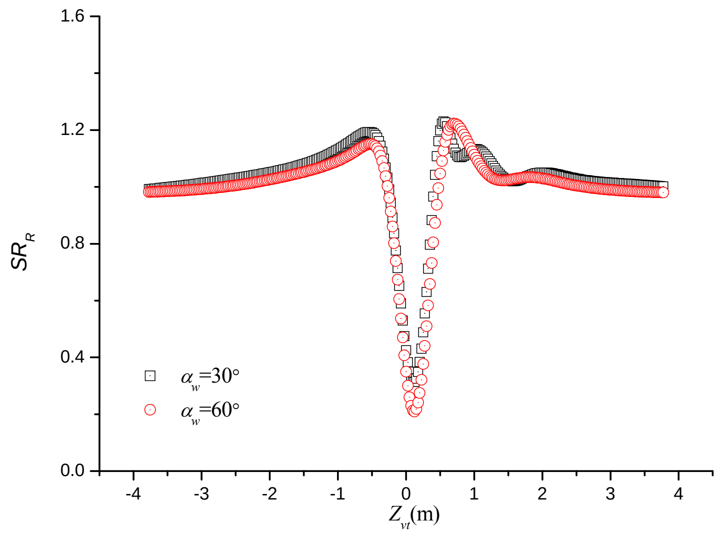

Figure 8.6 Shielding ratio of the rotating moment coefficient SR_R

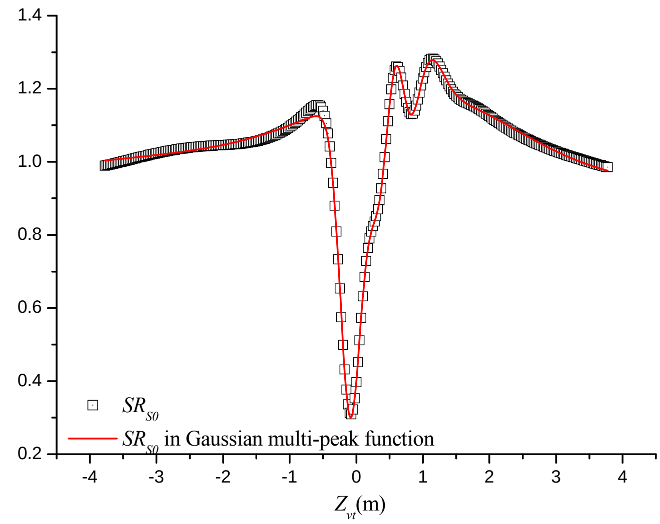

Figure 8.7 Linear constants of the shielding ratio of the side coefficient: SR_{S0}

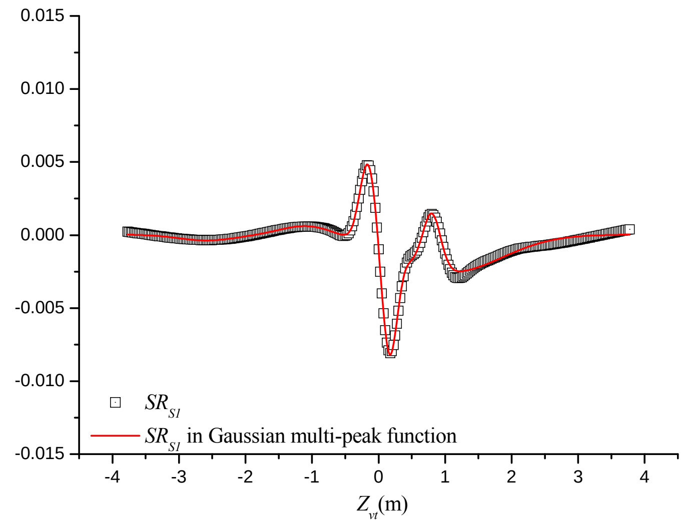

Figure 8.8 Linear constants of the shielding ratio of the side coefficient: SR_{S1}

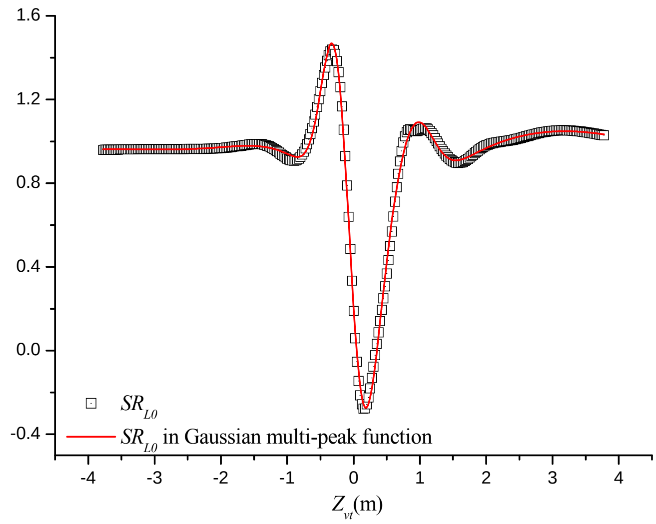

Figure 8.9 Linear constants of the shielding ratio of the lift coefficient: SR_{L0}

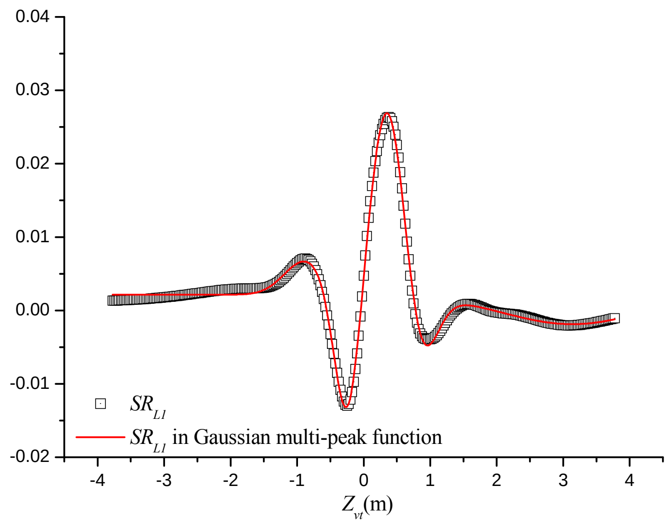

Figure 8.10 Linear constants of the shielding ratio of the lift coefficient: SR_{L1}

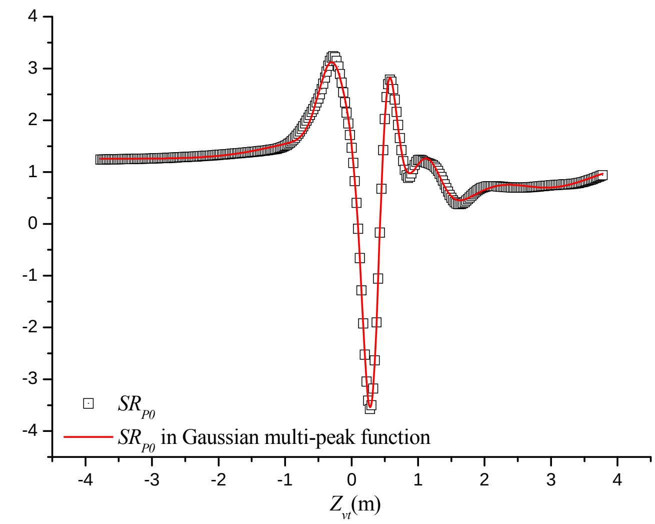

Figure 8.11 Linear constants of the shielding ratio of the pitching moment coefficient: SR_{P0}

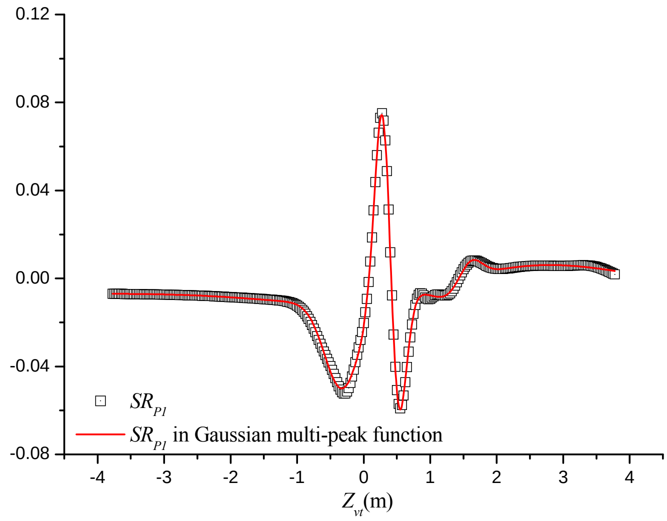

Figure 8.12 Linear constants of the shielding ratio of the pitching moment coefficient: SR_{P1}

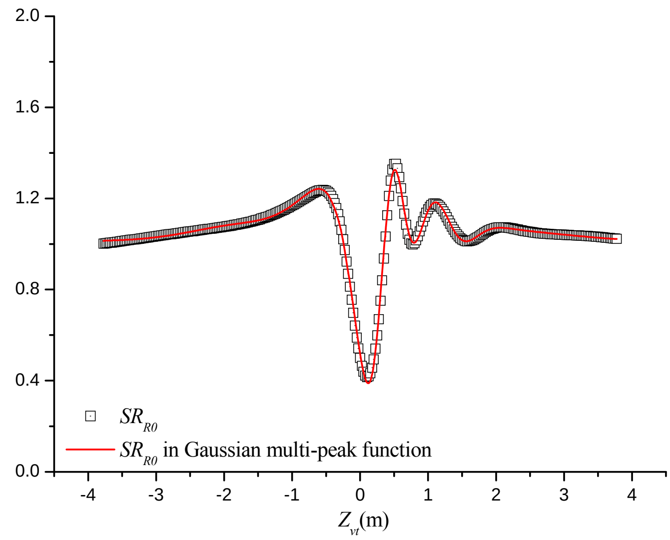

Figure 8.13 Linear constants of the shielding ratio of the rotating moment coefficient: SR_{R0}

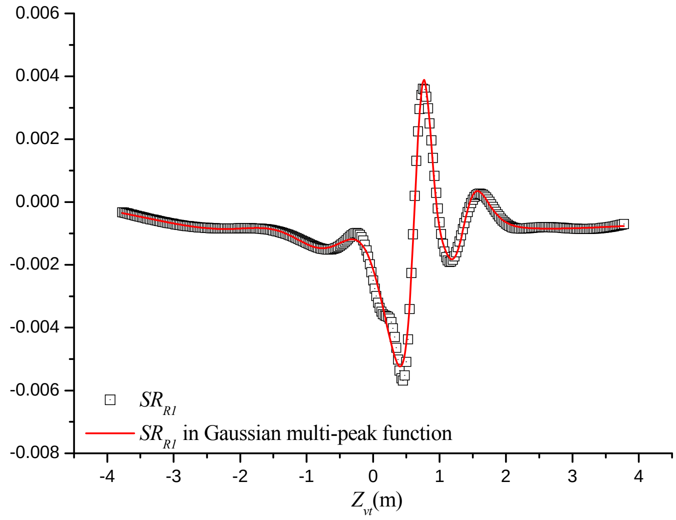

Figure 8.14 Linear constants of the shielding ratio of the rotating moment coefficient: SR_{R1}

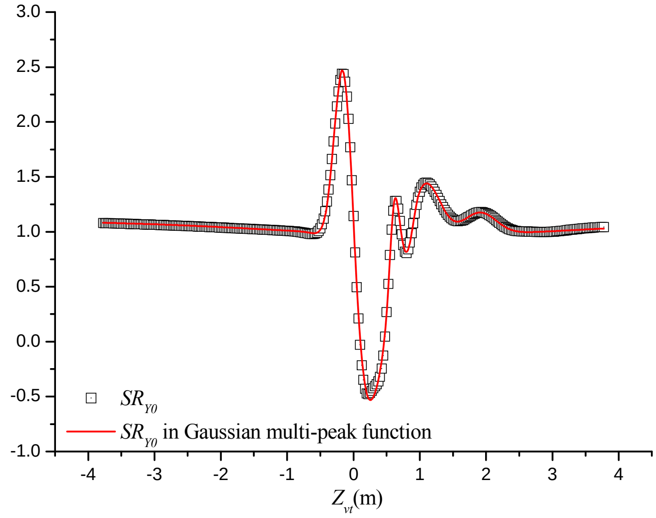

Figure 8.15 Linear constants of the shielding ratio of the yawing moment coefficient: SR_{Y0}

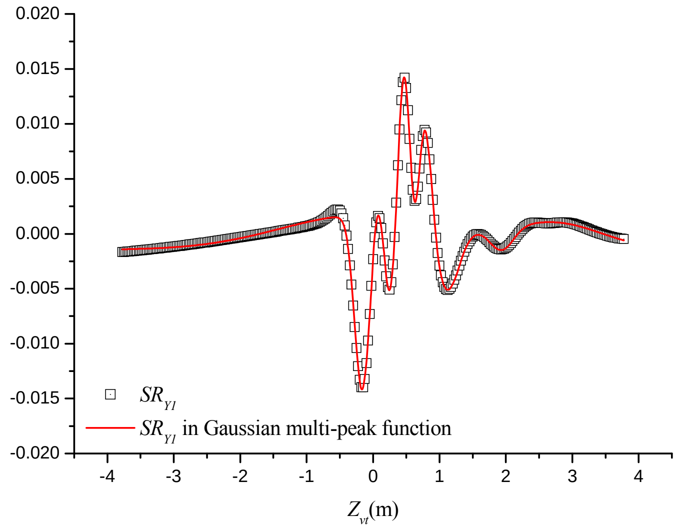

Figure 8.16 Linear constants of the shielding ratio of the yawing moment coefficient: SR_{Y1}

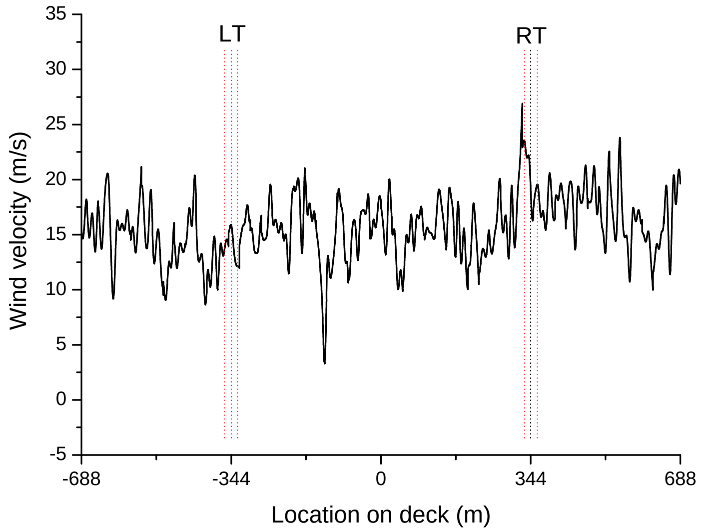

Figure 8.17 Wind speed at the location of the moving vehicle

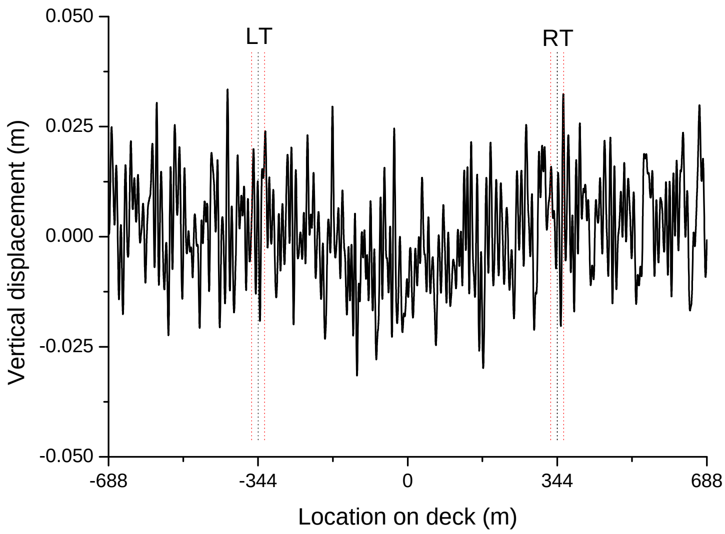

Figure 8.18 Vertical displacement of the vehicle body

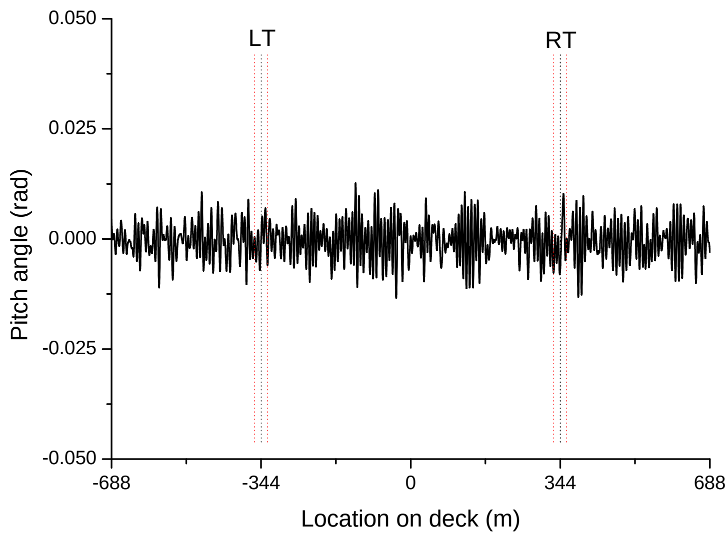

Figure 8.19 Pitch angle of the vehicle body

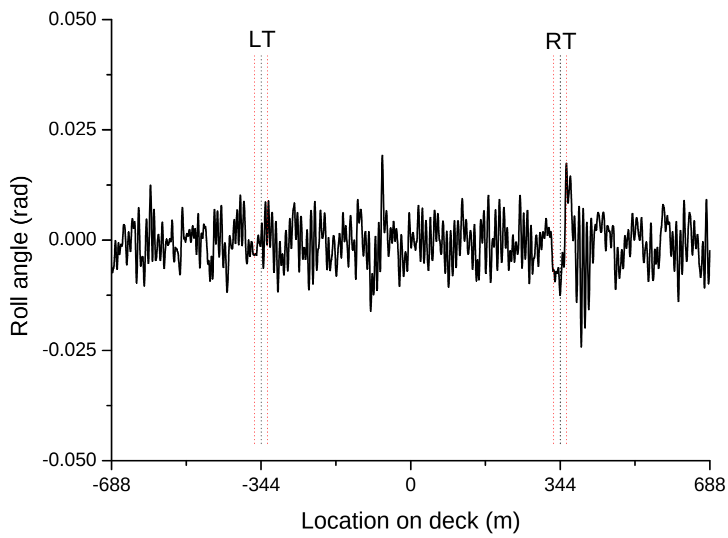

Figure 8.20 Roll angle of the vehicle body

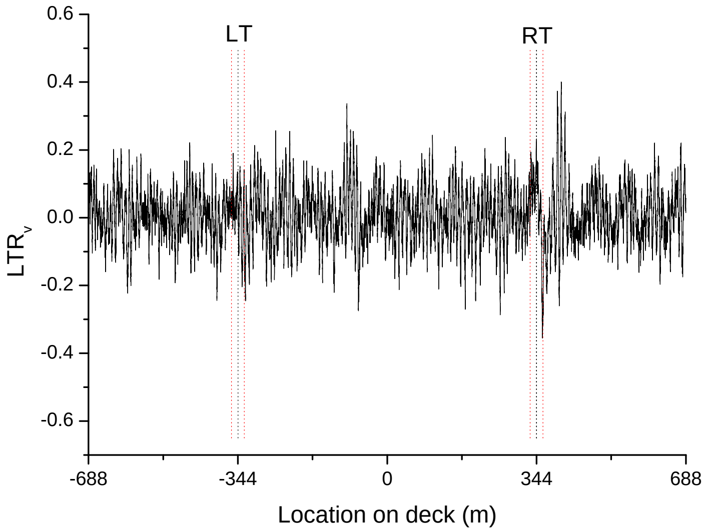

Figure 8.21 LTR_v of the vehicle body

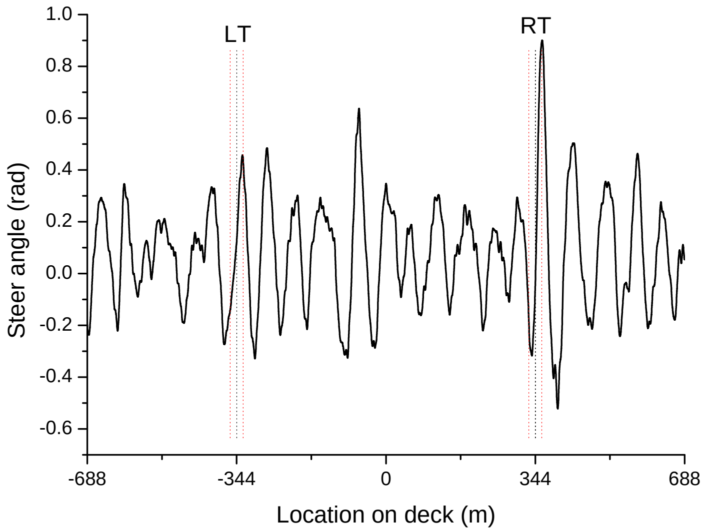

Figure 8.22 Steer angle of the vehicle body

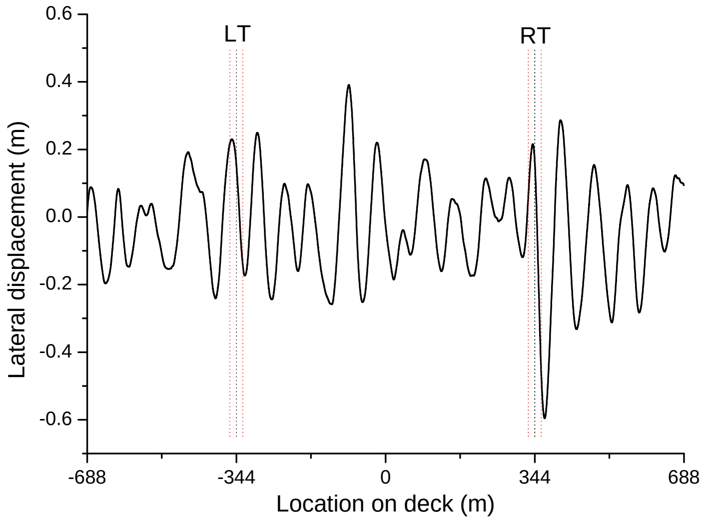

Figure 8.23 Lateral displacement of the vehicle body

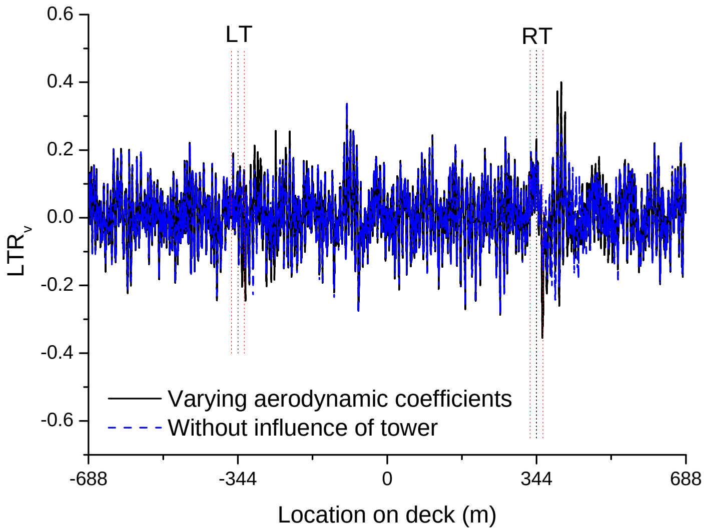

Figure 8.24 Comparison of LTR_v of the vehicle body

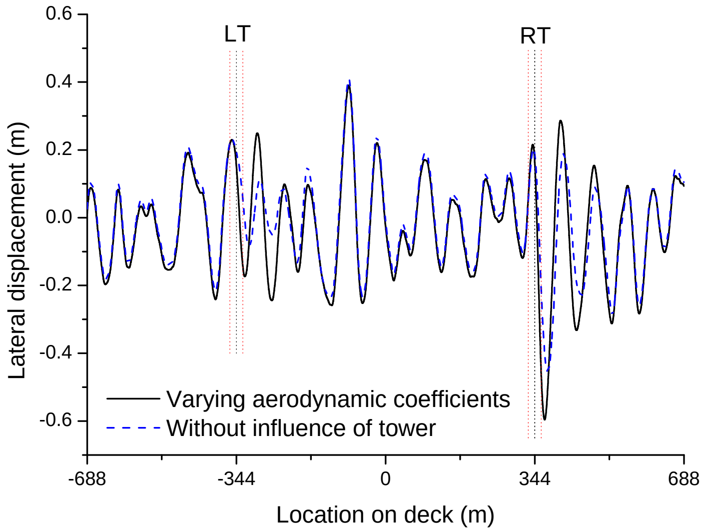

Figure 8.25 Comparison of the lateral displacement of the vehicle

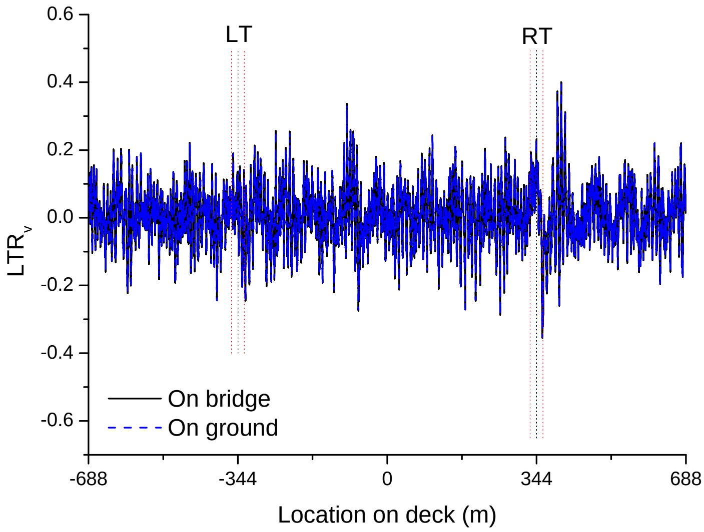

Figure 8.26 Comparison of the LTR_v of the vehicle body

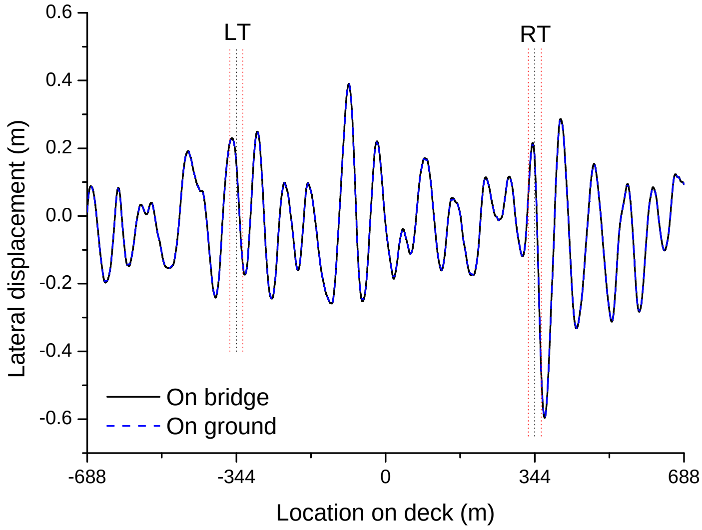

Figure 8.27 Comparison of the lateral displacement of the vehicle

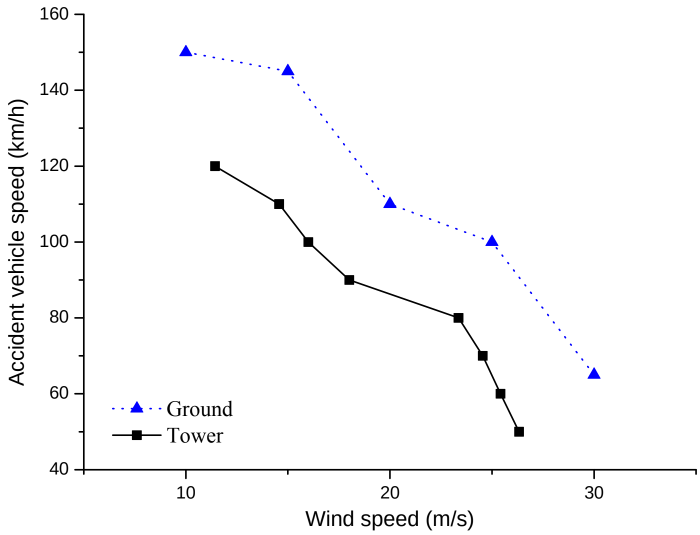

Figure 8.28 Accident speeds and comparison with the ground condition

CHAPTER 9

CONCLUSIONS AND RECOMMENDATIONS

9.1 CONCLUSIONS

This thesis mainly investigates the ride comfort and safety of road vehicles moving on either the ground or long-span bridges under crosswinds using advanced vehicle models and considering aerodynamic interferences among moving vehicles, bridge deck, bridge tower and the ground. In particular, this research is devoted to: (1) analyzing the aerodynamic interferences between a moving vehicle and the ground using CFD, (2) developing an advanced vehicle model able to demonstrate the progressive instability of the moving vehicle on the ground with emphasis on the lateral motions under the action of both crosswinds and drivers, (3) exploring the aerodynamic interferences between a moving vehicle and the deck of a real long span bridge employing CFD, (4) forming a new framework of the coupled Road Vehicle-Bridge-Wind system by incorporating the advanced road vehicle model, the road roughness in plane, and the driver's model to evaluate the ride comfort of the vehicle, (5) studying the variation of the aerodynamic forces on the vehicle during the time when it passes by a bridge tower using CFD, (6) applying the framework of the RVBW and the varying aerodynamic coefficients to assess the safety of the vehicle passing by a bridge tower. The main conclusions of this thesis are summarized as follows.

1. A numeral model is set up to simulate the flows around a stationary vehicle on the ground using the CFD. The flows separate at different locations, and form different vortices in the wake of the vehicle at different yaw angles. Particularly, the separated flows from the corner between the upwind side surface and the top surface reattach to the top surface at 30° yaw angle. The variations of the

computed aerodynamic coefficients of the stationary vehicle with yaw angle agree with the results from wind tunnel tests. The differences of the aerodynamic coefficients between the simulations and the wind tunnel tests are smaller than the variation from the different wind tunnel tests. The numerical model is then extended to simulate the flows around the moving vehicle by considering a moving ground simulation. The influences of the relative motion between the vehicle and the ground are only in the boundary layer near the ground. The effects become weaker and weaker with the increase of the yaw angle. The differences in the aerodynamic coefficients between the moving vehicle and the stationary vehicle with the same yaw angle are not obvious.

2. The progressive instability of the road vehicle moving on the ground under a crosswind gust is explored using the advanced vehicle model. The wheels of the road vehicle jump from the ground at different occasions. Although both wheels on the upwind side lose contact with the ground, the maximum roll angle of the vehicle is not large. The off-road wheels can even go back to the ground. The safety of the moving vehicle is then analyzed. Using the LTR_v index instead of the LTR_f/LTR_r index as the overturning criterion can remove the misjudgment as one wheel jumps from the ground. Roughness in plane has no significant contribution to the overturning compared with roughness in line. The displacements and LTR value of the high-sided vehicle are hard to control in a 0.5s crosswind gust due to the time delay of the reaction of the driver. The ride comfort of the moving vehicle is further studied. As the vehicle moves on the ground, its vertical acceleration at the driver's seat is mainly excited by the vertical movement of the vehicle due to road roughness. The lateral acceleration at the driver's seat is mainly excited by the rotating movement due to the crosswinds and the steer angle controlled by the driver. In the low frequency domain, the behavior of the driver, in addition to the fluctuating crosswinds, has a significant effect on the ride comfort in the lateral direction. The lateral acceleration response at the driver's seat rises significantly around the natural

frequency of rotating movement. As a result, road roughness in plane has to be considered in the evaluation of the ride comfort, particularly in the lateral direction. The total FWRMSA and FWRMSA in the vertical direction increase with the increase of the vehicle speed in general, while the FWRMSA in the lateral direction increases first, and then keeps a relatively stable level.

3. A CFD numerical model is formed to simulate the flows around the stationary vehicle on the first lane of a real long span bridge deck. Compared with the tested aerodynamic coefficients of the stationary vehicle on the deck, the varying patterns of all the six computed aerodynamic coefficients with the yaw angle agree with the results from the wind tunnel tests. The computed drag coefficients and rotating moment coefficients are almost the same as those tested in the wind tunnel. The maximum difference of the aerodynamic force coefficients is about 1.06 for the lift coefficient at the 60° yaw angle. The maximum difference of the aerodynamic moment coefficients is about 0.16 for the pitching moment coefficient at the 90° yaw angle. With the presence of the vehicle, the aerodynamic coefficients of the bridge deck change abruptly. The numerical model is then extended to simulate the relative motion between the vehicle and the deck. The flows beneath the moving vehicle are more complicated than those beneath the stationary vehicle. The movement of the vehicle on the first lane of the bridge deck does affect the aerodynamic coefficients of the bridge deck, but has only slight effects on the aerodynamic coefficients of the vehicle if the relative motion between the vehicle and the wind is taken into account.

4. A new framework of the coupled Road Vehicle-Bridge-Wind (RVBW) system is formed by incorporating the advanced road vehicle model. The feasibility of the established framework of the RVBW system is confirmed. For a single road vehicle passing by a long span bridge, there are only slight differences in the vertical and lateral responses of the bridge deck when either using the aerodynamic coefficients of the moving vehicle on the deck or using the

aerodynamic coefficients of the moving vehicle on the ground. The adoption of the aerodynamic coefficients of a road vehicle on the ground and the aerodynamic coefficients of the pure bridge deck for a single vehicle passing over the bridge deck may lead to an underestimation of the torsional angular response of the bridge. The adoption of the aerodynamic coefficients of a road vehicle on the ground and the aerodynamic coefficients of the pure bridge deck for a single vehicle passing over the bridge deck may lead to the same level of the rms accelerations of the vehicle as compared with the actual aerodynamic coefficients in the situation of the moving vehicle on the deck. With the increase of vehicle speed, the ride comfort becomes worse. Slight differences exist in the ride comfort of the single vehicle moving on the ground and the bridge deck.

5. The flows around the stationary vehicle immerging in the wake of a bridge tower are simulated using CFD. The simulated side coefficient, lift coefficient, and absolute yawing moments are larger than the measured ones while the rotating moment coefficients are close to the measured ones. The differences in aerodynamic coefficients between the simulations and wind tunnel tests are expected in the current study, if considering the complexity of the problem and uncertainties involved in wind tunnel tests and numerical simulations. The flows around the moving vehicle-deck-tower system are simulated with different yaw angles. The flows around the vehicle changes from the lengthwise feature to the crosswise feature as the yaw angle increases. The shielding effects of the tower on the aerodynamic forces of the vehicle are significant in the cases with the yaw angle of 30° and 60°. As the vehicle approaches the tower, the absolute values of the side coefficient, the yawing moment coefficient and the rotating moment coefficient increase continuously to their respective peak values. The side coefficient and the rotating moment coefficient then decrease to the lowest values as the vehicle is totally immerged by the tower. These two coefficients reach peak values again as the vehicle moves out of the tower. The yawing moment reaches a maximum value when the side force decreases at the location

near $-B_T$, and it then reduces and increases again. The lift and pitching moment also yield peak values at the sides of the tower; and they are small, as the vehicle is directly behind the tower. The drag force decreases at the two sides of the tower and approaches to the same value as in the case of no crosswind if the vehicle is just behind the tower.

6. The varying aerodynamic coefficients of the moving vehicle on the bridge influenced by the tower are used in the framework of RVBW. As the road vehicle passes by the bridge tower, its vertical displacement and the pitch angle are not influenced obviously. Its roll angle, LTR_v index, and lateral displacement are influenced significantly due to the shielding effects of the tower. To keep the right course of the vehicle, the quick action with a high steer angle needs to be taken by the driver. Neglecting the varying aerodynamic coefficients induced by the tower would underestimate both overturning and course deviation risk of the vehicle passing by the bridge tower. The influence of the dynamic responses of the bridge on the safety of the single vehicle passing by the bridge tower under crosswinds is insignificant. It can be a practical way to assess the safety of the single vehicle passing by the bridge tower by considering the vehicle on the ground, but with the varying aerodynamic coefficients induced by the tower. The accident vehicle speeds of a single road vehicle passing by the bridge tower are calculated using the practical way. It is found that course deviation occurs before overturning as the vehicle passes by the bridge tower. This finding is different from that for the moving vehicle on the ground where overturning occurs first. It is also found that the accident vehicle speeds of the vehicle passing by the bridge tower are lower than those for the vehicle moving on the ground.

9.2 RECOMMENDATIONS

Although some progress has been made in this thesis for the ride comfort and safety evaluation of the road vehicle moving on the ground or the long-span bridge, several important issues that deserve further studies remain.

1. Only one particular type of vehicle is studied in this thesis. Different types of road vehicles require evaluation in the future. The aerodynamic forces on the bridge deck under a group of vehicles also need to be calculated to reflect a real situation.

2. Unsteady wind loads on both the road vehicle and the bridge excited by the vortex shedding and their influence to the safety and ride comfort of the vehicle should be further investigated.

3. CFD with RANS method is employed to simulate the flows around and the aerodynamic forces on the moving vehicle on the ground, on the bridge deck, and passing by a bridge tower. Due to the limitation of the used computer facility, only several cases with a few yaw angles have been carried out. With the further development of computer capacity, more cases shall be considered to obtain more accurate aerodynamic force data. Compared with RANS method, more advanced CFD method such as Large Eddy Simulation or Detached Eddy Simulation can be employed to study the possible unsteady flows and aerodynamic forces on the vehicle in a high accuracy.

4. More samples of the fluctuating wind velocities and road roughness shall be simulated in the future so that reliability analysis can be performed in order to have more accurate evaluation of the safety and ride comfort of the road vehicle.

REFERENCES

Agar T.J.A. (1989). Aerodynamic flutter analysis of suspension bridge by a model technique. *Engineering Structures*, *11*, 75-82.

Akin E. and Mofid M. (1989). Numerical solution for response of beams with moving mass. *Journal of Structural Engineering*, *115*(1), 120–131.

Akoussah E., Fafard M., Talbot M. and Beaulieu D. (1997). Parametric study of the dynamic amplification factor of single span concrete bridges. *Canadian Journal of Civil Engineering*, *24*(2).

Amandolèse X. and Crémona C. (2005). Analysing fluid loadings on moving bluff bodies using properorthogonal decomposition. *Journal of Fluids and Structures*, *20*(4), 577-587.

Ammon D. (1991). Problems in road surface modeling. *Vehicle system dynamics*, *20*, 28-41.

Ansys, Inc. Fluent help in Ansys 13.0

Argentini T., Ozkan E., Rocchi D., Rosa L. and Zasso A. (2011). Cross-wind effects on a vehicle crossing the wake of a bridge pylon. *Journal of Wind Engineering and Industrial Aerodynamic*s, *6-7*, 734-740.

Ayre R.S. and Jacobsen L.S. (1950). Transverse vibration of a two-span beam under the action of a moving alternating force. *Journal of Applied Mechanics*, *17*(3), 283-90.

Ayre R.S., Ford G. and Jacobsen L.S. (1950). Transverse vibration of a twospan beam under the action of a moving constant force. *Journal of Applied Mechanics*, *17*(1), 1-12.

Bai Y., Sun D. and Lin J. (2010). Three dimensional numerical simulations of long-span bridge aerodynamics, using block-iterative coupling and DES. *Computers & Fluids*, *39*(9), 1549-1561.

Baker C.J. (1986). A simplified analysis of various types of wind-induced road vehicle accidents. *Journal of Wind Engineering and Industrial Aerodynamics*, *22*, 69-85.

Baker C.J. (1987). Measures to control vehicle movement at exposed sites during windy periods. *Journal of Wind Engineering and Industrial Aerodynamics*, *25*(2), 151-161.

Baker C.J. (1988). High sided articulated road vehicles in strong cross winds. Journal of Wind Engineering and Industrial Aerodynamics, *31*, 67-85.

Baker C.J. (1993). The behaviour of road vehicles in unsteady cross winds. *Journal of Wind Engineering and Industrial Aerodynamics*, *49*, 439-448.

Baker C.J. (1994). The quantification of accident risk for road vehicles in cross winds. *Journal of Wind Engineering and Industrial Aerodynamics*, *52*, 93-107.

Baker C.J. and Humphreys N.D. (1996). Assessment of the adequacy of various wind tunnel techniques to obtain aerodynamic data for ground vehicles in cross winds. *Journal of Wind Engineering and Industrial Aerodynamics*, *60*, 49-68.

Baker C.J. and Reynolds S. (1992). Wind-induced accidents of road vehicles. *Accident Analysis & Prevention*, *24*(6), 559-575.

Beauvais F.N., Tignor S.C. and Turner T.R. (1968). Problems of ground simulation in automotive aerodynamics. *SAE Paper 680121*.

Bettle J., Holloway A.G.L. and Venart J.E.S. (2003). A computational study of the aerodynamic forces acting on a tractor-trailer vehicle on a bridge in cross-wind. *Journal of Wind Engineering and Industrial Aerodynamics*, *91*, 573–592.

Bogsjö K. (2008). Coherence of road roughness in left and right wheel-path. *Vehicle system dynamics*, *46*, 599-609.

Bonis B., Quagliotti F. and Dallara G. (1987). Is the 'moving belt ground plane' really necessary for automobile testing in the wind tunnel. *SAE 870719*.

Boonyapinyo V., Miyata T. and Yamada H. (1999). Advanced aerodynamic analysis of suspension bridges by statespace approach. *Journal of Structural Engineering*, *125*(12), 1357-1366.

Boonyapinyo V. and Janesupasaeree T. (2010). Data-driven stochastic subspace identification of flutter derivatives of bridge decks. *Journal of wind engineering and industrial aerodynamics*, *98*, 784-799.

Braun A. and Awruch A. (2008). Finite element simulation of the wind action over bridge sectional models: Application to the Guamá River Bridge (Pará State, Brazil). *Finite Elements in Analysis and Design*, *44*(3), 105-122.

Bruno L. and Khris S. (2003). The validity of 2D numerical simulations of vortical structures around a bridge deck. *Mathematical and Computer Modelling*, *37*(7-8), 795-828.

Bruno L., Khris S. and Marcillat J. (2001). Numerical simulation of the effect of section details and partial streamlining on the aerodynamics of bridge decks. *Wind & Structures*, *4*(4), 315-332.

Bucher C.G. and Lin Y.K. (1988). Stochastic stability of bridges considering coupled modes, *Journal of Engineering Mechanics*, *114*(EM12), 2055-2071.

Burgin K., Adey P. and Beatham J. (1986). Wind tunnel tests on road vehicle models using a moving belt simulation of ground effect. *Journal of Wind Engineering and Industrial Aerodynamics*, *22*(2-3), 227-236.

Cai C.S. and Chen S.R. (2004). Framework of vehicle–bridge–wind dynamic analysis. *Journal of Wind Engineering and Industrial Aerodynamics*, *92*, 579-607.

Cao Y.H., Xiang H.F. and Zhou Y. (2000). Simulation of stochastic wind velocity field on long-span bridges. *Journal of Engineering Mechanics*, *126* (1), 1-6.

Charuvisit S., Kimura K. and Fujino Y. (2004). Experimental and semi-analytical studies on the aerodynamic forces acting on a vehicle passing through the wake of a bridge tower in cross wind. *Journal of Wind Engineering and Industrial Aerodynamics*, *92*(9), 749-780.

Cheli F., Belforte P., Melzi S., Sabbioni E. and Tomasini G. (2006). Numerical-experimental approach for evaluating cross-wind aerodynamic effects on heavy vehicles. *Vehicle System Dynamics*, *44 supplement,* 791-804.

Chen S.R. and Cai C.S. (2004). Accident assessment of vehicles on long-span bridges in windy environments. *Journal of Wind Engineering and Industrial Aerodynamics*, *92*(12), 991-1024.

Chen S.R. and Cai C.S. (2007). Equivalent wheel load approach for slender cable-stayed bridge fatigue assessment under traffic and wind: feasibility study.

Journal of Bridge Engineering, *12*(6), 755-764.

Chen F. and Chen S. (2011). Reliability-based assessment of vehicle safety in adverse driving conditions. *Transportation Research Part C*, *19*, 156-168.

Chen S. and Chen F. (2010). Simulation-based assessment of vehicle safety behavior under hazardous driving conditions. *Journal of Transportation Engineering*, *136*(4), 304-315.

Chen S.R., Chang C.C. and Cai C.S. (2008). Study on stability improvement of suspension bridge with high-Sided vehicles under wind using tuned-liquid-damper. *Journal of Vibration and Control*, *14*(5), 711-730.

Chen S. and Wu J. (2010). Dynamic performance simulation of long-span bridge under combined loads of stochastic traffic and wind. *Journal of Bridge Engineering*, *15*(3), 219-230.

Chen Z.Q. and Yu X.D. (2002). A new method for measuring flutter self-excited forces of long-span bridges. *China Civil Engineering Journal*, *35*, 34-41.

Chen X., Matsumoto M. and Kareem A. (2000). Time domain flutter and buffeting response of bridges. *Journal of Engineering Mechanics*, *126*(1), 7-16.

Chen X.D. (2007). Anaysis of vehicle safety under cross wind on long span bridges. PhD thesis, Tongji University (in Chiness).

Chen Z.W., Xu Y.L., Li Q. and Wu D.J. (2011). Dynamic stress analysis of long span suspension bridges under wind, railway, and highway loadings. *Journal of Bridge Engineering*, *16*(3), 383-391.

Cheung M.S. and Chan B.Y.B. (2010). Operational requirements for long-span bridges under strong wind events. *Journal of Bridge Engineering*, *15*(2), 131-143.

Chowdhury A.G. and Sarkar P.P. (2003). A new technique for identification of eighteen flutter derivatives using a three-degree-of-freedom section model. *Engineering Structures*, *25*, 1762-1772.

Chowdhury A.G. and Sarkar P.P. (2004). Identification of eighteen flutter derivatives. *Wind & Structures*, *7*(3), 187-202.

Chu C.R., Chang C.Y., Huang C.J., Wu T.R., Wang C.Y. and Liu M.Y. (2013).

Windbreak protection for road vehicles against crosswind. *Journal of Wind Engineering and Industrial Aerodynamics*, *116*, 61-69.

Cochran L. and Derickson R. (2011). A physical modeler's view of computational wind engineering. *Journal of Wind Engineering and Industrial Aerodynamics*, *99*, 139-153.

Cole D.J. (2001). Fundamental issues in suspension design for heavy road vehicles. *Vehicle System Dynamics*, *35*, 319-360.

Coleman S.A. and Baker C.J. (1990). High sided road vehicles in cross winds. *Journal of Wind Engineering and Industrial Aerodynamics*, *36*, 1383-1392.

Coleman S.A. and Baker C.J. (1994). An experimental study of the aerodynamic behaviour of high sided lorries in cross winds. *Journal of Wind Engineering and Industrial Aerodynamics*, *53*, 401-429.

Davenport A.G. (1962). Buffeting of a suspension bridge by storm winds. *Journal of Structural Engineering*, *88*(6), 233-264.

Diana G.., Bruni S., Cigada A. and Zappa E. (2002). Complex aerodynamic admittance function role in buffeting response of a bridge deck. *Journal of Wind Engineering and Industrial Aerodynamics*, *90*, 2057-2072.

Dorigatti F., Sterling M., Rocchi D., Belloli M., Quinn A.D., Baker C.J. and Ozkan E. (2012). Wind tunnel measurements of crosswind loads on high sided vehicles over long span bridges. *Journal of Wind Engineering and Industrial Aerodynamics*, *107-108*, 214-224.

Dung N.N., Miyata T., Yamada H. and Minh N.N. (1998). Flutter response in long span bridges with wind-induced displacement by mode tracing method. *Journal of Wind Engineering and Industrial Aerodynamics*, *77&78*, 367-379.

Esmailzadeh E. and Ghorashi M. (1997). Vibration analysis of a Timoshenko beam subjected to a traveling mass. *Journal of Sound and Vibration*, *199*(4), 615-628.

Fafard M., Bennur M. and Savard M. (1997). A general multi-axle vehicle model to study the bridge-vehicle interaction. *International Journal of Engineering Computations*, *14*(5), 491-508.

Fago B., Lindner H. and Mahrenholtz O. (1991). The effect of ground simulation on the flow around vehicles in wind tunnel testing. *Journal of Wind Engineering and Industrial Aerodynamics*, *38*(1), 47-57.

Falco M., Curami A. and Zasso A. (1992). Nonlinear effects in sectional model aeroelastic parameter identification. *Journal of Wind Engineering and Industrial Aerodynamics*, *42*, 1321-1332.

Felszeghy S.F. (1996a). The Timoshekno beam on an elastic foundation and subject to a moving step load, part 1: Steady-state response. *Journal of Vibration and Acoustics*, *118*, 277-284.

Felszeghy S.F. (1996b). The Timoshekno beam on an elastic foundation and subject to a moving step load, part 2: transient response. *Journal of Vibration and Acoustics*, *118*, 285-291.

Federal Highway Administration (2014). How do weather events impact roads? http://www.ops.fhwa.dot.gov/weather/q1_roadimpact.htm. Retrieved February 6, 2014.

Fransos D. and Bruno L. (2010). Edge degree-of-sharpness and free-stream turbulence scale effects on the aerodynamics of a bridge deck. *Journal of Wind Engineering and Industrial Aerodynamics*, *98*(10-11), 661-671.

Fuller J., Best M., Garret N. and Passmore M. (2013). The importance of unsteady aerodynamics to road vehicle dynamics. *Journal of Wind Engineering and Industrial Aerodynamics, 117*, 1-10.

Fujiwara A., Kataoka H., and Ito M. (1993). Numerical-simulation of flow-field around an oscillating bridge using finite-difference method. *Journal of Wind Engineering and Industrial Aerodynamics*, *46-7*, 567-575.

Fung Y.C. (1995). An introduction to the Theory of aeroelasticity. Wiley, New York.

Ge Y.J., Lin Z.X., Cao F.C., Pang J.B. and Xiang H.F. (2002). Investigation and prevention of deck galloping oscillation with computational and experimental techniques. *Journal of Wind Engineering and Industrial Aerodynamics*, *90*(12-15), 2087-2098.

Ge Y.J. and Tanaka H. (2000). Aerodynamic flutter analysis of cable-supported bridges by multi-mode and full-mode approaches. *Journal of Wind Engineering* *and Industrial Aerodynamics*, 86, 123–153.

Gong An Bu Jiao Tong Guan Li Ju (2014). http://www.mps.gov.cn/n16/n85753/ n85870/ index.html. Retrieved February 6, 2014.

Gohlke M., Beaudoin J., Amielh M. and Anselmet F. (2010). Shape influence on mean forces applied on a ground vehicle under steady cross-wind. *Journal of Wind Engineering and Industrial Aerodynamics*, *98*(8-9), 386-391.

Green M.F. and Cebon D. (1997). Dynamic interaction between heavy vehicles and highway bridges. *Computers & Structures*, *62*(2), 253-264.

Gu M. and Qin X.R. (2004). Direct identification of flutter derivatives and aerodynamic admittances of bridge decks. *Engineering Structures*, *26*, 2161-2172.

Gu, M. Zhang, R.X. and Xiang H.F. (2000). Identification of flutter derivatives of bridge decks. *Journal of Wind Engineering and Industrial Aerodynamics*, *84*(2), 151-162.

Guilmineau E. and Chometon F. (2009). Effect of side wind on a simplified car model: experimental and numerical analysis. *Journal of Fluids Engineering-transactions*, *131*(2), 021104.

Guo W.H. (2003). Dynamic analysis of coupled road vehicle and long span cable-stayed bridge systems under cross winds. PhD thesis, The Hong Kong Polytechnic University.

Guo W.H. and Xu Y.L. (2001). Fully computerized approach to study cable-stayed bridge-vehicle interaction. *Journal of Sound and Vibration*, *248*(4), 745-761.

Guo W.H. and Xu Y.L. (2006). Safety analysis of moving road vehicles on a long bridge under crosswind. *Journal of Engineering Mechanics*, *132*(4), 438-446.

Han T. (1989). Computational analysis of three-dimensional turbulent flow around a bluff body in ground proximity. *AIAA Journal*, *27*(9), 1213-1219.

Han W.S. (2006). Three-dimensional coupling vibrations of wind-vehicle-bridge system. PhD thesis, Tongji University (in Chiness)

Hargreaves D. and Morvan H. (2008). Initial validation of cross wind effects on a static high-sided vehicle. *International Journal of CFD Case Studies*, 7, 17-31.

Hatanaka A. and Tanaka H. (2002). New estimation method of aerodynamic admittance function. *Journal of wind engineering and industrial aerodynamics*, *90*, 2073-2086.

Heath A.N. (1989). Modeling and simulation of road roughness, Suppl. *Vehicle System Dynamics*, *18*, 275-284.

Henchi K. and Fafard M. (1997). Dynamic behavior of multi-span beams under moving loads. *Journal of Sound and Vibration*, *199*(1), 33-50.

Huang L. and Liao H. (2011). Identification of flutter derivatives of bridge deck under multi-frequency vibration. *Engineering Applications of Computational Fluid Mechanics*, *5*(1), 16-25.

Huang L., Liao H., Wang B. and Li Y. (2009). Numerical simulation for aerodynamic derivatives of bridge deck. *Simulation Modelling Practice and Theory*, *17*(4), 719-729.

Humphreys N.D. and Baker C.J. (1992). Forces on vehicles in cross winds from moving model tests. *Journal of Wind Engineering and Industrial Aerodynamics*, *41-44*, 2673-2684.

Hwang E.S. and Nowak A.S. (1991). Simulation of dynamic for bridges. *Journal of Structural Engineering*, *117*, 1413-1434.

ISO 8608 (1995). Mechanical vibration – road surface profiles – reporting of measured data , International Organization for Standardization, ISO.

ISO (1997). Mechanical vibration and shock – Evaluation of human exposure to whole-body vibration, ISO 2631-1, International Organization for Standardization, ISO.

Jancauskas E.D. and Melbourne W.H. (1986). The aerodynamic admittance of two-dimensional rectangular section cylinders in smooth flow, *Journal of Wind Engineering and Industrial Aerodynamics*, *23*, 395-408.

Jeong U.Y. and Kwon S. (2003). Sequential numerical procedures for predicting flutter velocity of bridge sections. *Journal of Wind Engineering and Industrial Aerodynamics*, *91*(1-2), 291-305.

Kaimal J.C., Izumi Y., Wyngaard J.C. and Cote, R. (1972). Spectral Characteristics of Surface-Layer Turbulence. *Quarterly Journal of the Royal Meteorological Society*, *98*(417), 563-589.

Kamash K.M.A and Robson J.D. (1978). The application of isotropy in road surface modeling. *Journal of Sound and Vibration*, *57*(1), 89-100.

Khondge A.D., Sovani S.D., Lokhande B.S., Jain S.K. and Long M.P. (2004). Simulation of the flow-field around a generic tractor-trailer truck. S*AE technical paper 2004-01-1147*.

Kozmar H., Butler K. and Kareem A. (2012). Transient cross-wind aerodynamic loads on a generic vehicle due to bora gusts. J*ournal of Wind Engineering and Industrial Aerodynamics*, *111*, 73-84.

Krajnovic S. (2009). Large eddy simulation of flows around ground vehicles and other bluff bodies. *Philosophical Transactions. Series A, Mathematical, physical, and engineering*, *367*, 2917-2930.

Krajnovic S. and Davidson L. (2003). Numerical study of the flow around a bus-shaped Body. *Transactions of the ASME*, *125*, 500-509.

Krajnović S., Ringqvist P. and Basara B. (2012). Comparison of partially averaged Navier–Stokes and large-eddy simulations of the flow around a cuboid influenced by crosswind. *Journal of Fluids Engineering*, *134*, 101202.

Kuroda S. (1997). Numerical simulation of flow around a box girder of a long span suspension bridge. *Journal of Wind Engineering and Industrial Aerodynamics*, *67-68*, 239-252.

Larose G.L., Tanaka H., Gimsing N.J. and Dyrbye C. (1998). Direct measurements of buffeting wind forces on bridge decks. *Journal of Wind Engineering and Industrial Aerodynamics*, 74-76, 809-818.

Larsen A. and Walther J.H. (1997). Aeroelastic analysis of bridge girder sections based on discrete vortex simulations. *Journal of Wind Engineering and Industrial Aerodynamics*, *67-68*, 253-265.

Larsen A. and Walther J.H. (1998). Discrete vortex simulation of flow around five generic bridge deck sections. *Journal of Wind Engineering and Industrial Aerodynamics*, *77-78*, 591-602.

Li C. and Wang L. (2004). An immersed boundary finite difference method for LES of flow around bluff shapes. *International Journal for Numerical Methods in Fluids*, *46*(1), 85-107.

Li L. (2009). Aerodynamic Coefficients of Typical Vehicles and Disturbance of Bridge Deck and Tower. Master thesis, Tongji University, Shanghai, China (in Chinese).

Lowan A.N. (1935). On transverse oscillations of beams under the action of moving variable loads. *Philosophical Magazine Series 7*, *19*(127), 708-15.

Lumley J.L. and Panofsky H.A. (1964). The Structure of Atmospheric Turbulence. Wiley, New York.

Macadam, C. C. (1992). The Crosswind Sensitivity of Unladen Doubles and Triples Combinations and Their Susceptibility to Wind-Induced Offtracking and Rollover. *Vehicle System Dynamics, 20*, 432-445.

Mansor S. and Passmore M.A. (2013). Effect of Rear Slant Angle on Vehicle Crosswind Stability Simulation on a Simplified Car Model. *International Journal of Automotive Technology, 14*(5), 701-706.

Maruyama Y., Yamazaki F. (2006). Driving simulator experiment on the moving stability of an automobile under strong crosswind. *Journal of Wind Engineering and Industrial Aerodynamics*, *94*, 191-205.

Menter F.R. (1994). Two-equation eddy-viscosity turbulence models for engineering applications. *AIAA Journal*, *32*(8), 1598-1605.

Mishra S.S., Kumar K. and Krishna P. (2006). Identification of 18 flutter derivatives by covariance driven stochastic subspace method. *Wind & Structures*, *9*(2), 159-178.

Miyata T. and Yamada H. (1990). Coupled flutter estimate of suspension bridges. *Journal of Wind Engineering and Industrial Aerodynamics*, *33*, 341-348.

Murakami S. (1997). Current status and future trends in computational wind engineering. *Journal of Wind Engineering and Industrial Aerodynamic*s, *67-68*, 3-34.

Nieto F., Hernandez S., Jurado J. and Baldomir A. (2010). CFD practical application in conceptual design of a 425 m cable-stayed bridge. *Wind and Structures*, *13*(4), 309-326.

Oliva J., Astiz M.A., Goicolea J.M. and Antolin P. (2013). Fully three-dimensional vehicle dynamics over rough pavement. *Proceedings of the Institution of Civil Engineers-Transport, 166*(3), 144-157.

Onyemelukwe O.U., Torkamani M.A.M. and Bosch H.R. (1997). Numerical simulation of wind-induced forces on bridge deck sections of long-span bridges. *Computers & Structures*, *62*(4), 667-679.

Passmore M.A, Richardson S. and Imam A. (2001). An experimental study of unsteady vehicle aerodynamics. *Proceedings of the Institution of Mechanical Engineers, Part D: Journal of Automobile Engineering*, *215*(7), 779-788.

Petzäll J., Torlund P.Å., Falkmer T., Albertsson P. and Björnstig U. (2008). Aerodynamic design of high-sided coaches to reduce cross-wind sensitivity, based on wind tunnel tests. *International Journal of Crashworthiness*, *13*(2), 185-194.

Petzäll J., Albertsson P., Falkmer T. and Björnstig U. (2005). Wind forces and aerodynamics: contributing factors to compromise bus and coach safety? *International Journal of Crashworthiness*, *10*(5), 435-444.

Phillips W.F. (2010). Mechanics of flight, second editions. John Wiley & Sons.

Proppe C. and Wetzel C. (2010). A probalibistic approach for assessing the crosswind stability of ground vehicles. *Vehicle System Dynamics*, *48supplement*, 411-428

Poulsen N.K., Damsgaard A. and Reinhold T.A. (1992). Determination of flutter derivatives for the Great Belt Bridge. *Journal of Wind Engineering and Industrial Aerodynamics*, *57*, 295-305.

Quinn A.D., Sterling M., Robertson A.P. and Baker C.J. (2007). An investigation of the wind-induced rolling moment on a commercial vehicle in the atmospheric boundary layer. *Proceedings of the Institution of Mechanical Engineers Part D-Journal of Automobile Engineering*, *221*(D11), 1367-1379.

Rocchi D., Rosa L., Sabbioni E., Sbrosi M. and Belloli M. (2012). A numerical-experimental methodology for simulating the aerodynamic forces acting on a moving vehicle passing through the wake of a bridge tower under cross wind. *Journal of Wind Engineering and Industrial Aerodynamics*, *104-106*, 256-265.

SAEJ670 (2008).Vehicle dynamics terminology. SAE international.

Sadiku S. and Leipholz H.H.E. (1987). On the dynamics of elastic systems with moving concentrated masses. *Ingenieur-Archiv*, *57*, 223-242.

Sarkar P.P., Jones N. and Scanlan R.H. (1994). Identification of aeroelastic parameters of flexible bridges. *Journal of Engineering Mechanics*, *120*(8), 1718-1741.

Sarkar P.P., Caracoglia L., Haan F.L., Sato H. and Murakoshi J. (2009). Comparative and sensitivity study of flutter derivatives of selected bridge deck sections, part 1: analysis of inter-laboratory experimental data. *Engineering Structures*, *31*, 158-169.

Sarwar M., Ishihara T., Shimada K., Yamasaki Y. and Ikeda T. (2008). Prediction of aerodynamic characteristics of a box girder bridge section using the LES turbulence model. *Journal of Wind Engineering and Industrial Aerodynamics*, *96*(10-11), 1895-1911.

Scanlan R.H. (1978a). The action of flexible bridge under wind I: flutter theory. *Journal of Sound and Vibration*, *60*(2), 187-199.

Scanlan R.H. (1978b). The action of flexible bridges under wind. II: Buffeting theory. *Journal of Sound and Vibration*, *60*(2), 201-211.

Scanlan R.H. (2001). Reexamination of sectional aerodynamic force functions for bridges. *Journal of Wind Engineering and Industrial Aerodynamics*, 89 (14-15), 1257-1266.

Scanlan R.H., Beliveau J.G. and Budlong K.S. (1974). Indicial Aerodynamic Functions for Bridge Decks. *Journal of the Engineering Mechanics*, *100*, 657-672.

Scanlan R.H. and Tomko J.J. (1971). Airfoil and bridges deck flutter derivatives. *Journal of Engineering Mechanics*, *97*(6), 1717-1733.

Sears W.R. (1941). Some aspects of non-stationary airfoil theory and its practical application. *Journal of the Aeronautical Sciences*, *8*(3) 104-108.

Selvam R., Govindaswamy S. and Bosch H. (2002). Aeroelastic analysis of bridges using FEM and moving grids. *Wind and Structures*, *5*(2-4), 257-266.

Shinozuka M. (1971). Simulation of multivariate and multidimensional random process. *Journal of the Acoustical Society of America*, *49* (1), 357-368.

Shirai S. and Ueda T. (2003). Aerodynamic simulation by CFD on flat box girder of super-long-span suspension bridge. *Journal of Wind Engineering and Industrial Aerodynamics*, *91*(1-2), 279-290.

Sigbjörnsson R. and Snæbjörnsson J.T. (1998). Probabilistic assessment of wind related accidents of road vehicles: a reliability approach. *Journal of Wind Engineering and Industrial Aerodynamics*, *74-76*, 1079-1090.

Simiu P.D. and Scanlan R.H. (1996). Wind Effects on Structures, third editon, Wiley, New York.

Smith J.W. (1988). Vibration of structures: Applications in civil engineering design. Chapman and Hall, New York.

Stanišić M.M. and Hardin J.C. (1969). On the response of beams to an arbitrary number of concentrated moving masses. *Journal of The Franklin Institute*, *287*, 115-23.

Starossek U., Aslan H. and Thiesemann L. (2009). Experimental and numerical identification of flutter derivatives for nine bridge deck sections. *Wind and Structures*, *12*(6), 519-540.

Sterling M., Quinn A.D., Hargreaves D.M., Cheli F., Sabbioni E., Tomasini G., Delaunay D., Baker C.J. and Morvan H. (2010). A comparison of different methods to evaluate the wind induced forces on a high sided lorry. *Journal of Wind Engineering and Industrial Aerodynamics*, *98*(1), 10-20.

Sun L. and Deng X. (1998). Predicting vertical dynamics loads caused by vehicle-pavement interaction. *Journal of Transportation Engineering*, *124*(5), 470-478.

Sun L. and Su J. (2001). Modeling random fields of road surface irregularities.

International Journal of Road Materials Pavement Design, *2*(1), 49-70.

Tannehill J.C., Anderson D.A. and Pletcher R.H. (1997). Computational Fluid Mechanics and Heat Transfer, Second Edition. Taylor & Francis, London.

Taylor I. and Vezza M. (2001). Application of a discrete vortex method for the analysis of suspension bridge deck sections. *Wind & Structures*, *4*(4), 333-352.

Taylor I. and Vezza, M. (2002). Aeroelastic stability analysis of a bridge deck with added vanes using a discrete vortex method. *Wind & Structures*, *5*(2-4), 277-290.

Taylor I., Vezza M. and Salisbury I. (2008). Numerical investigation of the effects of pedestrian barriers on aeroelastic stability of a proposed footbridge. *Journal of Wind Engineering and Industrial Aerodynamics*, *96*(12), 2418-2437.

Taylor I. and Vezza M. (2009). A numerical investigation into the aerodynamic characteristics and aeroelastic stability of a footbridge. *Journal of Fluids and Structures*, *25*(1), 155-177.

Theodosen T. (1935). General theory of aerodynamic instability and the mechanism of flutter, *NACA Report No. 496*.

Timoshenko S., Young D.H. and Weaver W. (1974). Vibration Problems in Engineering, fourth edition. Wiley, New York.

Ting E.C., Genin J. and Ginsberg J.H. (1974). A general algorithm for the moving mass problem. *Journal of Sound and Vibration*, *33*(1), 49-58.

Tsubokura M., Nakashima T., Oshima N., Kitoh K., Zhang H., Onishi K. and Kobayashi T. (2007). Current status on high performance computing for vehicle aerodynamics using Large Eddy Simulation. *FEDSM 2007: Proceedings of the 5th Joint ASME/JSME Fluids Engineering*, 1191-1197.

Tsubokura M., Kobayashi T., Nakashima T., Nouzawa T., Nakamura T., Zhang H. and Onishi K. and Oshima N. (2009). Computational visualization of unsteady flow around vehicles using high performance computing. *Computers & Fluids*, *38*(5), 981-990.

Tsubokura M., Nakashima T., Kitayama M., Ikawa Y., Doh D.H. and Kobayashi T. (2010). Large eddy simulation on the unsteady aerodynamic response of a road vehicle in transient crosswinds. *International Journal of Heat and Fluid Flow*, *31*, 1075-1086.

Versteeg H.K. and Malalasekera W. (2007). An Introduction to Computational Fluid Dynamics: The Finite Volume Method, Second Edition. Pearson Education Limited, England.

Wetzel C. and Proppe C. (2010). Stochastic modeling in multibody dynamics: aerodynamic loads on ground vehicles. *Journal of computational and nonlinear dynamics*, *5*, 031009.

Wu J. and Chen S.R. (2011). Probabilistic dynamic behavior of a long-span bridge under extreme events. *Engineering Structures*, *33*, 1657-1665.

Xu Y.L. (2013). Wind effects on cable-stayed bridges. Wiley, Singapore.

Xu, Y.L. and W.H. Guo. (2003a). Dynamic analysis of coupled road vehicle and cable-stayed bridge systems under turbulent wind. *Engineering Structures*, *25*, 473-486.

Xu Y.L. and Guo W.H. (2003b) Dynamic behaviour of high-sided road vehicles subject to a sudden crosswind gust. *Wind and Structures*, *6*(5), 325-346.

Xu Y.L. and Guo W.H. (2004). Effects of bridge motion and crosswind on ride comfort of road vehicles. *Journal of Wind Engineering and Industrial Aerodynamics*, *92*(7-8), 641-662.

Xu Y.L. and Xia Y. (2012). Structural health monitoring of long-span suspension bridges. Spon Press (Taylor & Francis), UK.

Yamada H., Miyata T. and Ichikawa H. (1992) Measurement of aerodynamic coefficients by system identification methods. *Journal of Wind Engineering and Industrial Aerodynamics*, *42*, 1255-1263.

Yang W.W. and Chang T.Y.P. (1998). Numerical simulation of turbulent fluctuations along the axis of a bridge. *Engineering structures*, *20* (9), 837-848.

Yang W.W., Chang T.Y.P. and Chang C.C. (1997). An efficient wind field simulation technique for bridges. *Journal of Wind Engineering and Industrial Aerodynamics*, *67-68*, 697-708.

Yang Y.B., Chang, C.H. and Yau J.D. (1999). An element for analyzing vehicle-bridge systems considering vehicle's pitching effect. *International Journal for Numerical Methods in Engineering*, *46*(7), 1031-1047.

Yang Y.B. and Lin B.H. (1995). Vehicle-bridge interaction analysis by dynamic condensation method. *Journal of Structural Engineering*, *121*(11), 1636-1643.

Yang Y.B. and Yau J.D. (1997). Vehicle-bridge interaction element for dynamic analysis. *Journal of Structural Engineering*, *123*(11), 1512-1518.

Yoshimoto K. (1968). Simulation of driver-vehicle systems using a predictable model of driver's steering. *Journal of the Japan Society of Mechanical Engineers*, *71*(596), 1181-1186.

Zhou L. and Ge Y. (2008). Wind Tunnel Test for Vortex-induced Vibration of Vehicle-bridge System Section Model. *Journal of the Brazilian Society of Mechanical Sciences and Engineering*, *30*(2), 110-117.

Zhu L.D., Li L., Xu Y.L. and Zhu Q. (2012). Wind tunnel investigations of aerodynamic coefficients of road vehicles on bridge deck. *Journal of Fluids and Structures*, *30*, 35-50.

Zhu Z., Gu M. and Chen Z (2007). Wind tunnel and CFD study on identification of flutter derivatives of a long-span self-anchored suspension bridge. *Computer-aided Civil and Infrastructure Engineering*, *22*(8): 541-554.

Zhou Z., Ma R. (2010). Numerical simulation study of the Reynolds number effect on two bridge decks based on the deterministic vortex method. *Wind and Structures*, *13*(4), 347-362.